Search for new physics produced via Vector Boson Fusion in final states with large missing transverse momentum with the ATLAS detector

Marta Maria Perego

UNIVERSITÉ PARIS SUD
Comprendre le monde, construire l'avenir

Search for new physics produced via Vector Boson Fusion in final states with large missing transverse momentum with the ATLAS detector

Thèse de doctorat de l'Université Paris-Saclay
préparée à l'Université Paris-Sud au
Commissariat à l'Énergie Atomique et aux Énergies Alternatives (CEA),
au sein du Département de Physique des Particules (DPhP) de
l'Institut de Recherche sur les lois Fondamentales de l'Univers (IRFU)

École doctorale n°517 Sciences physiques: particules, hadrons, énergie, noyau, instrumentation, imagerie, cosmos et simulation (PHENIICS)

Spécialité de doctorat : physique des particules

Thèse présentée et soutenue à Saint Aubin, le 10 Avril 2018, par

Marta Maria Perego

Composition du Jury :

Dirk Zerwas Directeur de Recherche, Université Paris Sud	Président
Klaus Mönig Professeur associé, DESY	Rapporteur
Fabienne Ledroit Directeur de Recherche, Université Grenoble Alpes	Rapporteuse
Suzanne Gascon Professeur, Université Claude Bernard, Lyon	Examinatrice
Marco Taoso Chargé de Recherche, INFN Torino	Examinateur
Claude Guyot Directeur de Recherche, CEA Saclay, IRFU/DPhP	Directeur de thèse
Marco Cirelli Directeur de Recherche, LPTHE, CNRS & Sorbonne Université	Co-Directeur de thèse
Filippo Sala Junior Research Staff, DESY	Co-encadrant

"To my men:
Riccardo and Pietro"

This work is supported in part by the European Research Council (ERC) under the EU Seventh Framework Programme (FP7/2007-2013)/ERC Starting Grant (agreement n. 278234 - 'NEWDARK' project).

Contents

Aknowledgements

I started my Phd just before the beginning of the so called Run2 phase of the LHC. I was so excited to have the possibility to explore those new data, collected at energies never explored before, and discover if they were telling us some hints about new physics. Now that I defended my PhD thesis, I confirm that it has been an exciting experience. Even if no sign of new physics showed up (yet), analyzing the LHC data has been incredibly interesting.
I have been very lucky for the opportunity I had to meet and work with so many talented and knowledgeable scientists during these years.
Firstly I would like to thank my supervisors Claude Guyot and Marco Cirelli.
Thank you Claude for all the discussions we had, for your advice and your suggestions. You have shown me the real spirit of a scientist who never get discouraged in front of all the issues and challenges encountered but always faces them with curiosity, as an opportunity to learn something new and deepen our knowledge.
Thank you Marco for giving me the opportunity to be part of the New Dark group. Since the very first days I joined the group, I have been impressed by your curiosity and enthusiasm in the search for Dark Matter which have been inspiring to me.
Thank you Filippo for all your help, your useful suggestions and your curiosity in the hunt for dark matter. Without your help it would have not been possible to generate and test the signal DM samples. Thank you Marco Zaro for your precious help and tips for generating the events with Madgraph.
Thank you Samira for your support and for all the useful discussion we had. Thanks for being there whenever I needed some help.
Thank you Claudia Nones for the help and support.
A special thank you to Paolo Francavilla, I could not imagine a better person to work with during my qualification task. Thank you for introducing me to the $E_{\mathrm{T}}^{\mathrm{miss}}$ world and for all the time you spent explaining me things. Thank you also for the nice lunches and coffe breaks in Jussieu.
Thank you to the $E_{\mathrm{T}}^{\mathrm{miss}}$ group and to the $E_{\mathrm{T}}^{\mathrm{miss}}$ and $Jet/E_{\mathrm{T}}^{\mathrm{miss}}$ conveners: Claire Lee, Peter Loch, Cigdem Issever, David Lopez, David Miller and all the others.
A very special thanks goes to the VBF H invisible team that I have been working with for most of my PhD. It has been a great pleasure for me to work with you! Thank you Alex for all the help and suggestions you gave me and for always being available for advice. Thank you Andy for your useful comments and suggestions during the meetings. Thanks to Loan for all our discussion, for all the checks we did together for the fitting codes and for the all the nice skype calls/chats we had. Thank you Ben for your help and suggestions and for always reminding us that "everything will be fine". Thank you Christian for fighting so hard against multijets. Finally we have prevailed! Thank you Bill, Rui, Tae, Ketevi, Young Kee and all the others.
Thanks to the exotics and JDM conveners (Marie-Helene, Klaus, Gabriel and all the

others) who have been very helpful and gave us instructive suggestions.
Thank you to the jury members of my thesis who accepted to read and correct it and thanks for the nice discussion that we had at the defense.
Thank you the Milan ATLAS group people (Leonardo, Silvia, Donatella) who are always available for advice.
Thank you to the entire ATLAS group at CEA, in particular thanks to the other PhDs: thank you Oleh for always being available when I had some questions, thank you Remie for all the nice time spent together and for visiting me when I was at home with baby Pietro, thank you Aleksandra for organizing a surprise birthday party at SPP for me, thank you Maria, Matthias and all the others.
Thanks to my friends at CERN and all over the world and thanks to all the ones who helped me during these years (I can't list you all!). Thank you Rimo for your tips about Histfitter and for always being available for a coffee whenever I passed from CERN.
Last but not least, thanks to my family. To my parents and to my sisters, thank you for always helping me and for always being available even if 900 km away.
Finally thanks to my men. Thank you to my little big helper Pietro: your always-on-the-face smile has been the best motivation for me during these years. You have been the first person in the world to know the unblinded results of the VBF H invisible analysis, you now know many ATLAS secrets!
Thanks to my beloved husband for all your support and for each steps of this adventure that we faced together.

Résumé français

Cette thése présente des recherches sur la nouvelle physique produite par le processus de Fusion de Bosons Vecteur (VBF) dans les états finaux avec une grand impulsion transverse manquante ($E_{\mathrm{T}}^{\mathrm{miss}}$) en utilisant 36.1 fb^{-1} de données de collisions proton-proton avec une énergie dans le centre de masse de 13 TeV, recueillies par l'expérience ATLAS au Large Hadron Collider (LHC) au CERN en 2015 et 2016.

Le context expérimental

Le collisionneur LHC est un accélérateur et collisionneur de hadrons qui est situé au Cern (Geneva) et installé à l'intérieur d'un tunnel circulaire de 26.7km qui a été construit pour la machine LEP du CERN. Il est conçu pour faire des collision avec des faisceaux de protons et peut également collisionner des ions lourds (Pb). En 2015, le LHC est entré dans la phase dite *Run 2* et les faisceaux de protons sont en collision à un énergie dans le centre de masse de 13 TeV.
Pour collecter les données provenant des collisions du LHC, les détecteurs de particules sont construits autour des points d'interaction du LHC. Les détecteurs de particules à haute énergie sont les instruments utilisés pour mesurer les propriétés cinématiques des particules produites dans chaque collision.
Au LHC, quatre expériences indépendantes sont construites autour des points d'interaction: ATLAS (A Toroidal Lhc ApparatuS) et CMS (Compact Muon Solenoid) sont des expériences polyvalentes, conçues pour couvrir un vaste programme de physique, de la recherche de les mesures du boson de Higgs et du modèle standard à la recherche de phénomènes audelá du modéle standard, LHCb (LHC-beauty) sont consacrées aux études de physique des quarks b et à la violation de CP, tandis qu'ALICE (A Large Ion Collider Experiment) étudie les collisions de noyaux lourds.
Les détecteurs multi-usages modernes utilisés dans les collisionneurs de particules à haute énergie, tels que ATLAS et CMS, ont une structure commune. Le concept de base est de faire interagir toutes les particules dans le détecteur pour les distinguer par leurs interactions avec la matière et pour identifier et mesurer leurs propriétés. Par conséquent, les détecteurs sont construits comme une série de différents modules qui sont ordonnés radialement à partir du point d'interaction et qui sont consacrés à la détection des différents types d'interactions. En combinant les informations des différents sous-détecteurs, on identifie la cinématique et les propriétés des différentes particules produites dans la collision proton-proton.
Les données utilisées pour cette thèse ont été collectées en 2015 et 2016 par le détecteur ATLAS.
Le détecteur ATLAS présente une symétrie cylindrique autour de la ligne du faisceau. Il mesure 25 m de haut et 44 m de long, son poids total est d'environ 7000 tonnes. Le

détecteur ATLAS est (presque parfaitement) symétrique avant-arriére par rapport au point d'interaction.

L'impulsion transverse manquante

Toutes les particules du modèle standard de la physique des particules (SM), à l'exception des neutrinos, interagissent dans le détecteur et sont identifiées à partir des dépôts d'énergie ou des traces qu'elles laissent à l'intérieur. Les neutrinos sont un cas particulier: ils interagissent si faiblement qu'ils traversent le détecteur ATLAS sans laisser de traces. De même, si de nouvelles particules prédites par certains modèles de physique au-delà du modèle standard (BSM), telles que des particules de matière noire, étaient produites lors d'une interaction, elles s'échapperaient également du détecteur sans aucune trace ni aucun dépôt d'énergie.
Comment les particules invisibles peuvent-elles être détectées avec le détecteur ATLAS? Contrairement aux autres particules SM, elles peuvent être détectées indirectement, en s'appuyant sur la cinématique de l'événement.
Pour les particules relativistes et pour une réponse idéale du détecteur, si aucune particule invisible n'est émise et si toutes les particules produites dans l'événement sont reconstruites, la somme des impulsions transversales de toutes les particules produites dans un événement devrait être égale à zéro.
Le vecteur de l'impulsion transverse manquante est défini comme l'opposé de la somme des vecteurs négatifs des impulsions de toutes les particules détectées.

$$\mathbf{E_T^{miss}} = (E_x^{miss}, E_y^{miss})$$
$$E_T^{miss} = |\mathbf{E_T^{miss}}| = \sqrt{(E_x^{miss})^2 + (E_y^{miss})^2}$$

oú:

$$E_x^{miss}(E_y^{miss}) = -\sum E_x(E_y) \tag{1}$$

$E_{\mathrm{T}}^{\mathrm{miss}}$ est reconstruit comme une somme vectorielle de différents termes. Il y a deux contributions principales. La première est constitué d'objets dits *durs* (*hard*) identifiés et mesurés par l'analyse (leptons, photons, jets), la seconde provient de la composante dite *soft*, constituée des traces net des dépôts d'énergie dans le calorimètre non associés à des objets durs. Il existe différentes manières de définir et de reconstruire le composant soft (*soft term*). Le choix de la version de la composante soft influence la performance de la reconstruction de $E_{\mathrm{T}}^{\mathrm{miss}}$.

En plus de impulsion transverse manquante ($E_{\mathrm{T}}^{\mathrm{miss}}$) causée par des particules invisibles, un déséquilibre de quantité de mouvement peut être causé par la perte de particules qui échappent à la couverture (acceptance) du détecteur ou qui sont mal reconstruites. Dans ce cas, $E_{\mathrm{T}}^{\mathrm{miss}}$ est généralement appelé faux $E_{\mathrm{T}}^{\mathrm{miss}}$. $E_{\mathrm{T}}^{\mathrm{miss}}$ se révèle ainsi être une mesure importante pour quantifier la performance globale de reconstruction d'un événement.
Une bonne mesure d'$E_{\mathrm{T}}^{\mathrm{miss}}$ est donc cruciale au LHC: les analyses de recherche et les mesures de précision nécessitent une estimation précise d'$E_{\mathrm{T}}^{\mathrm{miss}}$. L'$E_{\mathrm{T}}^{\mathrm{miss}}$ joue un rôle important dans tous les processus SM impliquant des neutrinos et dans des processus avec d'éventuelles particules BSM faiblement interactives prédites.
Dans cette thèse, la définition de $E_{\mathrm{T}}^{\mathrm{miss}}$ est présentée, différents algorithmes de $E_{\mathrm{T}}^{\mathrm{miss}}$ sont décrits et leur performance est étudiée. Enfin, les méthodes utilisées pour estimer la systématique sont discutées.

Contexte théorique

En 2012, la découverte d'une nouvelle particule avec des propriétés compatible avec celles attendues pour le boson de Higgs du modèle standard a été annoncée au CERN. Grâce à cette découverte, la dernière pièce manquante du modèle standard a été définie et aucune divergence significative par rapport à ses prédictions n'a été observée sur un grand nombre de mesures de précision.
Cependant, nous savons que nous n'avons pas une description microscopique complète de la nature. Du point de vue de la physique des particules, plusieurs indices nous indiquent que, malgré son niveau de précision extraordinaire dans la description des phénoménes de physique des particules, le modéle standard (SM) ne répond pas à de nombreuses questions. Ainsi, plusieurs théories Beyond Standard Model (BSM) ont été proposées. De plus, à partir de mesures cosmologiques, nous ignorons la nature de 95% de l'Univers. Plusieurs indications observationnelles en faveur de l'existence d'une nouvelle composante de la matière (la matière noire, DM) ont été trouvées sur un large éventail d'échelles astronomiques, mais ses propriétés physiques sont encore inconnues. Par conséquent, l'une des principales questions sans réponse aujourd'hui est liée à la nature de la matière noire. Parmi les candidats DM, il y a les particules massives interagissant faiblement (WIMPs). De telles particules sont prédites dans des modéles de physique au-delá de SM, tels que la supersymétrie, les théories avec de grandes dimensions supplémentaires ainsi que des modèle plus phénoménologiques comme le modéle *Minimal Dark Matter*. La supersymétrie est l'une des théories les plus populaires proposées comme extension du SM. Il résout le problème de la hiérarchie de masse du Higgs et prédit un candidat DM viable. Les théories SUSY sont caractérisées par de nombreux paramétres et une phénoménologie complexe. Le modéle *Minimal Dark Matter* (MDM), en contraste avec ces théories, suit une approche minimaliste. L'idée derrière MDM est de se concentrer sur le problème de la matière noire et d'ajouter la quantité minimale de nouvelle physique BSM qui peut fournir un bon candidat DM. Leurs candidats constituent également une référence dans l'esprit des modéles simplifiés. Un lien naturel entre les particules SM et DM est que le boson de Higgs découvert pourrait se désintégrer en particules de matière noire ou en particules massives à vie longue. Ceci est appelé la désintégration invisible du boson de Higgs et peut être exploré au LHC.

Désintégration invisible du boson de Higgs

Cette thése se concentre sur la recherche de la désintégration invisible du boson de Higgs produit via le mode VBF.
Comme le modéle standard de la physique des particules (MS) prédit une désintégration invisible de Higgs uniquement à travers le mode $H \to ZZ^* \to \nu\bar{\nu}\nu\bar{\nu}$ avec un rapport d'embranchement BR$\sim$0.1%, si une désintégration en particules invisibles du boson de Higgs était observée avec un BR supérieur, ce serait un signe de nouvelle physique. Plusieurs modéles au-delá du modéle standard (BSM) prédisent des désintégrations du boson de Higgs en particules de matière noire (DM, non détectées) ou en particules massives neutres à vie longue.
Parmi les recherches H $\to$ particules invisibles, la plus sensible est celle où le Higgs est produit via le mode VBF. Son état final est caractérisé par deux jets énergétiques, avec les caractéristiques typiques du mode VBF (c'est-á-dire une grande séparation angulaire et une grande masse invariante des deux jets) et une grande impulsion transverse man-

quante ($E_{\mathrm{T}}^{\mathrm{miss}}$> 180 GeV) (Fig. 1).
Pour sélectionner un échantillon d'événements candidats de signal, une région de signal (SR) est définie pour maximiser la fraction d'événements de signal attendus par rapport au nombre d'événements prédits par le SM.
Les processus MS qui peuvent peupler la SR proviennent principalement des processus $Z \to \nu\nu + jets$ et $W \to \ell\nu + jets$, oú le lepton est perdu ou non reconstruit. Leur contribution est estimée avec une approche dite *semi-data driven*: des régions dédiées enrichies en événements $W \to \ell\nu / Z \to \ell\ell$ sont utilisées pour normaliser les données des estimations de Monte Carlo (MC) en utilisant une technique de fit simultané (méthode du facteur de transfert) et pour les extrapoler à la SR. Un autre bruit de fond provient des événements multijet où la grande impulsion transverse manquante est engendrée principalement par *mis-measurements* de jet. Cette contribution devrait être fortement réduite en exigeant une grande $E_{\mathrm{T}}^{\mathrm{miss}}$, mais il est difficile de l'estimer avec précision. Comme les simulations MC ne sont pas suffisamment fiables pour l'estimer, il est nécessaire d'utiliser une méthode basée sur les données elles-mêmes (data-driven).
L'estimation de fond SM prédit est comparée aux données SR observées. Comme aucun excés n'est trouvé, une limite supérieure sur le BR (H→ invisible) est calculée.

WIMP triplet de matière noire

L'analyse est ensuite réinterprétée dans le cadre de modéles inspirés du modéle Minimal Dark Matter. Le cas d'un nouveau triplet fermionique électrofaible, avec une hypercharge nulle et respectant la conservation du le nombre B-L, ajouté au SM fournit un bon candidat Dark Matter (WIMP pur). Si on considére l'abondance thermique estimée dans l'Univers observable actuel, la masse du composant neutre est d'environ 3 TeV. Cependant des masses plus faibles sont également envisageables dans le cas de mécanismes de production non thermiques ou lorsque le triplet ne constitue qu'une fraction de l'abondance de DM. Il pourrait alors être produit auprès des collisionneurs proton-proton tels que le LHC et il peut être exploré de différentes maniéres.
Une fois produites, les composantes chargées du triplet se désintégrent dans le composant neutre le plus léger, χ_0 , avec en plus des pions trés mous, en raison de la petite différence de masse entre les composants neutres et chargés. Ces pions de trés faible impulsion ne peuvent pas être reconstruits et sont donc perdus. Le χ_0 est reconstruit comme de l'$E_{\mathrm{T}}^{\mathrm{miss}}$ dans le détecteur. Par conséquent, lorsqu'il est produit via VBF, il donne lieu à une signature avec deux jets VBF et de l'$E_{\mathrm{T}}^{\mathrm{miss}}$, le même état final que celui qui a été étudié pour l'analyse de VBF Higgs→invisible.
Des points de masse différentes (de 90 GeV à 200 GeV) ont été engendrés avec les programmes Monte Carlo Madgraph + Pythia, dans le cadre du logiciel officiel ATLAS, et les limites supérieures sont calculées sur la section efficace fiducielle de production.
Des extrapolations à des luminosités plus élevées (Run3 et HL-LHC) en utilisant une approche simplifiée sont également présentées.

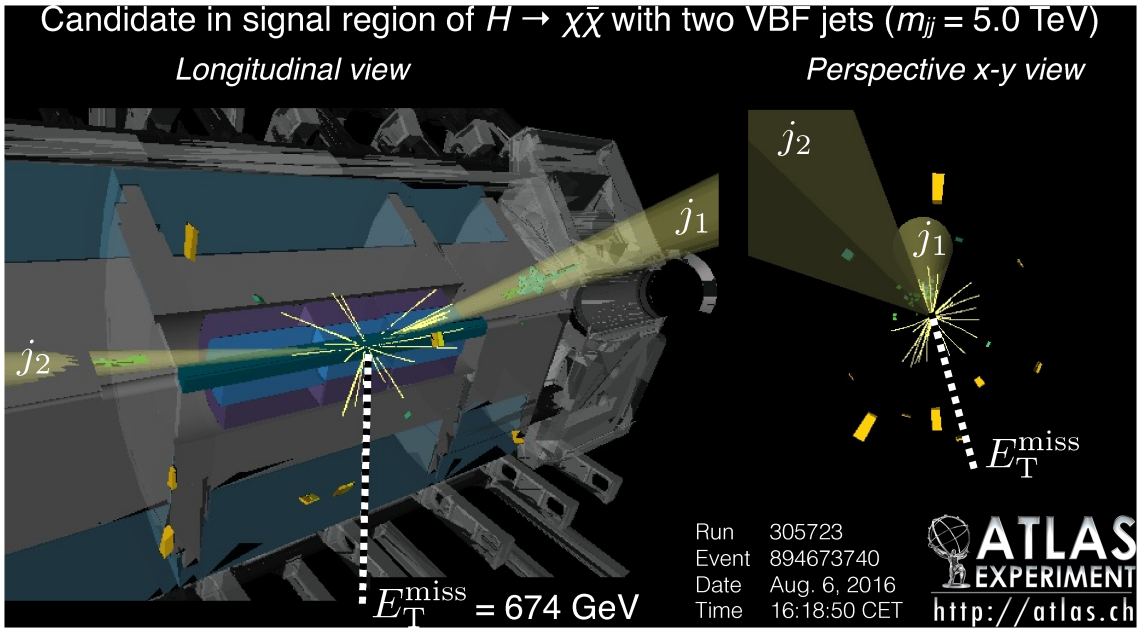

Figure 1: "Event display" d'événement candidat de signal dans la région de signal (SR) (M_{jj} =5.0 TeV, $\Delta\eta(j,j)$ =5.5, $\Delta\Phi(j,j)$ =0.7). [1]

Conclusions

Une recherche de la désintégration invisible du boson de Higgs produit via VBF en utilisant 36.1 des données fb^{-1} à $\sqrt{s} = 13$ TeV est présentée dans cette thèse. L'état final est défini par une grande énergie transverse manquante $E_{\mathrm{T}}^{\mathrm{miss}}$, provenant des particules invisibles issues de la désintégration du Higgs, et deux jets avec des caractéristiques typiques du VBF. Comme aucun excès n'est observé, une limite supérieure sur le BR(H→inv) est calculée.

Cette analyse est réinterprétée dans le contexte du modèle Minimal Dark Matter. Afin de tester le triplet MDM en mode de production VBF, les événements de signal ont dû être simulés. Différents points de masse ont été étudiés. Les résultats sont également extrapolés à des luminosités plus élevées.

Introduction

In 2012 the discovery of a new particle with properties very close to those expected for the Higgs boson of the Standard Model was announced at CERN. With this discovery, the last missing piece of the Standard Model has been set and no significant discrepancies with respect to its predictions have been observed over a large number of precision measurements. However, we know that we do not have a complete microscopic description of nature. From the particle physics point of view, several clues tell us that, despite its incredible level of precision in describing particle physics phenomena, the Standard Model (SM) does not answer many questions. Hence, several Beyond Standard Model (BSM) theories have been proposed. Moreover, from cosmological measurements we know that 95% of the universe is obscure to us. Several observational probes for the existence of a new component of matter (the so called *Dark Matter*, DM) have been found on a wide range of astronomical scales but its physical properties are still unknown. Hence, one of the main unanswered questions today is related to the nature of Dark Matter.
Among the most compelling DM candidates there are the *weakly interacting massive* particles (WIMPs), i.e. particles with $SU(2)_L$ Standard Model interactions and with a mass typical of the weak scale ($\sim$100 GeV). These particles are natural thermal relics of the early universe since a weak scale cross section gives the correct abundance to account for the predicted fraction of Dark Matter. This coincidence is called "WIMP miracle" and provides a strong indication for a WIMP (χ) in the mass range $\sim$10 MeV$< m_\chi <$ 100 TeV. Such particles are predicted in models of physics beyond SM, such as Supersymmetry, Large Extra Dimensions and the Minimal Dark Matter model. Supersymmetry is one of the most popular theory proposed as extension of the SM. It solves the Higgs mass hierarchy problem and it predicts a viable DM candidate. SUSY theories are characterized by many parameters and a complex phenomenology. The Minimal Dark Matter (MDM) model (chapter 6), as a contrast to these theories, follows a minimalistic approach. The idea behind MDM is to focus on the dark matter problem and add the minimal amount of new BSM physics which can provide a good DM candidate. Their candidates also provide a benchmark in the spirit of simplified models.
A natural link between the SM and the DM is that the discovered Higgs boson might decay into dark matter or long-lived massive particles. This is referred to as the invisible decay of the Higgs boson and can be probed at the LHC. As the SM predicts a Higgs invisible decay only through $H \to ZZ^* \to \bar{\nu}\nu\bar{\nu}\nu$ with Branching Ratio (BR) $\sim$0.1%, if an invisibly decaying Higgs boson would be observed with a higher BR, this would be a sign of new physics.
Typically, the final states of direct searches for $H \to$ invisible are defined by the presence of the invisible particles from the Higgs decay and by the particles and kinematics depending on the specific Higgs production mode. The only way to detect invisible final state particles (i.e. not interacting with the detector, such as DM particles), is to rely on the kinematics of the event: their presence can be inferred by an imbalance in the

vectorial sum of transverse momenta of all particles of the event. This quantity is usually called Missing Transverse Momentum and denoted as $E_{\mathrm{T}}^{\mathrm{miss}}$. The $E_{\mathrm{T}}^{\mathrm{miss}}$ reconstruction is therefore very important and complex, as it involves the transverse momenta of all the objects and energy deposits of an event. Different $E_{\mathrm{T}}^{\mathrm{miss}}$ algorithms, their performance and their systematic evaluation are discussed in the following.
In case of $H \rightarrow$ invisible decays, in order to have reconstructed $E_{\mathrm{T}}^{\mathrm{miss}}$ from the invisible particles, the Higgs boson needs to be produced with rather large transverse momentum (*boosted*). Typical ways to look for it are searches of associated production with Z and W of H($\rightarrow inv$), *gluon gluon fusion* $H(\rightarrow inv)$ plus initial state radiation and Vector Boson Fusion (VBF) $H(\rightarrow inv)$ searches. Among them, the VBF $H(\rightarrow inv)$ is the most sensitive one so far.
In this context, this thesis deals with a search looking for a Higgs decaying to invisible particles produced via Vector Boson Fusion and its reinterpretation in the context of models inspired by the MDM using data from LHC proton-proton collisions at $\sqrt{s}$=13 TeV recorded by ATLAS detector. Its final state is characterized by two energetic jets, with the typical features of the VBF mode (i.e. large separation in pesudorapidity and large invariant mass) and large missing transverse momentum ($E_{\mathrm{T}}^{\mathrm{miss}}$ >180 GeV) given by the invisible particles from the Higgs decay.

0.1 Author's contribution

The thesis presented here has been performed within the ATLAS collaboration, which is comprised of ∼3000 members who contribute to the detector related activities, calibrations, performance studies, management of the computing resources, physics analysis and many other activities. Therefore, the study of any individual is needed by all the rest of the collaboration and relies on the work of many others. Also in case of this thesis, this research work is the fruit of the work on many people. The author's contributions are summarized below.
The author contributed to the studies of missing transverse momentum reconstruction, performance and systematic estimation within the ATLAS Jet/Etmiss group. She participated to the effort of preparing for the Run2 data taking, therefore the studies have been performed both on simulated samples (before the start 2015 data taking) and on early Run2 data.
The author was one of the main analyzers for the VBF Higgs invisible search, performed using Run2 data at $\sqrt{s}$ =13 TeV. She was involved in all the main steps of the analysis giving contributions of major importance. She was involved in all the steps (from running in grid the samples, applying the event selection, optimizing the signal region and control region definitions, to writing the code for the statistical analysis) needed to arrive to a result.
The author worked on the generation of events for a model new to ATLAS together with F. Sala and M. Cirelli. Events have been generated with Madgraph+Pythia and official Atlas Fast samples have been produced by ATLAS. She tested the model using the same analysis requirements and strategy that have been used for the Higgs invisible search.

Chapter 1

Theoretical background

Particle Physics is aimed at the comprehension of nature at fundamental level. It aims to provide a microscopic description of nature, by studying the elementary particles and fundamental forces.
During 1960-1970 a theory has been developed to describe all the known elementary particle interactions (apart from gravity). This theory is the so called *Standard Model of particle physics*.
The Standard Model (SM) has an enormous success in explaining most phenomena and is an extremely well tested theory. Its predictions are tested with very accurate precision and it provides the best description of particles and interactions that we currently have. A key part of the SM is the spontaneous symmetry breaking mechanism, which is responsible for the generation of the masses of elementary fermions and bosons. As a consequence, the SM predicts the existence of a massive scalar boson, the so called Higgs boson.
In 2012 the discovery of a new particle with properties very close to those expected for the Higgs boson of the SM was announced at CERN. Thanks to this discovery, the last missing piece of the SM has been set and no significant discrepancies with respect to its predictions have been observed over a large number of precision measurements.
However, we know that we do not have a complete microscopic description of nature. From the particle physics point of view, several clues tell us that, despite its incredible level of precision in describing particle physics phenomena, the SM does not answer many questions. Hence, several Beyond Standard Model (BSM) theories have been proposed and a big effort is ongoing among theorists to find compelling SM extensions. Moreover, from cosmological measurements we know that we understand quite well only $\sim$5% of the total content of the universe. The remaining part is still *dark*.

In this chapter a brief (and non-exhaustive) introduction to the Standard Model and to the Higgs mechanism is presented. The SM limitations are discussed. Emphasis is given to the motivations for new physics and to the Dark Matter problem, since these topics are of particular relevance for the analysis discussed in this document.

1.1 The Standard Model of particle physics

The Standard Model is a relatively recent theory (completed in the 1970's) which describes the fundamental interactions and particles of nature. It is a gauge quantum field theory based on the group $SU(3) \times SU(2) \times U(1)$ where particles are described as exci-

tations of the quantum fields.

According to the SM the fundamental particles are classified as: leptons, quarks (which are fermions, i.e. $\frac{1}{2}$ spin particles which obey Fermi-Dirac statistic and satisfy Pauli exclusion principle) and mediators of interactions between all the particles (bosons, integer spin). Each particle is unambiguously identified by a set of quantum numbers. The fundamental forces are four: electromagnetic, weak, strong and gravitational. The latter one is not included in the SM, it is too weak at the level of elementary particle physics to play an important role.
The leptons are six, they are grouped into three generations of increasing mass for the charged ones (Table 1.1) and are classified according to the following quantum numbers: charge, electron number, muon number and tau number. Similarly, the quarks are six and are grouped in three generations (Table 1.1). For each lepton and each quark, a corresponding antiparticle exists with opposite quantum numbers.
While leptons are observed in nature as free particles, quarks bind to form composite particles called hadrons. This is due to a property of the strong force which is called confinement. Hadrons are classified into baryons, which are composed of 3 quarks and have spin $\frac{1}{2}$ or $\frac{3}{2}$, and mesons which are composed of quark-antiquark pairs and have integer spin.
Quantum electrodynamics (QED) and quantum chromodynamics (QCD) are the theories describing the electromagnetic and strong interaction respectively. QED, the weak interaction and the higgs mechanism are unified into the electroweak theory (proposed in 1968 by Glashow, Weinberg, Salam[1]).
The interactions are mediated by bosons: the photon (γ) for electromagnetic, Z and $W^{\pm}$ bosons for weak, and gluon (g) for strong interaction, as summarized in Table 1.2.

As mentioned earlier, the SM is a gauge theory.
A theory is invariant under a certain transformation if the lagrangian of the theory is unchanged after this transformation of the fields. Gauge theories are theories where the invariance is retained also when the transformation is local (i.e. depends on the space-time coordinates). Gauge theories benefit from properties that make them very appealing for building a model of fundamental interactions. One of them is that the theory is renormalizable.
One simple example of a gauge theory is QED. The Dirac free lagrangian, which describes the kinematic of a fermionic field, is:

$$\mathcal{L}_{free} = \bar{\psi}(i\gamma^{\mu}\partial_{\mu} - m)\psi \tag{1.1}$$

where m is the fermion mass, γ_{μ} are the Dirac matrices, ψ, $\bar{\psi}$ are Dirac spinors. This lagrangian is invariant under the $U(1)$ global transformation $\psi \to e^{i\alpha}\psi$. If the transformation become local ($\alpha \to \alpha(x)$) the theory is still invariant by:

- introducing a vector field A^{μ} which transforms as $A^{\mu} \to A^{\mu} + \frac{1}{e}\partial^{\mu}\alpha(x)$;
- introducing a Maxwell lagrangian for the vector field $\mathcal{L}_{Maxwell} = -\frac{1}{4}F^{\mu\nu}F_{\mu\nu}$, where $F^{\mu\nu} = \partial^{\mu}A_{\nu} - \partial^{\nu}A_{\mu}$ which is gauge invariant;
- replacing the derivative ∂^{μ} with the covariant derivative $\partial^{\mu} \to D^{\mu} = \partial^{\mu} - ieA^{\mu}$.

[1] Nobel Prize in Physics 1979 was awarded jointly to Glashow, Salam and Weinberg "*for their contributions to the theory of the unified weak and electromagnetic interaction between elementary particles, including, inter alia, the prediction of the weak neutral current*".

Table 1.1: List of the elementary fermions and their properties in the SM.

Fermions	Families			Electric Charge	Interactions
	1^{st}	2^{nd}	3^{rd}	(e)	
Quarks	u	c	t	$+2/3$	Strong
					Weak
	d	s	b	- 1/3	Electromagnetic
Leptons	ν_e	ν_μ	ν_τ		Weak
	e^-	μ^-	τ^-	-1	Weak and Electromagnetic

Table 1.2: List and properties of the gauge bosons and the Higgs boson.

Boson		Mass	Electric Charge	Associated Interaction
photon	γ	0	0	electromagnetic
Z-boson	Z	91.2 GeV	0	weak
W-boson	W	80.4 GeV	$\pm$ 1	
gluon	g	0	0	strong
Higgs boson	h	125 GeV	0	-

The lagrangian becomes

$$\mathcal{L} = \mathcal{L}_{Dirac} + \mathcal{L}_{Maxwell} + \mathcal{L}_{int} \tag{1.2}$$

where $\mathcal{L}_{int} = -e\bar{\psi}\gamma^\mu\psi A^\mu$, which is the interaction term between the fermionic field ψ and the field of the photon A^μ. The quantum of the electromagnetic field is the photon, and the electromagnetic interaction can be interpreted as the exchange of photons.
Similarly, the SM is a gauge theory under $SU(3)_C \times SU(2)_L \times U(1)_Y$. The $SU(3)_C$ component is QCD while the $SU(2)_L \times U(1)_Y$ component is the electroweak model, which unifies the electromagnetic and weak forces. The gauge boson for QCD is the gluon, while the gauge bosons for the electroweak forces are γ, $W^\pm$, Z (already presented in Table 1.2).

1.2 The Higgs boson

In 2012, the ATLAS and CMS collaborations announced the discovery of a new particle with properties very close to those expected for the Higgs boson of the Standard Model [6], which was the last missing piece of SM. In 2013, the Nobel Prize in Physics was awarded jointly to François Englert and Peter W. Higgs "*for the theoretical discovery of a mechanism that contributes to our understanding of the origin of mass of subatomic particles, and which recently was confirmed through the discovery of the predicted fundamental particle, by the ATLAS and CMS experiments at CERN's Large Hadron Collider*".

1.2.1 The Higgs mechanism

In the SM, the Higgs field generates the masses of all elementary particles. The Higgs mechanism was first introduced to explain why the gauge boson fields which are massless in the electroweak lagrangian have mass in nature. The same happens for fermions.
In the Higgs mechanism, a gauge symmetry is spontaneously broken by a two component scalar field Φ.

In 1963 a mechanism was proposed by Philip Warren [2] to explain why particles obtain mass. The relativistic version of this mechanism was developed by three groups independently one year later. These groups were composed by Peter Higgs; Robert Brout and Francois Englert; and Gerald Guralnik, Carl Hagen, and Tom Kibble [3], [4], [5]. A term of the following form is added to the lagrangian:

$$\mathcal{L}_{higgs} = (D_\mu \Phi)^\dagger (D^\mu \Phi) - (\mu^2 \Phi^\dagger \Phi + \lambda (\Phi^\dagger \Phi)^2) = (D_\mu \Phi)^\dagger (D^\mu \Phi) - V(\Phi) \tag{1.3}$$

where $\lambda > 0$ is required for the stability of the vacuum. The potential $V(\Phi)$ is given by the last two terms. The Higgs field Φ is a complex scalar SU(2)-doublet field with hypercharge $Y = \frac{1}{2}$ and weak isospin equal to $\frac{1}{2}$:

$$\Phi = \begin{pmatrix} \phi^+ \\ \phi^0 \end{pmatrix} = \frac{1}{\sqrt{2}} \begin{pmatrix} (\phi_1 + i\phi_2) \\ (\phi_3 + i\phi_4) \end{pmatrix} \tag{1.4}$$

where the quantum numbers of ϕ^+ and ϕ^0 are shown in Table 1.3. The vacuum state can be found by solving the equation $V'(\Phi) = 0$, as it corresponds to the minimum value of the potential. For $\mu^2 > 0$, the minima correspond to $\Phi_i = 0$ while for $\mu^2 < 0$ the potential is the so called *Mexican hat* (as illustrated in Fig. 1.1). The minima are found at values of:

$$\Phi^\dagger \Phi = \frac{1}{2}(\phi_1^2 + \phi_2^2 + \phi_3^2 + \phi_4^2) = -\frac{\mu^2}{2\lambda} \tag{1.5}$$

The ground state is degenerate. A minimum defined by $\phi_1 = \phi_2 = \phi_4 = 0$ and $\phi_3 = v = -\frac{\mu^2}{2\lambda}$, where v is called vacuum expectation value, can be chosen without loosing generality. By choosing a minimum the symmetry is spontaneously broken (the rotational symmetry of the potential $V(\Phi)$ is broken). After choosing this minimum and expanding the field around the vacuum by a perturbation $H(x)$, the Higgs field can be written as:

$$\Phi = \frac{1}{\sqrt{2}} \begin{pmatrix} 0 \\ v + H(x) \end{pmatrix} \tag{1.6}$$

By parametrizing the field with another SU(2) transformation, the field becomes:

$$\Phi = e^{i \frac{\vec{\tau} \cdot \vec{\xi}}{2v}} \frac{1}{\sqrt{2}} \begin{pmatrix} 0 \\ v + H(x) \end{pmatrix} \tag{1.7}$$

where $\vec{\xi} = (\xi^1, \xi^2, \xi^3)$, ξ^i are the Goldstone bosons. These are massless and do not correspond to any physical particle. It is possible to transform to another basis with a physics interpretation. The so called unitary gauge is used. It is a $SU(2)$ transformation given by $U(\vec{\xi} = e^{-i \frac{\vec{\tau} \cdot \vec{\xi}}{2v}})$. Under this transformation the potential term of the Higgs Lagrangian is:

$$V(\Phi') = \frac{\mu^2 v^2}{4} + \frac{1}{2} 2\mu^2 H^2 + \lambda v H^3 + \frac{\lambda}{4} H^4. \tag{1.8}$$

All this implies the existence of a gauge field of spin 0 that is called Higgs boson with mass $M_H = \sqrt{2\mu^2}$. The H^3 and H^4 terms show that the Higgs has triple and quartic self couplings.

To derive the masses of the gauge bosons, one has to expand $(D_\mu \Phi)^\dagger (D^\mu \Phi)$ in $\mathcal{L}_{higgs}$ in the unitary gauge, where $D_\mu = \partial_\mu + i\frac{g}{2} \mathbf{W}_\mu \cdot \tau + i\frac{g'}{2} B_\mu Y$. From this, it is possible to identify the terms which can be interpreted as the mass of the gauge bosons:

$$\mathcal{L}_{mass} = -\lambda v^2 h^2 + \frac{1}{4} g^2 v^2 W_\mu^+ W^{-\mu} + \frac{1}{8} (g^2 + g'^2) v^2 Z_\mu Z^\mu \tag{1.9}$$

	Q	T_3	Y
ϕ^+	1	$\frac{1}{2}$	1
ϕ^0	0	$-\frac{1}{2}$	1

Table 1.3: Quantum numbers of the Higgs doublet.

The Higgs boson has mass $m_H = \sqrt{2\lambda}v$ (at tree level) while the interaction of the weak bosons with the Higgs-field generates the mass terms $m_W = \frac{1}{2}vg$ and $m_Z = \frac{1}{2}v\sqrt{g^2 + g'^2}$. The photon remains massless.
Knowing the W boson mass (m_W), the Z boson mass and the fine structure constant α_{EM}, it is possible to derive the value of v which is measured $v \sim$246 GeV. The mass of the Higgs boson could not be predicted without the knowledge of λ. m_H has been measured after the Higgs boson discovery. The most up to date combined measurement between ATLAS and CMS is $m_H = 125.09 \pm 0.21$ (stat) ± 0.11 (syst) GeV/c^2.

The mass of the fermions can be obtained by adding an additional term that couples fermions to scalars. This term is the Yukawa coupling of the Higgs-field to fermions. Coupling constants (y_f) are introduced and the masses of the fermions (m_f) are proportional to these couplings: $m_f = \frac{1}{\sqrt{2}}y_f v$. The couplings y_f are not predicted by the theory, therefore the masses of fermions need to be experimentally measured.

1.2.2 Higgs boson at hadron colliders

Higgs boson production modes

The Higgs boson at hadron colliders can be produced in different modes. The cross sections of each production mode depend on the Higgs mass and on $\sqrt{s}$. In order of decreasing cross sections, the production modes for a Higgs boson with m_H =125 GeV, at $\sqrt{s}$ =13 TeV, are gluon-gluon fusion (ggH), vector boson fusion (VBF), associated production to vector bosons (VH), associated production to heavy quarks pair ($b\bar{b}H$, $t\bar{t}H$), associated production to single top quark (tH). Some illustration diagrams for these process are shown in Fig. 1.2, the associated cross sections are shown in Fig. 1.3.

- *gluon gluon fusion*: the Higgs boson has no direct coupling to massless particles, such as gluons. Therefore the ggF production is induced via a virtual fermion loop (mainly with heavy quark, such as top quarks). At $\sqrt{s}$ =13 TeV, for m_H = 125 GeV, ggF production is the dominant production mechanism for a SM Higgs boson at the LHC;

- *Vector boson fusion production*: The initial quarks radiate W/Z bosons which then produce the Higgs boson. Even if about one order of magnitude lower than ggF, the VBF production mode is playing a central role in the Higgs searches. In fact the two final state hard jets with peculiar characteristics provide a clear experimental signature. The VBF production mode is discussed in detail in Sec. 5.4.

- *Associated production with Z and W (Higgs-strahlung)*: A high energy off-shell vector boson (W or Z) radiates a Higgs boson. The final state is defined by the presence of the Higgs boson and of a W/Z boson (decaying either hadronically or leptonically).

- *Production in association with heavy quarks*: $b\bar{b}H$, $t\bar{t}H$ and tH processes have the lowest cross sections. The $t\bar{t}$ and tH production modes are important for the direct

measurement of the Yukawa coupling between the Higgs field and the top quark. It is experimentally challenging because of the small production cross section and because of the final state with missing transverse momentum and b jets from the top decay.

Higgs boson decays

Once produced, the Higgs boson rapidly decays[2] and it is detected by reconstructing in the detector its decay products. The branching ratio (BR) to any single mode is expressed as the ratio of the partial width to the total width, where the total width is the sum of all possible partial widths:

$$BR(H \to XX) = \frac{\Gamma(H \to XX)}{\sum_i \Gamma(H \to X_i X_i)} \tag{1.10}$$

The decays allowed in the SM and their BR are shown in Fig. 1.4. The corresponding values for a Higgs boson mass m_H =125 GeV are summarized in table 1.4. The highest BR is to bottom quarks (BR $\sim$ 58%). However, this final state is experimentally very challenging and first evidences of the Higgs boson in this decay mode have been recently published by ATLAS and CMS [8].
This is followed by decays to W bosons, with one of the W off-shell. Both the hadronic and leptonic channels are challenging: the hadronic channel presents high jet activity, while the leptonic channel has neutrinos in the final state.
The decay into gluons is not studied at the LHC as it is not distinguishable from the QCD backgrounds.
The Higgs decaying into τ pairs is studied in different channels, according to the decay modes of the tau leptons. It is a complex channel: because of the presence of neutrinos in case the τ is leptonically decaying and, in case the τ is hadronically decaying, because of the jets which need to be discriminated from the light quark background.
The decay into charm quarks has not yet been studied at the LHC (small BR and high backgrounds).
The $H \to ZZ^* \to 4l$ channel is the so called *golden channel*. Despite the relatively small cross section, the signature is clear and the background is small.
The $\gamma\gamma$ decay has a lower decay rate, but as the previous case, it has a clear experimental signature. The Higgs has no direct couplings to photons, therefore the $H \to \gamma\gamma$ is loop induced (mainly from top quark and W boson loops). The $Z\gamma$ decay is a similar process, with lower BR. The Higgs boson in the $Z\gamma$ channel has not yet been observed.
Lastly, the $\mu\mu$ decay has a clear signature (muon pair with invariant mass corresponding to m_H) and a small associated background. However the BR is very small and makes it very challenging.

Decays into invisible BSM particles have not been taken into account here, as they are not predicted within the SM. The only way an Higgs boson can decay into invisible particles within the SM is via the process $H \to ZZ^* \to 4\nu$, with BR$\sim$0.1% [9], which is well below the current sensitivity of searches for Higgs invisible decays (see sec. 5.1). The state of the art of Higgs invisible searches and the current limits to $BR(H \to invisible\ particles)$ are presented in chapter 5 in sec. 5.1.

[2] Lifetime $\sim 1.5\ 10^{-22}$s in the SM.

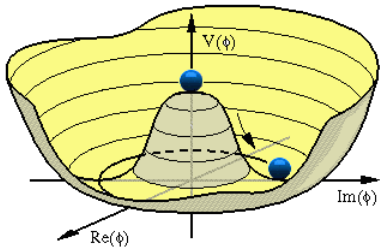

Figure 1.1: The potential, $V(\Phi)$, in the Higgs Lagrangian, for $\lambda > 0$, and $\mu^2 < 0$. This potential is usually referred to as *Mexican hat*.

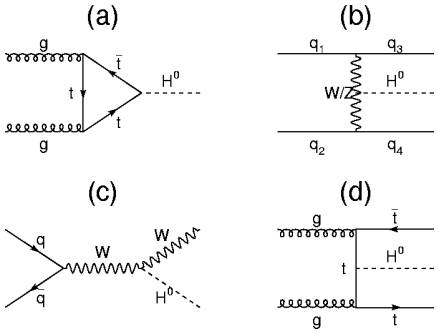

Figure 1.2: The most important processes for Higgs production at hadron colliders. Gluon fusion (a), vector boson fusion (b), associated production with W (c) and an example of the diagrams having associative production with a top pair (d).

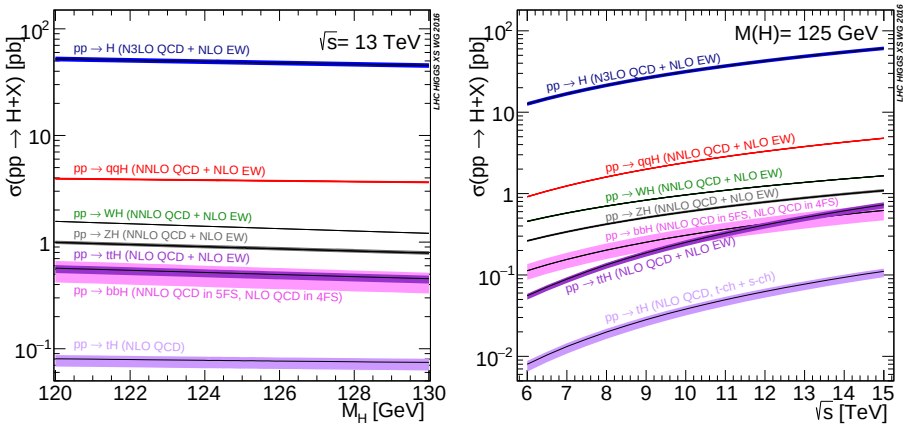

Figure 1.3: Standard Model Higgs boson production cross sections at $\sqrt{s}$ =13 TeV as a function of Higgs boson mass and Higgs boson production cross sections as a function of the centre-of-mass-energies. [7]

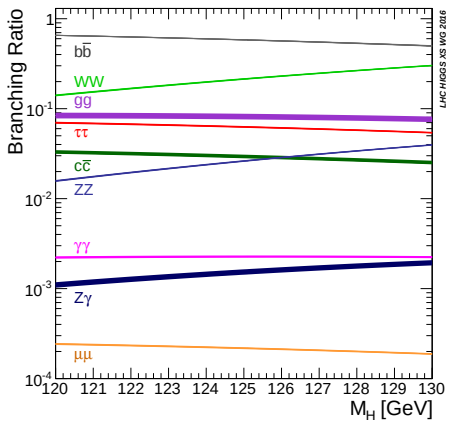

Figure 1.4: Standard Model Higgs boson decay branching ratios as a function of Higgs boson mass. [7]

Process (X)	BR(H→X)
bb	0.58
WW	0.22
$\tau\tau$	0.06
ZZ	0.027
$\gamma\gamma$	0.0023
$Z\gamma$	0.0016
$\mu\mu$	0.0002

Table 1.4: Summary of BR for Higgs of mass 125.0 GeV [7].

1.3 Limitations of the SM and open questions

Despite its success in describing many phenomena, the Standard Model is not considered as the complete theory of nature. Different limitations and unsolved questions point to the possibility that a more fundamental theory exists. The reasons to go beyond the SM can be classified as experimental and theoretical reasons and are summarized below.

1.3.1 Theoretical reasons

One of the most discussed issue of the SM is the *hierarchy problem*.
The electroweak scale is $\mathcal{O}(100$ GeV), whereas the Planck scale is $\mathcal{O}(10^{19}$ GeV). It is unknown why the two scales are so different. The Standard Model Higgs field receives large mass corrections at energies above the electroweak scale; and fine tuning is required

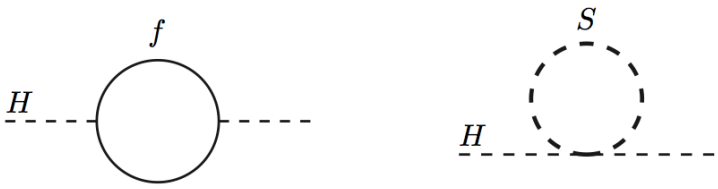

Figure 1.5: Loops corrections to the Higgs boson propagator, in case of fermions (left), and bosons (right)

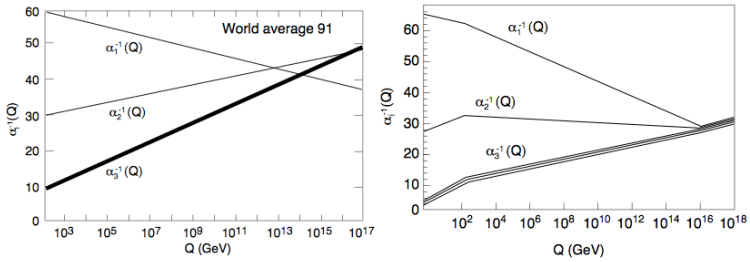

Figure 1.6: Running of the gauge couplings in the SM (left) and the MSSM (right) (LEP). [10]

to compensate and avoid these large corrections. The reason is the following.
When computing the Higgs mass including the radiative corrections, the Higgs mass m_H can be written as the sum of the bare mass m_{H_0} and the radiative corrections:

$$m_H^2 = (m_{H_0})^2 + \Delta m_H^2 \tag{1.11}$$

Considering the contribution to the Higgs mass given by a loop of fermions as the one in Fig. 1.5, these corrections can be written in the following form:

$$\Delta m_H^2 = -\frac{\lambda_f^2}{8\pi^2}\Lambda^2 + ... \tag{1.12}$$

where λ_f is the Yukawa coupling of fermions with the Higgs field, Λ is an energy cutoff and represents the energy scale up to which SM is valid ($\mathcal{O}(10^{19}$ GeV) in case the SM is valid up to the Plank scale or ($\mathcal{O}(10^{16}$ GeV) in case of the GUT scale). The corrections to the mass are of the same order of magnitude of the cutoff scale. To observe an Higgs mass such as the one we observe, these corrections should be canceled out, requiring a large fine tuning which seems to be highly unnatural.
There are different solution to the hierarchy problem, one of these is Supersymmetry (Sec. 1.5.1).

A second theoretical reason to go beyond the SM is usually referred to as *unification of coupling constants*. The interaction strength depends on the energy, in other words, the coupling constants of the SM interactions are running coupling constants, as their value depends on the energy scale. An example of this is the asymptotic freedom, a property of QCD which implies that the strong interactions become asymptotically weaker for increasing energies.
The SM gauge couplings, at high energies, converge to a common region, however they do not match to a single point. In supersymmetric models[3] they match at energies $\sim 10^{16}$ GeV (Fig. 1.6). This convergence at high energies suggests that the gauge groups of the SM ($SU(3)_C$, $SU(2)_L$, $U(1)_Y$) may be unified in a single group above the unification scale. These theories are called Grand Unified Theories (GUTs).

Even in case no new physics would be discovered, the SM seems to be incomplete as *Gravity* is not described within the SM. A complete quantum theory of gravity is not available and it does not seem possible to generate this interaction from the SM.

[3]Such as in the Minimal Supersymmetric extension of the SM (MSSM).

A further open question is the so called *strong CP* problem. Quantum chromodynamics allows for a violation of CP symmetry in the strong interactions, however such a process has not been experimentally observed. The question is therefore why QCD does not break the CP-symmetry. Fine tuning is required in order to solve the problem without predicting the existence of new particles. As a different approach to solve the problem, a new particle (axion) has been proposed, its presence forbids CP violation and it constitutes a dark matter candidate. However axions have not (yet) been observed.

Fermions in the SM are grouped into three generations. The three families have the same gauge quantum numbers but they differ for their Yukawa couplings to the Higgs field. This raises some fundamental questions: why there are three fermionic families? What is the origin of the spread of quark and lepton masses?
Regarding the former question, there is no hint in the SM itself about the reason of three different generation, instead of one, or of any other number.
The second question raises from the fact that the top quark is 6 orders of magnitude heavier than the electron.

1.3.2 Experimental reasons

According to the SM, *neutrinos* are left handed massless particles. However neutrino oscillations have been experimentally observed and neutrinos appeared to have tiny masses. To introduce neutrino mass terms in the SM lagrangian there are two possibilities: either considering neutrinos to be Dirac fermions (like all the other SM fermions) or Majorana fermions. The first case implies the existence of the right handed neutrino, called sterile neutrino as it does not interact with the SM particles. The mass would be generated, as in case of the other SM fermions, through the Higgs mechanism. However there is no experimental confirmation of the sterile nutrino's existence and the Yukawa coupling constants for neutrinos would be extremely small compared to the ones of the other fermions.
The latter case, proposed by Majorana in 1937, considers the neutrinos as their own antiparticles (Majorana neutrinos). If neutrinos are Majorana particles, neutrino masses can be explained through the so called see-saw mechanism. A Majorana mass term is introduced in the lagrangian. The Majorana mass of the right-handed neutrinos is a free parameter of the model and can take any value, while the mass of the observed neutrinos comes out to be naturally light. Furthermore it explains why neutrinos have always been observed to be left-handed in all performed experiments: the light states are mostly left-handed.
At the moment the Dirac or Majorana nature of neutrinos is still an open question.

Another unsolved question is related to the *matter-antimatter asymmetry*. The observed content of the universe is composed entirely by matter, while the Big Bang should have produced equally matter and antimatter. Part of this asymmetry can be accounted for by the Charge-Parity (CP) symmetry violation which is allowed in SM via the CKM mixing. However, it is still not yet understood what can explain the remaining part.

Astrophysical and cosmological observations point out that in the Universe there is an elusive and unknown substance, that we call *Dark Matter* [10], [11], [12]. Only ∼4-5% of the total content of the universe is made of baryonic (known) matter, the remaining higher fraction is still unknown and is thought to be made of dark matter and dark

energy. In the SM there is no viable *dark matter* candidate. This is one of the most relevant experimental indications which is guiding the current theoretical efforts. A description of this problem and of the evidences for dark matter is given in the following section (Sec. 1.4).

1.4 The Dark Matter problem

There are several astronomical observations and discoveries to support the existence of dark matter. In this section, a brief summary of the most compelling evidences is presented.

1.4.1 Experimental probes for dark matter

In the last 30 years, thanks to precise cosmological and astrophysical measurements, our knowledge of the Universe structure increased considerably. Three main sets of evidences which support the existence of the Dark Matter are:

- rotation curves of stars in galaxy;
- gravitational lensing;
- cosmic Microwave background.

All of this evidence for dark matter derives from its gravitational interaction with matter.

Rotation Curves of stars in galaxy

The study of rotation curves of stars in galaxies constitutes one of the most compelling evidence for the existence of Dark Matter. Spiral galaxies are stable gravitationally bound systems. In these systems stars occupy small regions and are not distributed spherically but in a thin disk. To require stability, the centrifugal acceleration should be equal to the gravitational pull. Considering the circular velocity of a star V and $M(r)$ the mass of the galaxy inside a radius r, this can be written as:

$$\frac{V^2}{r} = \frac{GM(r)}{r^2} \tag{1.13}$$

which implies that the velocity follows the Kepler's law:

$$V = \sqrt{\frac{GM(r)}{r}} \tag{1.14}$$

The behavior observed from astronomical measurements is different from this expectation: rotation curves are approximately constant after r$\sim$5 kpc.
The easiest explanation to this behaviour is to assume the presence of a huge Dark Matter halo in the galaxy. If the mass distribution is proportional to r then the velocity distribution should be constant. In this scenario, Dark Matter and visible matter should counterbalance to reproduce what we see from measurements.
Fitting the rotation curves is a complex problem, the main elements used the the fit are a stellar and gaseous disk and a Dark Matter halo modeled by a quasi–isothermal sphere [13].
Figure 1.7 shows a typical rotation curve which is fitted using the three components mentioned above.

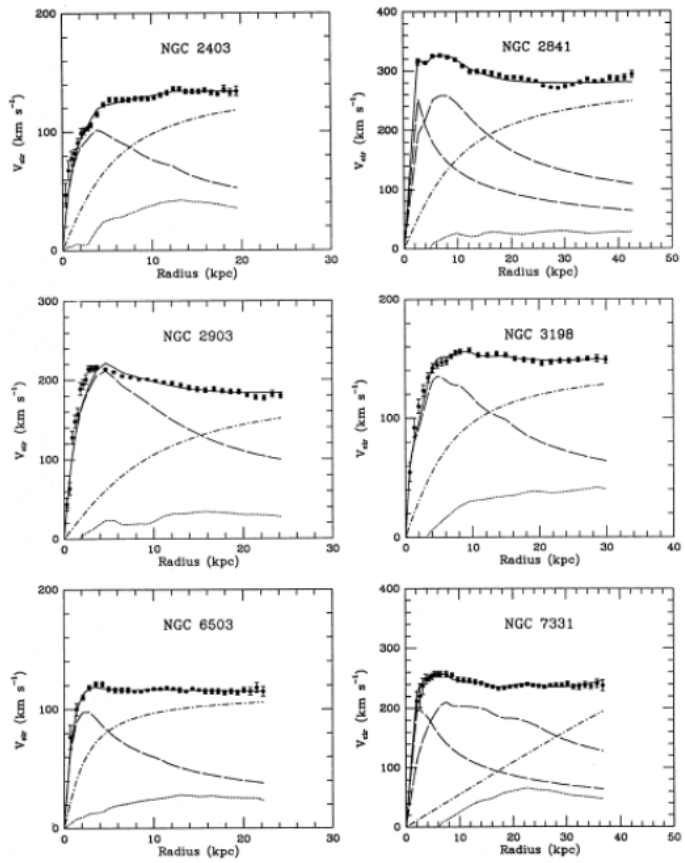

Figure 1.7: Rotation curves of several galaxies. The fit is performed using three-parameters. In each figure, the solid line represents the total fit. The individual contributions are also shown: luminous components (dashed), gas (dotted), and dark matter (dash-dotted). [14]

Figure 1.8: Bullet Cluster, superposition of optical, X-ray (red) and Lensing Map (Blue).

Gravitational lensing

The second set of evidences for Dark Matter comes from the gravitational lensing. A typical case is the Bullet Cluster (1E 0657-558). It consists of two colliding clusters of galaxies. Fig. 1.8 shows the clusters after collision. The red halo, superimposed to the optical image, is the distribution in the X ray. It shows where gaseous matter is located. The result of lensing measurements is shown in blue: the main amount of matter is concentrated elsewhere and do not correspond to the red halo. This contribution is interpreted as Dark Matter.

CMB

One of the strongest evidences comes from cosmological measurements, in particular from the study of the *Cosmic Microwave background* (CMB). CMB is a relic thermal radiation background permeating the Universe which is almost isotropic (2.73 K). It has been emitted $\sim 3 \times 10^5$ years after Big Bang. Before that time, radiation and matter were tightly coupled resulting in a ionized plasma. As the universe was expanding and cooling, the temperature was decreasing. When it reached temperature $\sim$1 eV, free electrons and protons formed hydrogen atoms (recombination). This lead to the decoupling of photons from matter. CMB radiation had its origin at that time. Before decoupling, radiation was tightly coupled to matter and once decoupled it was not largely perturbed. Hence, CMB provides a sort of *footprint* of the Universe at that time. From the study of CMB anisotropies different information can be inferred. One of these is the fractional amount of ordinary matter and dark content of the universe. The most precise measurements of the CMB comes from the PLANCK experiment. It provides the following density estimation: density of the ordinary matter 4.860 $\pm$ 0.073%, DM 25.89 $\pm$ 0.41%, and dark energy 69.11 $\pm$ 0.62% [25].

1.4.2 Dark Matter candidates

Even though the evidence for the existence of DM in the universe is solid, its nature is unknown. The most popular hypothesis is that DM is made of particles. There are some general properties that DM must have:

- electrically neutral: DM is dark, therefore it should not interact with photons, at least at tree-level;

- feebly interacting: since DM has not yet been detected it should be very feebly interacting;
- colorless: if DM particles were strongly interacting, like SM quarks, they would form bound states. Constraints come from cosmological searches;
- stable or long-lived: DM particles must be stable or long-lived[4], otherwise they would have disappeared with the evolution of the universe;
- cold: in order to cluster and form structures.

The SM does not provide valid DM candidates. The only SM particles fulfilling most of these criteria are neutrinos. Neutrinos seem to be the perfect candidate for Dark Matter: they are known to exist (without invoking exotic models) and to have mass. However, Standard Model neutrinos cannot explain the whole Dark Matter content but they can only constitute a tiny fraction of the dark matter content. The reason is their lightness. Moreover, if neutrino masses are of the order of the eV, neutrinos would be a hot DM component of the universe. Numerical simulations show that it would suppress the formation of structures at small scales and the galaxy formation would be impossible. Constraints on the neutrinos relic density come from CMB studies [25].

The hypothesis that DM is made of *dark* astrophysical objects made of baryonic matter, such as Massive Astrophysical Compact Halo Object (MACHO) [22] and primordial black holes, is ruled out in large regions of the parameter space but it is still possible in some windows of the phase space. A hot debate is currently ongoing on this topic in view of the recent LIGO discoveries.

Therefore, dark matter is most likely made of non-baryonic matter: if DM is a particle it has to be a new Beyond the SM (BSM) particle. Different BSM models provide dark matter candidates. Within these candidates there are:

- sterile neutrino: these hypothetical particles (introduced in sec. 1.3.1) have been proposed as DM candidates in the 90s [16]. Several experiments are looking for them (for example MiniBooNE, MicroBooNE experiments) but there is no experimental confirmation of their presence in nature;
- axions: they are introduced in order to solve the strong CP problem (sec. 1.3.1) and they can be a dark matter candidate [23]. Different experiments are ongoing all over the world to search for the existence of axions, they look for the axion conversion into photons;
- Weakly interacting Massive Particles (WIMPs): WIMPs are a class of particles which constitute appealing DM candidates. Due to their importance and popularity, WIMPs are described below.

In addition to these, there is a plethora of predicted particles which are viable DM candidates, such as super-heavy DM candidates such as WIMPZILLAs [27], Q–balls [28], self–interacting DM [29], etc. (refer to [31] and the reference therein).
Moreover, there is no reason why DM should be composed by a unique type of particles, on the contrary DM can be made of different species of particles.

[4] Constraints exists for $t > 10^{28}$ sec.

Weakly interacting Massive Particles

There is a broad class of particles which are called Weakly Interacting Massive Particles (WIMPs) which are considered compelling DM candidates. WIMPs are particles charged under SM $SU(2)_L$ group[5]. A very important property of WIMPs is that, in the standard cosmological thermal history they can be thermal relics of the early universe. Having additional interactions besides the gravitational one, processes of annihilation and decay into SM particles are possible for WIMPs.
In particular, at the time the temperature of the Universe was above the DM mass, DM was in thermal equilibrium and processes of production and annihilation of DM and SM particles

$$\chi\chi \longleftrightarrow j\bar{j} \tag{1.15}$$

$$j\bar{j} = (e^+e^-, \mu^+\mu^-, q\bar{q}, W^+W^-, ZZ...) \tag{1.16}$$

happened in both directions. When the temperature decreased, the interaction rate dropped below the expansion rate of the Universe, the equilibrium was not maintained and the only processes which could occur were annihilation:

$$\chi\chi \rightarrow j\bar{j} \tag{1.17}$$

The number density follows the following equation [10]:

$$\frac{dn_\chi}{dt} + 3Hn_\chi = - < \sigma V > (n_\chi^2 - n_{\chi,eq}^2) \tag{1.18}$$

where n_χ is the particle number density, $< \sigma V >$ is the thermal average of the annihilation cross section times the velocity, n_χ^{eq} is the number density at thermal equilibrium and H is the Hubble constant[6].
The number density is a function of time t and when the Hubble term becomes important, the annihilation freeze out occurs. At that time, the comoving number density stopped changing and it reached a final value which corresponds to the relic abundance of DM we observe today. Figure 1.9 shows this process. The later this process happens, the less DM abundance we have. The earlier it freezes out, the higher the number DM density is. Smaller annihilation cross-sections lead to larger relic densities.
If DM is a thermal relic, a weak scale cross section gives the correct abundance we observe today. The mass range allowed for WIMPs is about 10 MeV$< m_\chi <$ 100 TeV. (For details refer for example to [10] and [26]).
Many Beyond Standard Model theories predict WIMPs candidates. For example, the lightest neutralino predicted by supersymmetric models is a WIMP DM candidate; the neutral component of EW multiplets in Minimal Dark Matter models (see Chapter 6) are WIMP DM candidates.

1.4.3 Modified theories of gravity

Modified theories of gravity (like for instance MOND, *MOdified Newtonian Dynamics*) and Tensor-Vector-Scalar theories of gravity (TeVeS) [17] attempt to explain the phenomena attributed to Dark Matter and discussed above without additional new particles.

[5] Another definition is also widely used in the scientific community. According to this broader definition WIMPs are particles with a *SM weak scale* cross section but not necessarily charged under $SU(2)_L$ group.

[6] The Hubble term is introduced since these processes take place in an expanding universe.

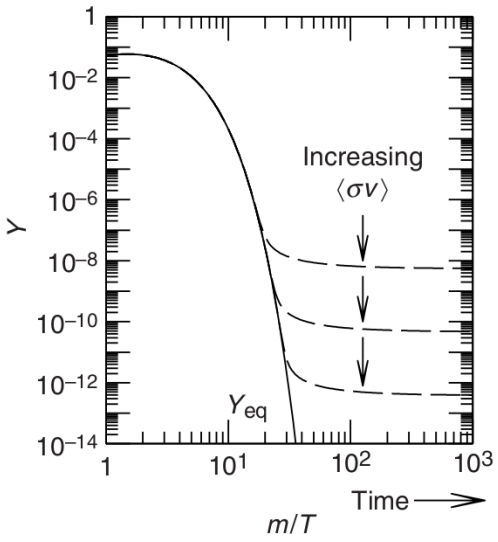

Figure 1.9: Evolution of the number density in the early Universe at the time of the freeze-out processes for annihilating particles. Refer to [31] for details.

In general these theories are able to describe observations of galactic rotation curves [18]. However, their main issue is that they fail to describe the whole ensemble of observations ([19], [17], [20]). It is possible to explain the Bullet cluster by adding a 2 eV neutrino [21] but currently these theories fail in explaining the whole CMB power spectrum without assuming DM existence [17]. By contrast it is much more economical and easy to explain everything by introducing Dark Matter particles. In this case, well justified theories exist and some are testable.

1.4.4 Dark matter searches

Besides the evidences of DM through its gravitational interaction with ordinary matter, it is very important to have direct observations of DM which would prove its particle nature and would help in the understanding of its properties.
In the recent past a lot of efforts have been done to look for Dark Matter particles and to reveal something about their nature. Several experiments are actively running and taking data.
As represented in a cartoon in Fig. 1.10 there are three different approaches to look for Dark Matter.
One way is to look for DM annihilation or decay, as it is done by Indirect Detection experiments (ID) [39]. It is possible also to look at the interaction between Dark Matter and Standard Model particles, this is the aim of Direct Detection (DD) experiments [38]. The last possibility is to search DM at colliders by looking for its production arising from SM particles collision [40].

Direct Detection

The underlying idea of Direct Detection experiments is the following. If our galaxy is filled by Dark Matter particles, since the Dark Matter halo is extending beyond our planet, there is a certain rate of DM particles which are passing through the Earth. The flux of DM particles on the earth is estimated to be of the order of 10^5(100

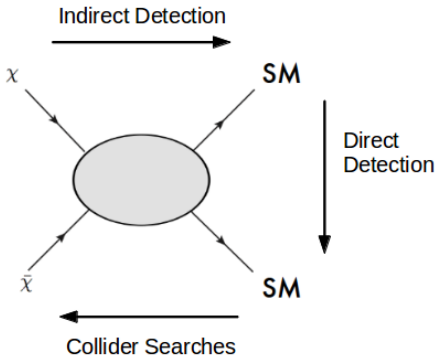

Figure 1.10: Diagram representing three approaches to search for DM. If DM has some couplings to ordinary matter we can detect it: 1) by looking at its annihilation products (Indirect Detection), 2) looking for its scattering with nuclear matter (Direct Detection), 3) producing it at colliders (Collider Searches).

$\mathrm{GeV}/\mathrm{m}_\chi)\mathrm{cm}^{-2}\mathrm{s}^{-1}$ [31]. Most of them pass through without interacting, while a small but potentially detectable fraction can interact with nuclei. The aim of Direct Detection experiments is to detect these extremely rare interactions with normal matter.
In particular these experiments aim at measuring the rate of nuclear recoils and the nuclear recoil energies E_R caused by the interaction of a DM particle with the nuclei. To make it possible it is necessary to reduce as much as possible every kind of background which could fake the DM signal. Indeed, the background comes from cosmic rays, environmental radioactivity and detector material radioactivity. Sophisticated experiments are located in underground sites (such as Gran Sasso laboratories in Italy and SNOLab in Canada) to reduce the cosmic ray background. Their main challenge is to make the experimental environment extremely with an extremely low level of radioactivity in order to be able to detect the recoiling nucleus kicked off by a DM particle and develop sophisticated background-rejection techniques. In particular there are two classes of Direct Detection experiments, time independent and time dependent, which look at different energy signals and use different techniques and technologies to detect the energy released in the detector.

Indirect Detection

Indirect Detection experiments aim at detecting DM annihilation or decay products. If DM can annihilate (i.e. particle-antiparticle reactions can occur), this is expected to happen in regions where the Dark Matter density is high, such as the galactic center where the dark matter density profile is expected to grow as a power law of the radius. The annihilation products are SM stable particles (gamma rays, neutrinos, electrons, positrons, protons, antiprotons, deuterons, and antideuterons). Therefore, it is possible to search for DM particles by observing these potentially detectable SM particles. These experiments are either ground based instrument (like HESS, or neutrino telescopes such as IceCube), space satellites (Fermi-LAT Telescope, Pamela) or space-based experiments (AMS). The dark matter annihilation signal depends both on particle physics properties, such as the annihilation cross section, and on the density distribution of Dark Matter. The key point is to be able to distinguish the background coming from known astrophysical processes from the Dark Matter signal. For this reason among the secondary products, antiparticles, gamma-rays and neutrinos are particularly interesting. Antiparticles

(positrons, antiprotons, antideuterons) are less abundant than the respective particles while gamma rays and neutrinos travel in straight lines and almost unabsorbed in the local Universe.

Collider Searches

The third strategy to search for Dark Matter is to look for its production at colliders: if Dark Matter has some couplings to normal matter, it can be produced in collisions at particle accelerators, provided that the collision energy is large enough compared to the DM particle mass. In particular, it can be produced at the LHC.
There are many ways in which DM searches can be carried out at colliders. A simple scenario to reveal DM particles at colliders is to design model "*independent*" searches. If DM is the only new state accessible and if it is weakly interacting, once produced it will pass through the detector without leaving any trace and without decaying into other particles, similarly to what neutrinos do. Therefore the existence of Dark Matter particles escaping the detector may be inferred from an imbalance in the visible transverse momentum of the event ($E_{\mathrm{T}}^{\mathrm{miss}}$, see Chapter 4). In order to tag the event, to trigger it and to discriminate it from the backgrounds, it is necessary to have another final state particle tagging the event, so that the DM recoil against this particle. The minimal requirement which can be done is the request of a SM particle from initial state radiation (ISR). Therefore, the usual most model independent DM searches at colliders are the so called mono-X searches, characterized by large missing transverse momentum and an energetic particle in the final state, such as a boson (*W, Z, H*) or a particle from ISR such as a jet (mono-jet) or a photon (mono-photon). These searches are interpreted as WIMPs pair production, for example in the context of in the context of large extra-dimensions theories [37], SUSY related searches, in some cases invisible Higgs and other exotic channels.
Another way is to probe specific theories and models, by looking at all the decay channels predicted by the theory.
The searches described in this thesis are designed and optimized to look for the invisible decay of the Higgs boson (m_H =125 GeV). However, the results are also interpreted in the context of heavier Higgs and in the context of models inspired by the Minimal Dark Matter model.

Mono-X searches are usually interpreted in the context of Effective Field Theories (EFT). They provide a simplified theoretical description of how DM interacts with the SM: as the precise nature of the interaction is not known, to keep it as much as possible model independent, EFT are used to parametrize our ignorance of the fundamental interaction. EFT are the low energy, non-renormalizable, description of a fundamental theory. If the energy scale of the considered process is much smaller than the mediator masses involved in the interaction, it is possible to integrate the mediators out and to ignore them. The EFT approach is analogous to the Fermi theory, which applies at energy much smaller than the weak boson masses. In the EFT approach, if there is only one operator, the interaction is described by two parameters: the DM mass (m_χ) and a new energy scale M^*.The interaction can be described by an EFT if the momentum transfer (Q_{tr}) is much smaller than the mediator mass M ($Q_{tr} < M = M^* \sqrt{g_{SM}\ g_{DM}}$, where g_{SM} and g_{DM} are the couplings of the mediator with SM and DM particles respectively and are usually constrained by g_{SM},g_{DM}<4π to stay in the perturbative regime).
The EFT is used in Direct Detection experiments, where the momentum exchange is very

small (few KeV) and the masses of the particles other than the WIMPs are expected to be heavier. The problem is that at the LHC the momentum transfer involved in the interaction can be so high that EFT are not well justified.
The validity of the EFT approach at the LHC is under discussion and an intense study about this topic is ongoing [32]. To overcome this issue, simplified models (where a new mediator, exchanged between SM particles and DM particles, is introduced) are also considered.

1.5 Beyond the Standard Model

Different BSM models are built as extensions of the SM. In this section Supersymmetry and Higgs portal model are briefly described. Minimal Dark Matter models are presented in details in chapter 6.

1.5.1 Supersymmetry

Supersymmetry (SUSY) is one of the most popular extensions of the SM model. It provides a solution to the *hierarchy problem* and it offers a dark matter candidate.
The idea behind SUSY is the following.
As described in sec. 1.3.1, a complete calculation of the Higgs mass should include radiative corrections to the Higgs propagator which come from loops of all the other particles coupling to the Higgs boson. Loop diagrams for fermions and scalars coupling to the Higgs, such as the ones in Fig. 1.5, need to be taken into account.
Assuming the existence of a new heavy scalar particle S, which couples to the Higgs via the Lagrangian term $-\lambda_S|H^2||S^2|$, the contribution to the Higgs mass is given by:

$$\Delta m_H^2 = \frac{\lambda_S}{16\pi^2}\Lambda^2 + \ ... \tag{1.19}$$

Comparing eq. 1.19 to 1.12, it appears that if each of the quarks and leptons of the SM is accompanied by two complex scalars and if the coupling is the same, the two contributions would cancel.
In order to happen there must be a symmetry that relates fermions and bosons. This symmetry is Supersymmetry.
SUSY literature is extremely broad and different models within SUSY exist. The main general features of SUSY are the following:

- SUSY predicts that for each SM particle there exists another one with the same mass but different spin. These new particles are referred to as super partners;
- such new particles, having the same mass of SM particles, would have been already discovered. For this reason SUSY cannot be an exact symmetry, it is broken thus leading to masses of super-partners larger than those of SM particles. Unfortunately the scale where SUSY is broken is unknown;
- SUSY models typically respect a discrete symmetry called R-parity. The super particles have R parity equal to -1 while SM particles have parity 1. This parity stabilizes the *lightest supersymmetric particle* (LSP) which is a good dark matter candidate (neutral, colorless and stable).

Supersymmetric models are characterized by many different parameters, the drawback is that this creates a complex scenario and a plethora of possible channels which need dedicated analysis to be all probed at colliders.
Although the theoretical motivations for Supersymmetry are strong, there is no experimental confirmation of its existence.

1.5.2 Higgs portal model

How dark matter particles couple to SM particles is an open question.
Experimentally, only interaction through gravity have been observed, which suggests that they are massive and hence could also be coupled to the Higgs field.
The Higgs portal model is a model which directly couples the hidden sector to the SM through the Higgs field [41], [42]. Hidden sector particles can be stable and couple very weakly to the SM sector, therefore offering a dark matter candidate.
Experimentally, the Higgs portal can be probed with two complementary approaches: direct detection DM experiments and collider searches. The Higgs-portal model can be used to describe scenarios where dark matter is either a scalar (S), a vector (V) or a Majorana fermion (f)[7] which interacts with the SM fields only through the Higgs-portal.

A dark matter singlet χ, which only couples to the SM Higgs doublet, is introduced. The DM particle can interact elastically (at low energy transfer) with nuclei through the Higgs boson exchange, the resulting nuclear recoil can be detected by direct detection experiments.
If the DM particles are lighter than $m_H/2$, the exotic decay of the Higgs boson into χ pairs is allowed $H \to \chi\bar{\chi}$. This process can be searched for at colliders and is referred to as *Higgs invisible decay*.
From the upper limit on the branching ratio (BR) of Higgs decaying to invisible particles, measured with dedicated searches of Higgs invisible decay (such as the one described in chapter 5), it is possible to determine the maximum allowed decay width to the invisible particles via the relation:

$$\Gamma_H^{inv} = \frac{BR(H \to inv)}{1 - BR(H \to inv)} \times \Gamma_H \tag{1.20}$$

where Γ_H is the SM decay width of the Higgs boson. From ref. [42], the Higgs partial decay widths into the scalar, vector and Majorana-fermion DM particles are given by the following formulas:

$$\Gamma_{H\to SS}^{inv} = \frac{\lambda_{HSS}^2 v^2 \beta_S}{64\pi m_H} \tag{1.21}$$

$$\Gamma_{H\to VV}^{inv} = \frac{\lambda_{HVV}^2 v^2 m_H^3 \beta_V}{256\pi M_V^2}(1 - 4\frac{M_V^2}{m_H^2} + 12\frac{M_V^4}{m_H^4}) \tag{1.22}$$

$$\Gamma_{H\to ff}^{inv} = \frac{\lambda_{Hff}^2 v^2 m_H \beta_f^3}{32\pi\Lambda^2} \tag{1.23}$$

where:

- λ_{HSS}, λ_{HVV}^2, $\frac{\lambda_{Hff}^2}{\Lambda}$ are the coupling constants;

[7] The case of Majorana fermion is considered here, following [42] and [41], however, also the case of Dirac fermion is possible.

Table 1.5: Numerical values of the parameters in the Higgs-portal dark-matter model. Uncertainties on the Higgs-nucleon coupling form factor are shown as they are particularly important. Reduced theory uncertainty for the form factor have recently been published [43].

Vacuum expectation value	$\frac{v}{\sqrt{2}}$	174 GeV
Higgs boson mass	m_H	125.09 GeV
Higgs boson width	Γ_H	4.07 MeV
Nucleon mass	m_N	939 MeV
Higgs-nucleon coupling form factor	f_N	$0.33^{+0.30}_{-0.07}$ MeV

- v is the vacuum expectation value of the SM Higgs doublet;
- $\beta_\chi = \sqrt{1 - 4m_\chi^2/m_H^2}$ ($\chi = S, V, f$), with m_χ being the WIMP mass;
- Λ is the new physics scale, for the case of a fermion, in the EFT approach. It is assumed to be at the TeV scale or higher, well above the probed scale at the SM Higgs boson mass.

The DM-nucleon scattering cross section can be written in a general spin-independent (SI) form:

$$\sigma_{SN}^{SI} = \frac{\lambda_{HSS}^2}{16\pi m_H^4} \frac{m_N^4 f_N^2}{(m_S + m_N)^2} \tag{1.24}$$

$$\sigma_{VN}^{SI} = \frac{\lambda_{HVV}^2}{16\pi m_H^4} \frac{m_N^4 f_N^2}{(m_V + m_N)^2} \tag{1.25}$$

$$\sigma_{fN}^{SI} = \frac{\lambda_{Hff}^2}{4\pi\Lambda^2 m_H^4} \frac{m_N^4 m_f^2 f_N^2}{(m_V + m_N)^2} \tag{1.26}$$

where m_N is the nucleon mass and f_N is the form factor associated to the Higgs boson-nucleon coupling.
The numerical values of the parameters entering these equations are summarized in table 1.5.
This allows to compare results from collider searches to results from direct detection experiments in the context of an effective field theory, where the scale of new physics is assumed to be ∼(few TeV).

Chapter 2

The LHC and the ATLAS Detector

The research work documented in this thesis is based on data coming from proton-proton collisions at a center of mass energy ($\sqrt{s}$) of 13 TeV, collected by the ATLAS experiment [46–48] along 2015 and 2016. ATLAS is one of the four main experiments at the Large Hadron Collider (LHC) [44], located at the European Organization for Nuclear Research (CERN) near Geneva, in Switzerland. In this chapter, a brief introduction to the LHC collider and ATLAS detector is discussed.

2.1 The Large Hadron Collider

The LHC is a two-ring, circular, superconducting hadron accelerator and collider. It is installed in the existing 26.7 km underground tunnel that has been constructed for the CERN LEP [1] machine [49]. It is designed to collide proton beams and it can also collide heavy (Pb) ions with design center of mass energies ($\sqrt{s}$) of 14 TeV and 5.52 TeV per nucleon respectively. The LHC is currently the highest energy collider in the world. It belongs to the CERN accelerator chain (fig. 2.1), which is an ensemble of machines accelerating particles at increasingly higher energies. Each machine injects the beam into the next one and the LHC is the last acceleration step. Being a particle-particle collider, the LHC is composed of two separate rings with counter rotating beams, unlike particle-antiparticle colliders where a unique ring is used for the two beams. The two beam pipes are kept at ultra-high vacuum and the two proton beams are kept on their orbit by superconducting magnets operating at a temperature of 1.9 K and generating a magnetic field of 8.36 T which bends the beams. Particles acceleration is provided by 8 superconducting radio frequency cavities, operating at 400 MHz. The beams collide in dedicated interaction points, where experimental halls are built. There are 4 collision points, one of which hosts the ATLAS experiment. Each interaction point is preceded by a linear section where the two beams are focused by a quadrupole field generated by a system of three magnets placed at each side of the detector. The r.m.s width of the beam in the transverse plane is about 17 μm. Collisions take place when bunches of particles of each beam collide with bunches from the other beam. The design bunch crossing period is 25 ns. A schematic layout of the LHC is shown in Figure 2.2.
The LHC started operations on September 10, 2008, but immediately after, during the commissioning phase, a major accident imposed a one year stop. During Fall 2009 operations started again, culminating in the first 900 GeV collisions, recorded by the LHC experiments from November 23, 2009, and followed shortly after by collisions at

[1] Large Electron-Positron Collider

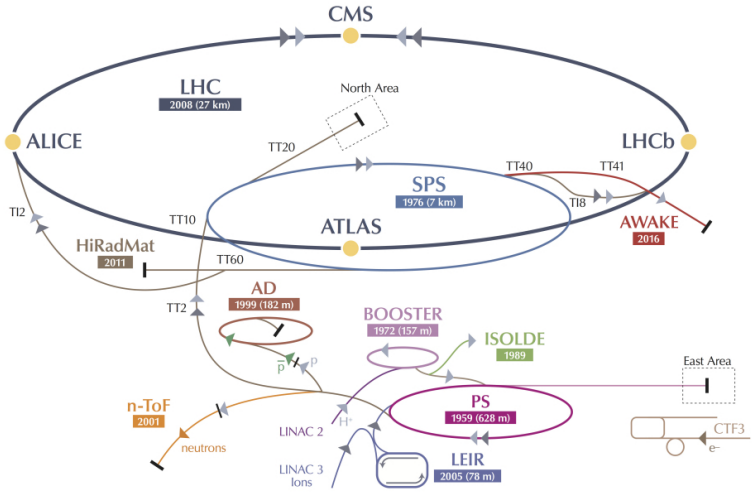

Figure 2.1: Schematic view of the CERN accelerator complex including the LHC.

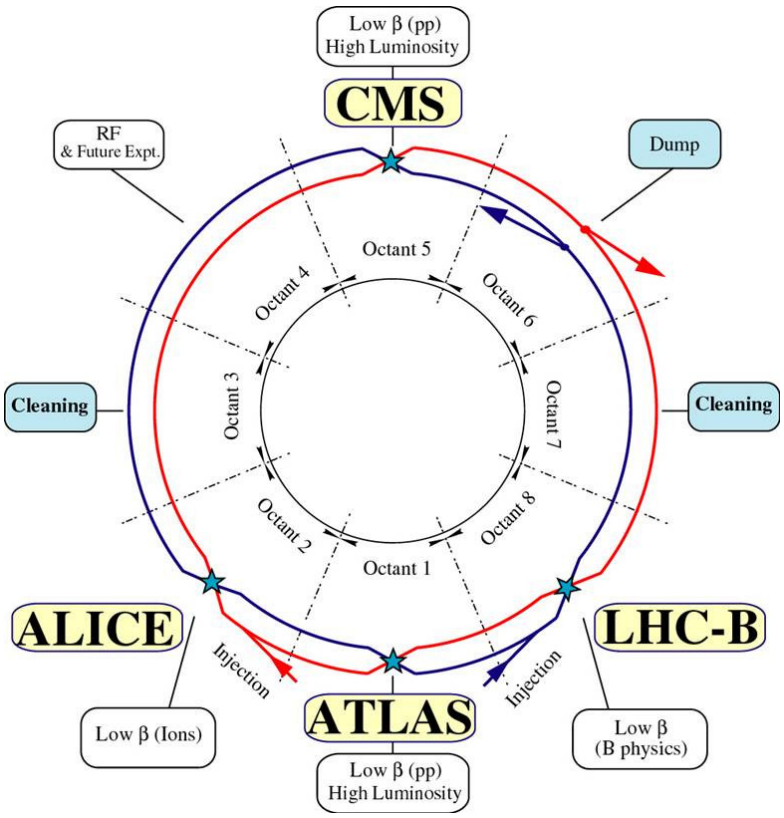

Figure 2.2: Schematic layout of the LHC. Along the ring four main experiments are located. They are: ATLAS, CMS, LHCb and ALICE.

2.36 TeV. For machine safety reasons it was decided to limit the maximum center of mass energy to 7 TeV, and the first collisions at this world record energy took place on March 30th, 2010. From then on the number of proton bunches and the number of bunches per beam have been increasing day by day. During 2012 the LHC ran at 8 TeV energy, this data taking period is usually referred to as Run 1. Run 1 has been followed by a long shutdown (LS1) lasting 2013 - 2014, during which the LHC machine and experiments underwent essential maintenance and upgrades needed to reach the center of mass energy of 13 TeV. Collisions started again in spring 2015 at the new energy frontier of 13 TeV. This new data taking period is called Run 2 and it will end in 2018 with the second long shutdown (LS2). At the time this work has been written the LHC is still running at $\sqrt{s} = 13$ TeV with 25 ns bunch crossing period.

Luminosity

One of the most important parameters denoting the performance of a collider is the luminosity. In a scattering experiment, the luminosity is defined as the proportionality factor between the cross section of the process, σ, and the number of observed events for that process, N. The interaction rate $R = dN/dt$ of a certain process with cross section σ [2] is given by the following equation:

$$R = dN/dt = \mathcal{L} \times \sigma; \tag{2.1}$$

where $\mathcal{L}$ is the instantaneous luminosity.
By integrating the rate over the time for a certain process, the total number of events collected in that period can be related to the integrated luminosity L:

$$N = L \times \sigma. \tag{2.2}$$

The instantaneous luminosity depends only on the parameters of the beams.
The simple example of a beam colliding on a fixed target can be instructive. Suppose that the beam is made of N particles per second, the target has a density n [atoms/cm^3] and a thickness d. The rate of events is therefore related to the cross section of the process via the following relation:

$$R = N\ n\ d\ \sigma \tag{2.3}$$

The instantaneous luminosity in this case is defined as $\mathcal{L} = N\ n\ d$ [cm$^{-2}s^{-1}$].
Similarly, in the case of colliders, the instantaneous luminosity can be expressed as a function of the characteristic parameters of the collider:

$$\mathcal{L} = \frac{N_{1b} N_{2b} n_b f}{4\pi\sigma_x\sigma_y} F \tag{2.4}$$

where:

- N_{1b} and N_{2b} are the number of particles per bunch for the two beams. At the LHC $N_{1b} \sim N_{2b}$;
- n_b is the number of bunches per beam;
- f is the revolution frequency of the machine;

[2] Measured in barns, 1 barn [b] is defined as 1 b = 10^{-28}m^2.

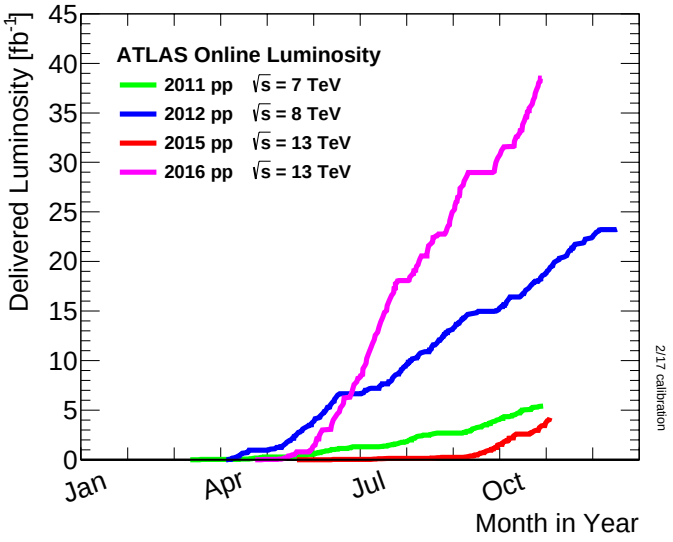

Figure 2.3: Integrated luminosity recorded by the ATLAS detector in 2011, 2012, 2015 and 2016 as a function of data taking periods.

- σ_x and σ_y are distribution's r.m.s. of the beams along the transverse plane. They are used to take into account the effective beam size;
- F is a reduction (i.e. <1) geometric factor accounting for the two beams crossing angle being different from zero (the two beams do not collide exactly head on).

Table 2.1 summarizes some of the nominal parameters of the LHC. Figure 2.4 shows the

Parameter	Nominal values for the LHC
Number of particles per bunch	10^{11}
Number of bunches per beam	2808
Revolution frequency	11245 Hz
Relativistic gamma factor	~7000
Geometric luminosity reduction factor	0.84
Geometrical factor F	0.84
Transverse beam size σ	~17μm

Table 2.1: Some nominal parameters entering the luminosity definition for the LHC

luminosity delivered by LHC in the last past years and the integrated luminosity recorded by ATLAS as a function of time. To maximize the sensitivity of rare processes such as new physics signals, it is important to increase the luminosity as much as possible. An increase in the luminosity can be achieved by adjusting the quantities entering equation 2.4: increasing the number of particles in the bunches, increasing the number of colliding bunches (resulting in a reduction of the bunch-spacing), reducing the beam transverse size. In particular the reduction of the beam transverse size, the reduction of the bunch crossing period and the increased number of particles per bunch have been adopted for Run2 data taking. However, the advantage of having more data delivered comes with undesired effects such as the pile-up.

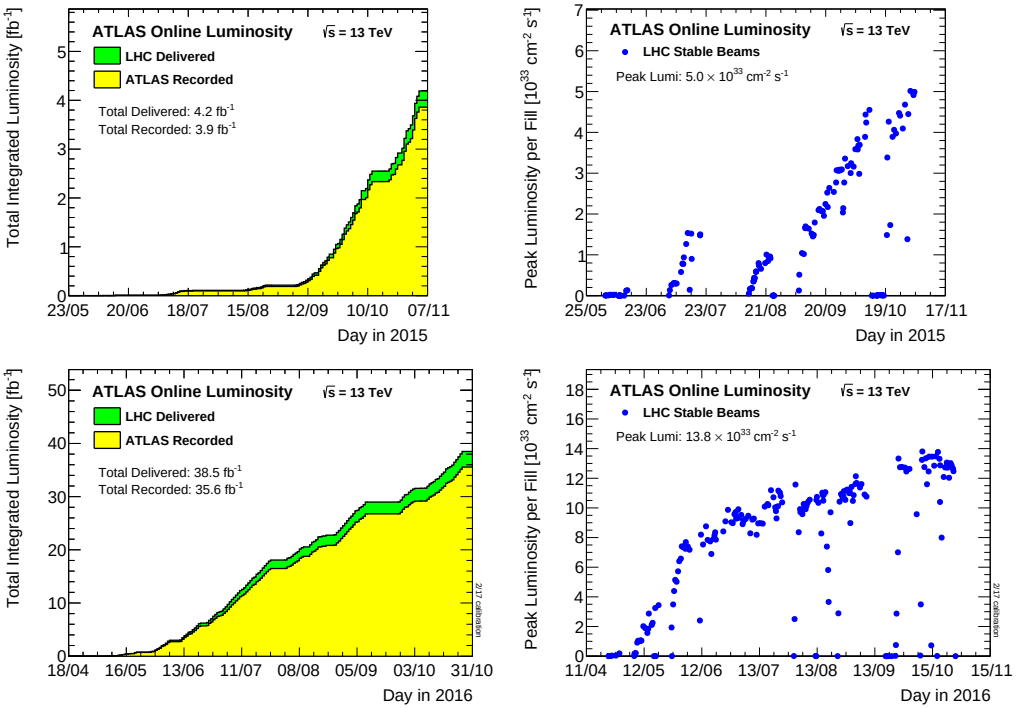

Figure 2.4: Left: integrated luminosity versus time delivered to (green) and recorded (yellow) by ATLAS during stable beams in 2015 (top) and 2016 (bottom). Right: peak instantaneous luminosity delivered to ATLAS during stable beams during 2015 (top) and 2016(bottom) [45].

Pile up

The pile up is created by multiple collisions overlapping the hard-scatter process and it takes two forms:

- in-time pile up: it is the phenomenon where multiple collisions happen in a single bunch crossing;
- out-of-time pile up: it comes from collisions happening in the neighbouring bunch crossings. It is related to the finite time required for the signals to develop in and be read from the detector: the residual energy from a previous bunch crossing or the energy from a future bunch crossing which is deposited before the read-out process is completed can contribute to the electrical signals associated to a given bunch crossing.

Pile up is typically parametrized in terms of the number of reconstructed primary vertices (N_{PV}) for the in-time contribution while the average number of interactions per bunch crossing ($\langle\mu\rangle$) is used for the out-of-time contribution. The N_{PV} is an event quantity which is calculated as the sum of the number of reconstructed vertices in the tracking detectors. The $\langle\mu\rangle$ quantity is averaged over a number of events. These two quantities provide independent estimates of the amount of pileup activity.
Figure 2.5 shows $\langle\mu\rangle$ calculated from the instantaneous luminosity recorded by the ATLAS detector in 2015 and 2016 .
The effects of the pile up in the analysis documented in this thesis and the ways used to mitigate it will be described in the next chapters.

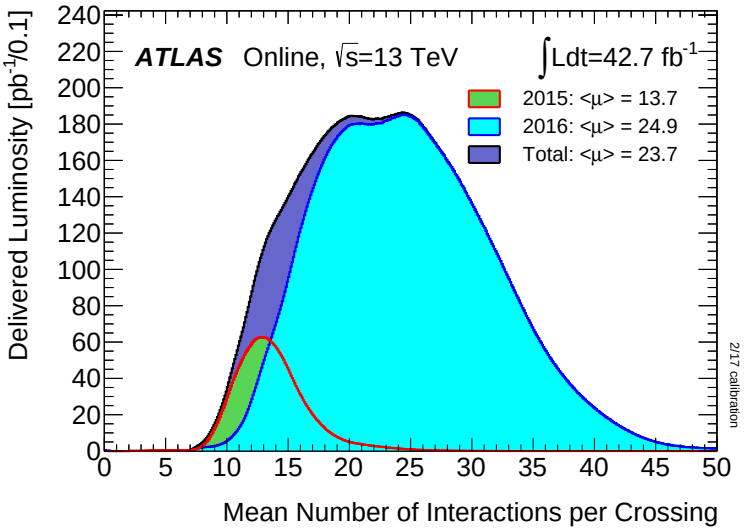

Figure 2.5: Luminosity-weighted distribution of the mean number of interactions per crossing for the 2015 and 2016 pp collision data at $\sqrt{s}$ =13 TeV [45].

2.2 The ATLAS Detector

2.2.1 General structure of modern collider experiments

To collect data coming from LHC collisions, particle detectors are built around the LHC interaction points. High energy particle detectors are the instruments used to measure the kinematics properties of the particles produced in each collision.
At the LHC there are four independent experiments built around the interaction points: ATLAS (A Toroidal Lhc ApparatuS) [46] and CMS (Compact Muon Solenoid) [50] are multipurpose experiments, designed to cover a broad physics program, from the search of the Higgs boson and Standard Model measurements to the search of phenomena beyond the Standard Model, LHCb (LHC-beauty) [51] is devoted to the b-quark physics and CP violation studies, while ALICE (A Large Ion Collider Experiment) [52] studies heavy nuclei collisions.
In addition to these main experiments, three other smaller facilities are installed on the LHC ring: TOTEM (TOTal cross section, Elastic scattering and diffraction dissociation Measurement in the lhc) [54], MoEDAL (MOnopole and Exotic Detector At the Lhc) [55] and LHCf (LHC Forward) [56]. The former is designed to measure the total elastic pp cross section, MoEDAL searches for magnetic monopoles and for exotic phenomena while the latter studies forward high-energy neutral pions.
Modern multi-purpose detectors used at high energy particle colliders, such as ATLAS and CSM, have a common layout. The basic concept is to ensure that all the particles[3] interact within the detector so that they can be distinguished through their interactions with matter and their properties can be identified. Therefore detectors are built as a series of different modules which are ordered radially from the interaction point and which are devoted to detect different kind of interactions. Combining information from the different sub-detectors, the kinematics and the properties of the particles passing trough are identified. In this section the specific case of the ATLAS detector is illustrated.

[3] Apart from neutrinos and other (possibly existing) invisible particles, as will be discussed later.

2.2.2 Introduction

ATLAS (A Toroidal Lhc ApparatuS) is a multi-purpose giant detector installed in one of the LHC experimental caverns, located in Meyrin, Switzerland.

The general layout of the ATLAS detector is shown in figure 2.6. The detector has a cylindrical symmetry around the beam line. It is 25 m high and 44 m long, its overall weight is approximately 7000 tonnes. The ATLAS detector is (alomost perfectly) forward-backward symmetric with respect to the interaction point.

Coordinate system

ATLAS uses a right–handed Cartesian system (figure 2.7) with its origin at the nominal interaction point in the centre of the detector and the z-axis along the beam pipe. The positive x-axis is defined as pointing from the interaction point to the centre of the LHC ring and the positive y-axis is defined as pointing upwards. Cylindrical coordinates (r, Φ) are used in the transverse plane, the azimuthal angle Φ is measured around the beam axis, while θ is the polar angle. At hadronic colliders, it is convenient to introduce another angular variable, the so called rapidity Y. Rapidity is defined as $Y = \frac{1}{2} ln[(E + p_z)/(E - p_z)]$, where E is the energy of the particle and p_z its momentum along the beam axis. The rapidity is a particularly convenient variable at hadronic colliders, where the parton-parton system is boosted along the z-axis, since it has a simple Lorentz transformation law under this boost[4]. For ultra-relativistic particles, the rapidity is equal to:

$$\eta = -\ln(tan(\frac{\theta}{2})) \tag{2.5}$$

which is called pseudorapidity and it is related to the polar angle θ. The pseudorapidity is usually used in ATLAS as the polar variable. Figure 2.8 shows the pseudorapidity for different values of θ.
The angular distance is measured in units of $R = \sqrt{(\Delta\eta)^2 + (\Delta\Phi)^2}$.

2.2.3 General layout of ATLAS

As already mentioned, modern multi-purpose high energy particle physics experiments have a general common layout. ATLAS is made up of several sub-detectors, in a typical onion-like structure, whose basic principle is shown in figure 2.9. Starting from the interaction point, charged particles (such as electrons, protons, charged pions, muons, ...) interact with the innermost layers: the ATLAS tracker which is immersed in a 2T magnetic field and serves as tracking detector. Neutral particles, such as photons and neutrons, cannot be detected by these first layers and they continue their flight into the next layers: the electromagnetic calorimeter and the hadronic calorimeters which are used to detect the particles with electromagnetic and strong interactions. Combining the signal from the different modules, it is then possible to distinguish these particles. Muons, being minimum ionizing particles (MIP) without strong interaction, are the only particles reaching the outermost layer of the detector which is the muon spectrometer. Neutrinos are a particular case as their interaction rate is too small to interact within the detector, thus they escape ATLAS without leaving any energy deposit. The only

[4] Only a constant term is added under the boost along z making the difference in rapidity ΔY conserved.

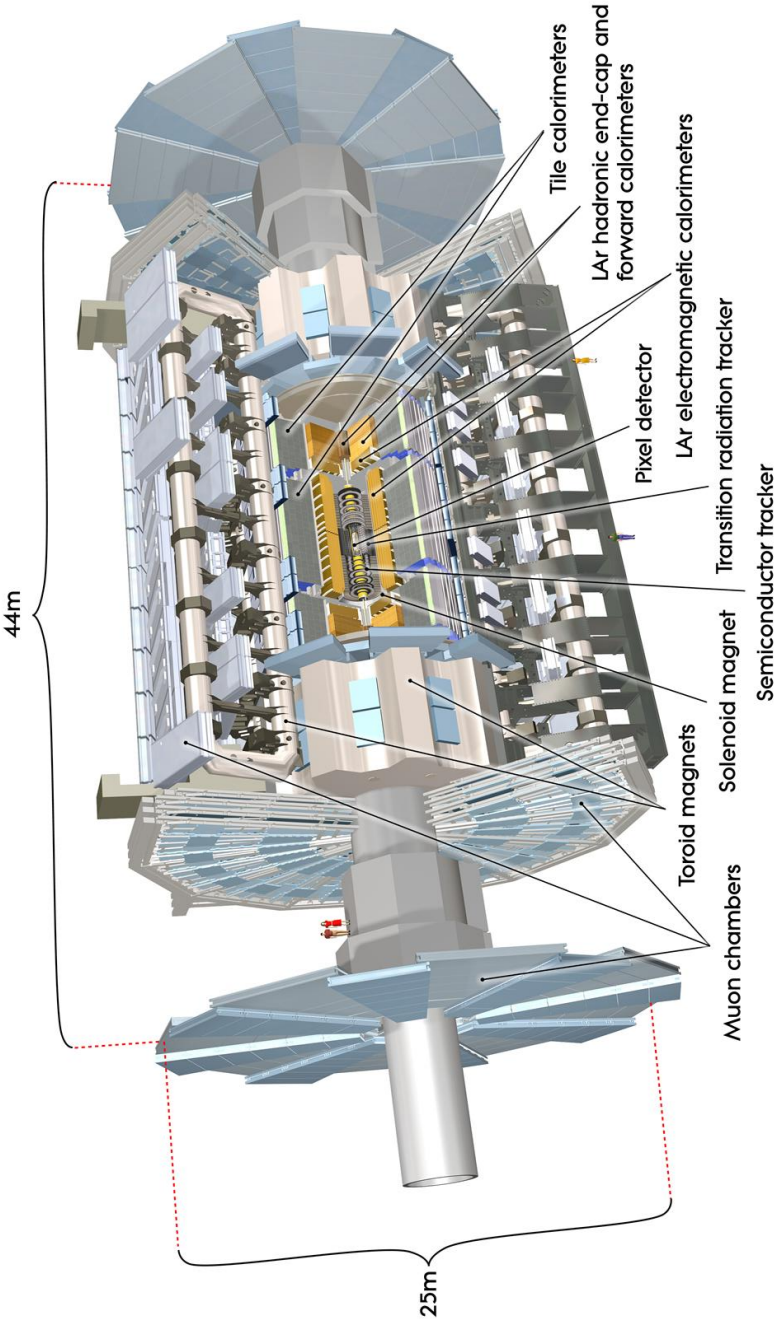

Figure 2.6: General layout of the ATLAS detector.

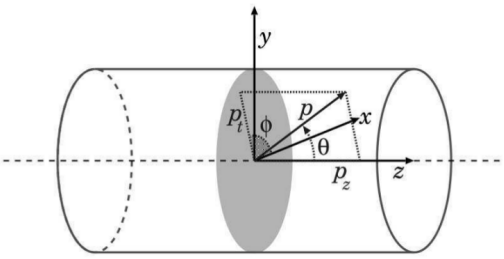

Figure 2.7: Schematic view of the coordinate system used at ATLAS and generally in a collider experiment.

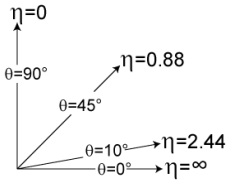

Figure 2.8: Some useful psudorapidity values and the respective θ values

way to infer their presence is to rely on the event kinematics as detailed in chapter 4. In the following sections all the ATLAS subdetectors are described separately.

2.2.4 Inner detector

The innermost module of the ATLAS detector is the Inner Detector (ID) [57] which is dedicated to the tracking, vertex reconstruction and momentum measurements of the charged particles. A charged particle in a uniform field can be characterized by 5 parameters: its azimuthal and polar angles (η and Φ), the charge of the particle divided by its transverse momentum ($\frac{q}{p_T}$), its transverse impact parameter d_0 [5] and the longitudinal impact parameter z_0 [6] (refer to fig. 2.10 for illustration).
To allow accurate vertex reconstruction and momentum measurements in a high track density environment such as the one close to the beam-pipe, the ID is designed with excellent spatial resolution (both in η and Φ coordinates). The ID covers a pseudo-rapidity acceptance up to $|\eta|$=2.5 while it has a full coverage in Φ. It is enclosed by a solenoid providing a 2T magnetic field which bends the particle's tracks and it comprises 3 submodules which make use of different technologies:

- Silicon Pixel detector and Inner B-Layer (IBL);
- Semi-Conductor Tracker (SCT);
- Transition Radiation Tracker (TRT).

Silicon Pixel detector

The Pixel detector [59] is the subdetector closest to the beam-pipe and it consists of silicon pixel modules arranged in three concentric layers in the barrel region (in order

[5] Track's distance of closest approach to the z axis in the plane transverse to the beam-line.
[6] Z coordinate of the closest approach point to the z axis.

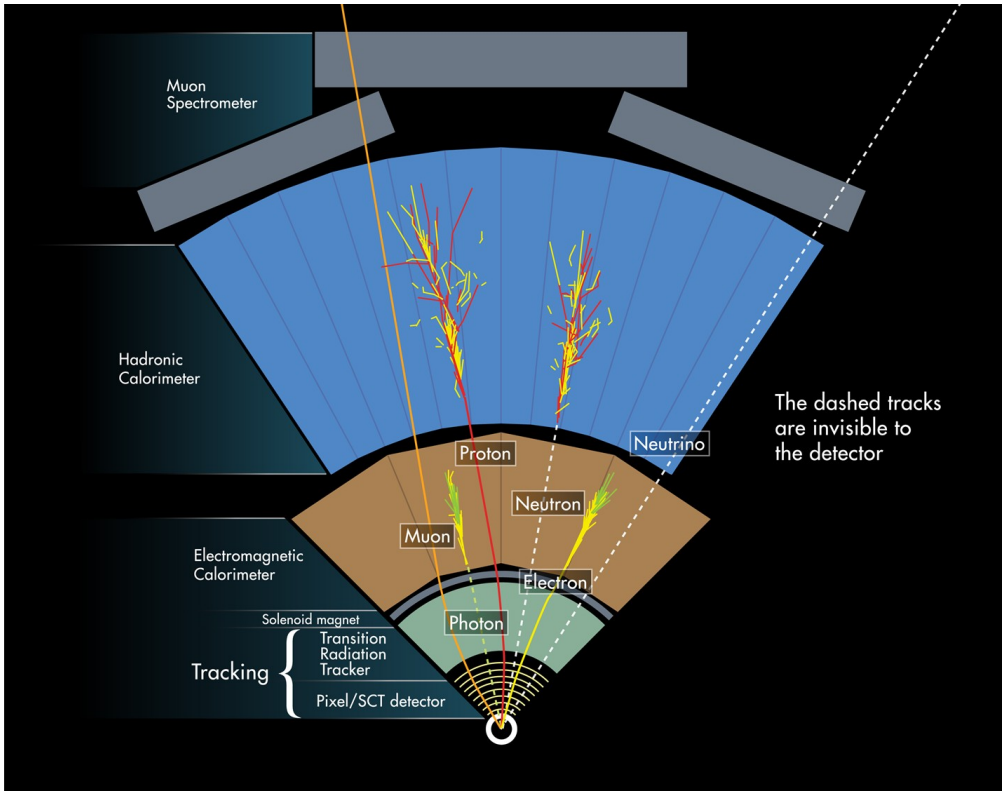

Figure 2.9: Schematic view of the general structure of a modern collider experiment. From the interaction point (bottom) to the outer side (top) the main components are shown: inner detector, electromagnetic and hadronic calorimeter, muon spectrometer. Different particles interact via different interactions, hence they can be detected through the kind of interaction they are subjected to. (ATLAS Experiment 2016 CERN [53])

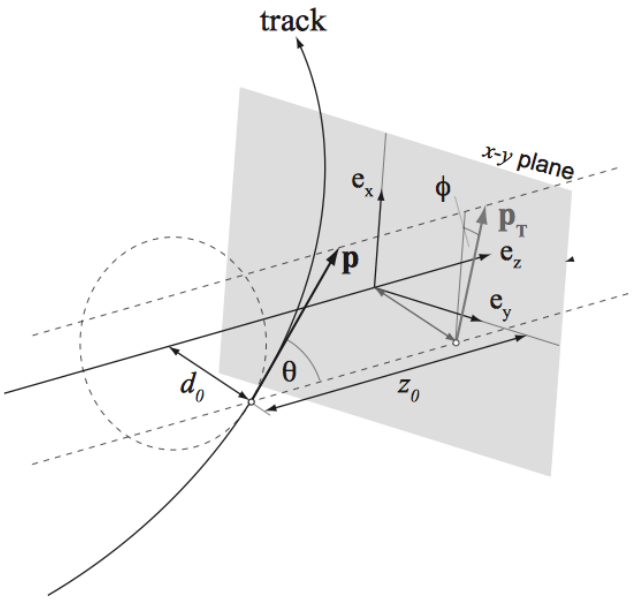

Figure 2.10: Schematic view of the track's coordinates. [58]

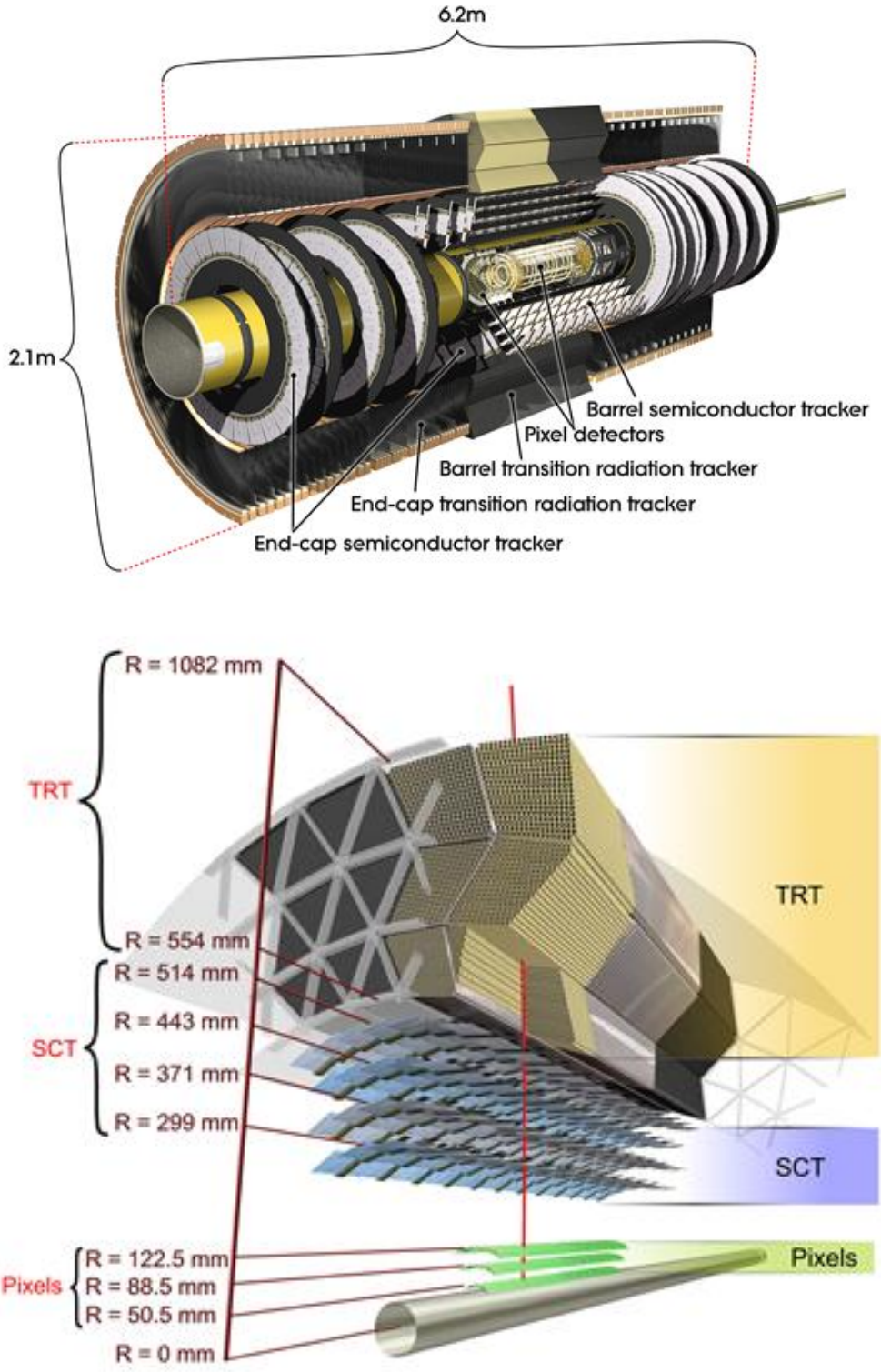

Figure 2.11: Top: Inner Detector (ID) layout. Bottom: Detailed view of the barrel Inner Detector. The ID includes: the Pixel detector, the SemiConductor Trackers (SCT) and the Transition Radiation Tracker (TRT).

to provide measurements in three points) and three discs in the end-cap regions on each side.
Being very close to the beam interaction point, it needs to be resistant to the radiation flux and needs an excellent track resolution.
The Pixel detector is characterized by an intrinsic hit position resolution of ∼12 μm along R-Φ and a resolution of ∼115 μm along the z direction. The Pixel detector cost and the enormous number of readout channels (∼80 millions) make possible to use it only in the inner region.

The Insertable B-Layer (IBL)

The IBL [60] is a fourth layer which has been added before the start of Run2 (during LS1) to the present Pixel detector between a new smaller beam pipe and the current inner Pixel layer. It is made of 14 staves and it is now the innermost layer of the pixel detector, with an average distance of the staves from the center of the beam pipe of ∼33 mm. It has been designed to achieve very good spatial resolution with special care to be resistant to high radiation. Each stave is 64 cm long with a coverage of $|\eta| < 2.9$. The IBL allows for an improved precision of the primary vertex position and a consequent reduction of the transverse impact parameter uncertainty ($20\mu m$ at $p_T = 10$ GeV, μ =0).

Semi-Conductor Tracker

Behind the pixel detector the SemiConductor Trackers (SCT) [61] completes the high precision tracking, with 4 additional hits per track expected in the barrel. The SCT follows the same principles of the pixel detector. It consists of modules of silicon strips (instead of pixels) arranged in four concentric barrels and two endcaps of nine disks each, covering an acceptance of $|\eta| < 2.5$. It is organized in 4 layers approximately at 30, 37, 44, 51 cm from the interaction point, each one composed of 2 microstrip sensors. The intrinsic hit resolution of the strips is ∼16 μm along R-Φ and ∼580μm along z axis.

Transition Radiation Tracker

The outermost ID module is the TRT. It is made up by 4 mm gaseous straw tubes, arranged parallel to the beams in the barrel region and radially in the end-cap. It has the worse spatial resolution among the ID sub-detectors and it provides only the R-Φ information, for which it has an intrinsic accuracy of 130 μm per straw. The lower precision per point is compensated by the large number of measurements and by the longer measured track length: in fact it provides a large number of hits (typically up to 36 per track) which are fundamental for tracks reconstruction, particle identification and momentum measurement.
The combination of precision trackers at small radii with the TRT at a larger radius gives very robust pattern recognition and high precision in both $R - \Phi$ and z coordinates.

2.2.5 Calorimetry

The ID is surrounded by the ATLAS calorimeter system which is the detector part dedicated to accurately measure the energy and direction of the particles passing through and interacting either electromagnetically or hadronically with the material. Only muons

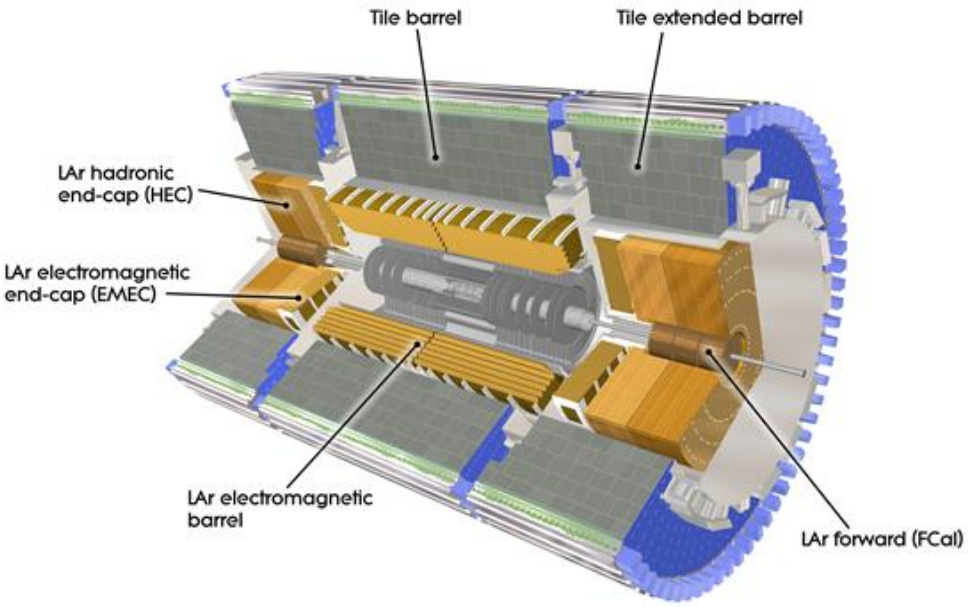

Figure 2.12: View of the ATLAS calorimeter system.

and neutrinos escape the calorimeters without (significant) energy deposits [7].
Particles coming from the collision and entering the calorimeters interact with the material creating cascades of particles, usually called showers. Depending on the incoming particle, these showers have substantially different properties, thus requiring different techniques for precise detection. Electromagnetic showers are caused by electrons and photons, while the hadronic ones arise from hadrons coming from a variety of different processes (fragmentation of quarks and gluons produced at the interaction point, pions from tau decays, etc.) and appear as *jets* in the detector (see Sec. 3.4). In order to precisely measure both electromagnetic and hadronic showers, the calorimeter system is composed by two separate subdetectors: an electromagnetic compartment and a hadronic compartment. A representation of the ATLAS calorimeters is shown in figure 2.12. To provide precise missing tranverse momentum measurements [8], a nearly full hermeticity in pseudorapidity (extending up to $|\eta|<4.9$) is required.
Good containment for jets and limited punch-through into the muon system are also important requirements which are achieved thanks to the calorimeter thickness. The ATLAS calorimeters are sampling calorimeters [9], which means that they are built as a serie of alternating layers of active material and absorber material: the absorber material generates signal by forcing the interactions (here the electromagnetic and hadronic showers are produced) while the active is meant to measure the amount of energy in the shower. The ATLAS electromagnetic calorimeter uses liquid Argon as an active medium while the barrel hadronic calorimeter employs a scintillator material.

[7] In the $E_{\mathrm{T}}^{\mathrm{miss}}$ chapter 4 the case of muons will be discussed in more detail. Muons can leave non negligible energy deposits in calorimeters, this effect is accounted for in $E_{\mathrm{T}}^{\mathrm{miss}}$ reconstruction.
[8] Missing transverse momentum will be introduced and discussed in detail in chapter 4
[9] Homogeneos calorimeters are the opposite of sampling calorimeters. In homogeneos calorimeters the entire volume is active material. They can be built with inorganic heavy scintillating crystals or non-scintillating Cherenkov radiators. CMS calorimeters are homogeneos calorimeters.

Electromagnetic Calorimetry

The Electromagnetic Calorimeter (EM) is optimized to contain electromagnetic showers, originated by electrons and photons. It is built as a LAr (liquid Argon) ionization chamber with lead absorbers. To keep the LAr liquid, the different components are installed into cryostats maintaining an operating temperature of 88.5 K. A particle traversing the calorimeter medium ionizes the LAr and the resulting charges are collected by the electrodes, where a high voltage is applied.
The EM calorimeter is divided into a barrel part and two end-cap components, each housed in their own cryostat. The two half-barrels cover the pseudorapidity range $|\eta|<1.37$ and the two endcap regions cover the range $1.52<|\eta|<2.37$. The region $1.37<|\eta|<1.52$ is usually called crack region and it suffers from slightly degraded performance because of the ID services passing through.
The characteristic interaction distance for an electromagnetic interaction is the radiation length (X_0), defined as the mean distance over which a high energy electron loses $\frac{1}{e}$ of its energy by bremsstrahlung. It corresponds also to $\frac{7}{9}$ of the mean free path of a photon before it undergoes pair production. An high energy electron lose his energy by bremsstrahlung if $\left\langle -\frac{dE}{dx} \right\rangle_{collision} < \frac{E}{X_0}$. The emitted photons can convert into electrons and positrons, which can irradiate photons, which again can undergo pair production, and other lower energy photons can be emitted. The process initiates a shower of particles, which is measured in length of X_0, and it develops until the electron energies fall below the critical energy and then dissipate their energy by ionization and excitation. X_0 is therefore an important parameter governing the longitudinal development of an EM shower and is carefully chosen in the design of a EM calorimeter as a compromise of having good shower containment, physical size and cost. As long as a good number of X_0 is adopted, the energy of electromagnetic showers is nearly fully absorbed. The total thickness of the ATLAS EM calorimeter is $> 22\ X_0$ in the barrel and $>24X_0$ in the endcaps.
The full EM calorimeter has an accordion geometry as illustrated in Fig. 2.13: the absorber and active layers are accordion-shaped, allowing for full azimuthal coverage without blind regions. The plates are oriented so that the showers cross the same plate repeatedly: in the barrel, the accordion shaped waves are parallel to the beam axis and their folding angle varies along the radius in order to keep the liquid argon gap as constant as possible while in the EM endcaps, the accordion waves run axially and the folding angle varies with radius. In the endcap the gap varies with the pseudorapidity due to the accordion geometry and therefore the high voltage needs to vary accordingly to maintain a constant calorimeter response as a function of the pseudorapidity.
To ensure precise measurements, the EM calorimeter is longitudinally segmented in three sections, called "strips", "middle" and "back" sections:

- strips: starting from the interaction point it is the first layer. It is finely segmented in η to provide a high resolution and an accurate position measurement. In addition it is used to distinguish photons from decaying neutral pions;
- middle: is the central layer in the EM calorimeter and collects the largest fraction of the energy of the electromagnetic shower being $\sim 10X_0$ in depth;
- back: is the last layer from the interaction point, it aims at collecting the tail of the electromagnetic shower which could leak the hadronic calorimeter. Its thickness is about $\sim 2X_0$.

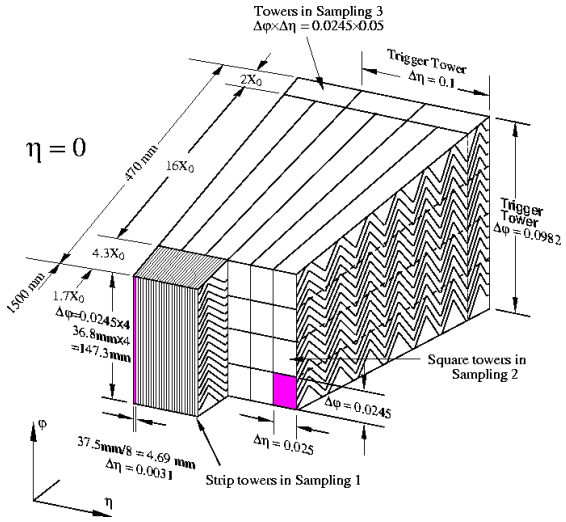

Figure 2.13: Representation of a section of the electromagnetic barrel calorimeter, showing the accordion geometry and the detector segmentation. The three layers of calorimeter cells and their corresponding sizes and radiation lengths X0 are shown.

Section	Segmentation ($\eta \times \Phi$)
Strip	0.003 × 0.1 for $\lvert\eta\rvert$<1.4 0.025 × 0.025 for 1.4<$\lvert\eta\rvert$<1.475 0.003-0.025 × 0.1 for 1.375<$\lvert\eta\rvert$<2.5 0.1 × 0.1 for 2.5<$\lvert\eta\rvert$<3.2
Middle	0.025 × 0.025
Back	0.050 × 0.025

Table 2.2: Electromagnetic Calorimeter segmentation

To precisely measure the energy of electrons and photons, energy losses in the material before the electromagnetic calorimeter need to be accounted for. For this reason an additional very thin (∼1mm) and finely segmented layer is set in front of the EM calorimeter (presampler) to recover the energy lost by electron and photons in the material in front of the calorimeter. It covers $|\eta|$ <1.7. The EM calorimeter segmentation values are shown in Table 2.2 for each section. The energy resolution $\frac{\sigma(E)}{E}$ of each sub-calorimeter was evaluated with beams of electrons and pions before their insertion in the ATLAS detector and cross checks in situ. The experimental measurements of the relative energy resolution, after noise subtraction, for the EM calorimeter can be parametrized as:

$$\frac{\sigma(E)}{E} = \frac{a}{\sqrt{E}} \oplus c \tag{2.6}$$

where $\oplus$ represents addition in quadrature, E is in GeV, a∼10%-17%$[\sqrt{GeV}]$ and c∼0.7% [65]. The energy scale is determined by in situ measurements with a precision of few % [10].

[10] Using $Z \to ee$ events, it can be refined to a precision of a few per mille (as it has been done for the recent W mass measurement [66])

Hadronic Calorimetry

While the dominant processes in EM showers are the e^+e^- pairs production from photons and the photon emission by bremsstrahlung for electrons and positrons, in hadronic showers the dominant process is the inelastic scattering of incoming hadrons with nuclei material. In fact in each LHC collision, a huge quantity of quarks, gluons, hadrons is produced. Quarks and gluons undergo hadronization originating a bundle of collimated particles resulting in jets. All the particles other than electrons and photons do not release all their energy and are not fully contained in the EM calorimeter. Muons enter the hadronic calorimeter without being stopped. Hadrons interact with the material nuclei producing other hadrons, which in turn will interact and produce other hadrons giving rise to an hadronic shower. The mean free path for nuclear interactions (i.e. the mean distance before hadrons interact with nuclear matter) is called interaction length λ_I and is proportional to $\lambda_I \sim \frac{1}{\rho}A^{\frac{1}{3}}$, where ρ is the nuclear density and A is the mass number of the atomic species. Hadronic showers are complicated processes with respect to electromagnetic showers. A large variety of particles can be produced: π^0 and η mesons, whose decaying photons generate high-energy EM showers, charged secondaries such as $\pi^{\pm}$ or p, neutrons, which can be produced in different ways. Moreover a high fraction of processes results in invisible processes (loss of nuclear binding energy, nuclear recoils...). In contrast to EM showers, where the most of the energy is absorbed, a significant fraction of the hadronic shower energy is undetectable making the intrinsic energy resolution of a hadronic calorimeter worse than the one of an EM calorimeter.
ATLAS has three hadronic calorimeters: the tile calorimeter, the Hadronic End-cap Calorimeter (HEC), and the Forward Calorimeter (FCal).
The tile calorimeter consists of a central barrel part and two extended barrels, segmented in depth in three layers, and covering the region $|\eta| < 1.7$. It is made of a steel absorber and, as the name suggests, scintillating tiles, made of a doped polystyrene scintillator, as the active medium. Particles entering this active medium release their energy through the interaction with the scintillator materials. Light is therefore produced and the energy measurement is made from the collected light. The HEC and FCal modules cover larger rapidities and they uses liquid argon technology.
The HEC, covering the region $1.5< |\eta| <3.2$, uses copper plates as absorbers and consists of two independent wheels per end-cap, each divided into two segments in depth, for a total of four layers in each end-cap. The FCal, covering the very forward region $3.1< |\eta| <4.9$, consists of three modules in each end-cap.
The energy resolution of the barrel and endcap detectors is $\frac{\Delta E}{E} = \frac{50\%}{\sqrt{E[GeV]}} \oplus 3\%$ while the energy resolution for the forward calorimeter is $\frac{\Delta E}{E} = \frac{100\%}{\sqrt{E[GeV]}} \oplus 10\%$.

2.2.6 Muon Spectrometer (MS)

Muons, being much heavier than electrons ($m_\mu \sim 200 m_e$), typically loose their energy through ionization and are therefore the most penetrating particles, thus requiring a dedicated detector. The detector devoted to detect muons and to measure their energy and position is the outermost ATLAS module and it defines the overall dimension of the detector. To achieve high resolution for momentum measurements (up to a few TeV) it is designed as a air-core spectrometer and it has its own trigger system and tracking chambers. A representation of the ATLAS muon system is shown in figure 2.14. The MS covers out to $|\eta| < 2.7$ and can trigger on particles within $|\eta| < 2.4$. A

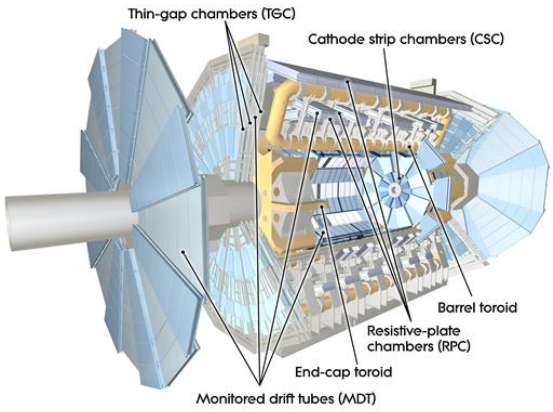

Figure 2.14: Overview of the ATLAS muon spectrometer components.

large volume magnetic field is necessary to bend the particle trajectories. It is provided by a barrel toroid in the region $|\eta| < 1.4$, by two smaller end-cap toroid magnets in the $1.6 < \eta < 2.7$ region and by a combination of the two in the transition region $1.4 < \eta < 1.6$. The tracking system is done in the barrel by three concentric modules at radii 5, 7.5 and 10m from the beam pipe. In the endcap it is performed by wheels at 7.4, 11, 13, 21.5m from the interaction point, along the z axis. These modules are the Monitored Drift Tubes (MDTs) and the Cathod Strips Chambers (CSCs) at large pseudorapidities. The muon detector has its own trigger system which covers the region up to $|\eta| < 2.4$, and is composed by Resistive Plate Chambers (RPCs) in the barrel and Thin Gap Chamber (TGC) in the end-caps. The triggering system provides bunch-crossing identification (BCID), well-defined p_T thresholds and a measurement of the muon coordinate in the direction orthogonal to the chambers dedicated to precision tracking. Momentum resolution $\sigma(p_T)/p_T$ of the ATLAS muon spectrometer system is of about $2 \div 3\%$ over most of the kinematic range, while it reaches 10% for momenta of the order of 1 TeV.

2.2.7 The ATLAS forward detectors

The ATLAS forward detectors are a set of smaller detectors. Located in the very forward region, they are meant to study elastic and inelastic pp scattering at small angles.

LUCID The luminosity measurement detector LUCID (LUminosity measurement using Cerenkov Integrating Detector) is situated at $\pm$ 17 m from the interaction point. It is monitoring the online luminosity delivered to ATLAS. It is built as an array of Cerenkov tubes to count charged particles: as charged particles from the collision pass through, it detects the produced Cerenkov radiation. To measure the instantaneous luminosity of the proton beam collisions it uses the proportionality between the particle multiplicity and the number of interactions.

ZDC ZDC (Zero-Degree Calorimeter) sits at $\pm$ 140 m from the interaction point. ZDC is designed to detect very forward ($|\eta| >8$) neutrons and photons from heavy-ion and pp collisions.

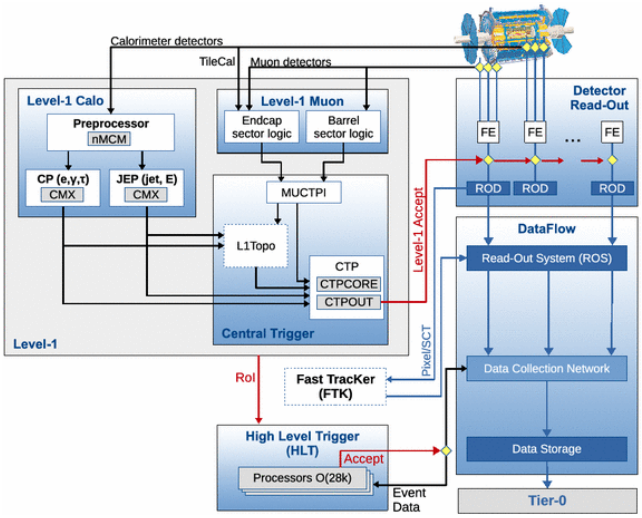

Figure 2.15: Schematic view of the ATLAS trigger system [68].

ALFA ALFA (Absolute Luminosity for ATLAS) being located at 240 m from the interaction point it is the furthest detector belonging to the ATLAS experiment. It measures the elastic proton-proton scattering cross section.

2.2.8 Trigger System

At a design luminosity of 10^{34} cm^{-2} s^{-1}, the bunch crossing rate at LHC is 40 MHz, with an average pile-up of 25 interactions per crossing, which corresponds to an interaction rate of $\sim$1 GHz. Such a rate exceed the maximum rate of events which ATLAS can record and store, thus the rate of selected events must be reduced. For each collision, among all the events produced it is necessary to record the ones that have a potential physical interest. For this reason a sophisticated trigger system ([67], [68]) is used to rapidly decide wheter an event should be retained or not, reducing the rate of events by a factor of $\sim 10^7$ but at the same time retaining an excellent efficiency for the interesting events (high p_T events against minimum bias processes). The ATLAS trigger system is split into two levels: a first fast trigger system called Level-1 (L1), which is hardware based, and a slower system (High-Level Trigger, HLT) which is software based, it consist of two sub-levels (level 2 and event filter) and it takes as inputs the events retained by the L1 trigger. The aim of L1 is to do a first coarse selection, within a few μs, looking for high transverse-momentum particles (electrons, photons, jets, muons, $E_{\mathrm{T}}^{\mathrm{miss}}$). When such objects are found, one or several regions of interest are identified (the η and Φ region, the subdetector hit and the threshold fired). L1 reduces the event rate to $\sim$100 kHz (for Run-2 collisions). HLT trigger processes within a few seconds the events retained by L1 and performs a more complete reconstruction of physics objects which is close to the offline reconstruction (but not with the final calibration constants). The average rate after HLT is $\sim$500 Hz. An illustration of the ATLAS trigger system is given in Fig. 2.15.

2.3 MC Simulations

All the physics analysis make use of simulated events: the physics events in data are compared to events that are simulated. More in detail, each analysis simulates events of

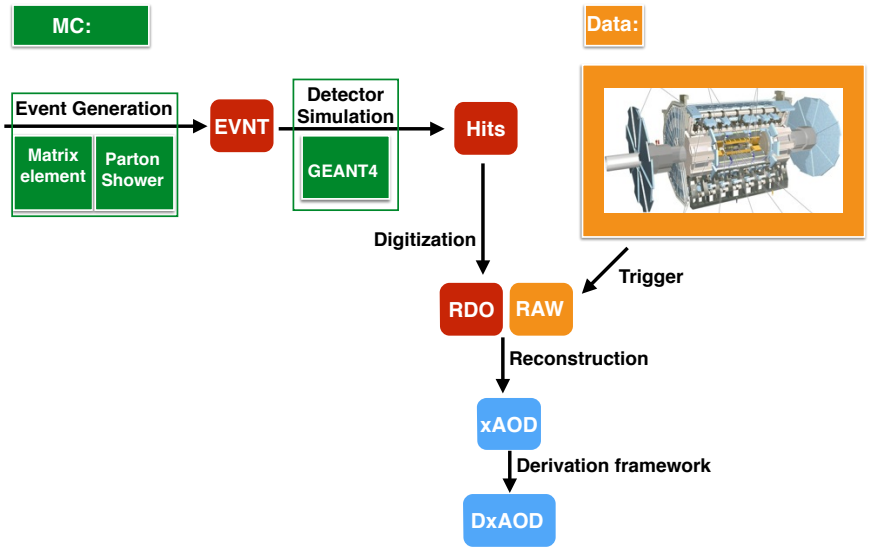

Figure 2.16: Schematic view of the MC simulation chain, from event generation to derived data format. Also the data chain is shown.

the signals the analysis is looking for and of the standard model background processes relevant for the final state under study. The production of simulated events is therefore of major importance for ATLAS. The state of the art generators are used to model the physics processes and to simulate the particles interactions with the ATLAS detector. The main steps for generating Monte Carlo (MC) samples can be summarized as follow:

- Event generation (*i.e. simulate proton collisions*):
  - Matrix Element ("hard interaction");
  - Parton Shower;
  - Underlying Event (proton debris not participating to the hard interaction);
- Detector simulation (i.e. *it simulates the detector and its response to the particles passing through*);
- Digitization (*i.e. the energy deposited in the detector is converted to signals and the output is similar to the one for data*)
- reconstruction (as for data).

A schema of these different phases is shown in Fig 2.16.

2.3.1 Event Generation

The details of the event generation part depend on the MC generators used. There are different MC generators types: complete generators which model both the hard-scatter process and parton showers, and generators which are specialized for certain generation steps, they can be interfaced to the event generator programs to simulate the parton shower and hadronization of a given process.

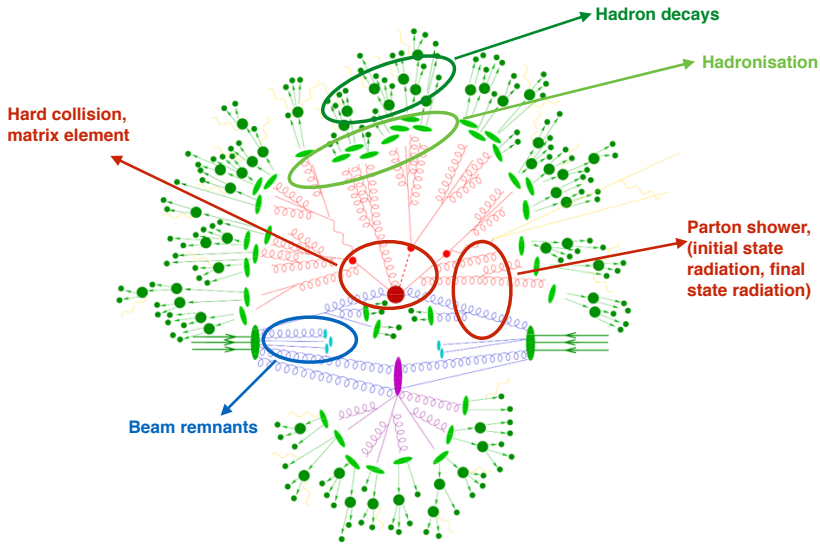

Figure 2.17: Sketch of a hadron-hadron collision as simulated by a Monte-Carlo event generator [69].

- Matrix Element: the first step is the calculation of the matrix element for the considered process to a certain order in QCD and QED. This step calculates the physics signal of interest from the partons of a LHC *proton-proton* collision. This is called the hard process and it is simulated by an event generator program. The matrix element calculation is the part containing the physics specific to the model considered (either SM or BSM). The pdf (parton distribution function) is given as input.

- Parton Shower: the partons from the hard interaction are colored and radiate gluons. causing initial and final state radiation. Radiated gluons emit new partons which again produce gluons, giving rise to a *shower*. This process continues until hadronization occurs. These processes are not perturbative and do not depend on the physics process that generated the hard process (hypothesis of factorization).

- Hadronization: because of confinement, the radiated partons cannot exist freely, they recombine to form colorless hadrons in a process called hadronization. Hadrons decay into particles that are ultimately detected in the detector.

- Underlying Event: the remnants of the original incoming protons (i.e. the non-hard scattered partons) constitute the *underlying event*. The interaction between these colored states needs to be modeled and included in the simulation. These interactions are characterized by many objects at low transverse momentum and small angle.

A visual representation of these different steps is shown in Figure 2.17.

2.3.2 Detector simulation

This part of the simulation process is devoted to simulate the interactions of the resulting long lived particles (leptons, hadrons) with the detector material. The ATLAS detector is described with `GEANT4` (GEometry ANd Tracking) [72], a software program which uses the best knowledge of the interactions between relativistic particles and materials, based on calculable cross sections, numerical models and phenomenological models tuned on experimental data. Simulations which uses entirely `GEANT4` for the description of the whole detector are referred to as *full simulations* [71]. They are computationally very expensive, in particular most of the CPU consumption is spent in the EM calorimeter for simulating showers. To overcome this problem, ATLAS uses also the so called *AtlasFast-II* [73] simulations which adopt parameterization of the showers in the calorimeter while for the inner detector and muon spectrometer the simulations are unchanged with respect to *Full simulations*.
After the simulation of the detector, another important step is needed to simulate the detector electronics. This phase is called *digitization*. The input to the digitization steps are the energy deposits which are in sensitive detector volumes (*hits*), which are coming from the detector simulation (`GEANT4`) step. The digitization software then converts these energy deposits into detector responses (*digits*), voltages or times from pre-amplifier outputs, and models the peculiarities of each detector's charge collection, including electronics noise, and channel-dependent variations in detector response [70]. The output format is a Raw Digital Object (RDO), which is the same format as for the data that is written out from the detector readout drivers.
The following step in MC simulation is the *reconstruction* phase. The inputs are RAW (for data) or RDO (for MC) [11] and the reconstruction is common between the two. The reconstruction in ATLAS is divided in many steps and needs many configuration settings, such as the pileup settings, trigger menu settings etc. This part is devoted to clustering regions of potentially interesting physics based on the detector response and apply criteria to define different particle types. The output of the reconstruction are samples in a format ready to be used for analysis: Analysis Object Data (xAOD) and dedicated derived formats (DAOD) for physics and performance studies.

2.3.3 Generator Filters

In order to increase statistics in a particular region of the phase space of the outcoming partons, there are different strategies which can be exploited:

- Generator Phase-Space Cuts: cuts imposed at generator level to generate only events passing these cuts. It helps to populate the region of phase space of interest. Generator phase space cuts are not filters.

- Generator Filters: after generation certain events are thrown away according to the filter criteria. The MC generator reports the total generated cross-section so the filtering efficiency needs to be applied. It is a single factor which should be multiplied to the total cross section, to account for the fact that not the full cross-section of that process has been generated.

[11] The main difference between the two is that RDO contains also truth information.

Chapter 3

Physics objects reconstruction

In this chapter a brief introduction to the reconstruction of the physics objects of interest for this work is given.

3.1 Electrons

Electrons and positrons (here after just referred to as electrons) in ATLAS give rise to tracks in the inner detector and energy deposits in the electromagnetic calorimeter. The electron and photon reconstruction process starts by searching for energy deposits in the EM calorimeter with a dedicated cluster finding algorithm which is called *sliding window*. The algorithm looks for energy deposits (*seed*) in the EM calorimeter and forms rectangular windows of fixed size around them. The size of these windows is 3×5 cells in $\eta \times \phi$ in the middle layer. A transverse energy exceeding 2.5 GeV is required. If such a cluster is found, it is a potential photon/electron cluster.
To distinguish between photon and electron candidates, the electron reconstruction procedure is completed by the track matching. The track is required to be reconstructed within a window of 0.05×0.10 in $\eta \times \Phi$ of the cluster barycentre. If at least a track is matched to the cluster, the cluster is assumed to be an electron candidate, otherwise the cluster is considered a photon candidate (as it is consistent with the case of an unconverted photon).

3.1.1 Electron Identification

As explained above, a cluster is considered an electron candidate if a matching track is found while no conversion is flagged. This early classification is the starting point of a more refined identification.
Sets of identification criteria with different levels of background rejection and signal efficiency are used to discriminate electron candidates from background, such as hadronic jets (for instance $\pi^{\pm}$, π^0) or converted photons.
These identification criteria rely on the shapes of electromagnetic showers in the calorimeter as well as on tracking and track-to-cluster matching quantities. The complete list of quantities used to discriminate between signal-like electrons and background-like objects can be found in [76]. The Run2 electron identification algorithm is a likelihood based method. It is a multivariate likelihood technique which uses many discriminating variables to discriminate between signal and background electrons objects.
There are three working points, referred to as *loose*, *medium*, *tight* (in order of increasing background rejection and decreasing identification efficiency).

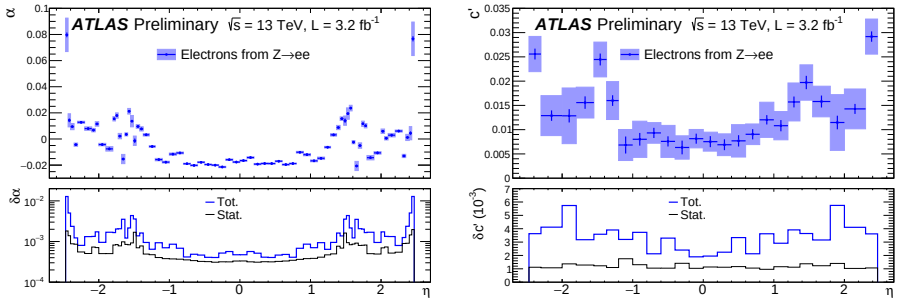

Figure 3.1: Left: Energy scale factor α, Right: constant term $c_i^{'}$ for energy resolution and their uncertainties measured in $Z \to ee$ events, as a function of η. [77]

3.1.2 Electron Isolation

Additionally, electrons can be required to be isolated from other activity in the calorimeter or inner detector to further distinguish them from background objects. The electron isolation is a measure of the energy of the particles which are produced around the electron. Two isolation variables are defined, one track based and the other calorimeter based. Using these two discriminating variables, different operating points for electron isolation are defined. In the analysis described in chapter 5 and 6, *gradient* isolation criteria are used, with an efficiency of 90% for true electrons with $p_T > 25$ GeV and 99% for true electrons with p_T >60 GeV.

3.1.3 Electron efficiency and energy

The efficiency to find and select an electron in the ATLAS detector is measured from different contributions: reconstruction, identification, isolation, and trigger efficiencies. To account for differencies in data and MC, the ratio of the data to MC efficiencies are used as multiplicative weights to be applied to simulated events as corrections.

The electron's total energy is the sum of the energy cluster deposit plus:

- the measured energy deposited in front of the electromagnetic calorimeter;
- the energy deposited outside the cluster (*lateral leakage*);
- the energy deposited beyond the electromagnetic calorimeter (*longitudinal leakage*).

These components are estimated using MC simulations [77].
In order to correct a possible residual disagreement in the energy scale and resolution between data and MC, an in-situ procedure using $Z \to ee$ events is applied so that the the electrons invariant mass reproduces the Z mass peak. The energy mis-calibration is given by the difference in response between data and MC and is parametrised by: $E_i^{data} = E_i^{MC}(1 + \alpha_i)$.
The difference in energy resolution between data and simulation can be modeled by an additional effective constant term ($c_i^{'}$) for a given pseudorapidity region: $(\frac{\sigma(E)}{E})_i^{data} = \frac{\sigma(E)}{E})_i^{MC} + c_i^{'}$.
The measured values and their uncertainties are shown in Fig. 3.1.

3.2 Muons

To reconstruct muons, track information from ID and MS is used. Firstly, muon reconstruction is performed independently in the ID and MS. As a second step the information from the different subdetectors is combined to form the muon tracks that are used in physics analyses.
In the ID, muon tracks are reconstructed like any other charged particles, as it is described in [75].In the MS, segments reconstructed from hits in the inner layer MDT and CSC (Sec. 2.2.6) are used. Muon track candidates are then built by fitting together hits from segments in different layers.
The muon reconstruction is performed with different algorithms. Four different muon types are defined depending on which subdetectors are used in reconstruction [78].

- *Combined* (CB) muons: tracks are independently reconstructed in the ID and MS. A global refit is used to form a combined track using both MS and ID information. The main strategy uses an *outside-in pattern recognition*: muons are reconstructed in the MS and then extrapolated inward and matched to an ID track. As opposite, an *inside-out* approach is also used: ID tracks are extrapolated outward and matched to MS tracks;

- *Segment-tagged* (ST) muons: a track in the ID is classified as a muon in case, once extrapolated to the MS, it is associated with at least one local track segment in the MDT or CSC chambers. This type of muons is used when a muon crosses only one layer of MS chambers, either because of its low p_T or because it falls in regions with reduced MS acceptance;

- *Calorimeter-tagged* (CT) muons: in case an ID track is matched to energy deposit in the calorimeter which is compatible with a minimum-ionizing particle (MIP), that track is identified as a muon. This muon type has the lowest purity but it helps to recover the acceptance where the MS is only partially instrumented (η <0.1);

- *Extrapolated* (ME) muons: muons are reconstructed from a MS track which is compatible with coming from the interaction point. These muons extend the muon reconstruction acceptance in the region which is not covered by the ID (2.5< η <2.7).

3.2.1 Muon identification

After reconstruction, muon identification is performed by applying quality requirements in order to discriminate *background* muons (from pion and kaon decays) from *signal* muons (prompt muons). Different variables (such as muon charge and momentum, χ^2 of the combined track fit) are used to discriminate between the former and the latter and different working point are defined: *Medium, Loose, Tight*, and *High-p_T* muons.
In the searches discussed in this thesis, *medium* muons are selected. The medium working point is the default selection for muons in ATLAS. It minimizes the systematic uncertainties which are associated with muon reconstruction and calibration. For this class of muons, only the CB and ME types are used.
Reconstruction efficiency for the medium muons is shown in Fig. 3.2 (left). The level of agreement of the measured efficiency (ϵ) in data and the one measured in MC, is defined as the ratio between the two and is called Scale Factor: $SF = \frac{\epsilon_{data}}{\epsilon_{MC}}$. It quantifies the discrepancy of MC samples from the real effect in data, and is used to correct simulated

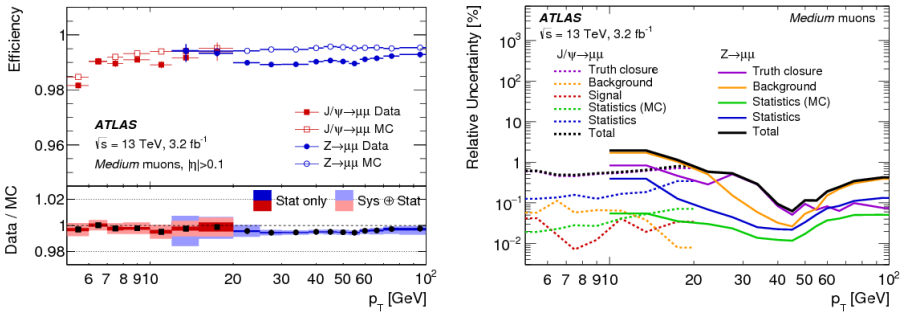

Figure 3.2: Left: Reconstruction efficiency for the Medium muon selection as a function of the p_T of the muon, in the region 0.1< $|\eta|$ <2.5 as obtained with $Z \to \mu\mu$ and $J/\psi \to \mu\mu$ events. Right: Total uncertainty in the efficiency scale factor for medium muons as a function of p_T. The combined uncertainty is the sum in quadrature of the individual contributions. [78]

events by applying the SF as a weight. The total uncertainty of the efficiency scale factors as measured in 2015 data is shown in Fig. 3.2 (right).

3.2.2 Muon isolation

Typically, muons which comes from W/Z/Higgs decays are well separated (*isolated*) from other objects. Therefore, the measurement of the activity (muon isolation) around a reconstructed muons can further reduce the contamination of *background* muons.
There are two different variables for muon isolation: track based and calorimeter based. The isolation criteria use the ratio of one the two variables to the muon p_T.
Different isolation working points are defined for physics analysis [78] and differ in the use of the discriminating variables and the efficiencies.
In the analysis described in chapter 5 and 6, the so called *gradient* isolation criteria are used, with an efficiency of 90% for true muons with p_T > 25 GeV and 99% for true muons with p_T >60 GeV.

3.3 Taus

The reconstruction and identification of tau leptons in ATLAS is performed for hadronically decaying tau-leptons only, as it is impossible to distinguish muons and electrons coming from tau decays from prompt ones. Hadronically decaying tau-leptons may be differentiated from jets based on their low track-multiplicity and narrow shower shape. These and other discriminating characteristics are combined in a Boosted Decision Tree. Tau leptons are not reconstructed in the analysis described in chapter 5 and 6.

3.4 Jets

In hadronic collisions jets play a major role. Quantum chromodynamics (QCD) describes strong interactions as resulting from the interaction of spin-1/2 quarks and spin-1 gluons. Quarks appears in different flavours (u, d, c, s, t, b) and each flavour appear in different colours (red, blue, green and the corresponding anticolours). The colour singlet is a combination of three colours. A single quark cannot be a colour singlet and thus should not appear as a physical particle. This property is called confinement. Quarks

are confined inside physical hadrons, which are always colour singlets (colourless). Also gluons carry colour charge. Another important feature of QCD is asymptotic freedom: quarks interact weakly at high energies and strongly at low energies, preventing the unbinding of baryons and mesons. Therefore, a quark or a gluon almost immediately after being produced fragments and hadronizes because it cannot emerge as an isolated coloured particle: with increasing separation of the quark from the parton it comes from, the potential energy stored in the pair increases. At some point the creation of a quark-antiquark pair becomes favorable. The initial quark or gluon materializes into a collimated bunch of hadrons flying roughly in the same direction of the original parton, leading to a collimated "spray" of energetic hadrons, which is the so called jet. The spray of hadrons is treated and reconstructed as a single object as coming from the same parton. The jet reconstruction is crucial to resolve the partonic flow coming from the hard scattering.

As discussed in [80], there are several important properties that a jet definition should have:

- it should be simple to be implemented both in an experimental analysis and in a theoretical calculation;
- it should be defined at any order of the theory;
- Yields finite cross-section at any order of perturbation theory;
- Yields a cross-section that is relatively insensitive to hadronization.

A review of jets and reconstruction alghoritms can be found in [88].

3.4.1 Jet Reconstruction

The first step to reconstruct jets is the identification of separate energy clusters, properly grouping cells in the calorimeters. Jet clustering algorithms start from these clusters to reconstruct jets.
To group cells in clusters there are different cluster-definition algorithms, within the main important one there are the *TopoTower* and *TopoCluster* [81]. The *TopoTower* selects cells around a seed and defines a cone of fixed radius around the seed: the energy of the final cluster is the sum of contributions coming from the cells within this cone. The *TopoCluster* algorithm selects seed cells according to their signal to noise ratio and builds a 3D cluster around these cells. An illustration is given in Fig. 3.3. Topo-clusters are built from a seed cells with $E_{cell} > 4\sigma_{noise}$, where σ_{noise} is the gaussian width of the cell energy distribution. Neighbouring cells with energy exceeding $2\sigma_{noise}$ are added iteratively and finally a ring of cells without further requirements is added to the topo-cluster.
All the jets considered in this document are reconstructed from *TopoClusters* using the anti-k_t algorithm.

The Anti–k_t Algorithm

The anti–k_t algorithms belong to the family of sequential recombination algorithms. Anti–k_t is the most used class of algorithms used at the LHC to reconstruct jets.

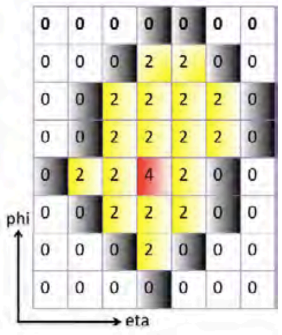

Figure 3.3: An illustration of *Topocluster*. Red: seed of the cluster. Yellow: neighbouring cells. Grey: ring of external cells.

In this class of algorithms, the distance $d_{i,j}$ between each pair of TopoClusters is defined as:

$$d_{i,j} = \min\left(k_{ti}^{2p}, k_{tj}^{2p}\right) \frac{\Delta_{i,j}^2}{R^2} \tag{3.1}$$

and a distance $d_{i,b}$ between object i and the beam b is defined as:

$$d_{i,b} = k_{ti}^{2p} \tag{3.2}$$

where $\Delta_{i,j}^2 = (y_i - y_j)^2 + (\Phi_i - \Phi_j)^2$, while k_{ti}, y_i, Φ_i are respectively the transverse momentum, rapidity and azimuth of particle i. R is a radius parameter, related to the jet size: Anti-kt jets are approximately cones with constant radius R in (y, Φ) space. p is a parameter governing the relative power of the energy versus geometrical ($\Delta_{i,j}$) scales. p=-1 corresponds to the Anti–k_t Algorithm.
The algorithm starts from a list of clusters and groups them into jets. It works as follows:

- loop over all the object pairs and find the minimum across the $d_{i,j}$ and $d_{i,b}$:
  - if the minimum distance is a $d_{i,b}$ then the ith object is a jet, add it to the jet list and remove it from the input list;
  - if the minimum distance is d_{ij} then combine together i and j, according to a recombination scheme, remove i and j from the input list and add the new object to the input list;
- the process is repeated until the input list is empty.

The idea which is at the basis of the anti–k_t algorithm is the following. Consider an event with a few well-separated hard particles and many soft particles. The distance $d_{i,j}$ between an hard particle and a soft particle, according to its definition 3.1, is exclusively determined by the transverse momentum of the hard particle and their geometrical separation. The $d_{i,j}$ between similarly separated soft particles will instead be much larger. Hence, soft particles will tend to cluster with hard ones long before they cluster among themselves. More details can be found in [79].

Jets considered in the analysis described in this document are reconstructed with the anti-k_T algorithm with radius 0.4.

3.4.2 Calibration

The topoclusters are initially calibrated at the electromagnetic (EM) scale, which correctly measures the energy deposited by electrons and photons.
Starting from these clusters, another topocluster collection is created by calibrating the calorimenters cells taking into account the different response to hadrons. This calibration is called Local Cell signal Weighting (LCW). LCW classifies the topoclusters either as electromagnetic or hadronic, then applies corrections which are derived from MC simulations of charged and neutral pions. These corrections are aimed to account for the calorimeter non compensation (i.e. differences in the detector response to hadrons versus leptons and photons), signal losses due to noise threshold effects and energy lost in non instrumented regions.
After this procedure, two classes of jets are available, which are reconstructed either starting from EM or LCW topoclusters. They are called *EM jets* and *LCW jets*. In this documents, EM jets have been used.

Other calibrations and corrections are further applied to EM and LCW jets [82]

- A so called *origin correction* is applied in order to adjust the jet direction, so that it points to the primary event vertex;
- an offset *pile up correction* is taken into account. In time and out of time pile up can affect the jet energy. Corrections to address these effects are derived from MC simulations as a function of NPV and μ in bins of the jet η and p_T;
- Jet energy scale (JES): using simulations, the jet energy energy is corrected to match the energy of the truth jet. Reconstructed jets are matched to the corresponding truth level jet and the average jet energy response is defined as

$$\mathcal{R}^{\mathcal{EM}(\mathcal{LCW})} = \frac{E_{jet}^{EM(LCW)}}{E_{jet}^{truth}} \tag{3.3}$$

  $\mathcal{R}$ is fitted with a Gaussian, the mean is considered the average jet energy response while the width is the jet energy resolution. The calibration correction factor is the inverse of the jet energy response (Fig. 3.4 left). It is studied as a function of the jet E^{truth} and η. After applying this correction, a bias in the reconstructed jet η remains (Fig. 3.4 right) and is corrected for with a dedicated η correction. Jets with this calibrations are referred to as EM+JES jets or LCW+JES jets.
- Global Sequential Corrections (GCW): This correction is aimed to reduce JES flavor dependence (quark/gluon), adjust for the energy loss due to punch through (i.e. hadronic energy deposited beyond the calorimetry system), adjust for calorimeter non-compensation. The GSC leaves the average energy of the jet unaffected while improving the resolution;
- Residual in situ calibration: this last correction is applied only to data and it is used to correct differences in data and MC which are due to imperfections in the detector and interactions modeling.

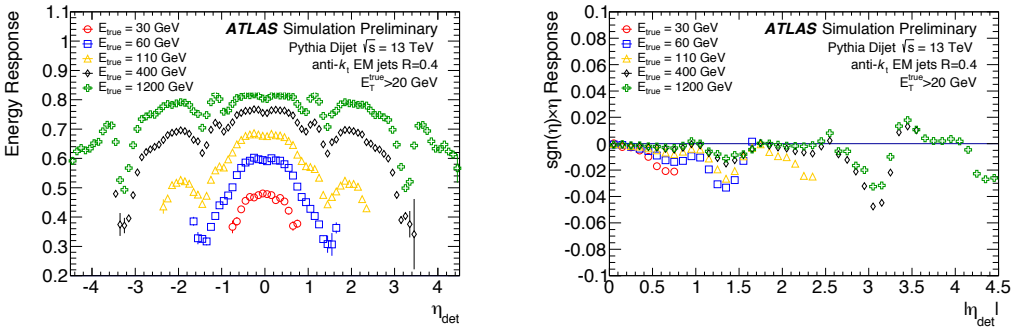

Figure 3.4: Energy response (left) and bias in the η reconstruction as a function of η for EM scale anti-kt, R=0.4 jets.

3.4.3 Jet Vertex Tagger

Pile up jets need to be distinguished from hard scatter jets. During Run1, the so called Jet Vertex Fraction (JVF) [83] technique was used. JVF is defined per each reconstructed jet as:

$$JVF = \frac{\sum_k p_T^{trk_k}(PV_0)}{\sum_l p_T^{trk_l}(PV_0) + \sum_{n\geq 1} p_T^{trk_l}(PV_n)} \tag{3.4}$$

where PV_0 is the hard scatter vertex[1], PV_j with $j \geq 1$ are the primary vertices due to pileup interactions in the same bunch crossing. $\sum_k p_T^{trk_k}(PV_0)$ is the scalar p_T sum of the tracks that are associated with the jet and originate from the hard scatter vertex, while $p_T^{PU} = \sum_{n\geq 1} p_T^{trk_l}(PV_n)$ is the scalar p_T sum of the tracks associated to the jet and originating from any of the other primary vertices (PU vertices).
JVF is bound between 0 and 1, but value -1 is assigned to jets with no associated tracks. JVF is a measure of the fraction of p_T from tracks which are associated to the hard scatter vertex with respect to the p_T associated to any other primary vertex. Values close to 1 are associated to hard scatter jets (negligible p_T^{PU}) while values close to 0 are associated to jets which are likely to be pile up jets. The efficiency of the JVF criteria depends on the number of vertices in the event.
In order to correct for this dependence, for Run2, new track-based variables have been developed.
A first variable is a variant of JVF and is defined as:

$$corrJVF = \frac{\sum_k p_T^{trk_k}(PV_0)}{\sum_l p_T^{trk_l}(PV_0) + \frac{\sum_{n\geq 1} p_T^{trk_l}(PV_n)}{k \cdot n_{trk}^{PU}}} \tag{3.5}$$

where n_{trk}^{PU} total number of pileup tracks per event. The factor $k \cdot n_{trk}^{PU}$ (with k =0.01) is intended to correct for the linear increase of p_T^{PU} with the total number of pileup tracks per event.
A second variable is R_{pT}, defined as the scalar p_T sum of the tracks that are associated with the jet and originate from the hard-scatter vertex divided by the fully calibrated

[1]Defined as the one with the highest $\sum_{trk} p_T^{2\ trk}$.

jet p_T, which includes pileup subtraction:

$$R_{pT} = \frac{\sum_k p_T^{trk_k}(PV_0)}{p_T^{jet}} \tag{3.6}$$

R_{pT} for pile jets is peaked at zero and steeply falling.
The jet-vertex-tagger (JVT) [84] is a new discriminant constructed using those two variables as a 2D likelihood. Similarly to JVF, JVT is defined between 0 and 1: JVT values close to 0 are associated to pile up jets, while hard scatter jets are associated to JVT values close to 1. Value -0.1 is assigned to jets with no associated tracks.

In the analysis described in chapter 5 and 6, jets with p_T <60 GeV and $|\eta|$<2.4 are required to satisfy the requirement JVT > 0.59, corresponding to a selection efficiency for non-pile-up jets of about 92%.

3.5 Overlap Removal

It is possible that a particle is reconstructed as different objects, therefore to resolve this ambiguity, an *overlap removal* procedure is performed. This is applied on all the reconstructed jets, electrons and muons with the quality criteria used in the analysis[2]. The overlap removal consists of a series of conditions which check if two objects overlap and give priorities to one of the two. In particular it follows this flow:

- if ΔR(jet, e)<0.4: remove the electron and keep the jet;
- if ΔR(jet, μ)<0.4 and the jets has ≥3 ID tracks: the jet is kept and the muon is removed;
- if ΔR(jet, μ)<0.4 and the jets has <3 ID tracks: the muon is kept and the jet is removed.

[2]Therefore, for instance the photons and loose electrons are treated as jets, if they have p_T >25 GeV.

Chapter 4

Missing Transverse Momentum

As discussed in the previous chapters, all the SM particles apart from neutrinos interact in the detector and are identified from the energy deposits or tracks that they leave inside. Neutrinos are a special case: they are so feebly interacting that they pass through the ATLAS detector without leaving any traces. Similarly, if new BSM particles, such as dark matter particles, would be produced in an interaction they would also escape the detector without any tracks or energy deposits.
How can invisible particles be detected with the ATLAS detector? In contrast to the other SM particles, they can be detected indirectly, relying on the kinematics of the event.

The first time invisible particles have been identified in a collider experiment has been at the time of the W boson discovery, which led to a Nobel Prize[1]. At that time, the process that was being investigated was the production of the W boson, decaying into electron and neutrino: $p+\bar{p} \rightarrow W^{\pm}+X$; $W^{\pm} \rightarrow e^{\pm}\nu$, where X is the debris coming from the underlying event. While the detection of the electron was quite straightforward, the observation of a neutrino could not be based on detector signals: it was impossible to look for neutrinos via their secondary interactions in the detector material because they are too rare. Hence the idea to rely on kinematics to reveal their emissions indirectly.
Since in the transverse plane xy the kinematics is closed[2] and energy and momentum are conserved, the transverse momentum of the collision products should sum to zero, therefore a momentum imbalance in the transverse plane (*Missing Transverse Momentum*, $E_{\mathrm{T}}^{\mathrm{miss}}$) may point out the presence of non interacting particles, SM neutrinos and/or weakly interacting BSM particles.

In addition to $E_{\mathrm{T}}^{\mathrm{miss}}$ caused by invisible particles, a momentum imbalance can be caused by the loss of particles either escaping the detector acceptance, or which are poorly reconstructed. In this case the $E_{\mathrm{T}}^{\mathrm{miss}}$ is usually referred to as *fake* $E_{\mathrm{T}}^{\mathrm{miss}}$. $E_{\mathrm{T}}^{\mathrm{miss}}$ thus results to be an important measure to quantify the overall event reconstruction performance.

A good measurement of $E_{\mathrm{T}}^{\mathrm{miss}}$ is therefore crucial at the LHC: both search analyses and precision measurements need an accurate estimation of $E_{\mathrm{T}}^{\mathrm{miss}}$. The $E_{\mathrm{T}}^{\mathrm{miss}}$ plays an important role in all the SM processes involving neutrinos and in processes with predicted weakly interacting BSM particles.

[1] Nobel Prize in Physics in 1984, awarded jointly to Carlo Rubbia and Simon van der Meer *for their decisive contributions to the large project, which led to the discovery of the field particles W and Z, communicators of weak interaction.*

[2] Provided that the detector acceptance is large enough (close to 4π).

In this chapter, $E_{\mathrm{T}}^{\mathrm{miss}}$ definition is presented, different $E_{\mathrm{T}}^{\mathrm{miss}}$ algorithms are described and their performance is studied. Finally, the methods used to estimate the systematics are discussed. Most of the results shown in this chapter have been published [85], [86].

4.1 $E_{\mathrm{T}}^{\mathrm{miss}}$ definition

As previously mentioned, for relativistic particles and for an ideal detector response, if no invisible particle is emitted and if all the particles produced in the event are reconstructed, the sum of the transverse momenta of all the particles in an event should sum to zero. It is therefore possible to define the missing transverse momentum as follow.
The missing transverse momentum vector is defined as the negative vector sum of the momenta of all the particles detected and is denoted $\mathbf{E_T^{miss}}$ while its magnitude is denoted $E_{\mathrm{T}}^{\mathrm{miss}}$:

$$\mathbf{E_T^{miss}} = (E_x^{miss}, E_y^{miss})$$
$$E_T^{miss} = |\mathbf{E_T^{miss}}| = \sqrt{(E_x^{miss})^2 + (E_y^{miss})^2}$$

where

$$E_x^{miss}(E_y^{miss}) = -\sum E_x(E_y) \tag{4.1}$$

$\sum E_x$ and $\sum E_y$ are the sum of the $x(y)$ component of all energy deposits reconstructed in the detector.
The azimuthal coordinate Φ^{miss} is defined as:

$$\Phi^{\mathrm{miss}} = \mathrm{atan}\left(\frac{E_x^{\mathrm{miss}}}{E_y^{\mathrm{miss}}}\right) \tag{4.2}$$

4.2 $E_{\mathrm{T}}^{\mathrm{miss}}$ reconstruction

$E_{\mathrm{T}}^{\mathrm{miss}}$ is reconstructed as a vectorial sum of different terms. There are two main contributions. The first is made of fully reconstructed, calibrated hard objects selected by each analysis, the second comes from the *soft* component, made of unassociated tracks and energy deposits. The missing transverse momentum of an event is then constructed as an ordered sum of the different objects which are reconstructed in an event:

$$\begin{aligned}\mathbf{E_T}^{miss} = & \\ & -\sum \mathbf{p_T}^{e} - \sum \mathbf{p_T}^{\gamma} - \sum \mathbf{p_T}^{\tau} - \sum \mathbf{p_T}^{\mu} - \sum \mathbf{p_T}^{jet} - \sum \mathbf{p_T}^{soft} = \\ & \mathbf{E_T}^{miss,e} + \mathbf{E_T}^{miss,\gamma} + \mathbf{E_T}^{miss,\tau} + \mathbf{E_T}^{miss,\mu} + \mathbf{E_T}^{miss,jet} + \mathbf{E_T}^{miss,soft} = \\ & \mathbf{E_T}^{miss,hard} + \mathbf{E_T}^{miss,soft}\end{aligned}$$

Equivalently, the $E_{x(y)}^{miss}$ components can be written as:

$$E_{x(y)}^{miss} = E_{x(y)}^{miss,e} + E_{x(y)}^{miss,\gamma} + E_{x(y)}^{miss,\tau} + E_{x(y)}^{miss,\mu} + E_{x(y)}^{miss,jet} + E_{x(y)}^{miss,soft}. \tag{4.3}$$

Each object term is given by the negative vectorial sum of the momenta of the corresponding calibrated objects. To avoid double counting, calorimeter signals are associated with the reconstructed objects in the following priority order: electrons (e), photons (γ),

hadronically decaying $\tau-$leptons, jets and muons (μ). Each analysis uses the selected hard objects to reconstruct the $E_{\mathrm{T}}^{\mathrm{miss}}$, this means that the $E_{\mathrm{T}}^{\mathrm{miss}}$ is analysis dependent. In addition to these *hard terms*, the soft term ($E_{x(y)}^{miss,soft}$) is reconstructed from detector signals which are not associated with any objects. There are different ways to define and reconstruct the soft component:

- use ID tracks only (track-based Soft Term) associated with the hard scatter vertex (largely insensitive to pile up);
- calorimeter signals (calorimeter-based Soft Term, sensitive to pile up).

The choice of the soft term version influences the performance of the $E_{\mathrm{T}}^{\mathrm{miss}}$ reconstruction.

Another important variable, which is used to estimate the event activity, is the scalar sum of the transverse momenta of all the objects used in the $E_{\mathrm{T}}^{\mathrm{miss}}$ reconstruction:

$$\sum E_T = \sum p_T^e + \sum p_T^\gamma + \sum p_T^\tau + \sum p_T^{jets} + \sum p_T^\mu + \sum p_T^{soft}. \tag{4.4}$$

A good hermeticity of the calorimeters is mandatory to accurately measure the $E_{\mathrm{T}}^{\mathrm{miss}}$ of an event. There are several effects which can cause fake $E_{\mathrm{T}}^{\mathrm{miss}}$ and make the $E_{\mathrm{T}}^{\mathrm{miss}}$ computation challenging. Among these effects there is the presence of dead detector regions, noise, pile-up which leads to a degradation of the performance due to fluctuations in the soft term determination causing a wrong $E_{\mathrm{T}}^{\mathrm{miss}}$ measurement.

4.2.1 $E_{\mathrm{T}}^{\mathrm{miss}}$ algorithms

There are different algorithms used to reconstruct the $E_{\mathrm{T}}^{\mathrm{miss}}$, which mainly differ for the way they reconstruct the soft term. The different algorithms used for the soft term reconstruction lead to some differences in the $E_T^{miss,\mathrm{jet}}$ terms, too.

Calorimeter Soft Term (CST) The calorimeter soft term is reconstructed from the energy deposits in calorimeter cells, grouped in TopoClusters (see Sec. 3.4.1), which are not associated with reconstructed hard objects used to build the other $E_{\mathrm{T}}^{\mathrm{miss}}$ terms. $E_{\mathrm{T}}^{\mathrm{miss}}$ reconstructed with this calorimeter-based soft term is called CST $E_{\mathrm{T}}^{\mathrm{miss}}$. Since the CST soft term includes soft contributions from all interactions, it is very sensitive to the pile up contribution. All jets with p_T >20 GeV (see Sec. 4.3.1) are used to build the CST $\mathbf{E_T}^{\mathrm{miss,jet}}$ term. Also jets which would be tagged as pile up jets by the JVT algorithm are included (otherwise an imbalance is observed, see Sec. 4.5.2).
The muon transverse momentum is measured from a combination of ID and muon spectrometer measurements and needs to be corrected for any calorimeter energy loss. In fact, in case there is any substantial calorimeter deposit, it may create a cluster adding to the p_T of a jet or modifying the CST soft term. To avoid double counting of signals, the muon p_T used for the $E_{\mathrm{T}}^{\mathrm{miss}}$ reconstruction is corrected by the energy lost in the calorimeter ($\sim$3 GeV on average). Studies presented in this chapter have been performed when this correction was still being optimized, therefore all the plots shown in this chapter either do not account for any correction, or use a non optimal muon energy loss correction.

Track based Soft Term (TST) The track based soft term is built from ID tracks satisfying the selection described in Sec. 4.3.2 but not matched to any other reconstructed object. Only those tracks associated with the hard scatter vertex are included. Since the tracks can be accurately matched to the primary vertex, the TST soft term is relatively insensitive to pile up. This $E_{\mathrm{T}}^{\mathrm{miss}}$ algorithm does not include contributions from soft neutral particles and from forward regions (outside the tracker acceptance: η >2.5). $E_{\mathrm{T}}^{\mathrm{miss}}$ reconstructed with this track-based soft term is called TST $E_{\mathrm{T}}^{\mathrm{miss}}$. Since the TST soft term is almost pile up free, pile up jets need to be removed also from the TST jet term, otherwise an imbalance would be observed (see Sec. 4.5.2). For this reason, to build the TST the $\mathbf{E_T}^{miss,jet}$ term, in addition to the requirements described in 4.3.1, also the Jet Vertex Tagger requirement is applied.
This is the only difference between the CST and TST $\mathbf{E_T}^{miss,jet}$ term: for CST $E_{\mathrm{T}}^{\mathrm{miss}}$ all the jets are included, while for TST $E_{\mathrm{T}}^{\mathrm{miss}}$ jets tagged as pile up are not included.

Track $\mathbf{E}_{\mathrm{T}}^{\mathrm{miss}}$ Another track based $E_{\mathrm{T}}^{\mathrm{miss}}$ algorithm is available. In this case, ID track information are used not only for the soft term reconstruction but also for the hard terms. The excellent vertex resolution of the ATLAS detector gives a pile up independent $E_{\mathrm{T}}^{\mathrm{miss}}$ measure. On the other hand, neutral particles are neglected and the Track $E_{\mathrm{T}}^{\mathrm{miss}}$ is limited to the region $|\eta|$ <2.5 (tracker acceptance). The Track $E_{\mathrm{T}}^{\mathrm{miss}}$ is reconstructed as the negative sum of the momenta of ID tracks and satisfying the requirements in Sec. 4.3.2. For electrons transverse momenta, the calorimeter cluster measurements is used instead of the p_T of the electron track[3]. The Track $E_{\mathrm{T}}^{\mathrm{miss}}$ soft term is reconstructed from ID tracks not associated to electrons and muons.

4.3 Object selection

$E_{\mathrm{T}}^{\mathrm{miss}}$ reconstruction software for Run2 allows flexibility to use the object's selections more suited to each analysis. Only the jet selection criteria used for $E_{\mathrm{T}}^{\mathrm{miss}}$ reconstruction are fixed.
In this section the jet selection used in the $E_{\mathrm{T}}^{\mathrm{miss}}$ algorithm is described. The other object selections presented here are the ones which have been used for the $E_{\mathrm{T}}^{\mathrm{miss}}$ performance studies discussed in this chapter.

4.3.1 Jet Selection

Jets are reconstructed from topoclusters using the anti$-k_T$ algorithm with distance parameter R =0.4 (Section 3.4). The jets considered here are calibrated using the EM+JES scheme [87].
As presented in Sec 3.4.3, the Jet vertex tagger technique (JVT) provides a way to discriminate pile up jets from jets coming from the hard scatter. For TST $E_{\mathrm{T}}^{\mathrm{miss}}$ only jets satisfying the JVT requirements are used to construct the $E_T^{\mathrm{miss,\ jet}}$ term. On the contrary, for CST $E_{\mathrm{T}}^{\mathrm{miss}}$ all the jets, regardless the JVT requirement, are used. Studies to justify this latter choice are shown in Sec. 4.5.2.
Both for CST and TST $E_{\mathrm{T}}^{\mathrm{miss}}$, only jets with p_T >20 GeV are included in the corresponding jet term. Figure 4.1 (left) shows the TST $E_{\mathrm{T}}^{\mathrm{miss}}$ resolution[4] for different thresholds of the minimum p_T of the selected jets in a region enriched of $Z \rightarrow \mu\mu$ events. The

[3]The p_T measured using the calorimeter information is more precise than the one from the tracks.
[4]The resolution is defined as the root mean square (RMS) width of the $E_{x(y)}^{miss}$ components.

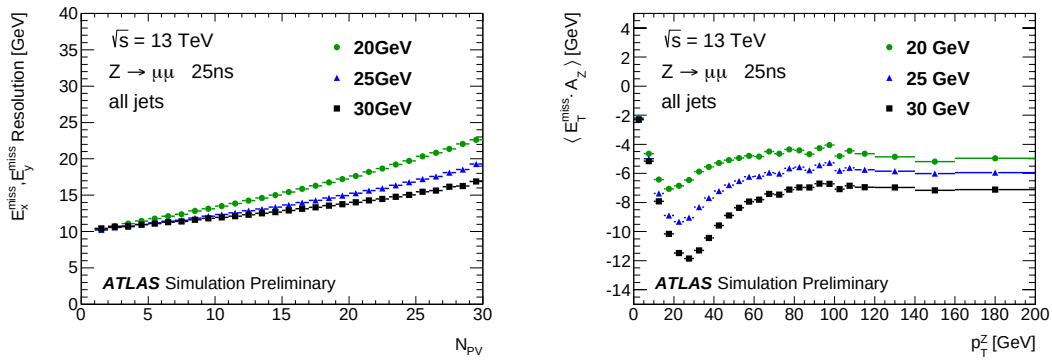

Figure 4.1: TST $E_{\mathrm{T}}^{\mathrm{miss}}$ performance for different values of the minimum jet p_T threshold in Powheg+Pythia simulated $Z \to \mu\mu$ events. Left: resolution as a function of the number of primary vertices. Right: $E_{\mathrm{T}}^{\mathrm{miss}}$ projection along the direction of the Z boson p_T.

resolution is studied as a function of the number of recontructed primary vertices, which is a measure of the in time pile up of the event. For higher jet p_T thresholds the $E_{\mathrm{T}}^{\mathrm{miss}}$ resolution is less dependent on the pile up thus improving the resolution. The drawback for the higher p_T threshold values is that a bias is introduced in the $E_{\mathrm{T}}^{\mathrm{miss}}$ direction: if the p_T threshold is raised, hard scatter jets are wrongly removed and this causes a bad balance between the $E_{\mathrm{T}}^{\mathrm{miss}}$ and the Z boson (Fig. 4.1, right). For this reason the minimum p_T threshold to select the jets is set to 20 GeV.

4.3.2 Track Selection

To ensure the quality of tracks which are used to reconstruct the $E_{\mathrm{T}}^{\mathrm{miss}}$, different criteria need to be satisfied:

- tracks must have a reconstructed transverse momentum p_T >0.5 GeV and $|\eta|$ <2.5;
- at least 7 hits in the silicon detectors and no more than two holes in the silicon layers or one hole in the pixel layers (to ensure an accurate reconstruction of the track's p_T and minimize the fake track rate).

The hard scatter of the event is the reconstructed primary vertex with largest value of $\sum_{trk} p_{T,trk}^2$.

4.3.3 Muon Selection

Muons are selected with *medium* quality criteria. The ones with $|\eta|$ <2.5 are required to be reconstructed in the MS with a matching track in the ID. In case there is a large imbalance between the momentum measured by the ID and by the MS, the muon is rejected. Muons with 2.5< $|\eta|$ <2.7 are reconstructed in the MS only, using tighter requirements on the number of MS track hits. Muons are required to have p_T >10 GeV.

4.3.4 Electron Selection

Electrons are selected requiring *medium* quality criteria (Sec. 3.1), $|\eta|$ <2.47 and p_T >10 GeV. Electrons in the so called crack region of the detector (1.37< $|\eta|$ <1.52) are not considered.

4.3.5 Photon Selection

Photons are selected requiring *tight* quality criteria (Sec. 3.1), $|\eta|$ <2.37 and p_T >25 GeV. Photons in the crack region of the detector are not considered since they are poorly measured.

4.3.6 Tau Selection

Hadronically decaying taus are selected requiring *medium* quality criteria, $|\eta|$ <2.5 and p_T >20 GeV. Taus in the crack region of the detector are not considered.

4.4 Event Selection for performance evaluation

In order to characterize the different $E_{\mathrm{T}}^{\mathrm{miss}}$ algorithms, to study their performance and to estimate the systematics, different event topologies have been considered. $Z \to ll$, $W \to l\nu$ and $t\bar{t}$ selections are used to cover different final states and to study the $E_{\mathrm{T}}^{\mathrm{miss}}$ in different conditions:

- $Z \to ll$ events: the genuine $E_{\mathrm{T}}^{\mathrm{miss}}$ (i.e. the one caused by invisible particles) is expected to be very small since no invisible particle is expected in this final state[5]. The measure of the reconstructed $E_{\mathrm{T}}^{\mathrm{miss}}$ depends on the intrinsic detector resolution, of the algorithms used and of the object reconstruction efficiencies;
- $W \to l\nu$ events: these events, where a neutrino is expected in the final state, have expected genuine $E_{\mathrm{T}}^{\mathrm{miss}}$ in the final state. They provide a useful case to test the $E_{\mathrm{T}}^{\mathrm{miss}}$ scale;
- $t\bar{t}$ events: final states from $t\bar{t}$ processes have a large jet multiplicity thus allowing to test the $E_{\mathrm{T}}^{\mathrm{miss}}$ performance in such environment.

4.4.1 $Z \to ll$ Event Selection

A region enriched in either $Z \to ee$ or $Z \to \mu\mu$ events is defined as follow. Events are selected with single lepton triggers. They are required to have exactly two leptons satisfying the criteria presented in Sec 4.3.3 and 4.3.4 with p_T >25 GeV. The two leptons must have the same flavor (muon or electron) and must have opposite charge. The reconstructed invariant mass of the two leptons must be consistent with the Z boson mass within 25 GeV.

4.4.2 $W \to l\nu$ Event Selection

$W \to e\nu$ and $W \to \mu\nu$ events are selected as follows. Events are selected with single lepton triggers. They are required to have exactly one lepton with the criteria outlined in Sec 4.3.3 and 4.3.4. In order to enrich the selection of W events and to reduce the multijet events, requirements on $E_{\mathrm{T}}^{\mathrm{miss}}$ and on the W transverse mass are set.
Events are required to have $E_{\mathrm{T}}^{\mathrm{miss}}$ >25 GeV. The transverse mass is defined as:

$$m_T = \sqrt{2p_T^{\ell} E_{\mathrm{T}}^{\mathrm{miss}} (1 - \cos\Delta\Phi)} \tag{4.5}$$

[5] Neutrinos are produced only through very rare heavy-flavour meson decays in the hadronic recoil.

where p_T^{ℓ} is the transverse momentum of the lepton while $\Delta\Phi$ is the azimuthal angle between the lepton p_T and the $E_{\mathrm{T}}^{\mathrm{miss}}$. In order to compare the same set of events, the TST $E_{\mathrm{T}}^{\mathrm{miss}}$ is always used for this definition. m_T is required to be greater than 40 GeV.

4.4.3 Top anti-top Event Selection

Only $t\bar{t}$ events with semileptonic decays are considered, the final state is then characterized by the presence of one lepton and jets.
Events are then required to contain exactly one lepton (electron or muon) and at least four jets. All jets are required to be at an angular distance of ΔR >0.4 from the lepton. This is a preliminary $t\bar{t}$ selection which has been further optmized for later studies.

4.5 $E_{\mathrm{T}}^{\mathrm{miss}}$ performance in simulated events

In early 2015, before Run2 data has been collected, the $E_{\mathrm{T}}^{\mathrm{miss}}$ performance has been studied for the different $E_{\mathrm{T}}^{\mathrm{miss}}$ algorithms with simulated events.
$Z \to \ell\ell$ events have been generated by Powheg [89] interfaced to Pythia8 [90]. The $t\bar{t}$ sample used Powheg interfaced to Pythia [125] and the PERUGIA2012 [91] tune. The Sherpa [117] and Herwig++ [92] generators are considered as alternatives and are used for the systematics estimation.
The samples assume a 25 ns bunch spacing. As the first period of Run2 data-taking the bunch spacing was 50 ns, some dedicated samples with 50 ns bunch spacing have been used in order to investigate the effect of this variation.

4.5.1 $E_{\mathrm{T}}^{\mathrm{miss}}$ distributions

In this section the three $E_{\mathrm{T}}^{\mathrm{miss}}$ algorithms presented in Sec. 4.2.1 are compared and their differences are outlined.
The total missing transverse momentum magnitude for $Z \to \mu\mu$ events is shown in Fig. 4.2 for TST $E_{\mathrm{T}}^{\mathrm{miss}}$, CST $E_{\mathrm{T}}^{\mathrm{miss}}$ and Track $E_{\mathrm{T}}^{\mathrm{miss}}$. The distributions are shown separately for different jet multiplicities (0, 1 and 2 jets) and for the inclusive case (no requirement on the number of jets)[6].
For events with 0 jets, the TST and Track $E_{\mathrm{T}}^{\mathrm{miss}}$ are expected to be very close since the soft term is reconstructed in the same way. Figure 4.2 shows tiny differences between the two for values of $E_{\mathrm{T}}^{\mathrm{miss}}$ >50 GeV. These differences come from jets which are wrongly reconstructed as photons and hadronically decaying taus which are included in the TST $E_{\mathrm{T}}^{\mathrm{miss}}$ while they are not in Track $E_{\mathrm{T}}^{\mathrm{miss}}$.
For events with a small number of jets in the final state, the TST $E_{\mathrm{T}}^{\mathrm{miss}}$ and the CST $E_{\mathrm{T}}^{\mathrm{miss}}$ look very different. The CST $E_{\mathrm{T}}^{\mathrm{miss}}$ spectrum is harder due to the fact that the CST $E_{\mathrm{T}}^{\mathrm{miss}}$ is very sensitive to pile up.
The soft term component is shown in figure 4.3. The CST soft term largely differs from the track and TST soft term, it is harder because of the pile up contribution.
The TST and track soft term only show minor differences. The TST and Track $E_{\mathrm{T}}^{\mathrm{miss}}$ soft term, in case no jets with p_T >20 GeV are selected in the final state, differ only for the contribution of hadronically decaying taus. In case of TST $E_{\mathrm{T}}^{\mathrm{miss}}$ the tracks associated to these reconstructed taus are matched to the calorimeter cluster and are included into the tau term ($E_T^{\mathrm{miss},\tau}$). In case of Track $E_{\mathrm{T}}^{\mathrm{miss}}$, the tracks are included into the soft term.

[6] The jet multiplicity condition is defined on jets without the JVT requirement, in order to allow comparisons between the different $E_{\mathrm{T}}^{\mathrm{miss}}$ versions.

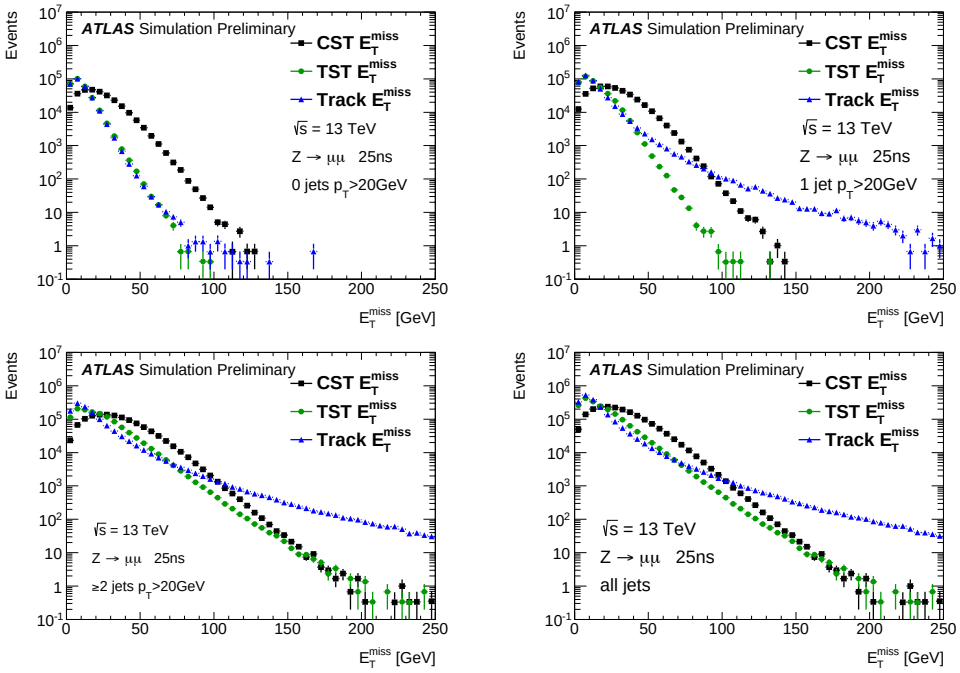

Figure 4.2: Distributions for the total TST, CST and Track $E_{\mathrm{T}}^{\mathrm{miss}}$ for simulated $Z \to \mu\mu$ events for events with different jet multiplicities. From the upper left: events with 0, 1, $\geq$2, inclusive are selected.

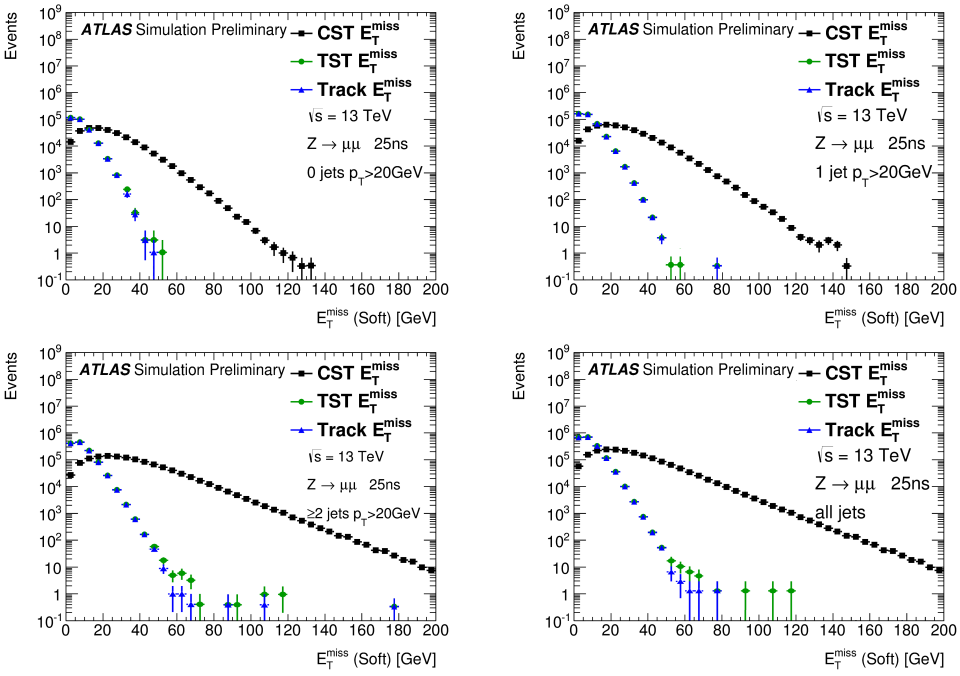

Figure 4.3: Distributions for the soft term component of TST, CST and Track $E_{\mathrm{T}}^{\mathrm{miss}}$ for simulated $Z \to \mu\mu$ events for events with different jet multiplicities. From the upper left: events with 0, 1, $\geq$2, inclusive are selected.

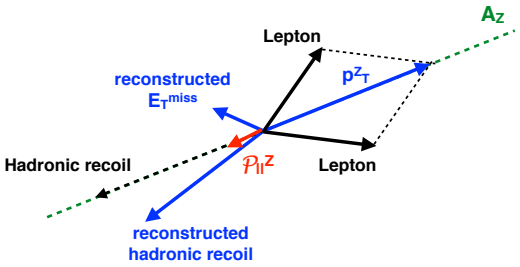

Figure 4.4: A schematic illustration of $\mathbf{A_Z}$ and $\mathcal{P}_{||}^{Z}$ described in Sec. 4.5.2. These quantities are used to study the $E_{\mathrm{T}}^{\mathrm{miss}}$ response in $Z \to \ell\ell$ events.

4.5.2 $E_{\mathrm{T}}^{\mathrm{miss}}$ response

In events where the genuine $E_{\mathrm{T}}^{\mathrm{miss}}$ can be considered null, such as $Z \to ll$ events, a measured non zero average $E_{\mathrm{T}}^{\mathrm{miss}}$ points to a bias in $E_{\mathrm{T}}^{\mathrm{miss}}$ while the spread over the mean is a measure of the $E_{\mathrm{T}}^{\mathrm{miss}}$ resolution.

Useful quantities can be defined for these studies. The axis defined by the Z boson p_T ($\mathbf{A_Z}$) is an usual metric to study the $E_{\mathrm{T}}^{\mathrm{miss}}$ scale and response. It is defined from the p_T of the Z boson decay products as:

$$\mathbf{A_Z} = \frac{\mathbf{p_T^{\ell^+}} + \mathbf{p_T^{\ell^-}}}{|\mathbf{p_T^{\ell^+}} + \mathbf{p_T^{\ell^-}}|} = \frac{\mathbf{p_T^Z}}{|p_T^Z|} \tag{4.6}$$

The $E_{\mathrm{T}}^{\mathrm{miss}}$ magnitude parallel to $\mathbf{A_Z}$ is defined as:

$$\mathcal{P}_{||}^{Z} = \mathbf{E_T^{miss}} \cdot \mathbf{A_Z} \tag{4.7}$$

An illustration is given in Fig. 4.4.
This projection is sensitive to the balance between the leptons and the hadronic recoil. In case of a perfect balance of the leptons and the soft term, $\mathcal{P}_{||}^{Z}$ would be zero. If deviations are observed, these can be the sign of a bias in the $E_{\mathrm{T}}^{\mathrm{miss}}$ reconstruction. Negative values of $\mathcal{P}_{||}^{Z}$ indicate that the reconstructed hadronic activity is too small to balance the Z boson, while positive values indicate an over estimation of the reconstructed hadronic activity.
The mean of $\mathcal{P}_{||}^{Z}$ is studied as a function of p_T^Z in Fig. 4.5 in case of zero and inclusive jets in the final state. The projection is always negative for all the $E_{\mathrm{T}}^{\mathrm{miss}}$ versions. In case events with any jet multiplicity are selected, Track $E_{\mathrm{T}}^{\mathrm{miss}}$ largely differs from TST and CST $E_{\mathrm{T}}^{\mathrm{miss}}$ and $\mathcal{P}_{||}^{Z}$ increases in absolute value as a function of p_T^Z. This is due to the loss of the neutral particles from the hadronic recoil. CST is more unbalanced than TST $E_{\mathrm{T}}^{\mathrm{miss}}$. This is probably due to the fact that the muon energy loss in the calorimeter was not corrected for in this CST version.

Dependence on pile up

As mentioned in Sec.4.2.1, CST $E_{\mathrm{T}}^{\mathrm{miss}}$ is particularly sensitive to pile up. Fig. 4.6 shows the average projection of $E_{\mathrm{T}}^{\mathrm{miss}}$ onto the Z boson transverse momentum direction for different ranges of $< \mu >$ and for inclusive $< \mu >$ values. The curves show a clear

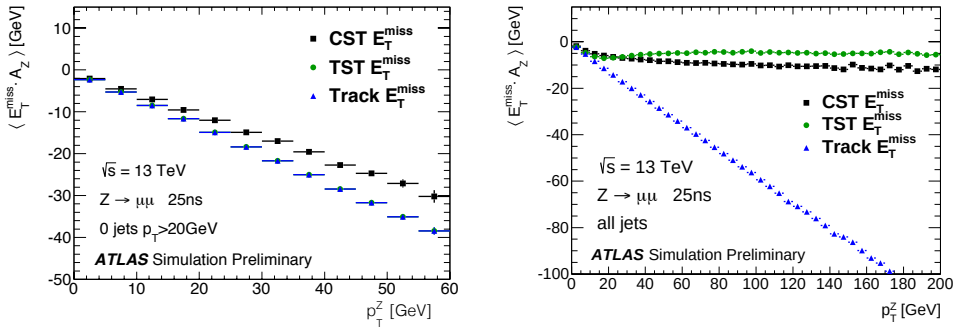

Figure 4.5: Average projection of $E_{\mathrm{T}}^{\mathrm{miss}}$ onto the Z boson transverse momentum direction ($\mathbf{A_Z}$) in simulated $Z \rightarrow \mu\mu$ events for the different $E_{\mathrm{T}}^{\mathrm{miss}}$ versions as a function of $|\mathbf{p_T^Z}|$. The cases where 0 jets and inclusive jets with p_T >20 GeV are reconstructed in the final state are shown.

dependence on $< \mu >$ which serves as pile up parametrization: for increasing $< \mu >$ the projection increase in absolute value, pointing to a higher imbalance. Figure 4.7 shows the corresponding curves for the TST $E_{\mathrm{T}}^{\mathrm{miss}}$, where the projection is more stable for the different $< \mu >$ values, indicating that the TST $E_{\mathrm{T}}^{\mathrm{miss}}$ scale is less affected by pile up.

Studies have been performed to investigate whether the CST pile up dependence could be mitigated by using JVT requirements on jets used to reconstruct the $E_{\mathrm{T}}^{\mathrm{miss}}$, in a similar way as it is done for TST $E_{\mathrm{T}}^{\mathrm{miss}}$. In particular, in order to study the impact on the $E_{\mathrm{T}}^{\mathrm{miss}}$ scale of the use of the pile up jets to reconstruct CST $E_{\mathrm{T}}^{\mathrm{miss}}$ and to check if the rejection of pile up jets could mitigate the CST pile up dependence, CST $E_{\mathrm{T}}^{\mathrm{miss}}$ has been reconstructed in two different ways:

- in the standard way as described in Sec. 4.2.1;
- in a modified way, using only jets with p_T >20 GeV and satisfying the JVT requirement. This additional requirement makes the CST jet term the same as the TST jet term.

The performance of these two $E_{\mathrm{T}}^{\mathrm{miss}}$ versions is then compared.
Fig. 4.8 shows the total $E_{\mathrm{T}}^{\mathrm{miss}}$ distributions and the jet term for these two cases of CST $E_{\mathrm{T}}^{\mathrm{miss}}$. In case the JVT requirement is used, the total $E_{\mathrm{T}}^{\mathrm{miss}}$ has a harder spectrum. This is due to the fact that the corresponding jet term is reduced, since the pile up contribution is not included, thus causing an unbalance between the jet and the soft term which is still affected by the pile up.
Fig. 4.9 shows the effect of the use of JVT on the jets used for CST $E_{\mathrm{T}}^{\mathrm{miss}}$ reconstruction on $\mathcal{P}_{||}^{Z}$. The additional JVT criteria creates an imbalance in the event which appears as an increased negative $\mathcal{P}_{||}^{Z}$. The use of only jets fulfilling the JVT criteria, instead of the use of all the jets, creates an imbalance: as the CST soft term is affected by pile up, if pile up jets are removed from the $E_{\mathrm{T}}^{\mathrm{miss}}$ jet term an imbalance is created in the $E_{\mathrm{T}}^{\mathrm{miss}}$. As expected, Fig. 4.10 shows that the impact of the use of JVT[7] requirement on jets used to reconstruct the $E_{\mathrm{T}}^{\mathrm{miss}}$ is not high for events with low $< \mu >$, it also shows that the use of JVF cut does not help to reduce pile up dependence.

[7]These studies have been performed during 2015, before the data taking, when the $E_{\mathrm{T}}^{\mathrm{miss}}$ reconstruction was still being finalized. For this reason in this particular plot Jet vertex fraction (JVF) criteria have been used instead of JVT (see Sec. 3.4.3). The conclusion is the same when using JVT.

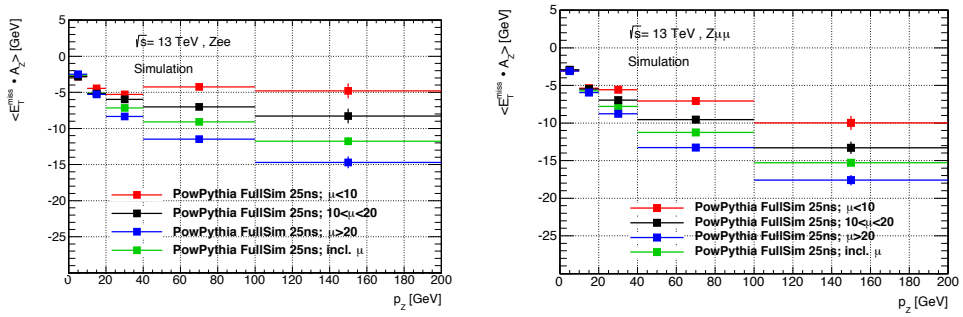

Figure 4.6: Average projection of $E_{\mathrm{T}}^{\mathrm{miss}}$ onto the Z boson transverse momentum direction ($\mathbf{A_Z}$) in simulated $Z \to ee$ (left) and $Z \to \mu\mu$ (right) events for CST $E_{\mathrm{T}}^{\mathrm{miss}}$ for different $< \mu >$ ranges (in red, black, blue) and for the inclusive $< \mu >$ case (green).

Also the CST $E_{\mathrm{T}}^{\mathrm{miss}}$ resolution (Fig. 4.9, right) is affected by the use of JVT requirements on jets: for an increasing number of pile up interactions the resolution is largely deteriorated.

4.5.3 $E_{\mathrm{T}}^{\mathrm{miss}}$ linearity

Events with genuine $E_{\mathrm{T}}^{\mathrm{miss}}$ generated by final state neutrinos such as $W \to \ell\nu$ events, are selected to study the $E_{\mathrm{T}}^{\mathrm{miss}}$ linearity. Linearity is defined as follows:

$$\text{linearity} = \left\langle \frac{E_{\mathrm{T}}^{\mathrm{miss}} - E_{\mathrm{T}}^{\mathrm{miss,true}}}{E_{\mathrm{T}}^{\mathrm{miss,true}}} \right\rangle \tag{4.8}$$

and measures the deviation of the reconstructed $E_{\mathrm{T}}^{\mathrm{miss}}$ from its truth value, which corresponds to the transverse momentum of the neutrinos. This quantity can only be calculated in simulations where the *truth* information about the generated particles is stored.
The linearity for $W \to \mu\nu$ and $t\bar{t}$ events is shown in Fig. 4.11 and 4.12 as a function of the true $E_{\mathrm{T}}^{\mathrm{miss}}$. In both figures, the linearity is positive for low values of $E_T^{miss,true}$ and negative for high values. This trend is expected: $E_{\mathrm{T}}^{\mathrm{miss}}$ is defined as being a positive quantity and has a finite resolution, thus leading to a positive linearity for small $E_T^{miss,true}$ values. For higher $E_T^{miss,true}$ values, the $E_{\mathrm{T}}^{\mathrm{miss}}$ scale is reconstructed with a 5% accuracy for CST and TST $E_{\mathrm{T}}^{\mathrm{miss}}$. In case of Track $E_{\mathrm{T}}^{\mathrm{miss}}$ it is underestimated as the neutral particles are not included.

4.5.4 $E_{\mathrm{T}}^{\mathrm{miss}}$ resolution

The $E_{\mathrm{T}}^{\mathrm{miss}}$ resolution is measured from the width of the $E_{x,y}^{miss}$ distributions for W/Z events. It is defined as the root mean square (RMS) width of the distributions. In Fig. 4.13 the resolution is studied as a function of the scalar sum of the transverse energy of the event for $Z \to \mu\mu$ and $W \to \mu\nu$ events.
Compared to TST and Track $E_{\mathrm{T}}^{\mathrm{miss}}$, CST $E_{\mathrm{T}}^{\mathrm{miss}}$ resolution is largely worse. It increases significantly with $\sum E_T$. Figure 4.14 shows the CST $E_{\mathrm{T}}^{\mathrm{miss}}$ resolution as a function of $\sum E_T$ for different ranges of $< \mu >$. It shows that different $< \mu >$ regions cover different regions of $\sum E_T$, which means that high $\sum E_T$ also corresponds to higher pile up activity, where the CST $E_{\mathrm{T}}^{\mathrm{miss}}$ resolution is worse.

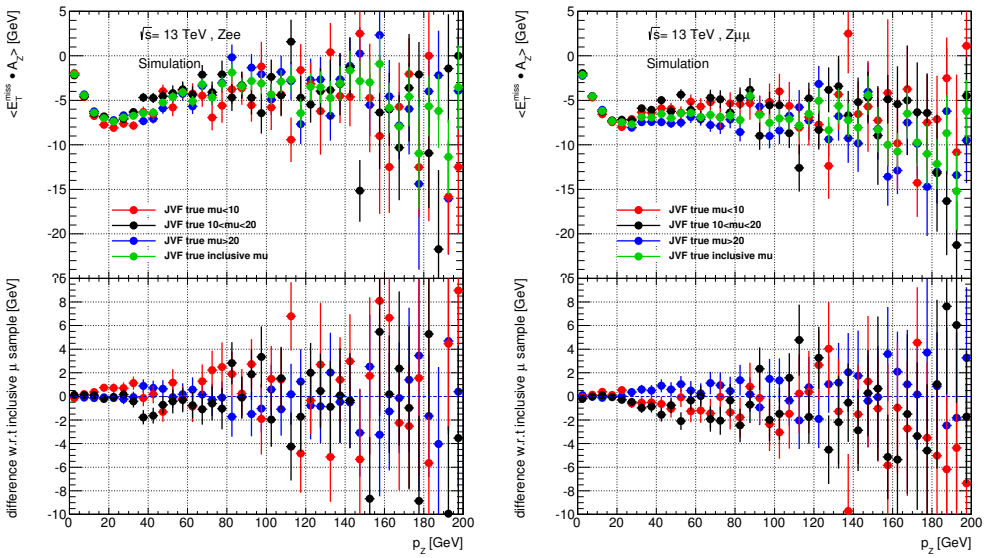

Figure 4.7: Average projection of $E_{\mathrm{T}}^{\mathrm{miss}}$ onto the Z boson transverse momentum direction ($\mathbf{A_Z}$) in simulated $Z \to ee$ (left) and $Z \to \mu\mu$ (right) events for TST $E_{\mathrm{T}}^{\mathrm{miss}}$ for different $< \mu >$ ranges (in red, black, blue) and for the inclusive $< \mu >$ case (green).

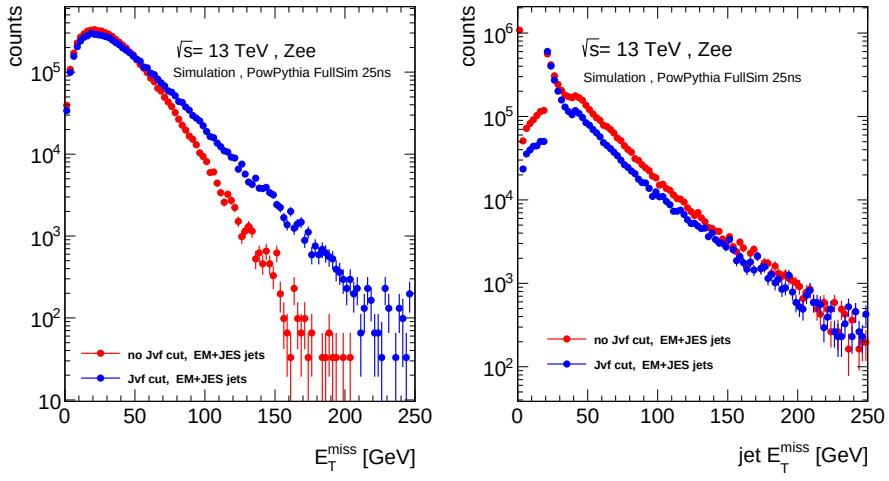

Figure 4.8: Comparison of CST $E_{\mathrm{T}}^{\mathrm{miss}}$ (left) and CST $E_T^{jet,miss}$ distributions in simulated $Z \to ee$ in case the JVT requirement is (blue) or is not (red) applied to jets.

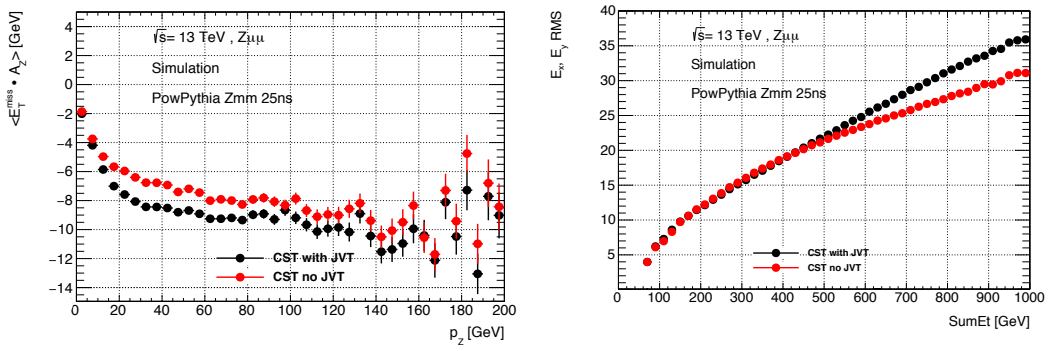

Figure 4.9: Left: average projection of $E_{\mathrm{T}}^{\mathrm{miss}}$ onto the Z boson transverse momentum direction ($\mathbf{A_Z}$). Right: $E_{\mathrm{T}}^{\mathrm{miss}}$ resolution measured as root mean square (RMS) width of $E_{x(y)^{miss}}$. In simulated $Z \rightarrow ee$ events for CST $E_{\mathrm{T}}^{\mathrm{miss}}$ in case all jets (with p_T >20 GeV) have been used to construct the $E_{\mathrm{T}}^{\mathrm{miss}}$ (black) and in case only jets passing the JVF criteria are used.

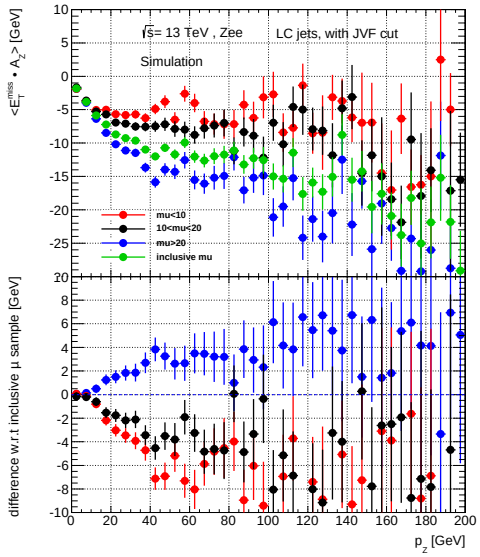

Figure 4.10: Average projection of $E_{\mathrm{T}}^{\mathrm{miss}}$ onto the Z boson transverse momentum direction ($\mathbf{A_Z}$) in simulated $Z \rightarrow ee$ events for CST $E_{\mathrm{T}}^{\mathrm{miss}}$ in case only jets (with p_T >20 GeV) satifying the JVF requirement have been used to construct the $E_{\mathrm{T}}^{\mathrm{miss}}$. Different curves correspond to different $< \mu >$ ranges: events corresponding to low, medium, high $< \mu >$ conditions, and inclusive $< \mu >$ values are represented in red, black, blue and gree respectively.

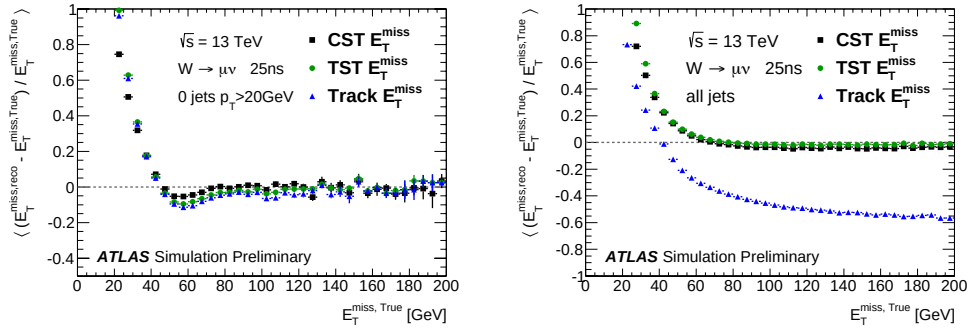

Figure 4.11: $E_{\mathrm{T}}^{\mathrm{miss}}$ linearity as a function of $E_T^{miss,true}$ for Powheg+Pythia $W \to \mu\nu$ events.

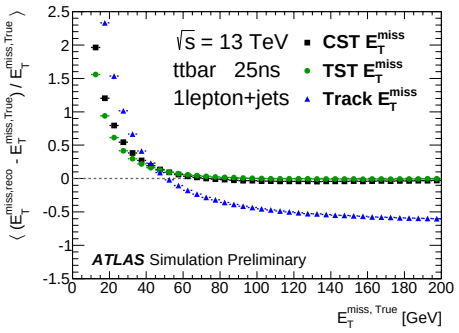

Figure 4.12: $E_{\mathrm{T}}^{\mathrm{miss}}$ linearity as a function of $E_T^{miss,true}$ for $t\bar{t}$ events.

For the other two $E_{\mathrm{T}}^{\mathrm{miss}}$ versions, the resolution is less sensitive to the event activity. The differences between the TST and Track $E_{\mathrm{T}}^{\mathrm{miss}}$ resolution are due to jet resolution. For small values of $\sum E_T$ in case of zero final state hard jets, TST $E_{\mathrm{T}}^{\mathrm{miss}}$ is closer to Track $E_{\mathrm{T}}^{\mathrm{miss}}$, since the soft term is the dominant component. For higher $\sum E_T$ values, in event with high jet activity, the jet term dominates and the TST $E_{\mathrm{T}}^{\mathrm{miss}}$ approaches the CST one.

The situation is different in $t\bar{t}$ events (Fig. 4.15) where the jet activity is higher compared to $W \to \ell\nu$ and $Z \to \ell\ell$ events. In these events the CST and TST resolutions are more similar, as the jet term dominates. Track $E_{\mathrm{T}}^{\mathrm{miss}}$ has a worse resolution since the contribution of neutrals is not included in the hadronic term.

Figure 4.16 shows the $E_{\mathrm{T}}^{\mathrm{miss}}$ resolution as a function of the number of reconstructed primary vertices (N_{PV}), which depends on the *in-time* pile up interactions. The CST $E_{\mathrm{T}}^{\mathrm{miss}}$ resolution worsen with increased N_{PV}, while the Track $E_{\mathrm{T}}^{\mathrm{miss}}$ is more stable since tracks can be efficiently associated the hard scatter vertex. In case of events with small N_{PV} but with hard jets in the final state, the CST $E_{\mathrm{T}}^{\mathrm{miss}}$ resolution is better than the Track $E_{\mathrm{T}}^{\mathrm{miss}}$ one, as the contribution from neutral particles is omitted. TST $E_{\mathrm{T}}^{\mathrm{miss}}$ resolution is the same as Track $E_{\mathrm{T}}^{\mathrm{miss}}$ for events with no hard jet in the final state and is somewhere between the two in case there are final state hard jets: it has better resolution than Track $E_{\mathrm{T}}^{\mathrm{miss}}$ for small N_{PV} and it has worse resolution for high N_{PV} values.

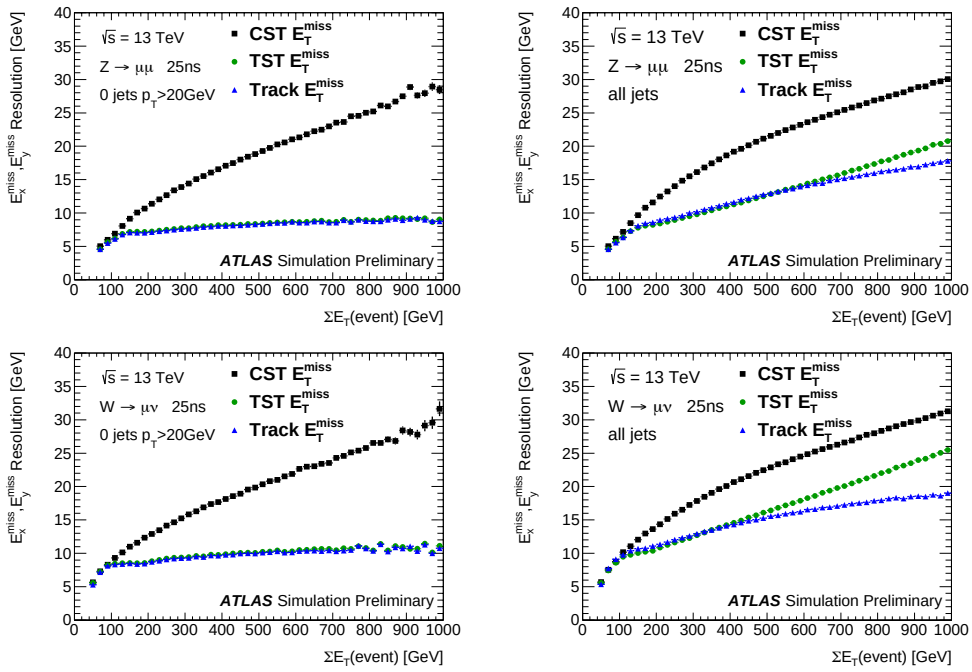

Figure 4.13: $E_{\mathrm{T}}^{\mathrm{miss}}$ resolution as a function of $\sum E_T$ for Powheg+Pythia $Z \to \mu\mu$ and $W \to \mu\nu$ events.

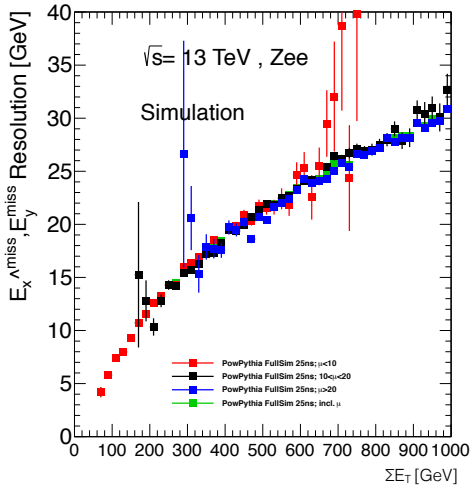

Figure 4.14: CST $E_{\mathrm{T}}^{\mathrm{miss}}$ resolution as a function of $\sum E_T$ for simulated $Z \to ee$ events. Different curves correspond to different $< \mu >$ ranges.

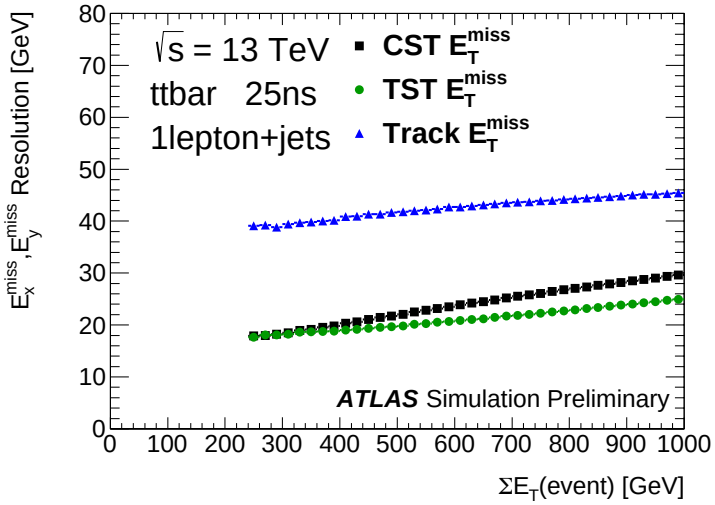

Figure 4.15: $E_{\mathrm{T}}^{\mathrm{miss}}$ resolution as a function of $\sum E_T$ for $t\bar{t}$ events.

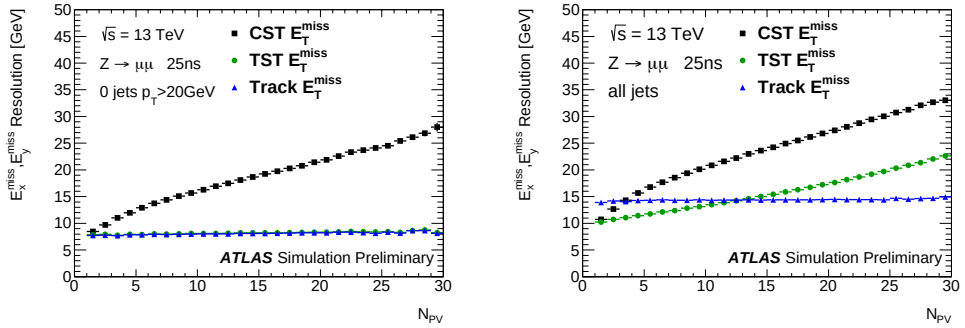

Figure 4.16: $E_{\mathrm{T}}^{\mathrm{miss}}$ resolution as a function of the number of reconstructed primary vertices (N_{PV}) for Powheg+Pythia $Z \rightarrow \mu\mu$ events. Left: Events with 0 jets with p_T >20 GeV are selected. Right: no requirement on the number of the final state jets.

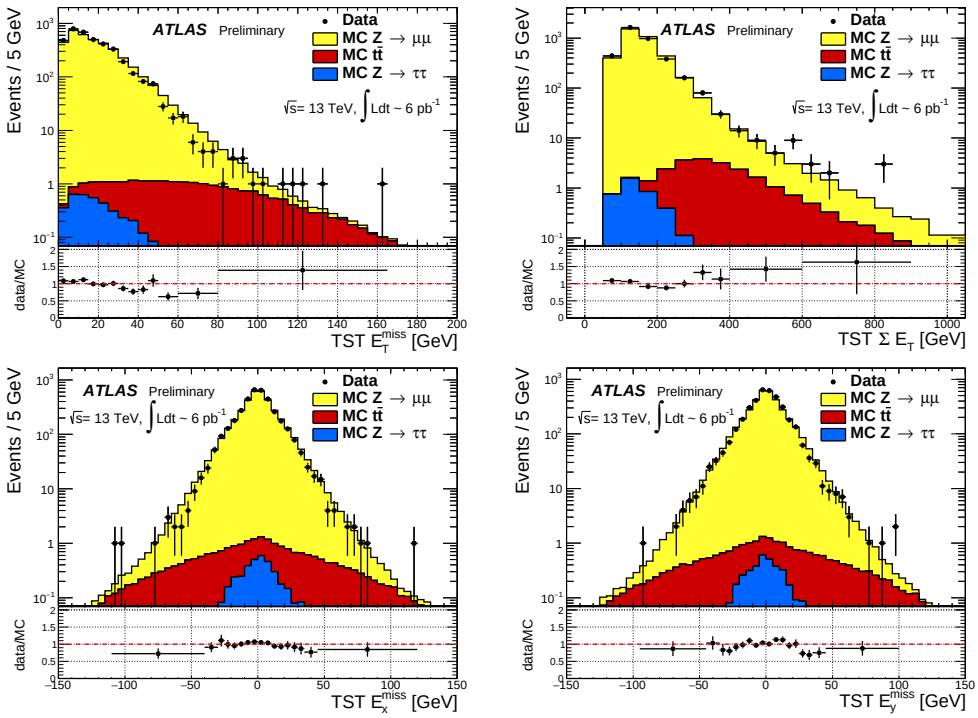

Figure 4.17: Data to MC comparisons in $Z \to \mu\mu$ events for TST $E_{\mathrm{T}}^{\mathrm{miss}}$, $\sum E_T$, E_x^{miss}, E_y^{miss}.

4.6 TST $E_{\mathrm{T}}^{\mathrm{miss}}$ performance in first 2015 data

In the following section, the TST $E_{\mathrm{T}}^{\mathrm{miss}}$ performance is studied in the first Run2 data. Data shown here have been collected in June 2015 and correspond to 6 pb^{-1}. The bunch spacing was 50 ns while it is set to 25 ns for all the rest of Run2 data taking . TST $E_{\mathrm{T}}^{\mathrm{miss}}$ is studied in data and in MC simulations[8] for $Z \to \mu\mu$ and $W \to e\nu$ events.

4.6.1 Data to MC comparisons in $Z \to \mu\mu$ events

Applying a $Z \to \mu\mu$ selection, about 4000 data events are selected. The data to MC comparisons for $E_{\mathrm{T}}^{\mathrm{miss}}$, $\sum E_T$, E_x^{miss}, E_y^{miss} are shown in Fig. 4.17. The separate terms ($E_T^{miss,jet}$, $E_T^{miss,\mu}$, $E_T^{miss,soft}$) are shown in Fig. 4.18. The first bin in the $E_T^{miss,jet}$ distribution is populated by events with zero jets (with p_t >20 GeV). The data and MC agree within 20%. For high $E_{\mathrm{T}}^{\mathrm{miss}}$ and $\sum E_T$ the data statistics is limited.

4.6.2 Data to MC comparisons in $W \to e\nu$ events

Similarly, data to MC comparisons are performed in $W \to e\nu$ events. About 40000 events are selected in data and are compared to the expected background MC. Fig. 4.19 shows the TST $E_{\mathrm{T}}^{\mathrm{miss}}$ and $E_T^{miss,soft}$.
In this case, the data to MC agreement for low $E_{\mathrm{T}}^{\mathrm{miss}}$ values is worse than for $Z \to \mu\mu$ events. This is due to multijet events, where one jet is reconstructed as an electron,

[8] Simulated samples used for these studies assume 50ns bunch spacing.

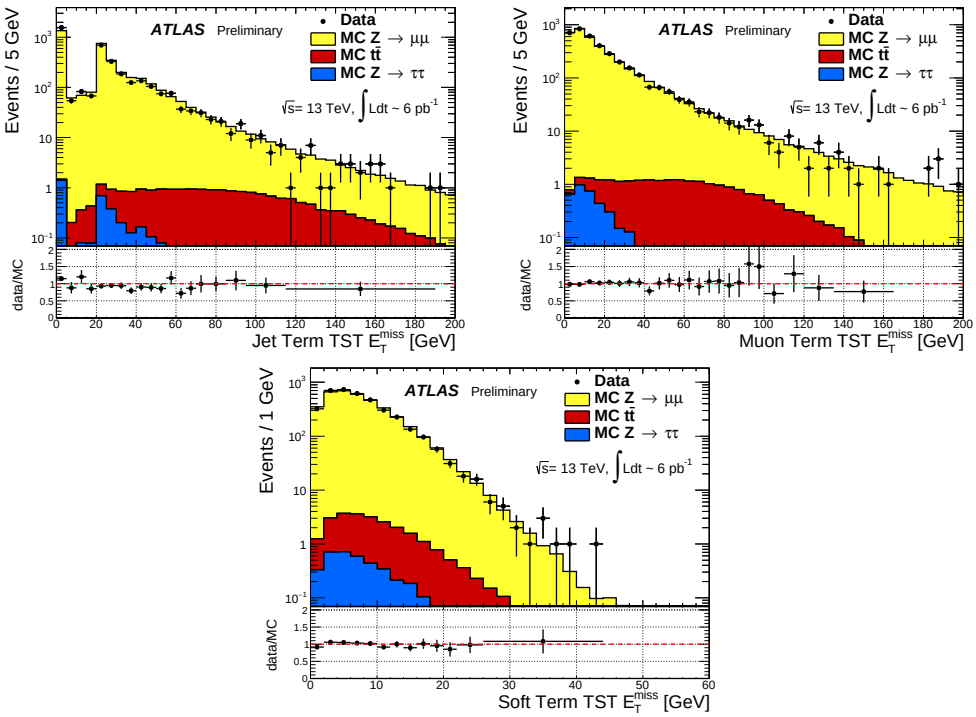

Figure 4.18: Data to MC comparisons in $Z \to \mu\mu$ events for TST $E_{\mathrm{T}}^{\mathrm{miss}}$ terms: $E_{T)}^{miss,jet}$, $E_T^{miss,\mu}$, $E_T^{miss,soft}$.

which are neither included in the simulated backgrounds nor estimated in this region[9].

4.6.3 TST $E_{\mathrm{T}}^{\mathrm{miss}}$ scale in data

As presented in Sec. 4.5.2 for simulated events, the TST $E_{\mathrm{T}}^{\mathrm{miss}}$ scale has been studied in data and compared to MC simulated events, in $Z \to \mu\mu$ events.
The mean value of the projection of $E_{\mathrm{T}}^{\mathrm{miss}}$ onto $\mathbf{A_Z}$ is shown in Fig. 4.20. The agreement between data and MC is good apart from fluctuations in data for high p_T^Z values. The negative bias of $\mathcal{P}_{||}^Z$ is due to an underestimate of the two contributions: the soft neutral particles are not included in the TST $E_{\mathrm{T}}^{\mathrm{miss}}$ soft term and the ID has a limited acceptance.

4.6.4 TST $E_{\mathrm{T}}^{\mathrm{miss}}$ resolution in data

Similarly to what has been presented in Sec. 4.5.4, the TST $E_{\mathrm{T}}^{\mathrm{miss}}$ resolution has been measured in data and compared to MC simulated events, in $Z \to \mu\mu$ events. The resolution is studied as a function of $\sum E_T$[10] and N_{PV}. The distributions are shown in Fig. 4.21 and a reasonable agreement between data and MC is found.

[9] Multijet backgrounds in $W \to e\nu$ regions will be discussed in detail in the context of the VBF $H \to inv$ analysis in Chapter 5, in Sec. 5.16 and 5.18.
[10] The CST $\sum E_T$ has been considered, in order to allow for comparison with previous studies.

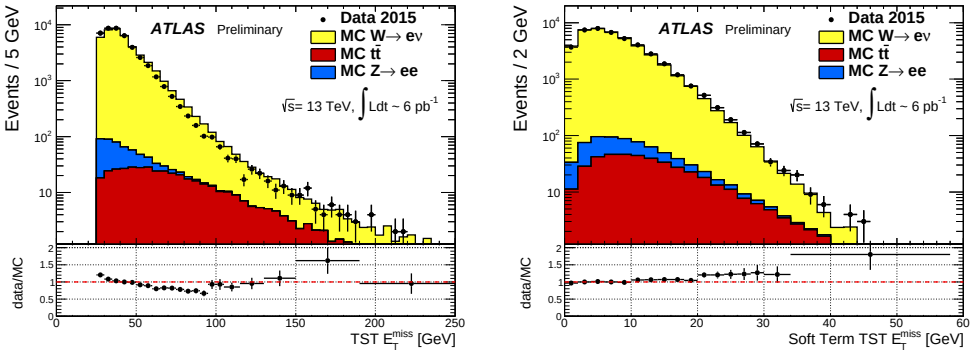

Figure 4.19: Data to MC comparisons in $W \to e\nu$ events for TST $E_{\mathrm{T}}^{\mathrm{miss}}$, $E_T^{miss,soft}$. TMultijet background is not included in MC (the lack of a multijet estimation explains why there are more data than simulated events at low $E_{\mathrm{T}}^{\mathrm{miss}}$).

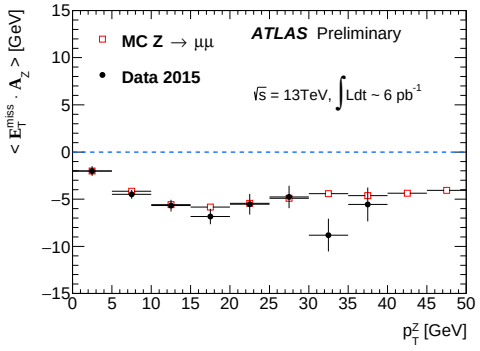

Figure 4.20: Data to MC comparisons in $Z \to \mu\mu$ events for the mean value of the projection of $E_{\mathrm{T}}^{\mathrm{miss}}$ onto $\mathbf{A_Z}$ as a function of p_T^Z.

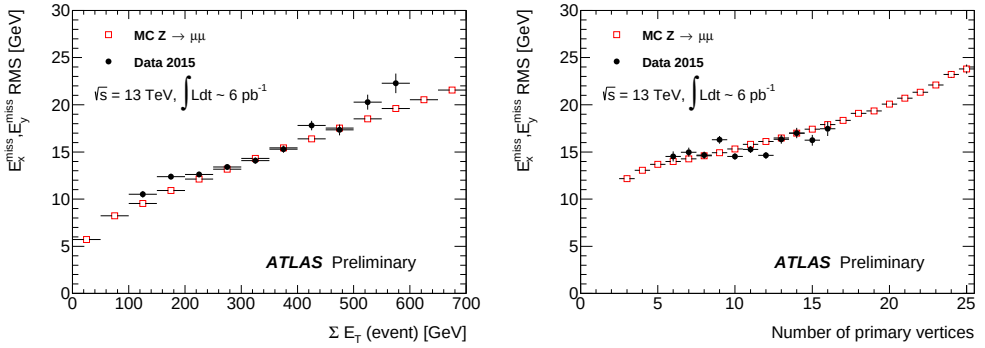

Figure 4.21: Data to MC comparisons in $Z \to \mu\mu$ events for TST $E_{\mathrm{T}}^{\mathrm{miss}}$ resolution as a function of $\sum E_T$ (left) and N_{PV} (right).

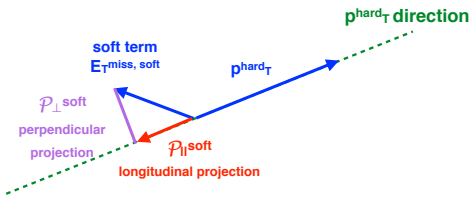

Figure 4.22: An illustration of the soft term metrics used to estimate the soft term systematics.

4.7 $E_{\mathrm{T}}^{\mathrm{miss}}$ systematics

As $E_{\mathrm{T}}^{\mathrm{miss}}$ is built as a sum of terms including all the different reconstructed objects (eq. 4.3), systematic uncertainties associated to each object need to be taken into account and are propagated to the corresponding $E_{\mathrm{T}}^{\mathrm{miss}}$ terms. Systematics for jets, electrons, photons, muons and taus are provided by the corresponding *combined and performance* ATLAS working groups, which consist of teams of people working on specific object reconstruction, performance and systematic estimation. The $E_{\mathrm{T}}^{\mathrm{miss}}$ soft term requires dedicated systematics and these are estimated separately within the ATLAS $E_{\mathrm{T}}^{\mathrm{miss}}$ working group. The overall systematic uncertainty on $E_{\mathrm{T}}^{\mathrm{miss}}$ is evaluated by combining the uncertainties on each term.
In this section the general methodology used to estimate the systematics related to the $E_{\mathrm{T}}^{\mathrm{miss}}$ soft term is presented. The systematics uncertainty estimation for TST $E_{\mathrm{T}}^{\mathrm{miss}}$ soft term is then shown. Ideas for estimating the systematic uncertainties for the CST soft term are also discussed.

4.7.1 The technique

Different sources of systematic uncertainties are taken into account for the $E_{\mathrm{T}}^{\mathrm{miss}}$ soft term which have an impact on the scale and the resolution.
In order to quantify these uncertainties an useful metric involving the soft term is defined. The soft term is projected along the $p_{\mathrm{T}}^{\mathrm{hard}}$ direction, which is defined as the vectorial sum of p_T all the hard objects (leptons and jets[11]). The soft term longitudinal and perpendicular projections are considered. An illustration of the observables used is given in Fig. 4.22. In the ideal case, the soft term should balance the hard component of the interactions: $\mathbf{E_T^{miss}} = -(\mathbf{p_T^{hard}} + \mathbf{p_T^{soft}}) = 0$. The longitudinal soft term component is therefore a measure of the response of the soft term, while the perpendicular component, which should be zero in average, is more sensitive to the resolution.

The average $P_{||}^{soft}$ projection onto the p_T^{hard} is universal, meaning that it does not depend on the particular event topology. This is shown in figure 4.23 for CST $E_{\mathrm{T}}^{\mathrm{miss}}$. Its universality allows to estimate the soft term systematics in $Z \to \ell\ell$ events and use them for any final state.

[11] In W events, the transverse momentum of neutrinos should also be taken into account. This is possible only using simulated events.

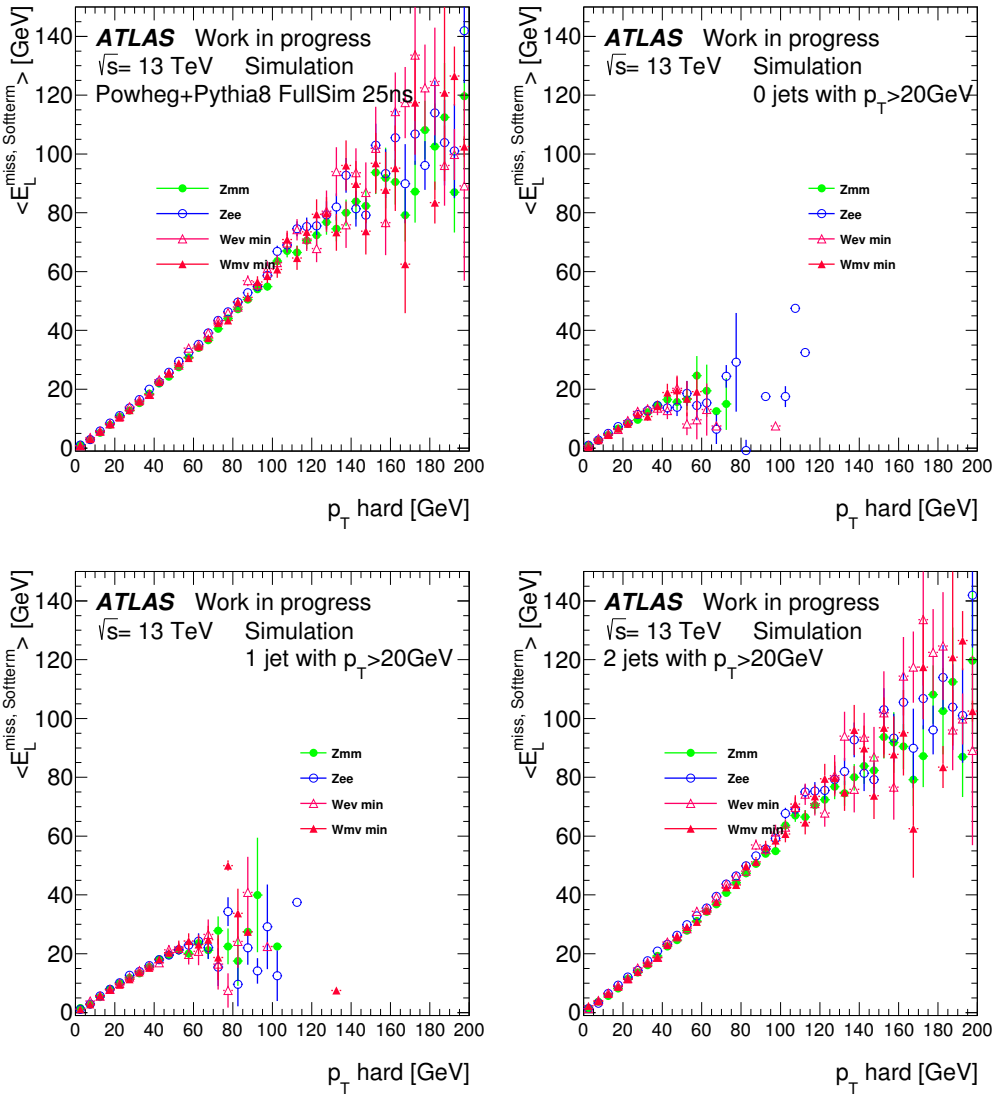

Figure 4.23: Average $P_{||}^{soft}$ versus p_T^{hard} for CST $E_{\mathrm{T}}^{\mathrm{miss}}$, for $Z \to ee$, $Z \to \mu\mu$, $W \to e\nu$ and $W \to \mu\nu$ events for different jet multiplicities. From the upper left, events with inclusive, 0, 1, 2 final state jets have been selected. Soft term are almost identical for TST and Track $E_{\mathrm{T}}^{\mathrm{miss}}$.

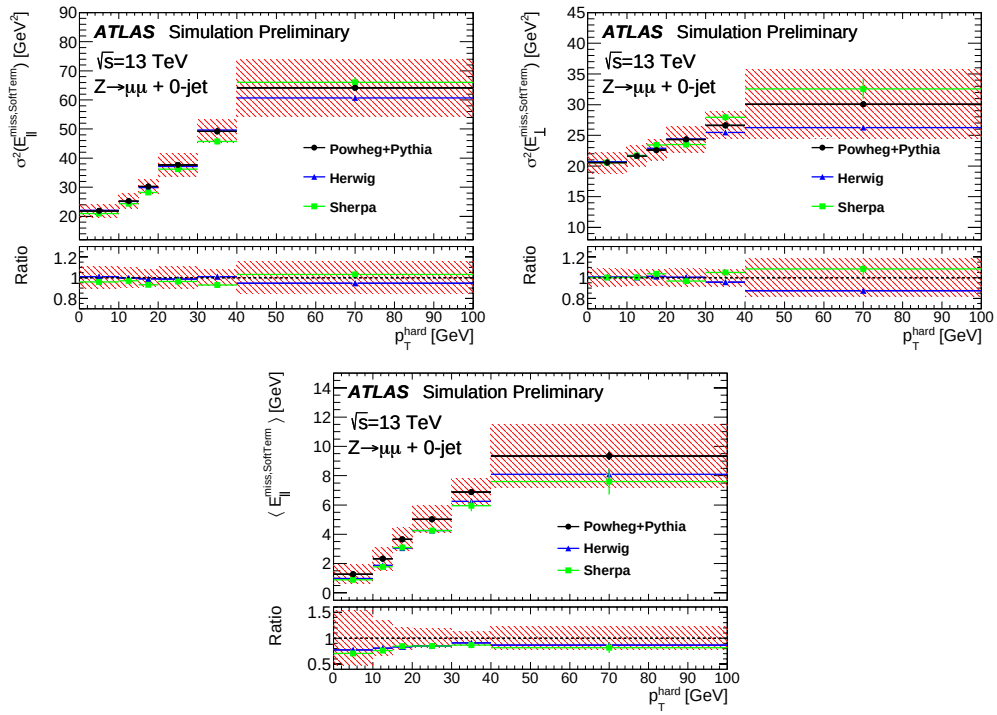

Figure 4.24: RMS and mean of the $E_{\mathrm{T}}^{\mathrm{miss}}$ soft term projected into components longitudinal and transverse to p_T^{hard} for $Z \to \mu\mu$ events with 0 hard jets. The shaded band shows the effect of the TST systematic uncertainties with contributions from the difference of generators, the change in detector geometry and the variation in bunch spacing.

4.7.2 TST $E_{\mathrm{T}}^{\mathrm{miss}}$ systematics

A first set of systematic uncertainty for the track based soft term has been estimated before the Run2 data taking for the physics analysis aiming at early 2015 data.
The systematic uncertainties need to quantify the level of agreement between data and MC. Studies on systematic estimate in Run1 have shown that differences between data and a nominal MC sample were smaller than the range obtained by comparing different MC generators.
The first Run2 estimation of TST soft term uncertainties is therefore obtained by a comparison of different generators with respect to a nominal one. POWEGH+PYTHIA8 is chosen as the nominal sample. Also uncertainties related to the detector simulation and running conditions have been taken into account with dedicated simulated samples.
$Z \to \mu\mu$ events have been used to estimate the systematic uncertainties associated to track based soft term used both in TST and Track $E_{\mathrm{T}}^{\mathrm{miss}}$ reconstruction.
The soft term longitudinal and perpendicular projection are compared between the different generators in bins of p_T^{hard} and also number of hard jets N_{jets} in the final state. The alternative generators are convoluted with a Gaussian smearing function and are fitted to the nominal sample distribution. The fitted width of the gaussian reflects the uncertainty in the resolution, while the fitted mean reflects the uncertainty on the scale. Fig. 4.24 shows the derived systematic uncertainties and Fig. 4.25 shows the effect of the combined uncertainties on the $E_{\mathrm{T}}^{\mathrm{miss}}$ distribution.

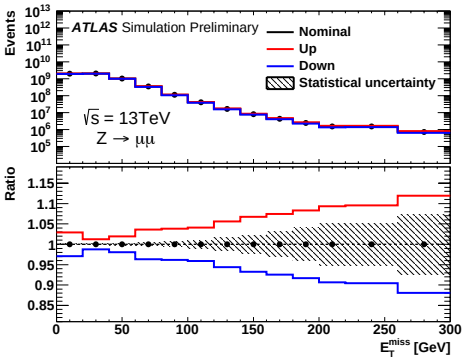

Figure 4.25: Total TST $E_{\mathrm{T}}^{\mathrm{miss}}$, and the variations resulting from the combined TST systematic uncertainties. Powheg+Pythia8 $Z \to \mu\mu$ events are shown. The hatched band shows the statistical uncertainty in the ratio.

4.7.3 Ideas for CST $E_{\mathrm{T}}^{\mathrm{miss}}$ systematic evaluation

The CST $E_{\mathrm{T}}^{\mathrm{miss}}$ terms mostly affected by pile up are the soft term and the jet term.
As shown in the previous sections, the pile up affects the $E_{\mathrm{T}}^{\mathrm{miss}}$ performance. The increasing average number of pile-up interactions leads to a large deterioration of the resolution. Moreover it also affects the $E_{\mathrm{T}}^{\mathrm{miss}}$ response and soft term linearity.
During Run1, two methods have been considered to estimate the uncertainties associated to the calorimeter based soft term. The first method considered $Z \to \mu\mu$ events with 0 final state hard jets. In this case only muons and the soft term contributes to the $E_{\mathrm{T}}^{\mathrm{miss}}$. Similarly to the method described in Sec. 4.7.2, the $E_{\mathrm{T}}^{\mathrm{miss}}$ is projected onto p_T^Z and the data to MC comparisons for the mean and the resolution in bins of $\sum E_T$ are used to quantify the uncertainties for the scale and the resolution. A global uncertainty is provided in this case.
The second approach used inclusive $Z \to \mu\mu$ events. The soft term is projected onto p_T^{hard}. The gaussian mean and width of the longitudinal component are studied as a function of p_T^{hard}. In this case systematic uncertainties as a function of p_T^{hard} are provided.
For Run2 different strategies have been investigated. Since the $E_{\mathrm{T}}^{\mathrm{miss}}$ performance depends on pile up, the underlying idea is to try to factorize out the effect of the uncertainties on the $E_{\mathrm{T}}^{\mathrm{miss}}$ from the pileup modelling.
Two strategies have been outlined.
The first idea is to factorize the soft term projections in bins of p_T^{hard} and $\sum E_T$. Inclusive $Z \to \mu\mu$ events are considered and the soft term is projected along p_T^{hard}. The mean and the resolution are considered for various MC samples for each p_T^{hard} bin. The differences with respect to the nominal sample are studied both in bins of p_T^{hard} and $\sum E_T$. This method is similar to the second approach described for Run1. Here, in addition, also $\sum E_T$ bins have been used: as $\sum E_T$ is the total transverse energy in the detector it catches the pileup contributions to $E_{\mathrm{T}}^{\mathrm{miss}}$ reconstruction.
For each p_T^{hard} bin the mean and the resolution of the soft term longitudinal projection are measured in bins of $\sum E_T$. Preliminary studies have been done based on MC samples, to take into account differences between:

- different generators;
- Atlas Fast simulations versus Full simulations;

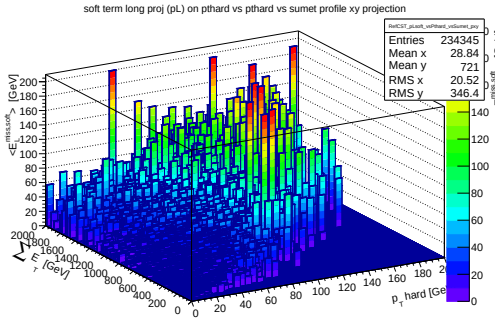

Figure 4.26: Three dimensional histogram showing the the soft term longitudinal projection (z axis) versus the $\sum E_T$ and p_T^{hard} of the event (x,y axis).

- different data taking conditions: 50 ns bunch spacing and 25 ns bunch spacing;
- different detector simulation geometries.

Figure 4.26 describes the method used. First comparisons between the different MC generators are shown in Fig. 4.27.

The second method exploits the same idea of trying to factorize out the systematics from the pile up modeling but using another slicing of the phase space. The idea is still to project the soft term onto p_T^{hard} and to consider bins of $< \mu >$ and number of primary vertices (N_{PV}) as a function of p_T^{hard}.
In order to use this second method, first it should be checked that $\sum E_T$ is well modeled in the $< \mu >$ and N_{PV} bins. In fact the CST $E_{\text{T}}^{\text{miss}}$ systematics depend on how well the pileup is modeled. If there would be any pileup mismodeling this will be reflected by a mismodel in the $\sum E_T$. Fig. 4.28 shows the data and MC $\sum E_T$ in different bins of $< \mu >$ and N_{PV}. The distributions show a good agreement. The N_{PV} and $< \mu >$ bins need to be optimized with more data statistics. The following step is to follow the method explained before, this time using the N_{PV} and $< \mu >$ bins.

4.8 Conclusions

$E_{\text{T}}^{\text{miss}}$ is an important event level quantity, especially for analysis with expected invisible particles in the final state. It is reconstructed as a sum of all the hard objects reconstructed in the event and the soft contribution, arising from unassociated tracks or energy deposits. Different algorithms have been developed in ATLAS to reconstruct $E_{\text{T}}^{\text{miss}}$ and the soft term.
Track based methods allow a good pile up suppression while calorimeter based methods take advantage of the nearly full coverage of the calorimeters.
TST $E_{\text{T}}^{\text{miss}}$ is a hybrid between a fully track based $E_{\text{T}}^{\text{miss}}$ and a calorimeter only $E_{\text{T}}^{\text{miss}}$: it uses tracks associated to the hard scatter vertex to build the soft term and calorimenter hard objects. This $E_{\text{T}}^{\text{miss}}$ version, is stable against pile up and shows good performance. For this reason this is the recommended $E_{\text{T}}^{\text{miss}}$ version for Run2 ATLAS analysis.

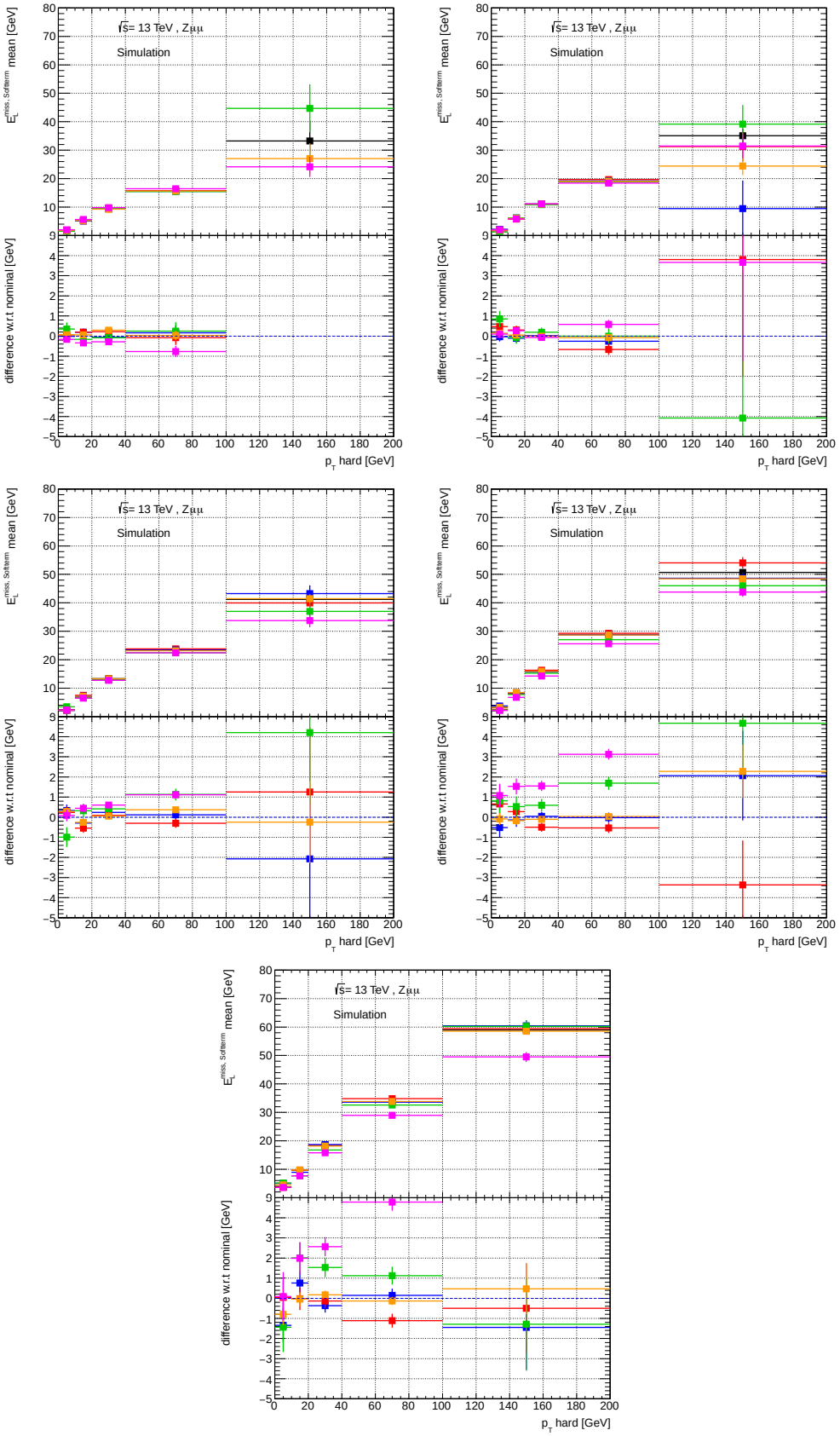

Figure 4.27: Comparisons of the soft term longitudinal projection versus p_T^{hard} in different bins of $\sum E_T$ for different MC generators.

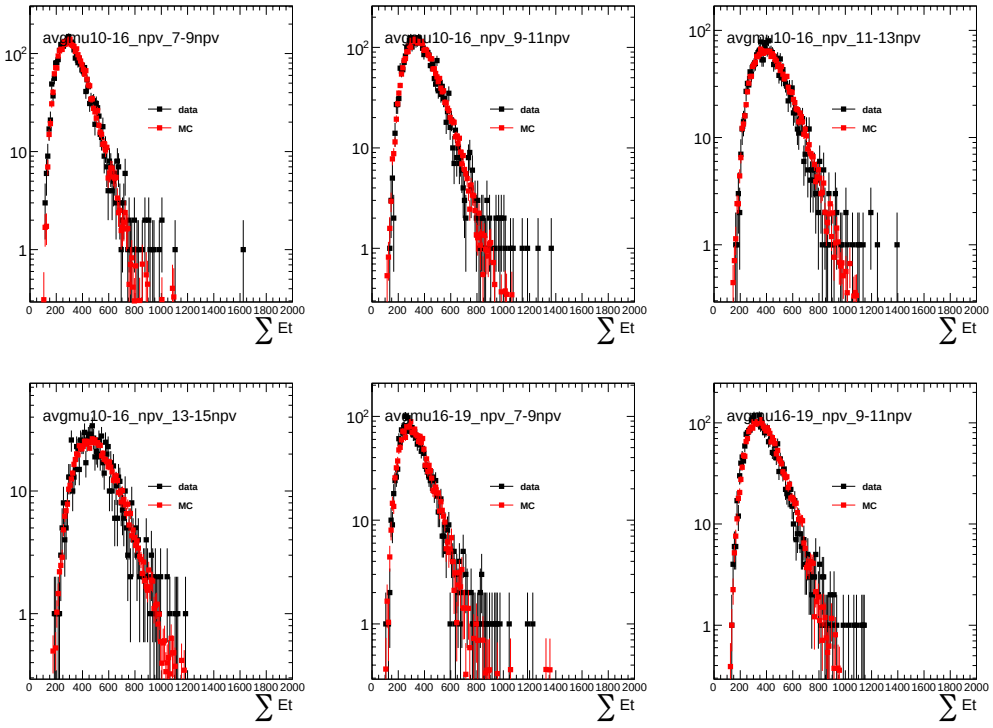

Figure 4.28: Data and MC comparisons for $\sum E_T$ in few different bins of $< \mu >$ and N_{PV}.

Chapter 5

The VBF Higgs to invisible analysis

5.1 State of the art of Higgs to invisible searches

The Standard Model predicts a Higgs invisible decay only through $H \to ZZ^* \to \bar{\nu}\nu\bar{\nu}\nu$ with Branching Ratio (BR) ∼0.1%. If an invisibly decaying Higgs boson would be observed with a higher BR, this would be a sign of new physics. Several Beyond the Standard Model (BSM) models (chapter 1) predict an invisibly decaying Higgs boson where the Higgs can decay into dark matter particles or neutral long-lived massive particles [93]- [98].
There are two main ways to look for Higgs invisible decays: *direct* searches or *indirect* constraints. Direct searches are designed to directly look for the Higgs (produced via its different production modes) decaying to invisible particles (i.e. not interacting with the detector). The final states are therefore defined by the presence of $E_{\mathrm{T}}^{\mathrm{miss}}$, given by the invisible particles from the Higgs decay, and by the particles and kinematics depending on the specific Higgs production mode. In particular, the Higgs boson needs to be produced with rather large momentum (*boosted*) in order to have reconstructed $E_{\mathrm{T}}^{\mathrm{miss}}$ from the invisible particles. Indirect constraints can be set on BR($H \to inv$) by gathering in a fit all the observations and measurements of Higgs BR decaying to *visible* particles[1]. In particular from a global fit of Higgs couplings to individual particles, while allowing contributions from BSM particles in loops and decays, the branching fraction of the Higgs boson into BSM particles may be up to 34% at 95% CL from ATLAS and CMS results at Run1 [99].
Direct searches have been performed by ATLAS and CMS in Run1 and Run2. They are characterized by final states with large missing transverse momentum associated with leptons or jets and include $VH(\to inv)$, ggF$H(\to inv)$ plus initial state radiation and VBF $H(\to inv)$ searches. Among them the VBF $H(\to inv)$ is the most sensitive one. The ATLAS Run 1 observed (expected) upper limit of 0.30 (0.35) for decays of the 125 GeV mass Higgs Boson produced via VBF and decaying to invisible particles was the best limit for Run 1 for an individual analysis for ATLAS and CMS [100]. When combining this result with another signal region (*monojet-like*), the result was improved to 0.28 (0.31) [100]. CMS has recently published a limit on Higgs invisible decays using a combination of VBF, ggF, and associated production of Higgs with a vector boson [112] with integrated luminosities of 4.9, 19.7, and 2.3 fb^{-1} at 7, 8, and 13 TeV respectively. The combination of all channels gives an observed (expected) upper limit of 0.24 (0.23) at 95% confidence level on the invisible branching fraction.

[1] Usually referred to as *visible* Higgs decays

A summary of the existing published results for Run1 and Run2 analysis from ATLAS and CMS is shown in table 5.1.

5.2 Introduction to the ATLAS Run 2 VBF Higgs to invisible analysis

This chapter describes the search for invisible decays of a Higgs boson produced principally via the Vector Boson Fusion (VBF) mechanism. A second but non negligible contribution comes from the gluon gluon fusion (ggF) signal with additional jets. Both for the VBF and ggF signals the couplings are assumed to be the SM couplings. The VBF Higgs to invisible analysis described here is performed with proton-proton collision data collected at center-of-mass energy of $\sqrt{s} = 13$ TeV with the ATLAS detector.
This version of the analysis is a counting experiment: it aims to count the number of observed events in a Signal Region (SR) (section 5.8) and to compare it to the Standard Model prediction (*backgrounds*, section 5.10). A precise estimation of all the sources of SM background entering the Signal Region (section 5.10) is therefore needed. In particular the background may be grouped in the following main subsets: the $Z \to \nu\nu + jets$ and $W \to \ell\nu + jets$ processes, where the lepton is lost or not reconstructed; the background which comes from $t\bar{t}$ and *single-top* processes; the multijet background. Different techniques are used to estimate each of them. The contribution of W/Z events is estimated with a semi data driven approach: dedicated regions (Control Regions, CR) enriched in $W \to \ell\nu$ (where the lepton is found) and $Z \to \ell\ell$ events are used to normalize to data the Monte Carlo (MC) estimates using a simultaneous fitting technique (transfer factor) and to extrapolate them to the SR. The *top* processes are a minor contribution and are estimated using simulations. The *multijet* background comes from QCD events where large missing transverse momentum is generated mainly by jet mismeasurements. This is expected to be highly reduced by a tight $E_{\mathrm{T}}^{\mathrm{miss}}$ cut but it remains tedious to be estimated precisely. As its estimation cannot rely on MC simulations, this background is estimated via data-driven methods (sections 5.15).
The analysis is optimized for a 125 GeV Higgs boson produced via VBF, assuming the SM production cross section, acceptance and efficiency. In absence of a significant excess in data, an exclusion upper limit is set on the BR(H$\to$ *inv*).
This chapter is organized as follows: firstly an overview on the data and simulated samples used through the full analysis will be provided. The main features of a VBF topology will be introduced and the SR event selection will be discussed in detail. The background estimation strategy will be presented and the different control regions will be defined. After presenting the multijet and fake lepton background estimation methods, the fit model will be discussed. Finally the results for unblinded data in SR will be shown and discussed.

5.3 Data and Simulation samples

5.3.1 Data

This analysis is performed on data from proton-proton collisions at $\sqrt{s} = 13$ TeV collected by the ATLAS detector in 2015 and 2016. Only events recorded during stable beam conditions and with all ATLAS sub-systems fully operational are considered. After application of data quality requirements, the total integrated luminosity corresponds to

Table 5.1: Summary of current limits on Higgs invisible decay from ATLAS and CMS with the corresponding references.

Analysis	**Run1 data** obs(exp)	**Run2 data** obs(exp)
ATLAS		
VBF H$\rightarrow$ *inv*	0.30 (0.35) 0.28 (0.31) [100]	0.37 (0.28)
Z($\rightarrow$ *ll*)H$\rightarrow$ *inv*	0.75 (0.62) [101]	0.98 (0.65) *13.3 fb*$^{-1}$ [102] 0.67 (0.39) *36.1 fb*$^{-1}$ [103]
V($\rightarrow$ *jj*)H	0.78 (0.86) [104]	-
Direct searches Combination	0.25 (0.27) [105]	-
Direct searches Combination and constraint from visible decays	0.24 (0.23) [105]	
CMS		
VBF H$\rightarrow$ *inv*	0.65 (0.49) [106] 0.57 (0.40) [107]	0.69 (0.62) *only 2.3 fb*$^{-1}$ [108] 0.28 (0.21) 35.9 fb^{-1} [109]
Z($\rightarrow$ *ll*)H	0.83 (0.86) [106]	0.86 (0.70) *12.9 fb*$^{-1}$ 0.40 (0.42) *35.9 fb*$^{-1}$ [110]
V($\rightarrow$ *jj*)H	0.60 (0.69) [107]	1.17 (0.72) *12.9 fb*$^{-1}$ [111]
Monojet	0.67 (0.71) [107]	0.48 (0.85) *12.9 fb*$^{-1}$ [111]
Direct searches Combination	0.32 (0.26)	0.24 (0.23) *Full Run1 data plus 2.3 fb*$^{-1}$ *Run2 data* [112] 0.24 (0.18) 35.9 fb^{-1} [109]
Direct searches Combination and constraint from visible decays	-	-
ATLAS and CMS		
constraint from visible decays	0.34 (0.35) [99]	

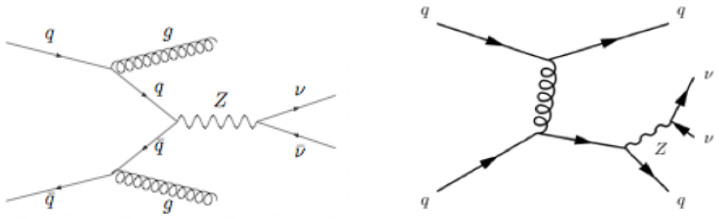

Figure 5.1: Some representative Feynman diagrams for the *strong produced* $W/Z + jets$ background processes.

36.1 fb^{-1} (3.2 fb^{-1} and 32.9 fb^{-1} for 2015 and 2016 dataset respectively) with 2.1% uncertainty on the luminosity.

5.3.2 MC samples

Simulated Monte Carlo samples used in this analysis were produced at $\sqrt{s} = 13$ TeV using different generators. The detailed list of the samples, their generator and their cross sections can be found in Tables C.1-C.10 in appendix.
All the backgrounds samples as well as the VBF $H(125) \rightarrow inv$ signal sample have been generated using full simulations of the detector (see section 2.3.2). All the other signal samples which are discussed in this document, i.e. :

- gluon gluon fusion $H(125) \rightarrow inv$ sample;
- higher mass points for VBF $H \rightarrow inv$;
- pure wimps triplet samples (see Chapter 6)

are generated using parametrizations of the calorimeter response (*Atlas fast* simulations, see section 2.3.2).
All the MC samples have been simulated with 25 ns bunch spacing collisions, to reflect the data conditions.

Background MC samples

***V*+*jets* samples:** The primary background processes $Z \rightarrow \nu\nu$+jets and $W \rightarrow l\nu$+jets, as well as $Z \rightarrow ll$ + jets, are modeled using the Sherpa 2.2.1 generator [117]. The W/Z background simulations are split into two components based on the order in the electroweak coupling constant α_{EW}:

- strong-produced W/Z: order α^2_{EW}
- electroweak-produced W/Z: order α^4_{EW}

Representative Feynman diagrams for the two different contributions can be found in Fig 5.1 and Fig 5.2 respectively. The strong-produced component of the simulation includes matrix elements with 0, 1, and 2 final-state partons at NLO, as well as 3 and 4 jets at LO. The electroweak component include matrix elements computed at LO in

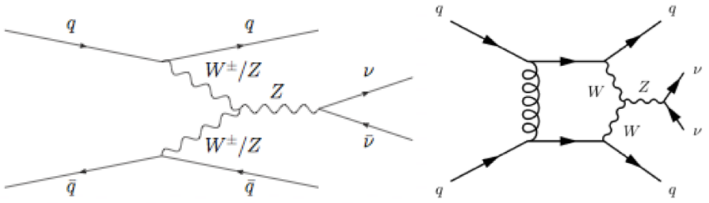

Figure 5.2: Some representative Feynman diagrams for the *ewk produced* $W/Z+jets$ background processes.

α_S for up to 3 final-state partons. Matrix elements are calculated using the Comix [118] and OpenLoops [119] matrix element generators and merged with the Sherpa parton shower [120] using the ME+PS@NLO prescription [121]. The NNPDF3.0 NNLO PDF parton distribution function [122] is used in conjunction with a dedicated parton shower tuning developed by the authors of Sherpa.
As mentioned in Sec. 2.3.3, simulated samples can use generator filters. Strong-produced $W/Z+jets$ samples are generated:

- in exclusive bins of the maximum between:
  - the boson transverse momenta (p_T^V),
  - the scalar sum of the momenta of the objects in the event (H_T)[2];
- with orthogonal c and b-quark filters[3].

For the $Z \rightarrow ll +$ jets samples, a generator-level filter requiring $m_{ll} > 40$ GeV was applied. The purpose of this is to remove the contribution from off-shell photons which is negligible in our signal and control regions.
In addition to these *strong-produced* $V+jets$ samples, during the analysis preparation, also other $V+jets$ samples have been used, both with a previous Sherpa version (2.2) and with different slice's scheme (boson p_T[4]).

Diboson samples: Diboson processes, with one of the bosons decaying hadronically and the other leptonically, are simulated using the Sherpa 2.2.1 generator. They are calculated for up to 1 additional parton at NLO and up to 3 additional partons at LO using the Comix and OpenLoops matrix element generators and merged with the Sherpa parton shower using the ME+PS@NLO prescription. The NNPDF30nnlo PDF set is used in conjunction with dedicated parton shower tuning developed by the Sherpa authors. The generator cross sections are used in this case (already at NLO).

[2]The different slices are: *MAXHTPTV 0-70*, *MAXHTPTV70_140*, *MAXHTPTV140_280*, *MAXHTPTV280_500*, *MAXHTPTV500_1000*, *MAXHTPTV1000_E_CMS*.

[3]To obtain an inclusive sample, events are generated with the following different filters: *c-veto, b-veto*; *c-filter, b-veto*; *b-filter*.

[4]The inclusive sample is made of several slices which correspond to different ranges of the simulated boson p_T.

Process	cross section (pb)	QCD scale (%)	PDF + α_s(%)	PDF (%)	α_s (%)
VBF	3.782	$^{+0.4}_{-0.3}$	2.1	2.1	0.5
Process	cross section (pb)	Theory (TH gaussian) (%)	PDF + α_s(%)	PDF (%)	α_s (%)
ggF	48.58	$^{+4.6}_{-6.7}$ (3.9)	3.2	1.9	2.6

Table 5.2: Cross sections for VBF and ggF produced Higgs of mass 125.0 GeV [7].

$t\bar{t}$ and single *top* samples: These processes constitute a minor contribution to this analysis. For the generation of $t\bar{t}$ and single top-quarks in the $Wt-$channel and $s-$channel, the Powheg-Box v2 generator [123] with the CT10 PDF sets [124] in the matrix element calculations is used. Electroweak t-channel single top-quark events are generated using the Powheg-Box v1 generator. For all top processes, top-quark spin correlations are preserved. The parton shower, fragmentation, and the underlying event are simulated using Pythia 6.428 [125] with the CTEQ6L1 PDF sets and the corresponding Perugia 2012 tune (P2012). The top mass is set to 172.5 GeV. The EvtGen v1.2.0 program is used for properties of the bottom and charm hadron decays.

***multijet* samples:** Multijet simulated events are used for cross checks through the analysis. They are simulated with Pythia. However, due to the large cross section for this process, the effective luminosity in MC for these samples is substantially smaller than the amount in data. For this reason it is impossible to use these samples for a direct cross check of the QCD estimation in SR (0 events pass the SR selection).

$H \to inv$ Signal samples

The primary signal process of SM Higgs produced via VBF is simulated using Powheg which computes the matrix elements at NLO. This is interfaced with Pythia for showering and hadronization. To simulate the invisible decay, the Higgs is forced to decay into two Z bosons, which are both then forced to decay into neutrinos. The Higgs width is sufficiently small that this is effectively equivalent to a direct decay into a pair of invisible particles lighter than $m_H/2$. The case where the Higgs is off-shell is not considered, as this analysis relies on the resonant enhancement for sensitivity.
The VBF signal sample is composed of two different samples which contain a truth requirement of $E_{\mathrm{T}}^{\mathrm{miss}} > (<)$ 125 GeV: the signal sample is binned in truth $E_{\mathrm{T}}^{\mathrm{miss}}$ with more statistics in the bin with $E_{\mathrm{T}}^{\mathrm{miss}} > 125$ GeV.
The cross sections used to normalize the VBF and ggF $H(125) \to inv$ are shown in table 5.2. They correspond to the cross section of Higgs boson mass $M_H = 125.0$ GeV. The cross sections for ggF are computed at N3LO, with the PDF set: PDF4LHC15_nnlo_100.

In addition to the ggF and VBF H(125) signal samples, also samples with a varied Higgs mass have been considered. In particular higgs samples of masses 75 GeV, 200 GeV, 300 GeV, 500 GeV, 750 GeV, 1 TeV, 2 TeV, 3 TeV, produced in VBF, have been used.
Both the samples where the Higgs mass is varied and the ggF H(125) sample are generated using fast simulation and with a truth filter requirement $E_{\mathrm{T}}^{\mathrm{miss}} > 75$ GeV to improve statistics in the region of interest.

5.3.3 MC reweighting

In order to correctly compare simulated events to data events, there are different effects which need to be taken into account.

Firstly, MC distributions should reflect data distributions but many experimental effects are only known after data taking and could not be simulated. For this reason some features are not part of the simulation process but need to be taken into account at a later stage. Among these experimental features there are pile-up corrections, lepton reconstruction, identification and isolation efficiencies, trigger scale factors, etc... Moreover, to correctly compare numbers of events between MC and data, it is necessary to normalize each MC event to a unit of integrated luminosity (taking into account the cross section of a given process) and reweigh it to the integrated luminosity of the considered dataset. Therefore, making use of the basic equation $N = L\sigma$ (see Sec. 2.1), relating the number of events N, cross section σ and luminosity L, each MC event should be weighted according to the following relation:

$$w = \frac{\sigma \times \epsilon \times k \times w_{MC} \times w_{\text{event}} \times L}{N_{\text{generated events}}} \tag{5.1}$$

w is the total weight each simulated events should be multiplied to, and includes the following terms:

- σ: is the cross section as calculated by the MC generator;
- ϵ: is the generator filter efficiency (see section 2.3.3);
- k factor: generators typically calculate the cross sections up to leading order or next-to-leading order. For processes where the cross-section at a higher order is known but not used in the simulation, a (usually constant) factor called *k-factor* is applied to the expected cross-section of the MC sample;
- MC weight w_{MC}: depending on the generator, there might be an event generator weight associated to each event;
- w_{event}: includes all the experimental weights which should be taken into account (pile up, reconstruction efficiencies, identification and isolation scale factors for leptons and jets, trigger scale factors, etc..)
- $N_{\text{generated events}}$: is the number of generated events, which includes the sum of all the weights;
- L: luminosity.

5.4 Vector Boson Fusion production mode

Among the Higgs boson production channels, gluon gluon fusion (ggF) is the dominant at the LHC. It is followed by the vector boson fusion (VBF) production mode with the second largest rate (see Fig. 1.3). Despite the smaller rate (which is about one order of magnitude smaller than ggF), VBF has a cleaner and distinct signature in the detector which makes it an important channel for the Higgs boson observation and related searches. VBF is a pure electroweak process at leading order (LO). The two main contributions to VBF Higgs production come from the $t-$channel and $u-$channel diagrams (Fig. 5.3) which represent the genuine VBF channel. VBF ($pp \rightarrow qq \rightarrow qqV^*V^* \rightarrow qqH$) topologies are characterized by two hard jets in opposite rapidity hemispheres and reduced contamination of QCD radiation. This peculiar final state allows a good background suppression by imposing appropriate selection cuts on the jet

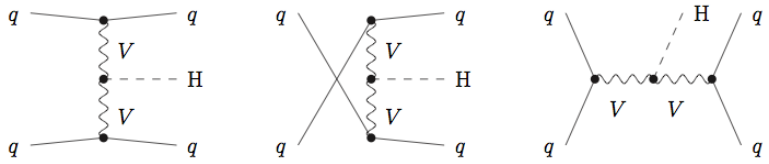

Figure 5.3: Topologies for $t-$, $u-$, and $s-$channel contributions to $qq \to qqH$ at leading order, where q denotes any quark or antiquark and V stands for W and Z bosons. [113]

transverse momenta, pseudorapidity, pseudorapidity gap between the two leading jets, the jet activity and di-jet invariant mass. $s-$channel diagrams and interferences tend to be suppressed, therefore the cross section can be approximated by the contribution of squared $t-$ and $u-$ channel diagrams. The QCD corrections at LO (considering $t-$ and $u-$ channel diagrams only) consist of vertex corrections to the weak boson quark coupling, explicit calculations at NLO QCD under this approximation show that these QCD corrections are small. NLO calculations with the full set of QCD diagrams (including $s-$channels and interferences) are also available [113], [114]. Also NLO EW corrections are calculated and are of the same size as the QCD corrections [113]. A first attempt to calculate the total cross sections to next-to-next-to-leading order (NNLO) in QCD calculations can be found in [115], [116].

5.4.1 Amplitude at LO

The distinguishing features of VBF processes can be inferred from the lowest order (LO) partonic amplitude, corresponding to the LO Feynman diagram shown in Fig. 5.4.
The LO amplitude is given by the following equation:

$$\mathcal{M}_{LO} = 2\sqrt{(\sqrt{2}G_F)}M_V^2 \frac{1}{q_1^2 - M_V^2}\frac{1}{q_2^2 - M_V^2}\bar{u}(p_3)\Gamma_\mu u(p_1)\bar{u}(p_4)\Gamma_\mu u(p_2) \tag{5.2}$$

where:

- p_1, p_2 are momenta of the initial state quarks
- p_3, p_4 are momenta of the final state quarks
- $q_1 = p_3 - p_1$ and $q_2 = p_4 - p_2$.

Γ_μ is the $Vq\bar{q}$ vertex and following the SM Feynman rules it can be rewritten as:

$$\Gamma_\mu = \sqrt{\sqrt{2}G_F}M_V(\nu_q\gamma_\mu - a_q\gamma_\mu\gamma_5), \tag{5.3}$$

where for vector and axial-vector couplings of the gauge bosons to fermions:

- for the W boson: $\nu_q = a_q = \frac{1}{\sqrt{2}}$;
- for the Z: $\nu_q = I_q^3 - 2Q_q \sin^2\theta_w$, $a_q = I_q^3$ (I_q^3 and Q_q being the isospin and charge respectively, related to the hypercharge by the Gell-Mann Nishijima formula [5]).

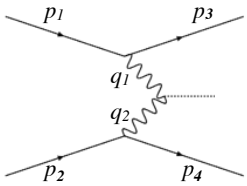

Figure 5.4: VBF diagram at LO ($t-$ channel).

The cross section is finite and the bulk of the cross section corresponds to small momentum transfers ($\lesssim M_V^2$, otherwise the cross section is suppressed). This implies that the two final state quarks prefer to travel in a collinear direction with respect to their initial one and they carry a high fraction of their initial momenta. From a jets perspective this means that the two final state quarks are reconstructed in the detector as jets in opposite η hemisphere, well separated in η and with large invariant mass.

5.5 Analysis strategy

As mentioned in the introduction, this analysis is a search designed as a *cut and count* analysis, which looks for an excess of observed data events in the signal region over the SM expectations.
In order to avoid being biased on the background estimate, the Signal Region data are included only when the analysis is finalized in all its steps and its robustness is proved. Before this step nobody can look at the SR data. In this phase the analysis is called *blinded*. Only data in Control Regions (signal free and enriched in a certain background) and Validation Regions (close to SR in background composition but with small signal contamination) can be included. In particular, all the background estimates, fit method and systematics correlation scheme need to be frozen before *unblinding* the SR.
Therefore, all the analysis procedure described in the next sections has been done with *blinded* SR data. The results presented in Sec. 5.19 include the SR data.

5.6 Analysis Objects

The physics objects used in this analysis have been described in detail in Chapter 3 and 4, in particular the requirements that those objects have to satisfy in order to be considered in the analysis are summarized below:

- jets: Antikt EM jets with radius 0.4 (Sec. 3.4), with p_T>25 GeV and $|\eta|<$ 4.5. The Jet Vertex Tagger (JVT) (Sec. 3.4.3) discriminant is used to identify jets originating from the hard-scatter interaction. Jets with $p_T < 60$ GeV and $|\eta| < 2.4$ are required to satisfy the requirement JVT > 0.59, corresponding to a selection efficiency for non-pile-up jets of about 92%;

- electrons: p_T >7 GeV, $|\eta|<$ 2.47 (not within the transition regions between barrel and endcap EM calorimeters at $1.37 < |\eta| < 1.52$); isolated and with *tight* quality criteria (Sec. 3.1);

[5] $Q = I_3 + \frac{1}{2}Y$, $Y = 2(Q - I_3)$

- muons: p_T >7 GeV, $|\eta|<$ 2.5, *medium* quality criteria, *gradient* isolation criteria (Sec. 3.2);
- $E_{\mathrm{T}}^{\mathrm{miss}}$: TST $E_{\mathrm{T}}^{\mathrm{miss}}$ (Sec. 4.2.1).

In addition to the $E_{\mathrm{T}}^{\mathrm{miss}}$, we define another event-level energy sum denoted $MHT(noJVT)$. This is the magnitude of the vector sum of all jets with p_T >20 GeV in the event, including both those which were selected and those which were rejected by the JVT requirement. Note that leptons are not included in this definition. The motivation for using this variable is to discriminate against events where *fake* $E_{\mathrm{T}}^{\mathrm{miss}}$ is introduced by the removal of jets from the JVT requirement. This is discussed in more detail in Sec. 5.8.4.

5.7 Preselection and cleaning cuts

5.7.1 Good Run List and Event cleaning

A first preselection consisting of *cleaning* cuts is common to all the regions used in the analysis. It consists of a set of requirements which ensure to only use not corrupted events or events not associated to bad detector conditions or other non optimal data taking conditions. The events recorded when such conditions occurred are tagged in an ATLAS database and added to a list which specifies that they should be excluded from analysis selections. This list is the so called *Good Run List* (GRL). The first requirement when selecting analysis events is therefore to use only data which belongs to the GRL. Events where noise bursts in the EM calorimeter and data corruption occurred in the Tile calorimeter are also rejected.
Each event is then required to have at least one primary vertex with at least two associated tracks with p_T^{trk} >400 MeV. Among all the reconstructed vertices, the primary vertex (i.e. the hard scatter one) is the one with the largest $\sum_{trk} {p_T^2}^{trk}$.

5.7.2 Jet Cleaning

Quality criteria for the selection of jets need to be applied in order to select jets from proton-proton collisions and to reject background jets from non-collision background. These criteria are referred to as *jet cleaning*: when fake jets have been identified, the entire event is vetoed.
The main background for jets coming from proton-proton collision events are:

- beam induced background: this background is due to proton losses on the LHC collimators and inelastic beam-gas interactions which produce secondary cascades of particles that can reach the detector. The energy deposits from these particles can be reconstructed as *fake* jets. These background depends on the LHC operational conditions (machine optics, collimator settings, residual gas densities and filling scheme);
- cosmic rays: cosmic rays showers can overlap with collision events. Cosmic rays particles reaching the detector are mainly muons.

Without dedicated selection criteria to identify these events, non collision background can be an important source of background in data events for $jets + E_{\mathrm{T}}^{\mathrm{miss}}$ final states. There are different quantities which can be used to discriminate *fake* jets from jets produced in collision events. These variables can be grouped in three different categories:

- variables based on signal pulse shape in the LAr calorimeters: provide good discrimination against noise in the LAr calorimeters;
- energy ratio variables;
- track-based variables: together with energy ratio variables, can be used both to reject the noise in LAr and Tile calorimeters and reject beam induced background and cosmic muon showers.

There are two *working points* which are provided for jet cleaning, a *loose* one and a *tight* one [126]. The tight working point provides a higher fake rate rejection with a few percent inefficiency. The tight working point is used in this analysis. Studies which show the necessity of it are collected in Sec. 5.11.

5.8 Signal Region Selection

To select a sample of signal candidate events, a Signal Region (SR) is designed to maximize the fraction of expected signal events with respect to the background ones. It is defined by a sequence of kinematic cuts which is applied both on data and MC, after preselection cuts (Sec. 5.7). The selection reflects the characteristics of a VBF topology presented in Sec. 5.4.
In the subset of events passing the cleaning cuts, signal-like events for the VBF $H \rightarrow inv$ analysis are selected by applying the following requirements:

- lowest unprescaled[6] $E_{\mathrm{T}}^{\mathrm{miss}}$ trigger (more in Sec. 5.8.1);
- the event contains at least 2 jets with $p_T > 25$ GeV and $|\eta| < 4.5$, which are not tagged as pile up jets (i.e. they pass JVT requirement, see Sec. 5.6);
- the leading jet has $p_T > 80$ GeV;
- the subleading jet has $p_T > 50$ GeV;
- the event contains exactly two jets: no additional jet with p_T >25 GeV and passing the JVT requirement is allowed (here after referred to as *third jet veto*), to suppress V+jets and QCD backgrounds;
- the two jets are not back to back in the transverse plane: $\Delta\Phi(j1, j2)$ <1.8, to suppress QCD background;
- the two jets lie in opposite longitudinal hemispheres $\eta(j1) \times \eta(j2) < 0$;
- the two jets are well separated in η: $\Delta\eta(j1, j2) > 4.8$;
- the event contains no electrons and muons (*lepton veto*), to suppress W/Z and top events;
- the event has $E_{\mathrm{T}}^{\mathrm{miss}}$ >180 GeV (more details in Sec. 5.8.2 and 5.8.3);
- the two leading jets are separated from the $E_{\mathrm{T}}^{\mathrm{miss}}$: $\Delta\Phi(E_{\mathrm{T}}^{\mathrm{miss}}, j_1)$ >1; $\Delta\Phi(E_{\mathrm{T}}^{\mathrm{miss}}, j_2)$ >1, to reject events where the $E_{\mathrm{T}}^{\mathrm{miss}}$ is produced by the (partial) loss of a jet or a mismeasured jet;

[6] *Unprescaled* means that all the events which fire the trigger are stored. *Prescaled* means that only a fraction of events is stored.

- the event has $MHT(noJVT)$ >150 GeV (more details in 5.8.4);
- the dijet system has a large invariant mass: $M(j_1, j_2) > 1$ TeV.

The selected events are then split into three categories (*bins*) of different signal purity according to the invariant mass of the dijet system. These categories are:

- SR1: 1< $M(j_1, j_2) < 1.5$ TeV;
- SR2: 1.5< $M(j_1, j_2) < 2.0$ TeV;
- SR3: $M(j_1, j_2) > 2.0$ TeV.

As the fraction of signal to background increases with higher $M(j_1, j_2)$ (see for instance the $M(j_1, j_2)$ distribution in the bottom left figure 5.32), one could expect that the analysis would benefit of a high improvement adding another higher $M(j_1, j_2)$ bin ($M(j_1, j_2) >$ 3.0 TeV). However, since W and Z control regions are used to estimate the W/Z background in SR (Sec. 5.13 and 5.18), the reduced control region statistics for $M(j_1, j_2) >$ 3.0 TeV is a limiting factor. Studies with a different binning show that an additional higher bin would not bring a significant improvement.

Distributions for $\Delta\eta(j1, j2)$, $M(j_1, j_2)$, $\Delta\Phi(j1, j2)$ and $E_{\mathrm{T}}^{\mathrm{miss}}$, for simulated multijet events and $H \to inv$ events, are shown in Fig. 5.33. They clearly show that cuts on these variables discriminate signal events from multijet events.

As will be detailed in Sec 5.18, cut and count experiments are performed in the $M(j_1, j_2)$ bins, the shape information of $M(j_1, j_2)$ is not used because a Sherpa mismodeling is known for this variable (see Appendix A).

5.8.1 $E_{\mathrm{T}}^{\mathrm{miss}}$ trigger

The signal region data used in this analysis were recorded with the lowest unprescaled $E_{\mathrm{T}}^{\mathrm{miss}}$ triggers used in 2015 and 2016 data taking periods. As introduced in Sec. 2.2.8, the trigger consists of two levels of selections, the first in hardware, (*level 1, L1*), and the second in software, (*high level trigger, HLT*). The L1 trigger uses as inputs coarse-spatial-granularity analog sums of the measured energy and requires $E_{\mathrm{T}}^{\mathrm{miss}}$ >50 GeV. The HLT uses calibrated clusters of cell energies in the calorimeter that are then used to cluster jets. The $E_{\mathrm{T}}^{\mathrm{miss}}$ at trigger level is computed by calculating the sum of all jets with $p_T > 7$ GeV. The threshold of the HLT $E_{\mathrm{T}}^{\mathrm{miss}}$ was raised several times through the 2015 and 2016 data-taking period from 70 GeV to 110 GeV, with the increasing instantaneous luminosity. In addition to the $E_{\mathrm{T}}^{\mathrm{miss}}$ triggers also a jet trigger (the so called HLT_noalg_J400) has been used: this trigger has no HLT selections applied (every event selected by L1 was saved) and it requires a 400 GeV L1 jet. The reason to use also this trigger is to recover some events that should have passed the $E_{\mathrm{T}}^{\mathrm{miss}}$ trigger at L1 but failed due to a firmware bug. The specific triggers used are listed in Table 5.3.

$E_{\mathrm{T}}^{\mathrm{miss}}$ Trigger efficiency

The performance of a trigger is measured in terms of the trigger *turn on curve*, which is a measure of the trigger efficiency as a function of the corresponding offline reconstructed variable. The $E_{\mathrm{T}}^{\mathrm{miss}}$ trigger turn on is therefore a function of the offline $E_{\mathrm{T}}^{\mathrm{miss}}$ variable. In order to measure the efficiency for a certain trigger it is necessary to use a sample of

Table 5.3: Triggers used for 2016 data taking. The years and run numbers where thresholds were changed are noted. From the trigger names one can deduce the actual trigger thresholds: "x"e stands for $E_{\mathrm{T}}^{\mathrm{miss}}$ while "J" for jets. HLT_xe is followed by the HLT threshold while _L1XE is followed by the L1 threshold.

Period	Trigger
All 2015	HLT_xe70_mht
2016, Runs $\leq$ 304008	HLT_xe90_mht_L1XE50
2016, Runs $>$ 304008	HLT_xe110_mht_L1XE50
All	HLT_noalg_J400

events triggered with a reference trigger. The reference trigger needs to be orthogonal to the trigger of interest.
For the $E_{\mathrm{T}}^{\mathrm{miss}}$ trigger turn on measurement, muon triggered events can be used as muon triggers are orthogonal to $E_{\mathrm{T}}^{\mathrm{miss}}$ triggers: since muons are almost invisible to the calorimeter they should always fire the $E_{\mathrm{T}}^{\mathrm{miss}}$ trigger for muons with enough momentum.
The trigger efficiency is the conditional probability that any single event passes the trigger, given all other conditions. A good estimator is the measured success frequency, that is the ratio between the number of events firing the trigger and the size of the initial sample. The efficiency is therefore measured in bins b_i of the reconstructed $E_{\mathrm{T}}^{\mathrm{miss}}$, where the optimal bin size should be balanced to have significant statistics in each bin but at the same time have to be sensitive to the rise of the turn on. The efficiency for each $E_T^{miss,\ offline}$ bin is defined as the fraction of muon triggered events passing the $E_{\mathrm{T}}^{\mathrm{miss}}$ trigger over the total number of events in that $E_T^{miss,\ offline}$ bin:

$$\epsilon(E_{\mathrm{T}}^{\mathrm{miss}} trigger) = \frac{\text{events with } E_T^{miss,\mathrm{offline}} \text{ in bin}_\mathrm{i} \text{ and passing the } E_{\mathrm{T}}^{\mathrm{miss}} \text{ trigger}}{\text{events with } E_T^{miss,\ \mathrm{offline}} \in bin_i} \quad (5.4)$$

In the ideal case, where the $E_{\mathrm{T}}^{\mathrm{miss}}$ at trigger level corresponds perfectly to the offline reconstructed $E_{\mathrm{T}}^{\mathrm{miss}}$, the turn on curve would be a step function, null below the HLT $E_{\mathrm{T}}^{\mathrm{miss}}$ value and 1 afterwards. In practice the trigger level and the offline $E_{\mathrm{T}}^{\mathrm{miss}}$ quantities do not match perfectly: the offline reconstructed $E_{\mathrm{T}}^{\mathrm{miss}}$ has further corrections that are not possible to apply in the trigger calculation, resulting in lower resolution for the L1 and HLT $E_{\mathrm{T}}^{\mathrm{miss}}$.
The trigger turn on curve is shown for data in figure 5.5, after the following selection:

- single muon trigger (see Table 5.7);
- at least two jets with $p_T > 25$ GeV, $|\eta|$ >4.5 and and passing the JVT requirement;
- $p_T(j1) > 80$ GeV , $p_T(j2) > 50$ GeV;
- third jet veto;
- the two jets are in an opposite η hemisphere;
- $|\Delta\eta(j1, j2)| > 2.5$;
- at least one muon ;
- $p_T(\mu) > 30$ GeV.

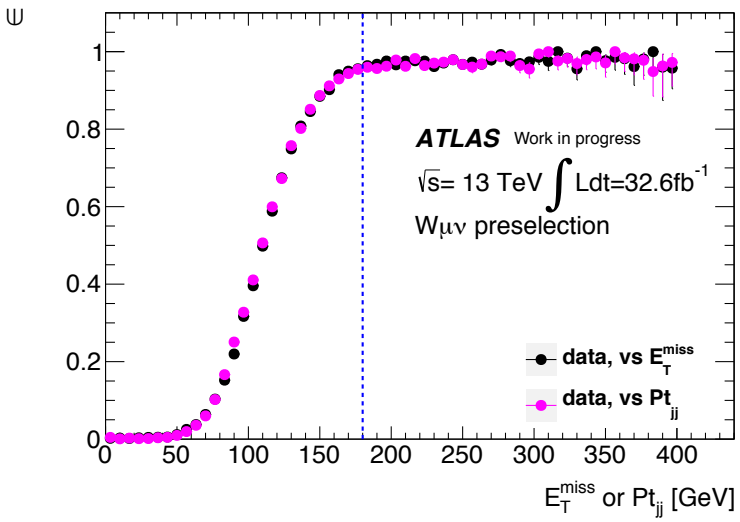

Figure 5.5: Trigger efficiency for the $E_{\mathrm{T}}^{\mathrm{miss}}$ triggers listed in Table 5.3 with respect to offline $E_{\mathrm{T}}^{\mathrm{miss}}$ and $p_T(jj)$, shown for data. (Clopper-Pearson confidence intervals have been used).

Since the $E_{\mathrm{T}}^{\mathrm{miss}}$ trigger sees the muon as invisible, the muon should also be treated as invisible in the offline $E_{\mathrm{T}}^{\mathrm{miss}}$ reconstruction. The $E_{\mathrm{T}}^{\mathrm{miss,offline}}$ quantity in eq. 5.4 is therefore corrected by adding vectorially the muon transverse momentum.
As shown in figure 5.5, in data the trigger is fully efficient for values of $E_T^{\mathrm{miss,offline}}$ greater than 200 GeV. At an offline cut $E_{\mathrm{T}}^{\mathrm{miss}} > 180$ GeV the efficiency is greater than 98%.
The trigger turn on curve in data is compared to the one for MC samples which shows that MC simulation overestimates the efficiency of very few %. This effect is corrected for in MC simulation using $E_{\mathrm{T}}^{\mathrm{miss}}$ *trigger scale factors* defined as the ratio of the efficiency in data divided by the efficiency in MC simulation. To simplify implementation and smooth statistical fluctuations, the scale factor is fit to the following function:

$$\frac{1}{2} \cdot [1 + Erf((E_{\mathrm{T}}^{\mathrm{miss}} - p_0)/\sqrt{2 \cdot p_1})]. \tag{5.5}$$

where p_0 =57.43 ±2.66 GeV and p_1 =55.97 ±1.96 GeV as they result from the fit.

5.8.2 $E_{\mathrm{T}}^{\mathrm{miss}}$ definition

As presented in Chapter 4, different algorithms can be used to recontruct $E_{\mathrm{T}}^{\mathrm{miss}}$. In particular a *track based* $E_{\mathrm{T}}^{\mathrm{miss}}$ (TST) and a *calorimeter based* $E_{\mathrm{T}}^{\mathrm{miss}}$ (CST) can be defined. While the former uses tracks associated to the primary vertex of the event to reconstruct the soft term, the latter uses only calorimeter signals not associated to the reconstructed hard objects.
Because of the particular VBF event topology, the jets selected in the analysis can be forward and fall beyond the tracker acceptance, therefore the primary vertex may be not well defined. In particular for the signal (background[7]) events ∼36% (∼25%) of the events passing the SR selection have both jets outside the tracker acceptance ($|\eta(j_1|)$ >2.5 and $|\eta(j_2)|$ >2.5). The remaining fraction of events has one jet falling in the tracker acceptance. For this reason detailed studies need to be performed to be sure that the TST

[7]Here as background W/Z simulated samples have been considered. Multijets are not included here.

$E_{\mathrm{T}}^{\mathrm{miss}}$ can be used for the analysis. A detailed presentation of the studies performed is given in appendix B. Those studies are based on signal and W/Z backgrounds and show that for high $E_{\mathrm{T}}^{\mathrm{miss}}$ values (>150 GeV) the differences between TST and CST $E_{\mathrm{T}}^{\mathrm{miss}}$ are minor. Based on this conclusion it has been decided to use the TST $E_{\mathrm{T}}^{\mathrm{miss}}$, as the one recommended for ATLAS Run2 analysis.
However, the special case of multijets events need to be studied in detail. In fact, for multijets events different problems related to the use of JVT may arise. As the JVT is used also in the TST $E_{\mathrm{T}}^{\mathrm{miss}}$ definition, this quantity is critical for this particular background. A discussion related to this topic is presented in Sec. 5.8.4.

$E_{\mathrm{T}}^{\mathrm{miss}}$ for this analysis is reconstructed using calibrated jets and the selected electrons and muons (same kinematic cuts and quality criteria as the ones used in the analysis).

5.8.3 $E_{\mathrm{T}}^{\mathrm{miss}}$ and transverse momentum of the dijet system

As described above, the hard objects in SR after the full selection are two jets and no lepton. This means that the main hard objects contributing to the $E_{\mathrm{T}}^{\mathrm{miss}}$ are the 2 leading jets. The $E_{\mathrm{T}}^{\mathrm{miss}}$ is then well approximized by the transverse momentum of the di-jet system ($p_T(j_1, j_2)$) (see Fig. 5.6).
During the analysis preparation, for a long period, the $E_{\mathrm{T}}^{\mathrm{miss}}$ cut has been replaced by a cut on the dijet system p_T.
There are some potential benefits using this quantity instead of the $E_{\mathrm{T}}^{\mathrm{miss}}$ one:

- the use of $p_T(j_1, j_2)$ harmonize the event selection in the signal and control regions: the selections would be perfectly parallel. This choice would avoid emulating the SR $E_{\mathrm{T}}^{\mathrm{miss}}$ by adding the lepton p_T in $Z \to \ell\ell$ and $W \to \ell\nu$ CRs, which are used to estimate the SR $Z \to \nu\nu$ and $W \to \ell\nu$ events in SR. A cut on $p_T(j_1, j_2)$ can be exactly the same everywhere, thus increasing the reliability of the CR to SR extrapolations;

- it simplifies the multijet background estimate in the signal region. The rebalance-and-smear technique (see section 5.15) is easier to apply when there is no soft term;

- it should be noted that the $E_{\mathrm{T}}^{\mathrm{miss}}$ trigger turn on as a function of $E_{\mathrm{T}}^{\mathrm{miss,offline}}$ or $p_T(j_1, j_2)$ is the same (Fig. 5.5);

- using $p_T(j_1, j_2)$ instead of $E_{\mathrm{T}}^{\mathrm{miss}}$ would avoid the problems related to the use of TST $E_{\mathrm{T}}^{\mathrm{miss}}$ in events where a wrong vertex is reconstructed as the primary vertex;

- it would avoid the use of $E_{\mathrm{T}}^{\mathrm{miss}}$ systematics (fewer degrees of freedom in the fit).

Although these motivations could bring to a potential simplification of the analysis, a $E_{\mathrm{T}}^{\mathrm{miss}}$ cut provides better background rejection and better signal efficiency than a cut on $p_T(j_1, j_2)$. For this reason it has been decided to use, as it was done in Run 1 [100], the $E_{\mathrm{T}}^{\mathrm{miss}}$ variable.
The use of $E_{\mathrm{T}}^{\mathrm{miss}}$ instead of $p_T(j_1, j_2)$ leads to a better result on the expected BR($H \to inv$) of ∼3% (absolute value) .

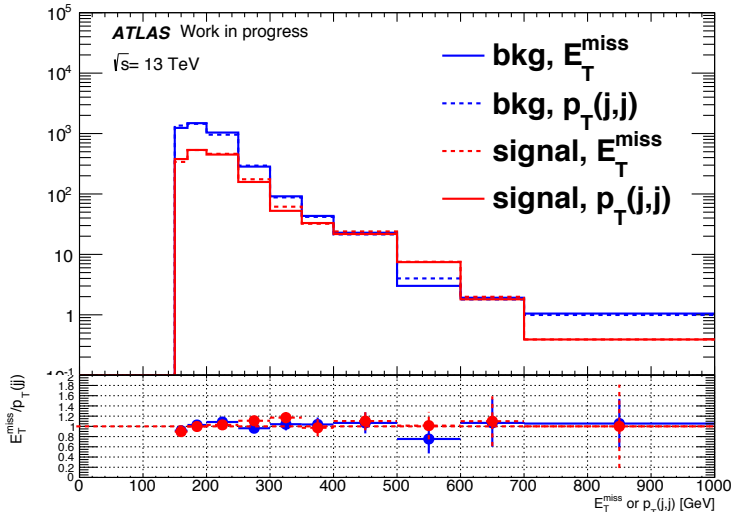

Figure 5.6: Comparison of $E_{\mathrm{T}}^{\mathrm{miss}}$ and $p_T(j_1, j_2)$ for signal and backgrounds MC samples (not including multijets) in SR, where a cut on $p_T(j_1, j_2) > 150$ GeV is also included in the selection. As shown in the plot the $E_{\mathrm{T}}^{\mathrm{miss}}$ is well approximized by the $p_T(j_1, j_2)$.

5.8.4 $MHT(noJVT)$ requirement

Multijet background can enter the signal region when a jet is mismeasured or lost due to its p_T being outside of acceptance. These effects are accounted for by our multijet background estimation method (see Section 5.15). However, there is a case when JVT removal removes an excessive amount of hard scatter p_T, resulting in "fake" $E_{\mathrm{T}}^{\mathrm{miss}}$. This comes about mainly when the leading jet has $|\eta| > 2.5$, meaning it has no tracks associated with it. In this topology of events, the hard scatter vertex may be wrongly reconstructed therefore the JVT requirement could wrongly remove hard scatter jets creating an unbalance in the event (*fake* $E_{\mathrm{T}}^{\mathrm{miss}}$).
This effect has been studied in a validation region.
Validation Regions (VR) are regions which are close to the SR in background composition, orthogonal to SR and with neglibible signal contamination. A validation region has been defined as the SR apart from the following requirements:

- relaxed η separation between the two jets: $|\Delta\eta(j_1, j_2)|$ >2.5;
- the dijet system has the invariant mass requirement reversed : $M(j_1, j_2)$ <1 TeV;
- the $E_{\mathrm{T}}^{\mathrm{miss}}$ requirement is relaxed: $E_{\mathrm{T}}^{\mathrm{miss}}$ >150 GeV;
- no requirement is set on the quantity $MHT(noJVT)$;

The $|\Delta\eta(j_1, j_2)|$ and $M(j_1, j_2)$ quantities are highly correlated and only few events would pass the $M(j_1, j_2)$ <1 TeV requirement if the $|\Delta\eta(j_1, j_2)|$ was not simultaneously relaxed. The signal contamination in this region is ∼8%.
This region is referred to as *2-jet, 0 lepton VR*. Figures 5.7 shows the $E_{\mathrm{T}}^{\mathrm{miss}}$ and leading jet η distributions in this region.The excess appears only when the leading jet is outside the tracker, which is consistent with misidentification of the primary vertex. The steeply falling shape of the excess in the $E_{\mathrm{T}}^{\mathrm{miss}}$ distribution is also characteristic of multijet events.

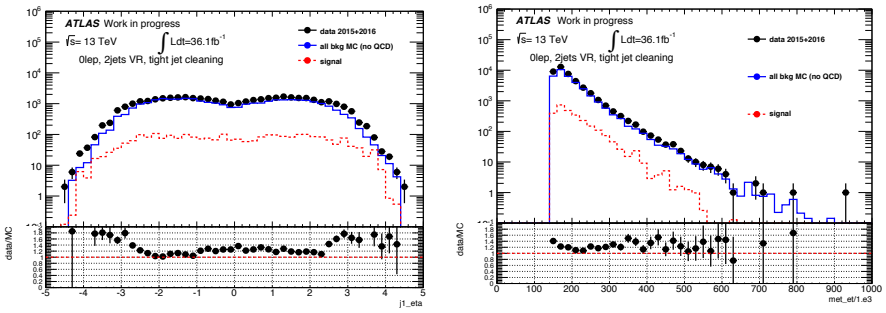

Figure 5.7: Leading jet η distribution (left) and $E_{\mathrm{T}}^{\mathrm{miss}}$ distribution (right) in the 2 jet validation region defined in Sec. 5.8.4 with $E_{\mathrm{T}}^{\mathrm{miss}} > 150$ GeV and no MHT cut.

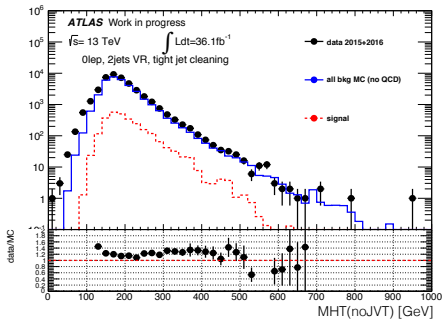

Figure 5.8: MHT(noJVT) variable as defined in Sec. 5.8.4 in the 2j VR with $E_{\mathrm{T}}^{\mathrm{miss}}$>150 GeV requirement.

This plot demonstrates that the problem only occurs when the leading jet is outside of the tracking volume, and that "fake" $E_{\mathrm{T}}^{\mathrm{miss}}$ is introduced as a result of the JVT requirement on each jet.
The proposed explanation for this effect relates to the definition of the primary vertex, which is used in the calculation of JVT. The fact that the leading jet is outside the tracker means that the sum p_{T}^2 of tracks that defines the primary vertex is smaller, and that could lead to picking the wrong vertex. This in turn may result in a lower JVT efficiency for hard scatter jets in this event topology, and thus introduce "fake" $E_{\mathrm{T}}^{\mathrm{miss}}$.
In order to remove this background, the $E_{\mathrm{T}}^{\mathrm{miss}}$ threshold has been raised from 150 GeV to 180 GeV and an additional cut on MHT(noJVT), which ignores the JVT requirement (see Section 5.6), shown in Fig. 5.8, is added. This reduces cases of fake $E_{\mathrm{T}}^{\mathrm{miss}}$ due to vertex misidentification to negligible levels, and The MHT(noJVT) requirement is roughly 99% efficient for the signal after $E_{\mathrm{T}}^{\mathrm{miss}} > 180$ GeV. The small impact of the MHT(noJVT) requirement after the $E_{\mathrm{T}}^{\mathrm{miss}} > 180$ GeV means that there is little sensitivity to the systematic uncertainties that the MHT(noJVT) cut might introduce.
The effect of these requirements in this VR is shown in figure 5.9.

5.9 Signal efficiency

The cutflow for the VBF and ggF $H \to inv$ signals (for 36.1 fb^{-1}) are shown in table 5.4. The VBF $H \to inv$ signal efficiency, defined as the number of events passing the SR selection over the number of generated events, is less than 1%. The VBF signal is ∼88% of the total $H \to inv$ signal and the ggF constitutes the remaining 12%, in the

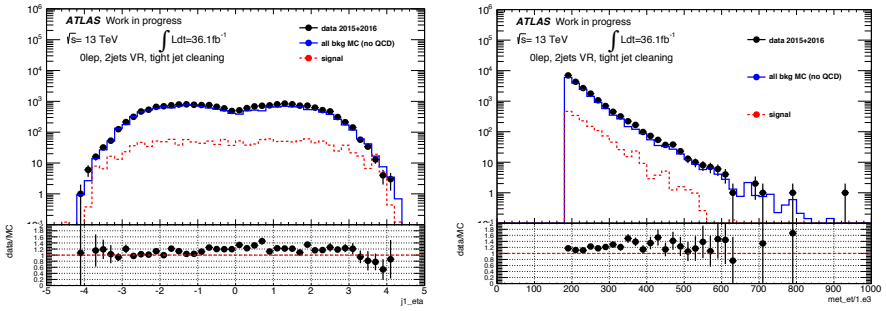

Figure 5.9: Leading jet η distribution (left) and $E_{\mathrm{T}}^{\mathrm{miss}}$ distribution (right) in the 2 jet validation region defined in Sec. 5.8.4 with $E_{\mathrm{T}}^{\mathrm{miss}} > 180$ GeV and with MHT cut (MHT>150 GeV).

Table 5.4: Cutflow for VBF and ggF signals.

	VBF H(125) signal		ggF H(125) signal	
	N events	Efficiency	N events	Efficiency
GRL, Lar, ...	135417.71	-	306830.12	-
tight jet cleaning	131719.22	0.97	298150.43	0.97
trigger	39883.99	0.37	135421.15	0.50
>=2 jets & jet pt cuts	16822.53	0.51	43469.96	0.44
0 leptons	16818.05	1.00	43451.82	1.0
Third jet veto	9178.84	0.55	14529.91	0.33
opposite η hemi	8012.06	0.87	5525.77	0.38
$\Delta\eta(j1, j2)$ >4.8	3244.63	0.40	404.02	0.07
$\Delta\phi(j1, j2)$ <1.8	2258.34	0.70	266.37	0.66
E_T^{miss} >180 GeV	944.97	0.42	139.40	0.52
MHT(noJVT)>150 GeV	934.08	0.99	136.65	0.98
$M(j1, j2)$ >1 TeV	926.90	0.99	136.65	1.00
total		0.7%		0.05%

inclusive $M(j_1, j_2)$ >1 TeV bin. The fractions for the three different $M(j_1, j_2)$ bins are:

- bin1 (1 TeV< $M(j_1, j_2)$ <1.5 TeV): 81% VBF, 19% ggF;
- bin2 (1.5 TeV< $M(j_1, j_2)$ <2 TeV): 85% VBF, 15% ggF;
- bin3 ($M(j_1, j_2)$ >2 TeV): 85% VBF, 15% ggF.

Kinematical distributions for the VBF H(125)$\rightarrow$ *inv* signal are shown in Fig 5.10 at different levels of the cutflow. The pseudorapidity distribution of the two leading jets show the typical VBF feautures discussed in section 5.4.
Table 5.5 shows the efficiency for signal samples of Higgs with varied mass decaying to invisible.

5.10 SM Backgrounds from pp collisions

The standard model processes passing the SR selection are listed in table 5.9, they are mainly coming from $Z \rightarrow \nu\nu +$ jets processes and $W \rightarrow l\nu +$ jets processes where the lepton is lost or not reconstructed.

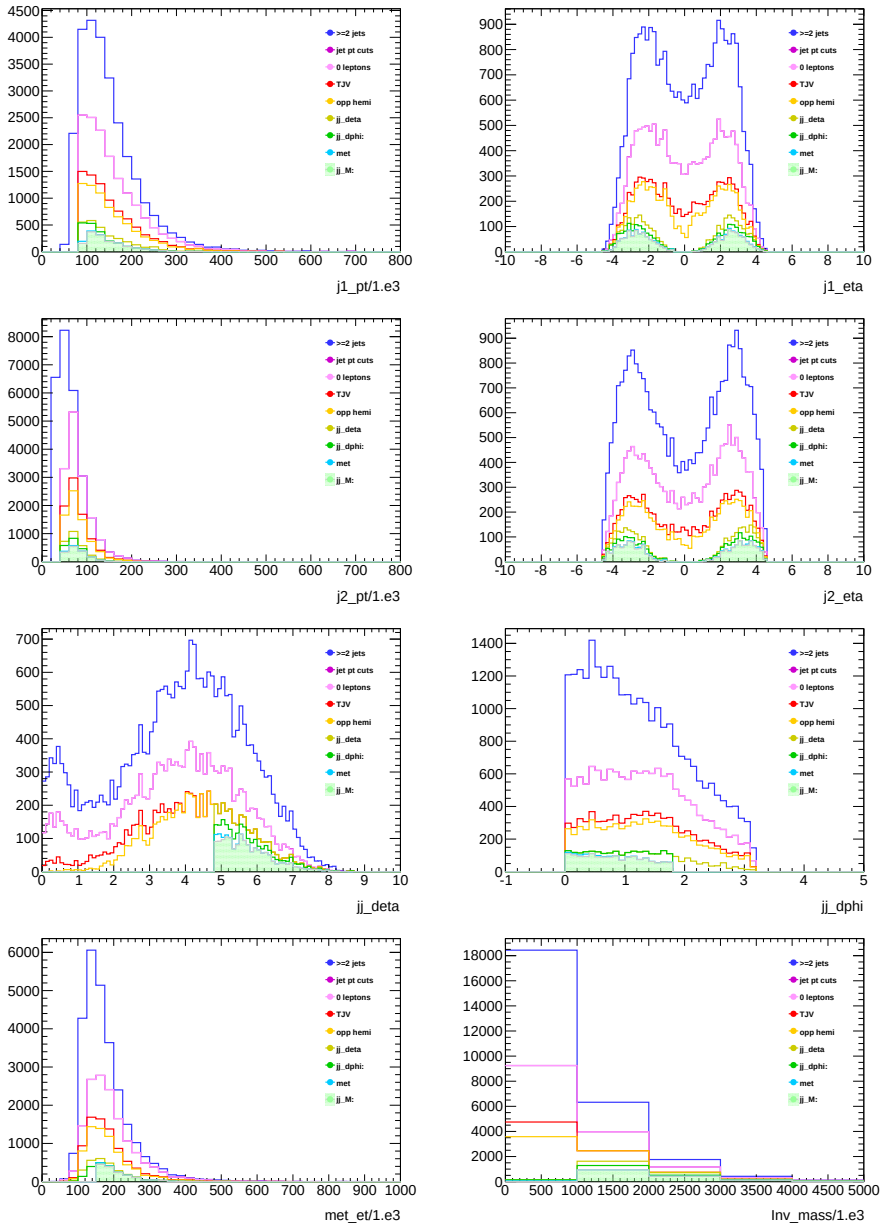

Figure 5.10: Kinematical distributions for the VBF $H \rightarrow inv$ signal at different levels of the cutflow. The dashed area represents the events passing the full SR selection (in an inclusive $M(j1, j2)$ >1 TeV bin).

Table 5.5: Selection efficiency for VBF $H \to inv$ signals with different higgs masses in the three SR bins. [130]

	Efficiency		
Higgs Mass	SR1	SR2	SR3
75 GeV	0.0041±0.0003	0.0036±0.0003	0.0047±0.0003
125 GeV	0.0054±0.0001	0.0043±0.0001	0.0058±0.0001
300 GeV	0.0073±0.0004	0.0062±0.0004	0.0115±0.0005
750 GeV	0.0076±0.0005	0.0093±0.0005	0.0211±0.0007
1 TeV	0.0071±0.0004	0.0112±0.0006	0.0247±0.0008
2 TeV	0.0057±0.0004	0.0093±0.0005	0.0306±0.0010
3 TeV	0.0047±0.0005	0.0092±0.0006	0.0293±0.0011

The primary source of SM backgrounds comes from $Z \to \nu\nu$+jets and accounts for ∼50% of the total background. The second main background in SR comes from $W \to \tau\nu$ events (∼24%), followed by $W \to \mu\nu$ (∼17%) and $W \to e\nu$ (∼7%), produced in association to jets. The electroweak-produced component of $Z \to \nu\nu +$ jets and $W \to l\nu +$ jets is an irreducible source of background: given that neutrinos are weakly interacting particles, it gives the same signature as the VBFH →inv signal. $Z \to ll +$ jets events constitute only ∼1% of the total background. Other minor sources of backgrounds come from $t\bar{t}$, single top events and diboson events (∼1%). Also multijet events contaminate the SRs but they are found to be a negligible contribution (∼<1%) (Sec. 5.15).
In the following section each of the $W \to l\nu +$ jets contributions is presented in more detail.

5.10.1 $W \to \tau\nu$ bakground in Signal Region

As previously mentioned, the $W \to \tau\nu$ background is the largest source of backgrounds in the $W \to l\nu +$ jets family. $W \to \tau\nu$ events contaminate the SR for different reasons:

- one tau is faking one of the two leading jets;
- the hadronic tau is not vetoed by the third jet veto (i.e. the pions from the tau decay are very soft, $p_T < 25$ GeV, and they pass below the third jet veto threshold);
- the leptonically decaying tau is not vetoed by lepton veto (the lepton is too soft or beyond the acceptance, or it is not identified as lepton).

As detailed in section 2.3, the simulation process involves different steps, from the proton-proton collision simulation to the detector simulation phase. During the event generation (sec. 2.3.1), generator-level *truth* particles are simulated. In the subsequent detector simulation stage, new particles produced by interactions with the detector material are appended to the MC sample. *Truth information* is kept in the reconstructed samples and matched with reconstructed objects and it can be used to connect the reconstructed object with the truth particle it corresponds to. Studies based on truth variables are often referred to as *truth level* studies.
Truth level studies have been performed at this stage to check where the taus are coming from.

Taus faking one of the two leading jets

Truth level taus have been selected in $W\tau\nu + jets$ MC samples (both the strong produced and electroweak produced $W\tau\nu$ samples have been used), after SR cuts. Among the truth level taus, only the matrix elements particles are considered[8]. The distance between the truth level taus and the selected jets is studied. If the tau overlaps with one of the two jets it means that the tau decayed hadronically and that jet is actually that tau (i.e. the tau is faking the jet).
Figure 5.12 shows the azimuthal separation $\Delta\Phi(j_{1(2)}, \tau)$ between each of the two jets and the tau, most of the times the tau is back to back with respect to the dijet system (i.e. the tau is recoiling against jets). Figure 5.13 shows the $\Delta R(j_{1(2)}, \tau)$ separation between each of the two jets and the tau. These plots show that after the full SR selection 1.5% of the times a tau is overlapping one of the leading or sub-leading jets (within ΔR <0.4) .
Figure 5.14 show the same distributions as Figure 5.13 at a previous step of the cutflow, when many of the subleading jets are overlapping a tau (ΔR <0.4), meaning that at this level of the cutflow in a high fraction of events a tau is faking the subleading jet. These events are rejected later in the cutflow.
These studies are in agreement with Run1 studies, when similar truth level studies have been performed and they demonstrated that the component of events with a tau overlapping one of the leading jet ($\Delta R(j_{1(2)}, \tau)$ <0.4) was a small fraction of the total and it became completely negligible after the final cut on $E_{\mathrm{T}}^{\mathrm{miss}}$.

Soft taus passing the third jet veto

Figure 5.11 shows the transverse momentum, η and Φ distributions for truth taus in $W\tau\nu$ events. In particular the transverse momentum distribution shows that a high fraction of tau leptons (68.5%) have p_T lower than 50 GeV, which could lead to soft pions ($p_T <$ 25 GeV) not rejected by the third jet veto. This is a first indication that the high $W\tau\nu$ contamination in SR is caused by τ leptons decaying into pions which are too soft to be rejected by the third jet veto.
The cascade decay of $W \to \tau\nu$ and $\tau \to \pi\nu$ has been simulated with a toy MC. In particular, for this toy MC, the W bosons are generated with a p_T distribution according to the transverse momentum of the dijet system ($p_T(j_1, j_2)$ [9]) which is measured in the W CR. Only W bosons with transverse momentum p_T >150 GeV are considered. The W and τ decays are simple two body decays with isotropic distributions in the center of mass frame. Figure 5.15 show the momentum distribution of the W bosons, τ leptons and the resulting pions from the τ decay: 30% of the pions have transverse momentum which falls below 25 GeV (black line). The pion p_T distribution coming from W generated with p_T > 200 GeV, is shown in figure 5.15 with a dashed line. It shows that a $p_T(j_1, j_2)$ (or $E_{\mathrm{T}}^{\mathrm{miss}}$) cut ($p_T(j_1, j_2)$ >200 GeV) would help to reduce this contamination.

Leptonically decaying taus

About ∼30% of the $W \to \tau\nu$ contribution originates from taus which decay leptonically, and the leptons are not vetoed by the lepton veto.

[8] This means requiring particles to have pdgId = ±15 and particle status equal to 3.
[9] As it is explained in 5.8.3, $p_T(j_1, j_2)$ is a good approximation of the $E_{\mathrm{T}}^{\mathrm{miss}}$.

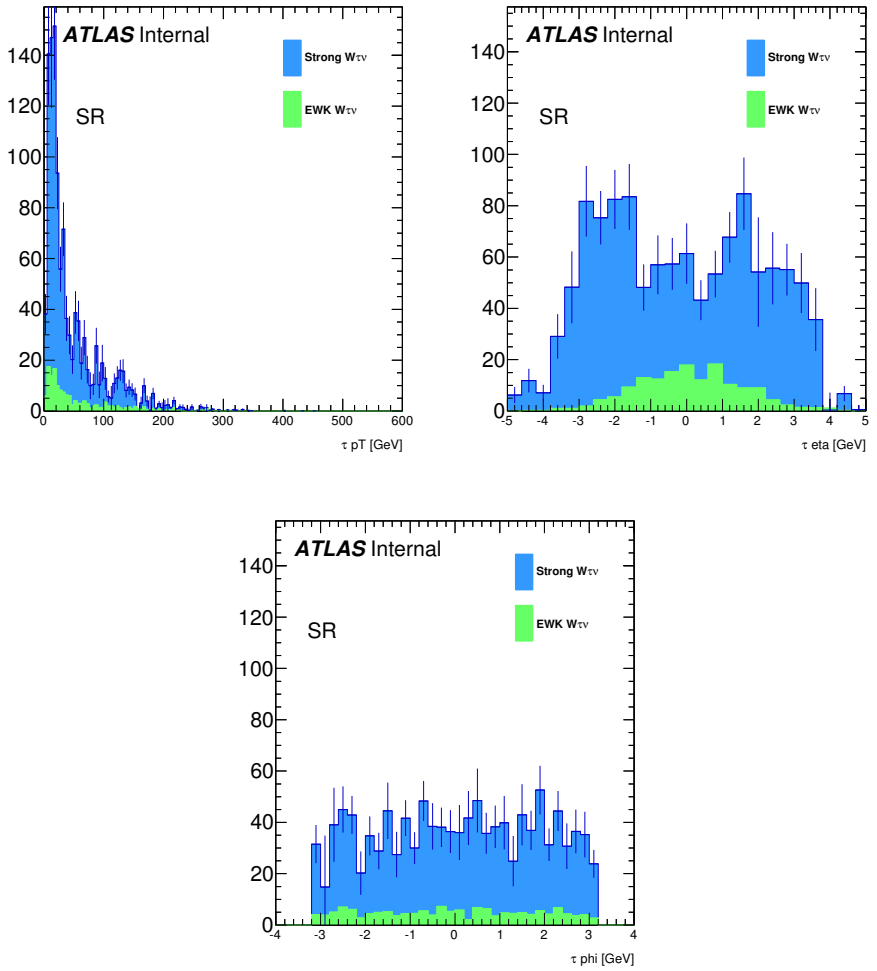

Figure 5.11: Transverse momentum, η and Φ distributions for $W\tau\nu$ events.

Summarizing: $W \to \tau\nu$ events entering the SR are 30% of the time leptonically decaying taus.
In the remaining 70% of the time, the taus are hadronically decaying: ∼1.5% of taus fake one of the leading or subleading jets while the remaining fraction decays into soft pions which are too soft to be rejected by the third jet veto.

5.10.2 $W \to e\nu$ and $W \to \mu\nu$ backgrounds

As shown in table 5.9, $W \to \mu\nu$ events entering the SR are three times $W \to e\nu$ events. Truth level studies have been carried out to investigate the origin of the higher contamination coming from $W \to \mu\nu$ with respect to $W \to e\nu$ events. SR events[10] have been selected in MC samples for $W \to \mu\nu$ and $W \to e\nu$ processes. For each of the selected events, truth level final state electrons and muons have been studied for for $W \to \mu\nu$

[10]These studies have been performed when the lepton veto p_T threshold in SR was set to 10 GeV instead of 7 GeV. This was due to limitations of the MC samples that were available at that time, where the low p_T tracks were not included. The conclusions of this section did not change when the lepton veto p_T threshold has been updated to 7 GeV.

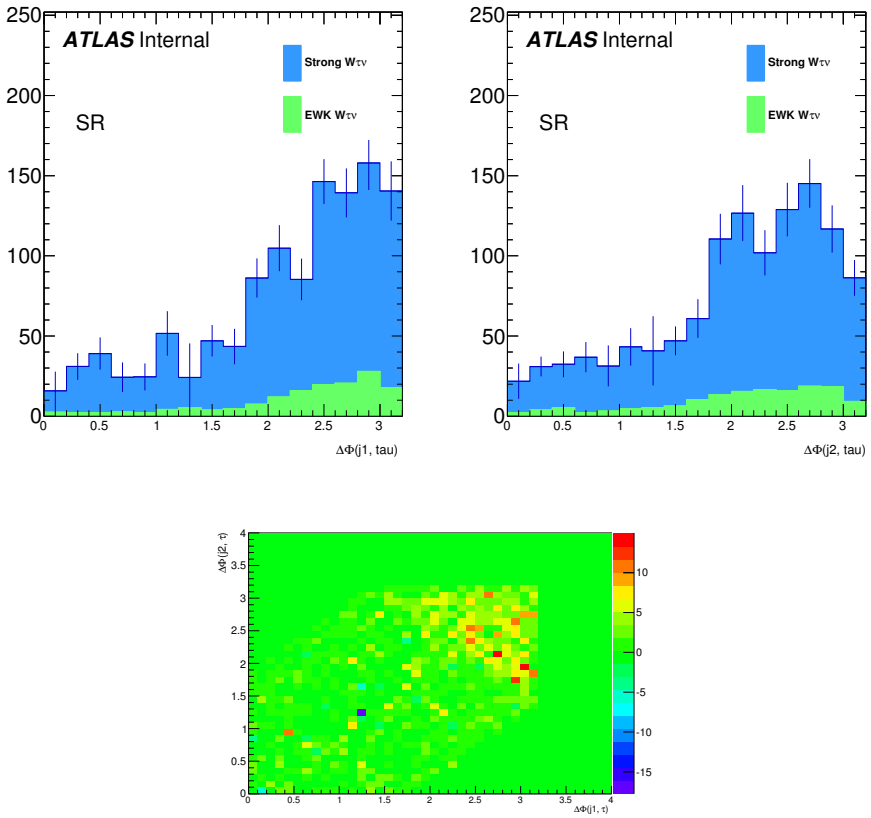

Figure 5.12: $\Delta\Phi(j_{1(2)}, \tau)$ between each of the two jets and the truth tau is $W\tau\nu$ events

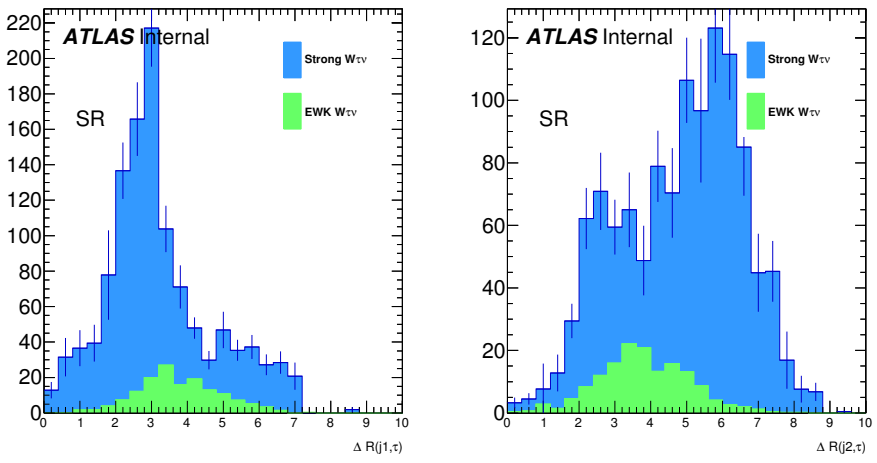

Figure 5.13: $\Delta R(j_{1(2)}, \tau)$ between each of the two jets and the truth tau is $W\tau\nu$ events after the full SR seletion

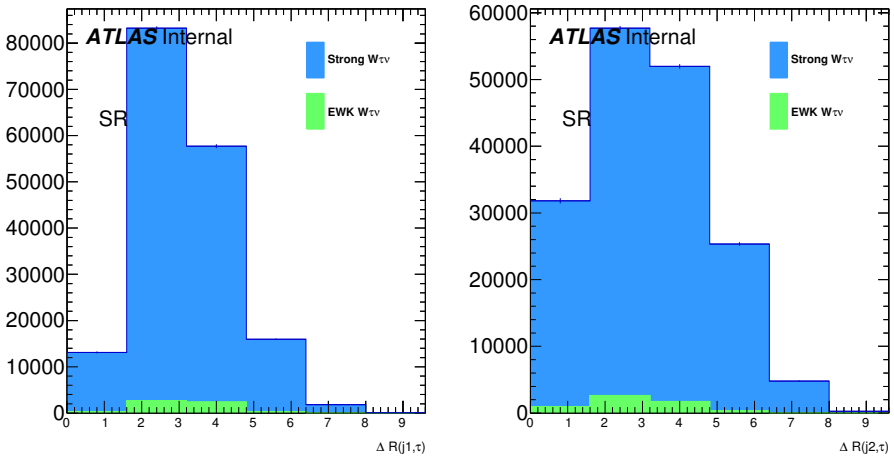

Figure 5.14: $\Delta R(j_{1(2)}, \tau)$ between each of the two jets and the truth tau is $W\tau\nu$ events after the following cuts: $E_{\mathrm{T}}^{\mathrm{miss}}$ trigger, lepton veto, at least 2 jets with $p_T(j1) > 80$ GeV and $p_T(j2) > 50$ GeV, third jet veto, $\Delta\eta(jj) > 2.5$, $E_{\mathrm{T}}^{\mathrm{miss}}$(or $p_T(jj)$)>150 GeV.

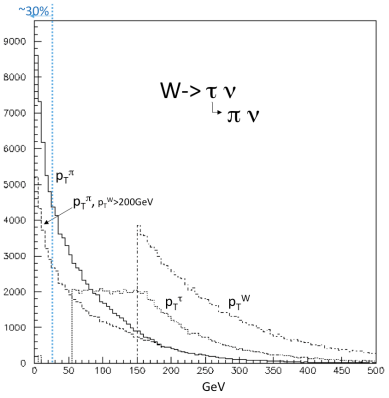

Figure 5.15: Momentum distribution for W bosons, τ leptons and the resulting pions from the τ decay, as simulated by a toy MC. The π p_T distribution is shown both in case of the W boson is generated with $p_T > 150$ GeV (continuous black line) and in case of W is generated with $p_T > 200$ GeV (dashed black line).

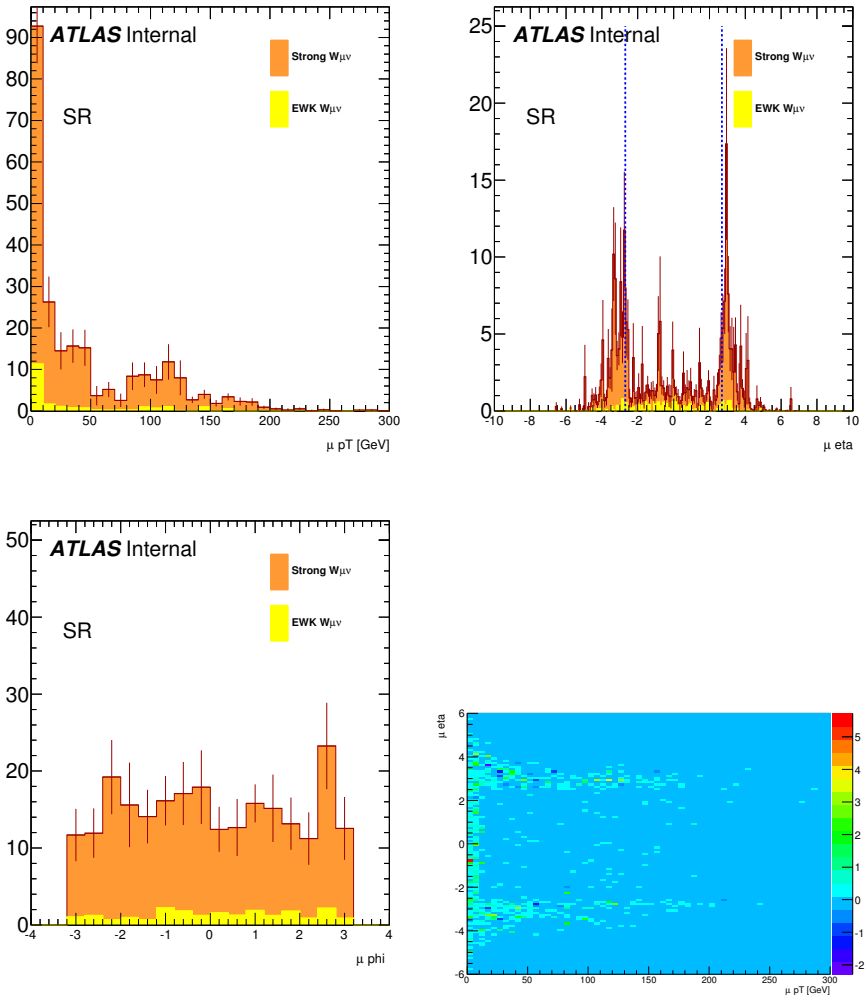

Figure 5.16: Transverse momentum, η, Φ and η vs p_T disributions for truth muons in $W\mu\nu$ events entering the SR.

and $W \to e\nu$ samples respectively.
The transverse momentum, η and Φ distributions for truth muons in $W\mu\nu$ events are shown in figure 5.16 while the ones for truth electrons in $We\nu$ events are shown in figure 5.17.
The truth muons η distributions show that a high fraction of events has muons beyond $|\eta| = 2.7$, i.e. muons which are out of acceptance and cannot be reconstructed. In particular 48 % of the muons in $W\mu\nu$ SR events have transverse momentum $p_T > 10$ GeV and $|\eta| > 2.7$ (see Figure 5.16).
The situation is different for electrons (figure 5.17) which do not show any event accumulations for $|\eta| > 2.7$. The reason is that, while electrons falling out of tracker η acceptance are reconstructed as jets and are vetoed by the third jet veto, muons are not reconstructed as jets and enter the SR selection.
In the scope of reducing the contamination from $W \to l\nu$ events, a tighter SR lepton veto has been investigated (see Appendix D). However the scenario presented here does not change when using a stricter lepton veto.

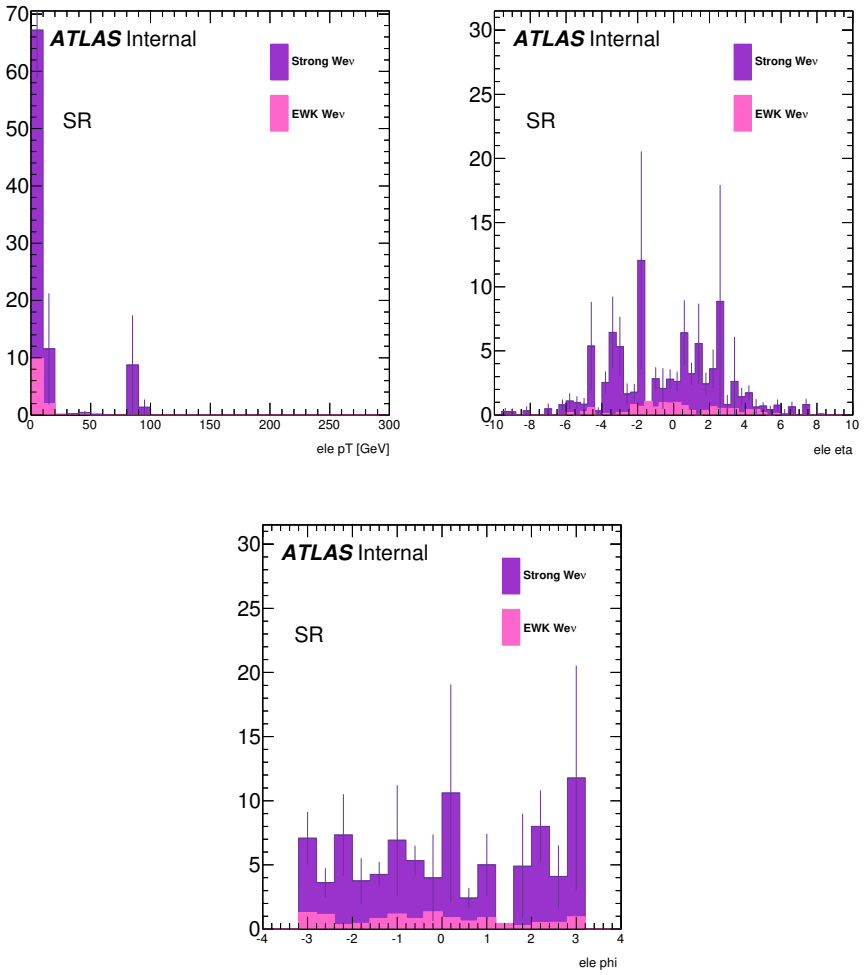

Figure 5.17: transverse momentum, η and Φ distributions for $We\nu$ events

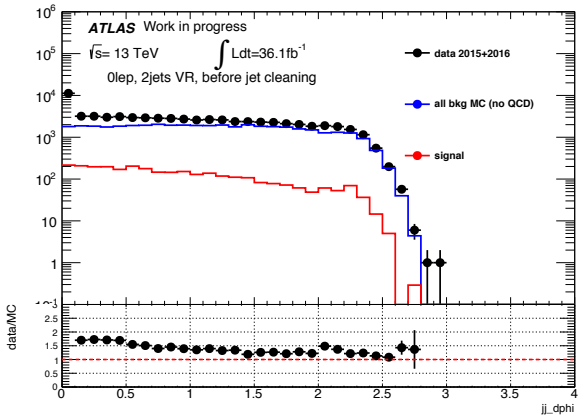

Figure 5.18: $\Delta\Phi(j_1, j_2)$ in the 0lepton, 2 jets validation region defined in 5.8.4, before the jet cleaning and before the $\Delta\Phi(j_1, j_2)$ <1.8 requirement.

5.11 Non collision background

In addition to SM events with signal-like final state which contaminate the SR, also events from non collision background (NCB, see Sec. 5.7.2) can enter the SR. Without dedicated selections, these events can be triggered at high rate by a $E_{\mathrm{T}}^{\mathrm{miss}}$ trigger. These events are characterized by the presence of jets non coming from LHC collisions, therefore the jet(s) does not balance in the event: they show up as events with jet(s) and $E_{\mathrm{T}}^{\mathrm{miss}}$. It is less probable to select these events in regions with leptons, where a lepton trigger is used to record the events and where an event should be reconstructed with a coincidence of lepton(s) and jets+$E_{\mathrm{T}}^{\mathrm{miss}}$ from NCB.
The usual way to suppress this source of background is the use of jet cleaning cuts (see Sec. 5.7.2).
In order to study the effect of the different jet cleaning working points in reducing NCB events, a validation region is used. In particular, the *2 jets, 0 lepton* VR defined in Sec. 5.8.4 has been used.
Before any jet cleaning requirement is applied, the data in this region are very rich in NCB events, the contamination of NCB events is up to ∼70% causing the data to MC disagreement for small values of $\Delta\Phi(j_1, j_2)$ in Fig. 5.18. These events are reconstructed as events with two jets with the same azimuthal angle and opposite η.
Fig. 5.20 shows the effect of the loose and tight jet cleaning criteria: only the use of the tight criteria reduces the NCB. As shown in figure 5.19, this background accumulates at $\Phi(jet_{1(2)}) \sim \pi$ and $\Phi(jet_{1(2)}) \sim 0$ but can also affect other points of the detector. Fig. 5.21 shows the $\Phi(j_1)$ and $\Phi(j_2)$ distributions when applying the tight jet cleaning requirement: the spikes at $\Phi \sim \pi$ and $\Phi \sim 0$ caused by the NCB are removed by the tight jet cleaning.
The remaining data to MC discrepancies in Fig 5.21 disappear when the $E_{\mathrm{T}}^{\mathrm{miss}}$ cut is raised to $E_{\mathrm{T}}^{\mathrm{miss}} > 80$ GeV and the MHT(noJVT) requirement is added.

5.12 Background estimation strategies

As mentioned in Sec. 5.2, different backgrounds are estimated with different techniques. Backgrounds originating from W/Z processes are estimated in a semi data driven way,

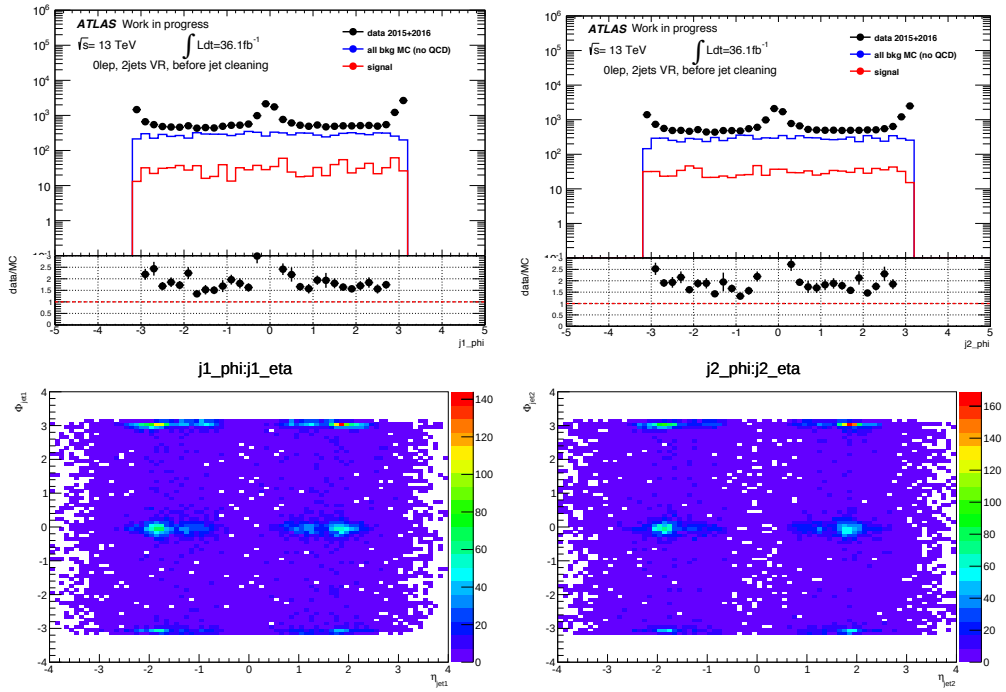

Figure 5.19: From the upper left: $\Phi(j_1)$, $\Phi(j_2)$, $\Phi(j_1)$ versus $\eta(j_1)$ and $\Phi(j_2)$ versus $\eta(j_2)$ distributions for data and MC events (prefit, no multijet event is shown here) in the 0 lepton, 2 jets validation region defined in 5.8.4, in the region where $\Delta\Phi(j_1, j_2)$ <0.5. Distributions are shown before the the jet cleaning requirements, to show the abundance of NCB events without dedicated requirements and how they show up in the detector.

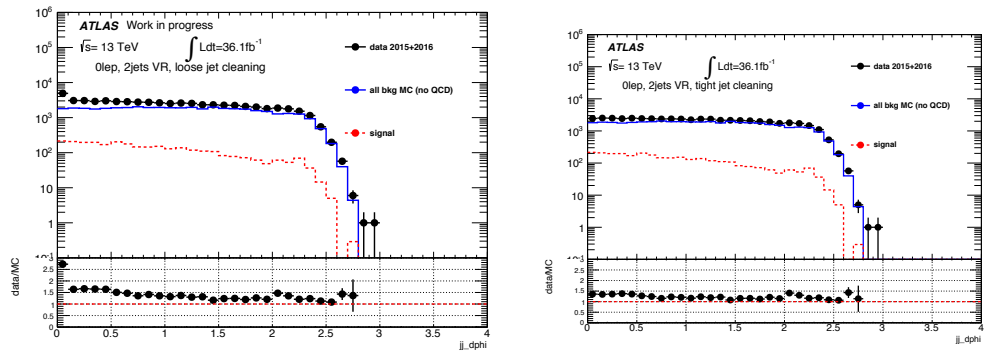

Figure 5.20: $\Delta\Phi(j_1, j_2)$ in the 0lepton, 2 jets validation region defined in 5.7.2, after the loose (left) and tight (right) jet cleaning and before the $\Delta\Phi(j_1, j_2)$ <1.8 requirement.

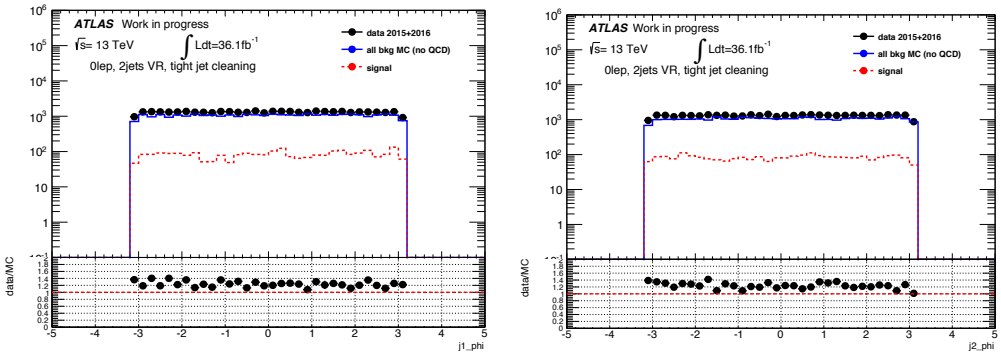

Figure 5.21: $\Phi(j_1)$ and $\Phi(j_2)$ distributions in the 0lepton, 2 jets validation region defined in 5.7.2, after the tight jet cleaning requirement.

based on a simultaneous fitting technique (Sec. 5.18), using data control regions enriched in W/Z processes (Sec. 5.13).
Multijets events are estimated with a data driven method referred to as *Rebalance and Smearing method* (R+S), described in Sec. 5.15.
The (small) contribution from $t\bar{t}$ and single top events is estimated using simulated samples.

5.13 Control regions

In order to estimate the amount of $Z \to \nu\nu$ and $W \to \ell\nu$, where the lepton is lost, backgrounds in SR, control regions enriched in $Z \to \ell\ell$ (with ℓ being electron or muon) and $W \to \ell\nu$ (where the lepton is *found*) events are designed. Control regions (CRs) are background-enriched regions where the presence of the signal is minimized while the presence of a certain background is maximized. They are used to measure on data the normalization of the different processes (W/Z) (as detailed in section 5.18). Control regions are carefully designed in order to not overlap to the SR and to maximize the fraction of a certain background. For this purpose, usually they are constructed by reverting a SR cut. In this analysis $W \to \ell\nu$-enriched and $Z \to \ell\ell$-enriched control regions are defined with the following general criteria:

- the $E_{\mathrm{T}}^{\mathrm{miss}}$ trigger is replaced by a single lepton trigger;
- all the CRs share with the SR the same jet selection (summarized in table 5.6) and the MHT(noJVT) >150 GeV requirement;
- the SR lepton veto requirement is reverted in order to select events with 1 or 2 leptons (electrons or muons);
- the SR $E_{\mathrm{T}}^{\mathrm{miss}} > 180$ GeV cut is replaced by a cut on the reconstructed $E_{\mathrm{T}}^{\mathrm{miss}}$ where the lepton(s) transverse momentum is added vectorially, in order to emulate the boson p_T;
- the same corrected $E_{\mathrm{T}}^{\mathrm{miss}}$ quantity is used to set a cut on $\Delta\Phi(j_{1,2}, E_T^{miss}) > 1.0$.

In total 8 different CRs are used, as summarized in Fig. 5.22. Following the SR selection, each of these is split in three bins of the invariant mass of the two leading jets ($M(j1, j2)$),

Table 5.6: Jet selections for each M_{jj} bin in SRs and CRs.

Cut	bin 1	bin 2	bin 3
N_{jet}	2	2	2
$p_{\mathrm{T}}(j_1)$	>80 GeV	>80 GeV	>80 GeV
$p_{\mathrm{T}}(j_2)$	>50 GeV	>50 GeV	>50 GeV
$E_{\mathrm{T}}^{\mathrm{miss}}$	>180 GeV	>180 GeV	>180 GeV
$MHT(noJVT)$	>150 GeV	>150 GeV	>150 GeV
$\lvert\Delta\Phi(jj)\rvert$	<1.8	<1.8	<1.8
$\eta(j_1) \times \eta(j_2)$	<0	<0	<0
$\lvert\Delta\eta(jj)\rvert$	>4.8	>4.8	>4.8
$M(jj)$	1–1.5 TeV	1.5–2 TeV	>2 TeV

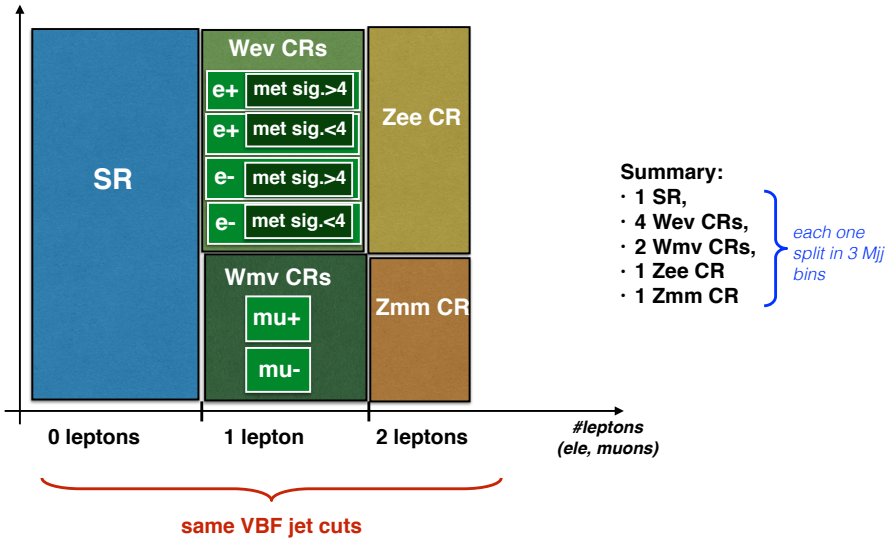

Figure 5.22: Scheme of control regions used in the analysis.

resulting in a total of 24 CRs. In the next sections all the CRs will be presented in more detail.

5.13.1 $Z \to ee$ CR

Data are recorded using single electron triggers, with 24 GeV $p_T(ele)$ threshold for 2015 and $p_T(ele)$ >26 GeV for 2016. Table 5.7 shows the complete list of triggers used [68]. The SR requirement of selecting events with 0 leptons is replaced by the requirement of having exactly two isolated electrons, with tight quality criteria and with p_T> 7 GeV. The leading electron must have p_T >30 GeV (in order to be in the region where the single lepton trigger is fully efficient) and the subleading electron is required to have p_T >10 GeV. Events with muons with p_T >7 GeV are vetoed. The two selected electrons must have opposite charge and their invariant mass must be compatible with the Z boson mass within 25 GeV. The SR $E_{\mathrm{T}}^{\mathrm{miss}}$>180 GeV requirement is replaced by a cut on the $E_{\mathrm{T}}^{\mathrm{miss}}$ corrected by adding vectorially the transverse momentum of the two leptons. Similarly to SR, a cut on $\Delta\Phi(j_{1,2}, E_T^{miss})$ >1.0 is set, where the $E_{\mathrm{T}}^{\mathrm{miss}}$ is the corrected $E_{\mathrm{T}}^{\mathrm{miss}}$.
All the jet cuts are exactly the same as for the SR and following SR selection, the $Z \to ee$

Table 5.7: List of single lepton triggers.

Period	Electron	Muon
All 2015	HLT_e24_lhmedium_L1EM20VH HLT_e60_lhmedium HLT_e120_lhloose	HLT_mu20_iloose_L1MU15 HLT_mu50
2016 Runs $\leq$ 304008	HLT_e24_lhtight_nod0_ivarloose HLT_e60_lhmedium_nod0 HLT_e140_lhloose_nod0	HLT_mu50 HLT_mu26_ivarmedium
2016 Runs $>$ 304008	HLT_e26_lhtight_nod0_ivarloose HLT_e60_lhmedium_nod0 HLT_e140_lhloose_nod0	HLT_mu50 HLT_mu26_ivarmedium

CR is also split in three bins of $M(j1, j2)$.

5.13.2 $Z \to \mu\mu$ CR

The $Z \to \mu\mu$ CR selection is perfectly parallel to the one used for the $Z \to ee$ CR, where the electrons are replaced with the muons.
Data are recorded using single muon triggers listed in Table 5.7. The SR requirement of selecting events with 0 leptons is replaced by the requirement of having exactly two isolated muons, with medium quality criteria and with $p_T >$ 7 GeV. Events with electrons with $p_T >$7 GeV are vetoed. All the other selection cuts are exactly the same as for the Zee CR, where electrons should be replaced by muons.

5.13.3 $W \to l\nu +$ jets CRs

For each $M(j1, j2)$ bin, $W \to \mu^+\nu$, and $W \to \mu^-\nu$, $W \to e^+\nu$, $W \to e^-\nu$ CRs are defined as follows.

- Events are selected with a single lepton trigger (see table 5.7);
- the SR requirement of zero electrons and muons in the event is replaced with a requirement of:
  - for the $W \to e\nu$ CRs: exactly 1 electron;
  - for the $W \to \mu\nu$ CRs: exactly 1 muon;
- the lepton transverse momentum must be greater than 30 GeV;
- for both $W \to e\nu$ and $W \to \mu\nu$ CRs, two different CRs are defined according to the charge of the lepton. This allows to exploit the W charge asymmetry to estimate the amount of events with fake leptons (see section 5.16 for more details);
- the jet cuts are the same as for SR selection;
- the SR $E_{\mathrm{T}}^{\mathrm{miss}}$ cut is replaced by a cut on the $E_{\mathrm{T}}^{\mathrm{miss}}$ corrected by adding vectorially the transverse momentum of the lepton (corrected $E_T^{miss}>$180 GeV).

A summary of the lepton selection can be found in table 5.8.

Table 5.8: Lepton selections

Cut	SR	$W \to e^- \nu$	$W \to e^+ \nu$	$W \to \mu^- \nu$	$W \to \mu^+ \nu$	$Z \to e^- e^+$	$Z \to \mu^- \mu^+$
Selected leptons	0	e^-	e^+	μ^-	μ^+	e^-, e^+	μ^-, μ^+
$p_{\mathrm{T}}(\ell_1)$	–	$>30\,GeV$	$>30\,GeV$	$>30\,GeV$	$>30\,GeV$	$>30\,GeV$	$>30\,GeV$
$p_{\mathrm{T}}(\ell_2)$	–	–	–	–	–	>7,GeV	$>7\,GeV$
$\lvert M(\ell\ell) - M_Z \rvert$	–	–	–	–	–	$<25\,GeV$	$<25\,GeV$

Misidentified leptons in $W \to l\nu +$ jets CR

After this selection, the $W \to e^+\nu$ and $W \to e^-\nu$ CRs are very rich in multijet events. Multijet events enter the $W \to e\nu$ CRs if one jet is misidentified as an electron, referred to here as *misidentified* or *fake* lepton. The contamination of fake leptons in $W \to e\nu$ CRs can reach a level of 50%. In order to reduce the fake lepton contamination in $W \to e\nu$ CRs, an additional requirement on $E_{\mathrm{T}}^{\mathrm{miss}}$ significance is introduced. The $E_{\mathrm{T}}^{\mathrm{miss}}$ significance is a variable used to discriminate events with real $E_{\mathrm{T}}^{\mathrm{miss}}$ from events with fake $E_{\mathrm{T}}^{\mathrm{miss}}$. It is defined as:

$$E_T^{miss} sig. = \frac{E_T^{miss}}{\sqrt{p_T(j1) + p_T(j2) + p_T(el)}} \tag{5.6}$$

The $E_{\mathrm{T}}^{\mathrm{miss}}$ in the numerator is the real reconstructed $E_{\mathrm{T}}^{\mathrm{miss}}$ of the event, it is not corrected by adding the lepton p_T. The denominator is the square root of the scalar sum of the momenta of the main objects of the event [11].
Fig. 5.23 shows the $E_{\mathrm{T}}^{\mathrm{miss}}$ significance distribution in $W \to e\nu$ events after a relaxed $W \to e\nu$ CR selection [12]. A cut on $E_{\mathrm{T}}^{\mathrm{miss}}$**sig.**$> 4$ GeV$^{\frac{1}{2}}$ removes events with a high fraction of misidentified electrons. As shown in Fig. 5.23, in $W \to \mu\nu$ events, this component is negligible.

Fig. 5.24 and Fig. 5.25 show that data are well modeled by the MC simulation after removing the misidentified lepton background: the data/MC agreement for all the kinematic distributions in $W \to e\nu$ CRs improves significantly.
Since the main backgrounds are estimated from CRs to SR via the transfer factor method (Sec. 5.18), the CR selection should be as close as possible to the SR one. Introducing a cut on this variable only for the $W \to e\nu$ CR, requires to prove that there is no bias using the transfer factor method. Extensive checks have been done on this purpose: shape comparisons of the relevant variables before and after the cut show that there is no significant change in the shape (Fig. 5.26).
Although the fake lepton background is heavily suppressed by introducing the $E_{\mathrm{T}}^{\mathrm{miss}}$ significance cut, their remaining contamination needs to be evaluated carefully. The method adopted to estimate it is outlined in detail in section 5.16 and it employs both events with $E_{\mathrm{T}}^{\mathrm{miss}}$ *sig.* > 4 GeV$^{\frac{1}{2}}$ and events with $E_{\mathrm{T}}^{\mathrm{miss}}$ *sig.* < 4 GeV$^{\frac{1}{2}}$ (rich in lepton fakes).
Summarizing, for each M_{jj} bin, the $W \to e\nu$ CRs used in the final fit to estimate the backgrounds in SR and for the limit setting are:

- $W \to e^+\nu$ with $E_{\mathrm{T}}^{\mathrm{miss}}$ *sig.* > 4;
- $W \to e^-\nu$ with $E_{\mathrm{T}}^{\mathrm{miss}}$ *sig.* > 4;

[11] The $E_{\mathrm{T}}^{\mathrm{miss}}$ resolution due to calorimetric measurements scales approximately as the square root of the scalar sum of all the hard and soft objects of the event.
[12] in the inclusive $M_{jj} >1$ TeV bin, not splitting $W \to e\nu$ events according to the electron charge.

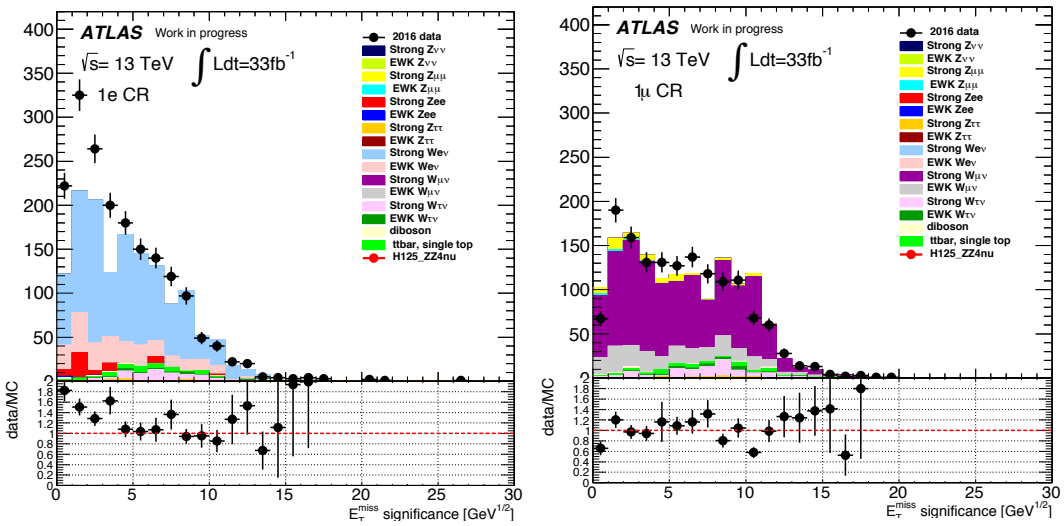

Figure 5.23: Left: $E_{\mathrm{T}}^{\mathrm{miss}}$ significance distribution in $W \to e\nu$ events. The selction applied correpsonds to the CR selection described in the text where the $E_{\mathrm{T}}^{\mathrm{miss}}$ cut is relaxed ($E_{\mathrm{T}}^{\mathrm{miss}}$ >180 GeV) and the $MHT(noJVT)$ cut is not applied. Distribution are shown for the inclusive M_{jj} >1 TeV bin. Right: $E_{\mathrm{T}}^{\mathrm{miss}}$ significance distribution in $W \to \mu\nu$ inclusive CR,

- $W \to e^{+}\nu$ with $E_{\mathrm{T}}^{\mathrm{miss}}$ $sig.$ < 4;
- $W \to e^{-}\nu$ with $E_{\mathrm{T}}^{\mathrm{miss}}$ $sig.$ < 4.

The lepton selections for each CR are summarized in table 5.8.

5.14 Data and MC distributions in CRs

A summary plot comparing the predicted yields from MC simulation with the number of observed events in data in each CR is shown in figure 5.27. The corresponding data and MC yields for the inclusive M_{jj} >1 TeV bin for the $Z \to \mu\mu$, $Z \to ee$, $W \to \mu\nu$ and $W \to e\nu$[13] CRs are shown in table 5.9. Yields for all the separate bins are given in table 5.10.
Data and MC distributions are shown for different kinematic distributions in the different control regions for an inclusive M_{jj} >1 TeV bin. Figures 5.28 and 5.29 show the distributions of several kinematic variables of interest in the $Z \to \ell\ell$ CR. Figures 5.30 and 5.31 show the same distributions in the $W \to \ell\nu$ CR, which can similarly be used to test the modeling of the $W \to \ell\nu$ process. For these plots, the $W \to \ell\nu$ CRs are not split according to the lepton charge.

[13] With $E_{\mathrm{T}}^{\mathrm{miss}}$ $sig.$ >4 $\mathrm{GeV}^{\frac{1}{2}}$.

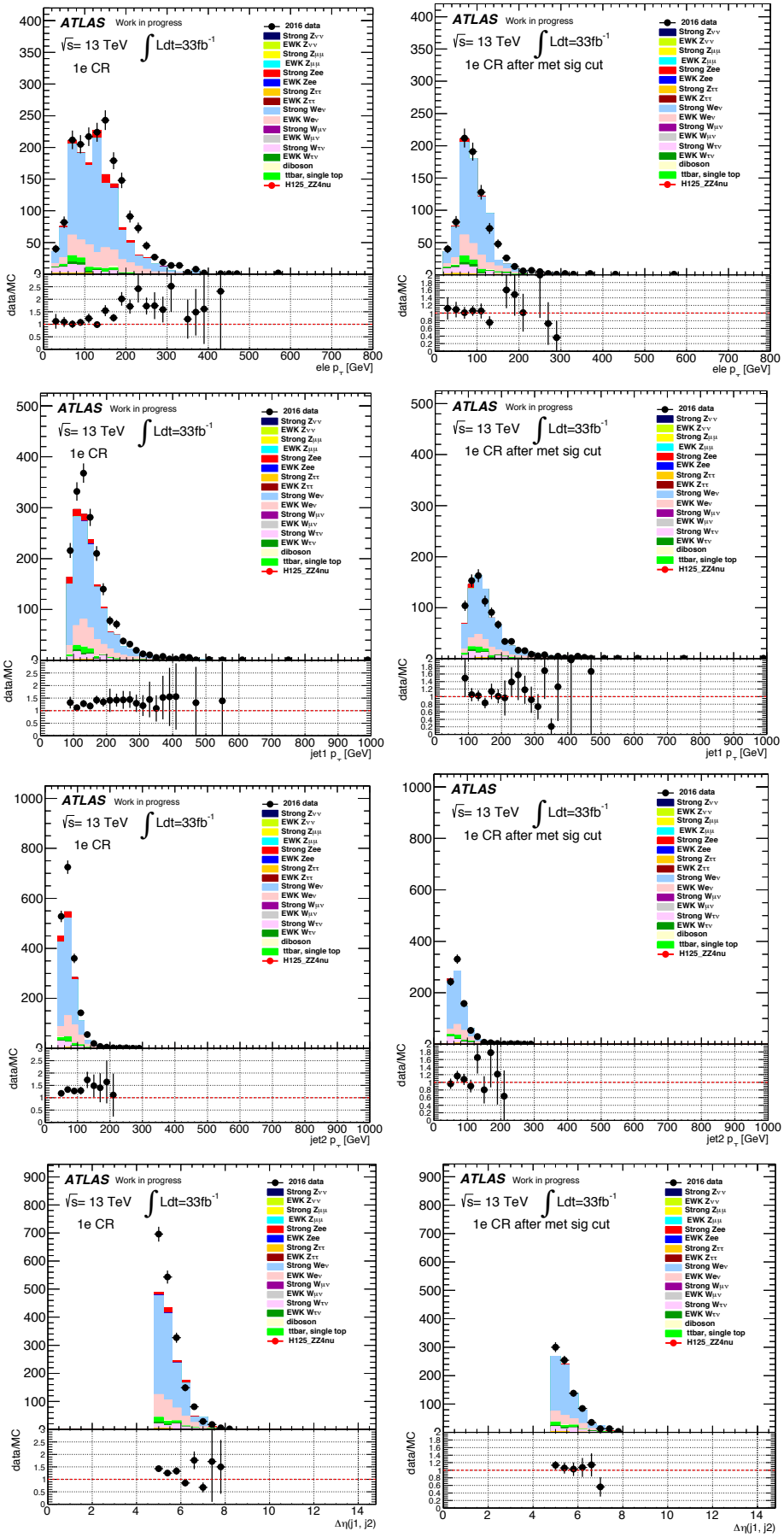

Figure 5.24: data/MC plots for different kinematical distributions in $W \to e\nu$ inclusive CR, Left: before $E_{\mathrm{T}}^{\mathrm{miss}}$ significance cut; Right: after $E_T^{miss} significance$ >4.0 $\mathrm{GeV}^{\frac{1}{2}}$

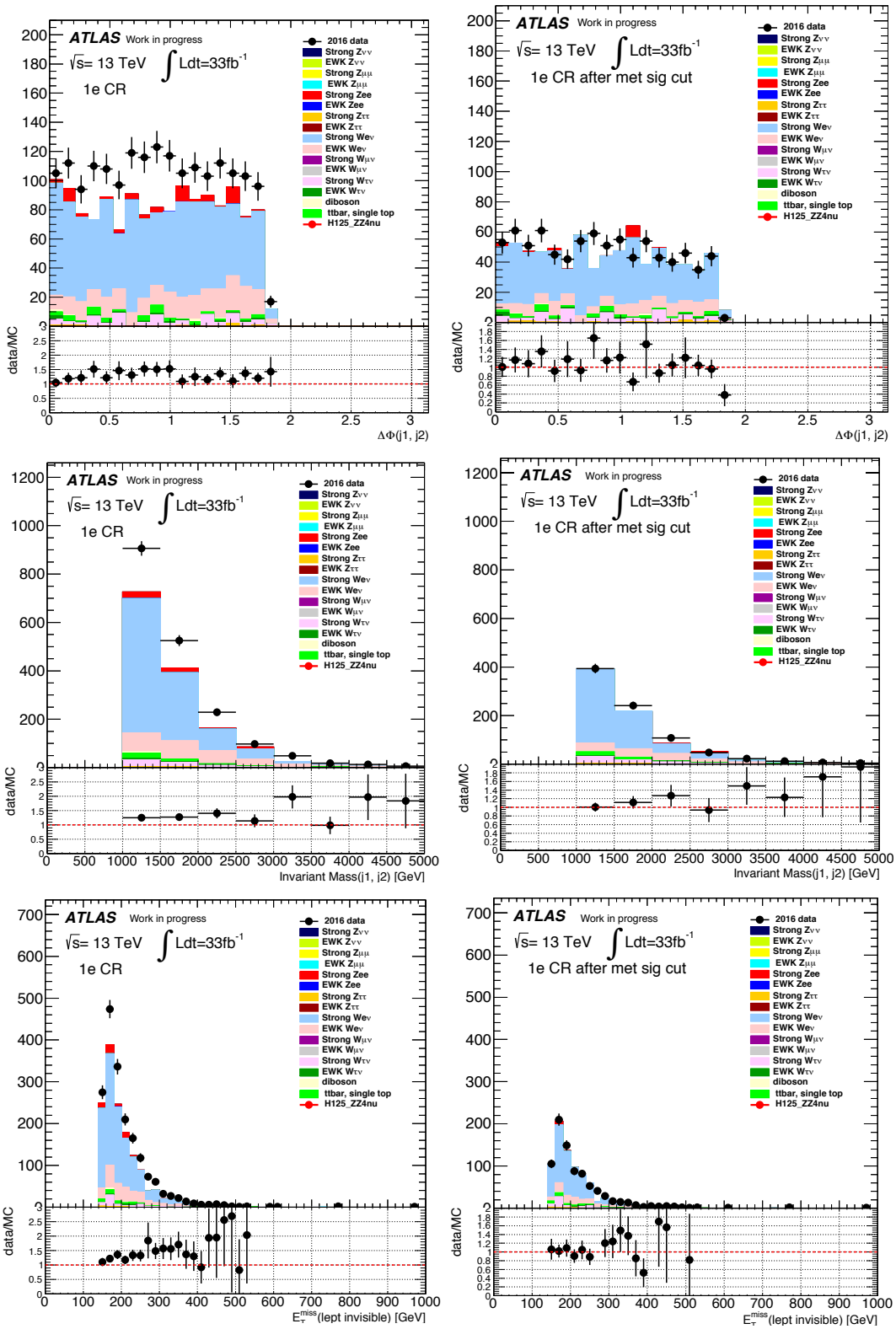

Figure 5.25: data/MC plots for different kinematical distributions in $W \rightarrow e\nu$ inclusive CR, Left: before $E_{\mathrm{T}}^{\mathrm{miss}}$ significance cut; Right: after $E_T^{miss} significance$ >4.0 GeV$^{\frac{1}{2}}$

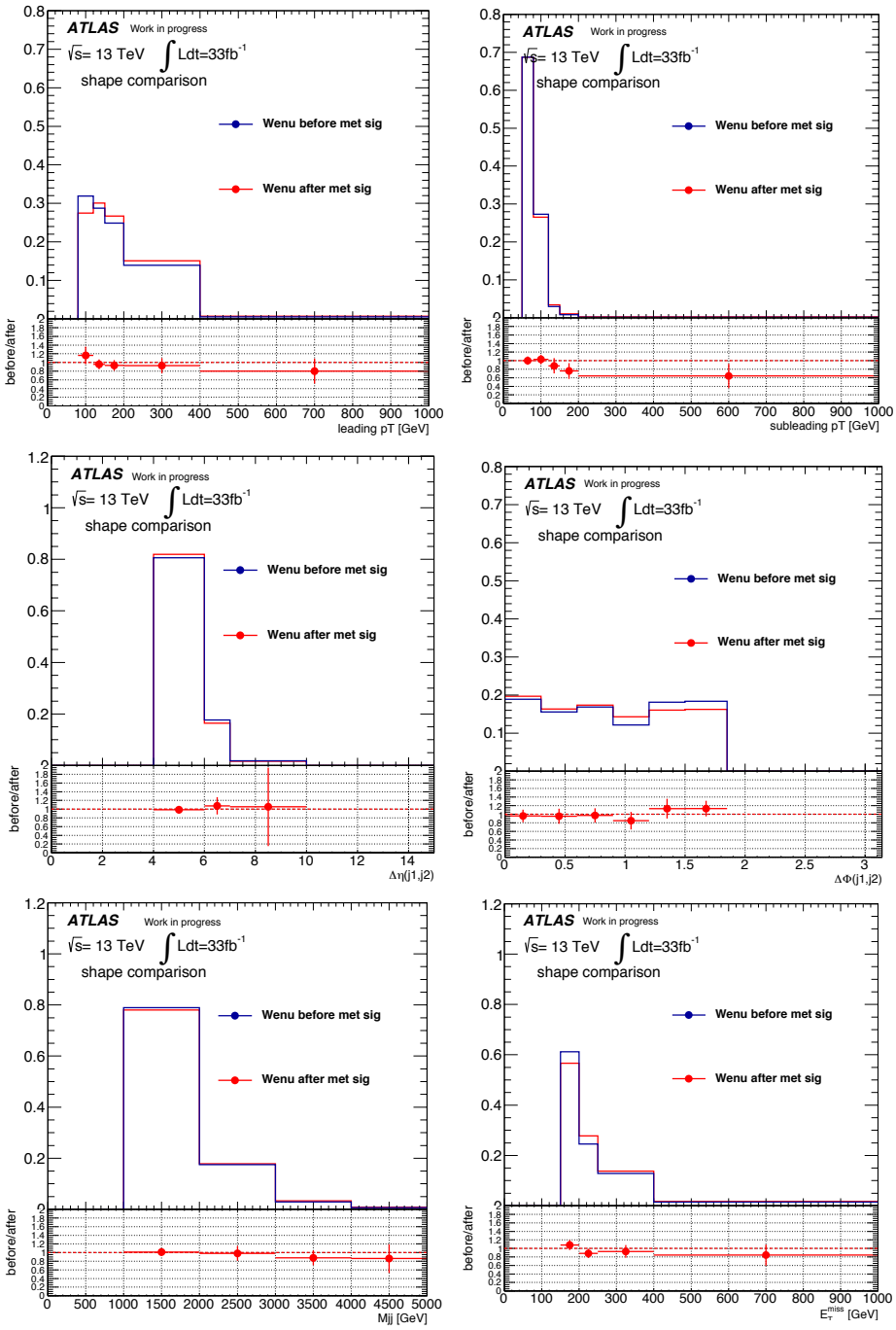

Figure 5.26: Shape comparison for different kinematical variables before and after a $E_{\mathrm{T}}^{\mathrm{miss}}$ *sig.* >4 $\mathrm{GeV}^{\frac{1}{2}}$ in the $W \to e\nu$ CR. From the upper left: $p_T(j1)$, $p_T(j2)$, $\Delta\eta(j1,j2)$,$\Delta\Phi(j1,j2)$, $M(j1,j2)$, $E_{\mathrm{T}}^{\mathrm{miss}}$ (corrected adding the lepton p_T), for background MC simulations.

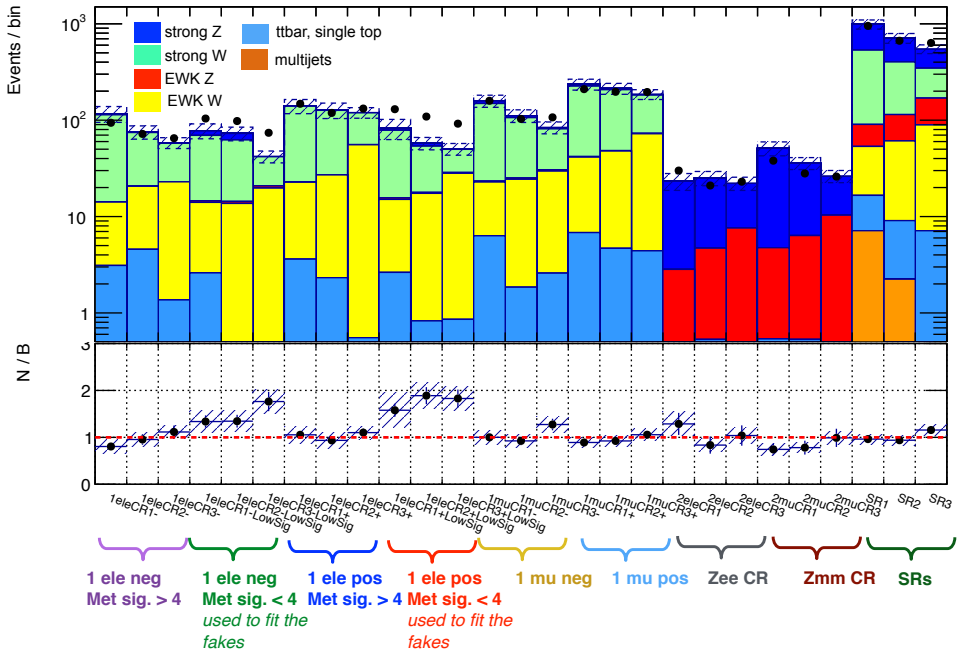

Figure 5.27: Histogram showing data/MC comparison for each bin in the control regions and SR for 36.1 fb^{-1}. CR1, CR2, CR3, SR1, SR2, SR3 correspond to the three M_{jj} bins. The error bars in the ratio plot are the statistical uncertainty (both on the MC statistics and the poisson uncertainty from the number of observed events in data). The systematic uncertainties (both the theoretical systematics on W/Z and the main experimental uncertainties) are represented as a shaded band. The poor data/MC agreement in some $W \to e\nu$ CRs is due to the lack of a pre-fit estimates for electron fakes.

Table 5.9: Summary of yields for $M(j1, j2) > 1$ TeV. The uncertainties listed are only the statistical uncertainty on the MC simulation. All numbers here are pre-fit, except for the misidentified leptons (which have no pre-fit estimate). The multijet yield in SR is estimated with the *Rebalance and Smear* method (Sec. 5.15).

Process :	SR	Z→ ee CR	Z→ $\mu\mu$ CR	W→ $\mu\nu$ CR	W→ $e\nu$ CR
Zvv :	945.2 ± 32.6	0.0 ± 0.0	0.0 ± 0.0	0.0 ± 0.0	0.0 ± 0.0
Zvv EWK :	162.3 ± 8.6	0.0 ± 0.0	0.0 ± 0.0	0.0 ± 0.0	0.0 ± 0.0
Zmumu :	11.3 ± 2.3	0.0 ± 0.0	77.0 ± 14.1	27.1 ± 3.3	0.0 ± 0.0
Zmumu EWK :	0.6 ± 0.3	0.0 ± 0.0	17.9 ± 1.6	3.6 ± 1.1	0.0 ± 0.0
Zee :	0.0 ± 0.0	55.5 ± 6.0	0.0 ± 0.0	0.0 ± 0.0	3.2 ± 1.4
Zee EWK :	0.0 ± 0.0	14.2 ± 0.9	0.0 ± 0.0	0.0 ± 0.0	0.0 ± 0.0
Ztautau :	7.5 ± 1.9	0.0 ± 0.0	0.0 ± 0.0	3.6 ± 1.0	9.4 ± 1.5
Ztautau EWK :	1.4 ± 0.3	0.0 ± 0.0	0.0 ± 0.0	0.9 ± 0.2	1.2 ± 0.3
Wenu :	126.0 ± 18.4	0.0 ± 0.0	0.0 ± 0.0	0.0 ± 0.0	843.4 ± 50.7
Wenu WEK :	31.6 ± 3.4	0.0 ± 0.0	0.0 ± 0.0	0.0 ± 0.0	254.7 ± 9.5
Wmunu :	335.4 ± 37.4	0.0 ± 0.0	0.0 ± 0.0	655.4 ± 36.1	0.0 ± 0.0
Wmunu EWK :	45.7 ± 3.8	0.0 ± 0.0	0.0 ± 0.0	194.5 ± 8.5	0.0 ± 0.0
Wtaunu :	442.4 ± 30.0	0.0 ± 0.0	0.0 ± 0.0	59.7 ± 12.0	74.0 ± 15.5
Wtaunu EWK:	91.9 ± 5.5	0.0 ± 0.0	0.0 ± 0.0	15.1 ± 2.3	35.8 ± 3.0
ttbar, single top:	23.0 ± 3.2	0.7 ± 0.6	1.3 ± 0.6	26.7 ± 3.1	31.1 ± 4.0
multijets (R+S):	9.82 ± 6.35	-	-	-	-
electron fakes (from fit):	-	-	-	-	15.1 ± 3.2
sum all bkg :	2234.12 ± 62.4	70.4 ± 6.0	96.2 ± 14.2	986.6 ± 39.3	1267.9 ± 54.2
signal VBF:	926.9 ± 13.4	0.0 ± 0.0	0.0 ± 0.0	0.0 ± 0.0	0.0 ± 0.0
signal ggF:	136.7 ± 15.3	0.0 ± 0.0	0.0 ± 0.0	0.0 ± 0.0	0.0 ± 0.0
S/sqrt(bkg) :	22.6	0	0	0	0
data :	2252.0	74.0 ± 8.6	92.0 ± 9.6	972.0 ± 31.2	1260.0 ± 35.5

Table 5.10: Full yields table for all the regions and bins. Numbers are prefit.

region :	tot W strong	tot W ewk	tot Z strong	tot Z ewk	ttbar single top	tot bkg	Nevents signal	Nevents data	data/MC
1e- SR1 :	92.0 ± 14.9	11.0 ± 1.9	3.0 ± 1.1	0.0 ± 0.0	3.1 ± 1.2	109.2 ± 15.1	0.0 ± 0.0	94.0	0.9 ± 0.1
1e- SR2 :	51.4 ± 13.3	16.0 ± 2.3	1.0 ± 0.4	0.1 ± 0.1	4.6 ± 1.6	73.1 ± 13.6	0.0 ± 0.0	72.0	1.0 ± 0.2
1e- SR3 :	27.2 ± 6.3	21.5 ± 2.5	0.7 ± 0.4	0.1 ± 0.0	1.4 ± 0.6	50.9 ± 6.9	0.0 ± 0.0	65.0	1.3 ± 0.2
1e+ SR1 :	120.2 ± 21.1	19.1 ± 2.1	0.6 ± 0.5	0.1 ± 0.1	3.6 ± 1.3	143.5 ± 21.3	0.0 ± 0.0	148.0	1.0 ± 0.2
1e+ SR2 :	102.0 ± 16.9	24.7 ± 2.8	0.7 ± 0.3	0.1 ± 0.1	2.3 ± 0.9	129.9 ± 17.1	0.0 ± 0.0	119.0	0.9 ± 0.1
1e+ SR3 :	65.9 ± 15.3	55.0 ± 4.8	0.3 ± 0.5	0.3 ± 0.1	0.6 ± 1.2	122.0 ± 16.1	0.0 ± 0.0	132.0	1.1 ± 0.2
1mu- SR1 :	127.8 ± 16.2	16.5 ± 2.2	9.4 ± 1.9	0.2 ± 0.1	6.3 ± 1.4	160.2 ± 16.5	0.0 ± 0.0	159.0	1.0 ± 0.1
1mu- SR2 :	83.3 ± 12.9	22.5 ± 2.9	4.5 ± 1.1	1.3 ± 0.5	1.9 ± 0.7	113.4 ± 13.3	0.0 ± 0.0	103.0	0.9 ± 0.1
1mu- SR3 :	51.0 ± 8.8	27.0 ± 2.6	1.9 ± 0.9	0.4 ± 0.2	2.6 ± 0.8	82.9 ± 9.2	0.0 ± 0.0	107.0	1.3 ± 0.2
1mu+ SR1 :	182.1 ± 21.9	34.6 ± 4.0	8.1 ± 1.9	0.4 ± 0.2	6.8 ± 1.5	231.9 ± 22.4	0.0 ± 0.0	210.0	0.9 ± 0.1
1mu+ SR2 :	160.8 ± 16.8	43.2 ± 4.1	4.4 ± 1.3	0.2 ± 0.1	4.7 ± 1.6	213.3 ± 17.4	0.0 ± 0.0	197.0	0.9 ± 0.1
1mu+ SR3 :	110.1 ± 13.3	67.8 ± 4.9	2.4 ± 0.8	2.1 ± 1.0	4.4 ± 1.3	186.9 ± 14.3	0.0 ± 0.0	196.0	1.0 ± 0.1
e+e- SR1 :	0.0 ± 0.0	0.0 ± 0.0	20.4 ± 4.1	2.6 ± 0.3	0.2 ± 0.2	23.3 ± 4.2	0.0 ± 0.0	30.0	1.3 ± 0.3
e+e- SR2 :	0.0 ± 0.0	0.0 ± 0.0	20.6 ± 2.9	4.2 ± 0.4	0.5 ± 0.5	25.3 ± 3.0	0.0 ± 0.0	21.0	0.8 ± 0.2
e+e- SR3 :	0.0 ± 0.0	0.0 ± 0.0	14.5 ± 3.1	7.6 ± 0.7	0.0 ± 0.0	22.1 ± 3.2	0.0 ± 0.0	23.0	1.0 ± 0.3
mu+mu- SR1 :	0.0 ± 0.0	0.0 ± 0.0	41.6 ± 13.4	5.0 ± 0.9	0.5 ± 0.4	47.1 ± 13.5	0.0 ± 0.0	38.0	0.8 ± 0.3
mu+mu- SR2 :	0.0 ± 0.0	0.0 ± 0.0	25.3 ± 3.9	5.0 ± 0.8	0.5 ± 0.4	30.8 ± 4.0	0.0 ± 0.0	28.0	0.9 ± 0.2
mu+mu- SR3 :	0.0 ± 0.0	0.0 ± 0.0	10.1 ± 2.0	8.1 ± 1.1	0.3 ± 0.3	18.5 ± 2.3	0.0 ± 0.0	26.0	1.4 ± 0.3
0lep SR1 :	437.9 ± 32.1	36.8 ± 3.4	455.1 ± 24.9	34.2 ± 3.8	9.5 ± 2.0	973.5 ± 41.0	297.0 ± 11.8	952.0	1.0 ± 0.1
0lep SR2 :	279.2 ± 34.8	51.8 ± 4.4	308.4 ± 16.9	48.4 ± 4.4	6.8 ± 1.7	694.8 ± 39.2	308.5 ± 9.8	667.0	1.0 ± 0.1
0lep SR3 :	186.6 ± 20.0	82.1 ± 5.1	200.4 ± 12.9	84.0 ± 6.3	6.7 ± 1.9	559.8 ± 25.2	458.1 ± 13.4	633.0	1.1 ± 0.1

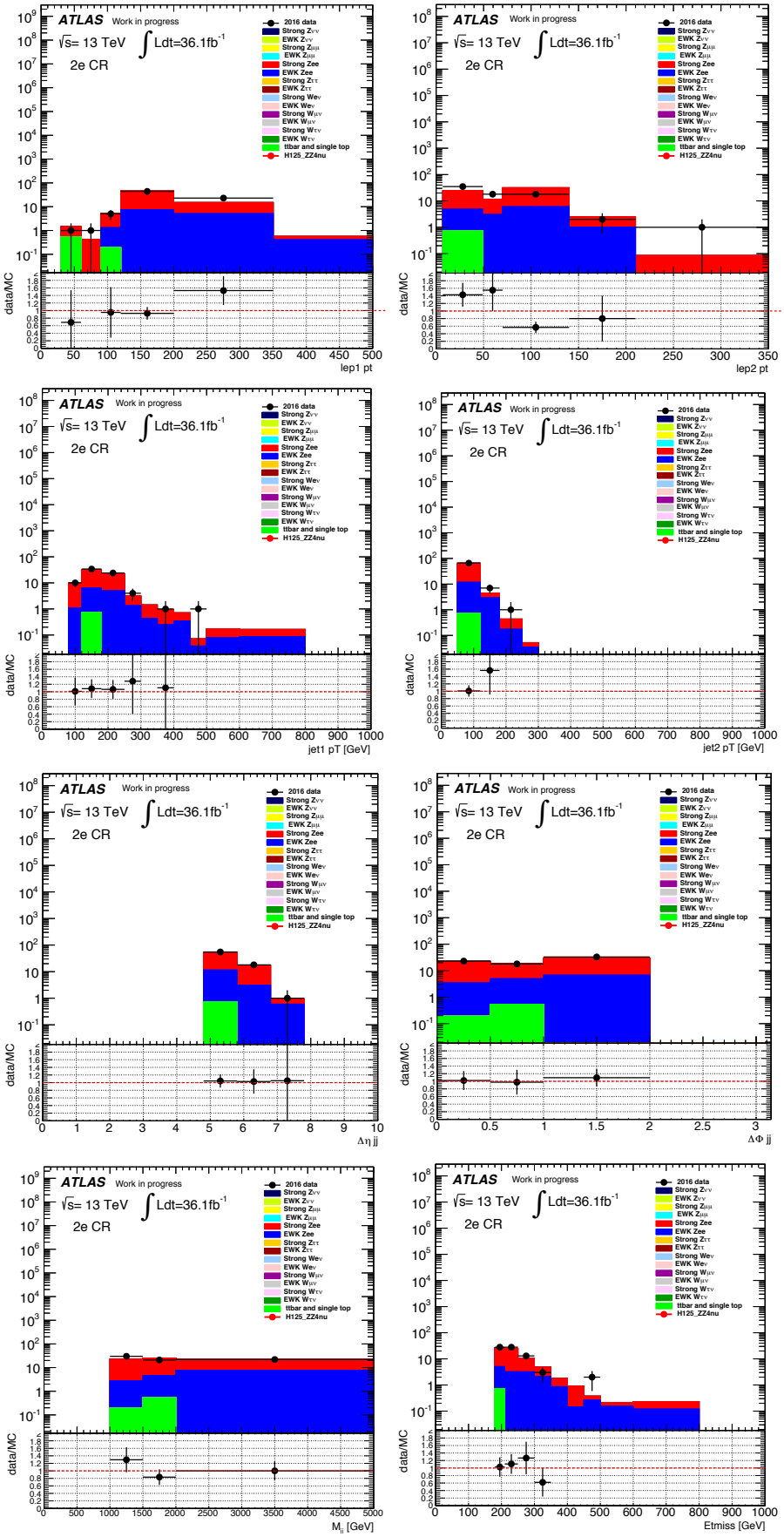

Figure 5.28: Several kinematic distributions for data and simulated events in the $Z \to ee$ CR, after all cuts.

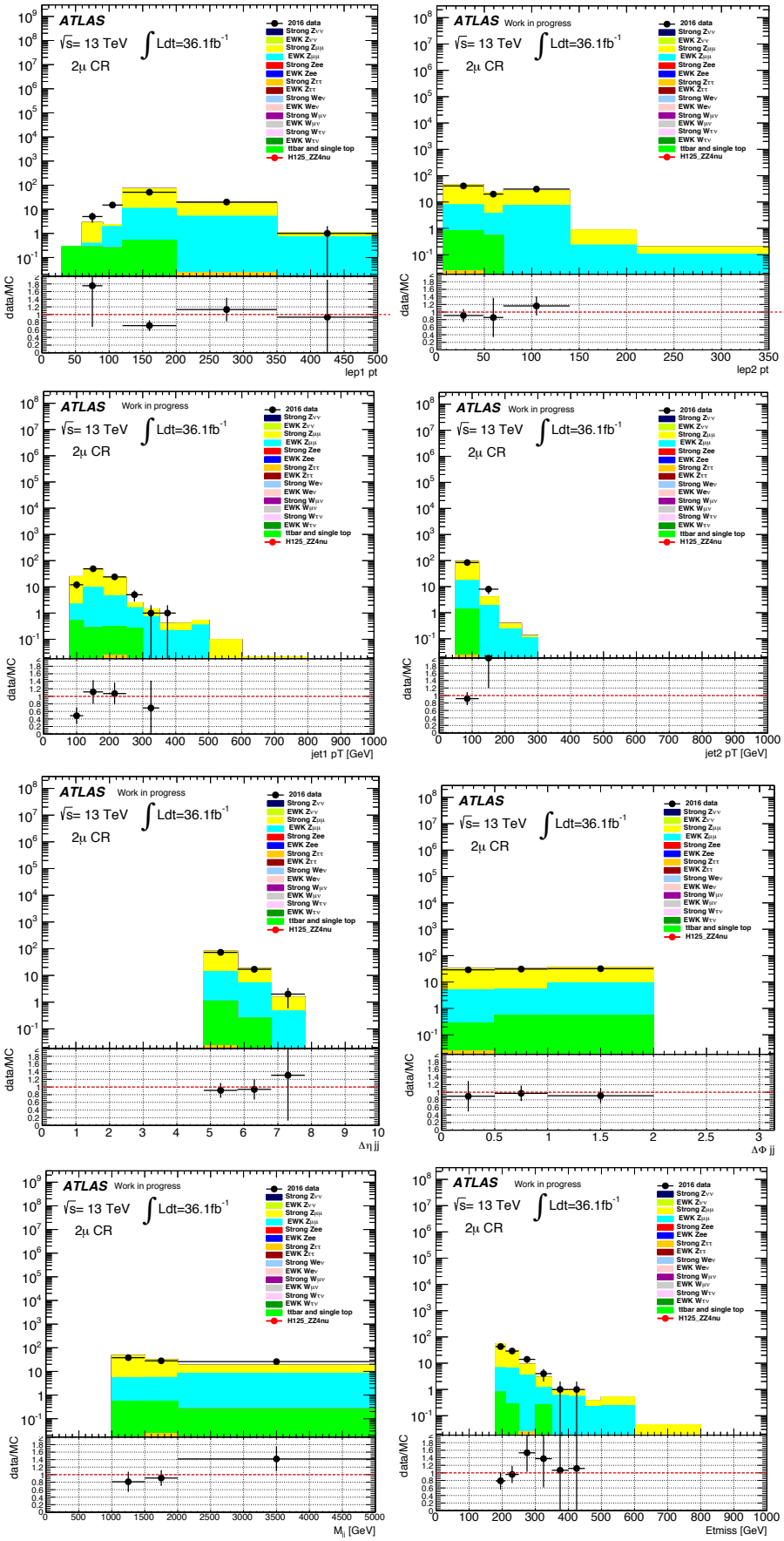

Figure 5.29: Several kinematic distributions for data and simulated events in the $Z \to \mu\mu$ CR.

5.15 Multijet background in SR

Multijet events can contaminate the SR for different reasons: jet mis-measurements causing fake $E_{\mathrm{T}}^{\mathrm{miss}}$, partial loss of a jet causing large $E_{\mathrm{T}}^{\mathrm{miss}}$, jets which are wrongly identified as pileup jets by the JVT criteria and thus they create fake $E_{\mathrm{T}}^{\mathrm{miss}}$[14] (as discussed in Sec. 5.8.4). Multijet events in SR are expected to be strongly reduced by the tight cuts on $E_{\mathrm{T}}^{\mathrm{miss}}$ and on VBF jets. Cuts which are particularly efficient in reducing this background are: tight $E_{\mathrm{T}}^{\mathrm{miss}}$ cut, large angular separation between the jets and the $E_{\mathrm{T}}^{\mathrm{miss}}$, small azimuthal separation between the two leading jets, high M_{jj} mass. Distributions of these variables for multijets events compared to signal events are shown in Fig. 5.33. However, because of the large cross section, a residual contribution can pass the SR selection and needs to be estimated carefully.

The constribution from multijet events is usually estimated via data-driven techniques which are more reliable than simulations. As mentioned in 5.3.2, the available QCD MC samples lack of statistics in the VBF phase space thus not even allowing for a direct cross check in SR. There are two main classes of methods to estimate QCD multijet background. The first one is usually referred to as *ABCD*-like methods. It uses multijet enriched CR which are built as sidebands of the SR, along two variables, and it extrapolates the background contamination in SR from the three sideband CRs. The idea of this method is illustrated in Fig. 5.34. Two variables are chosen such that region D corresponds to the SR where the background needs to be estimated and the other three regions A,B,C are enriched in multijets. For instance $E_{\mathrm{T}}^{\mathrm{miss}}$ and angular separation between the $E_{\mathrm{T}}^{\mathrm{miss}}$ and the jets $\Delta\Phi(jet, E_T^{miss})$, or the angular separation between the two leading jets $\Delta\Phi(j_1, j_2)$ can be used as such variables. The multijet background in SR is then estimated as $N_{QCD}^{SR} \sim N^C \frac{N^B}{N^A}$. One of the challenges of this method is the understanding of the correlation of the variables such as $E_{\mathrm{T}}^{\mathrm{miss}}$ and $\Delta\Phi$. To overcome these problems, new methods have been developed. The underlying idea of this class of methods is to try to predict the QCD background by emulating the detector response of each jet of a multi-jet seed sample multiple times to predict the full event kinematics of a QCD multijet sample.

The method used here belongs to this second class. It is called Rebalance and Smear (R+S) technique and uses a similar approach to the Smearing method widely used within ATLAS and explained in reference [129].

The R+S method starts by selecting events with single jet triggers. An unbiased sample of events with a negligible non QCD contributions is produced by rebalancing the zero lepton inclusive jet sample[15].

Rebalancing means that the momenta of jets above a certain p_T threshold (20 GeV) are adjusted within their experimental uncertainties by a kinematic fit to achieve a perfect transverse momentum balance. In order to account for the soft component of the $E_{\mathrm{T}}^{\mathrm{miss}}$, the jets are rebalanced not to zero transverse momentum but to $E_{\mathrm{T}}^{\mathrm{miss,soft}}$, which is computed here as the difference between the negative vectorial sum of all the jets with p_T >20 GeV (approximation of $E_{\mathrm{T}}^{\mathrm{miss}}$ without considering the soft term) and the recon-

[14] Consider the case where the two VBF jets are both outside the tracker. In this case the vertex with the highest $\sum_{trk} p_T^{trk}$ can be a secondary vertex and not the hard scatter one. Any additional jet associated to the true hard scatter vertex is not JVT tagged (i.e. is considered as pile up). These jets are neither in the TST $E_{\mathrm{T}}^{\mathrm{miss}}$ soft term (which uses only tracks associated to the PV), nor in the $E_{\mathrm{T}}^{\mathrm{miss}}$ TST jet term, nor vetoed by the third jet veto. It creates fake $E_{\mathrm{T}}^{\mathrm{miss}}$.

[15] This is the main difference with respect to the pure Smearing method, which selects a highly enriched QCD sample by selecting events with zero leptons and very low values of MET significance.

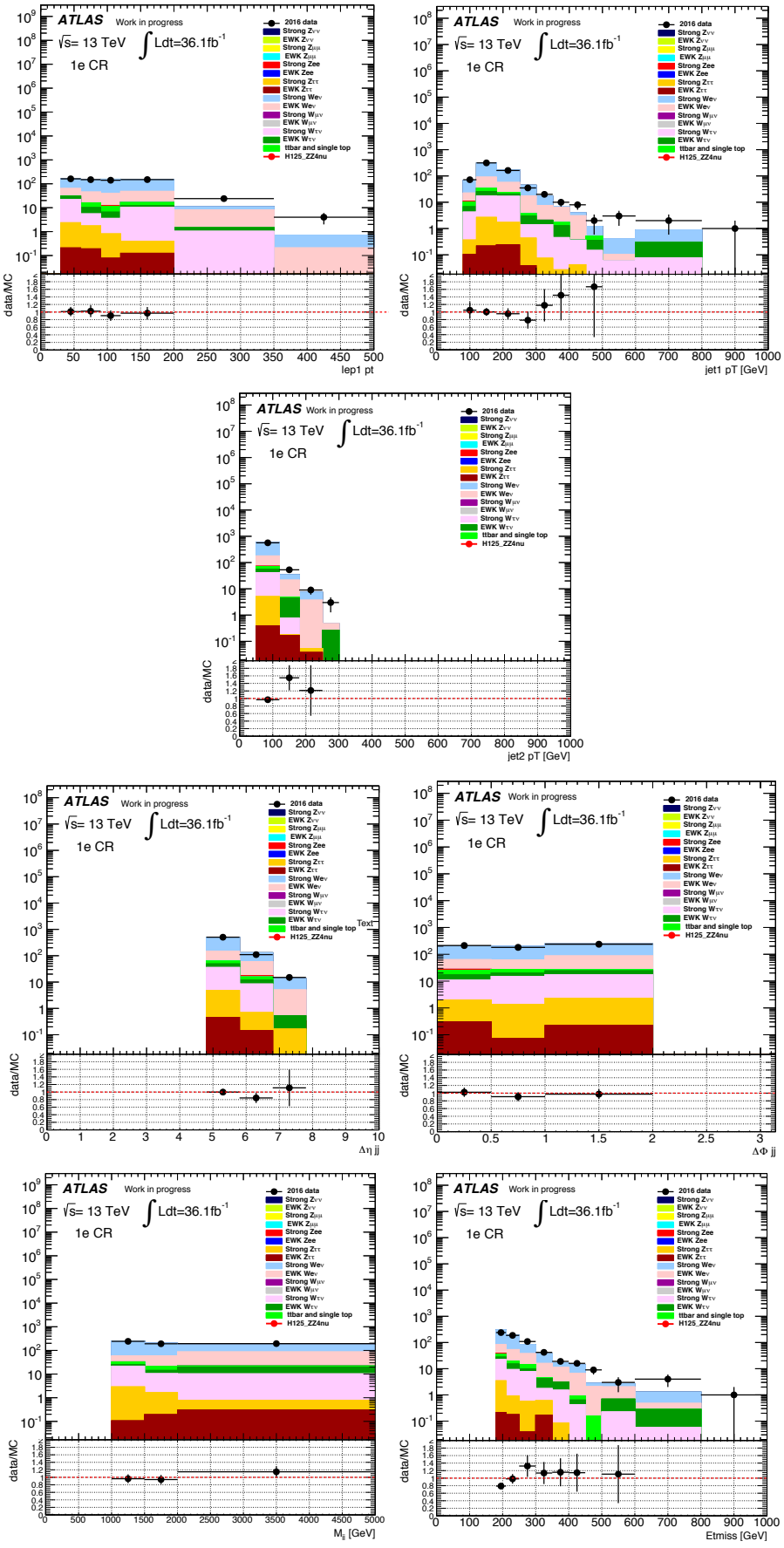

Figure 5.30: Several kinematic distributions for data and simulated events in the $W \to e\nu$ CR, after all cuts.

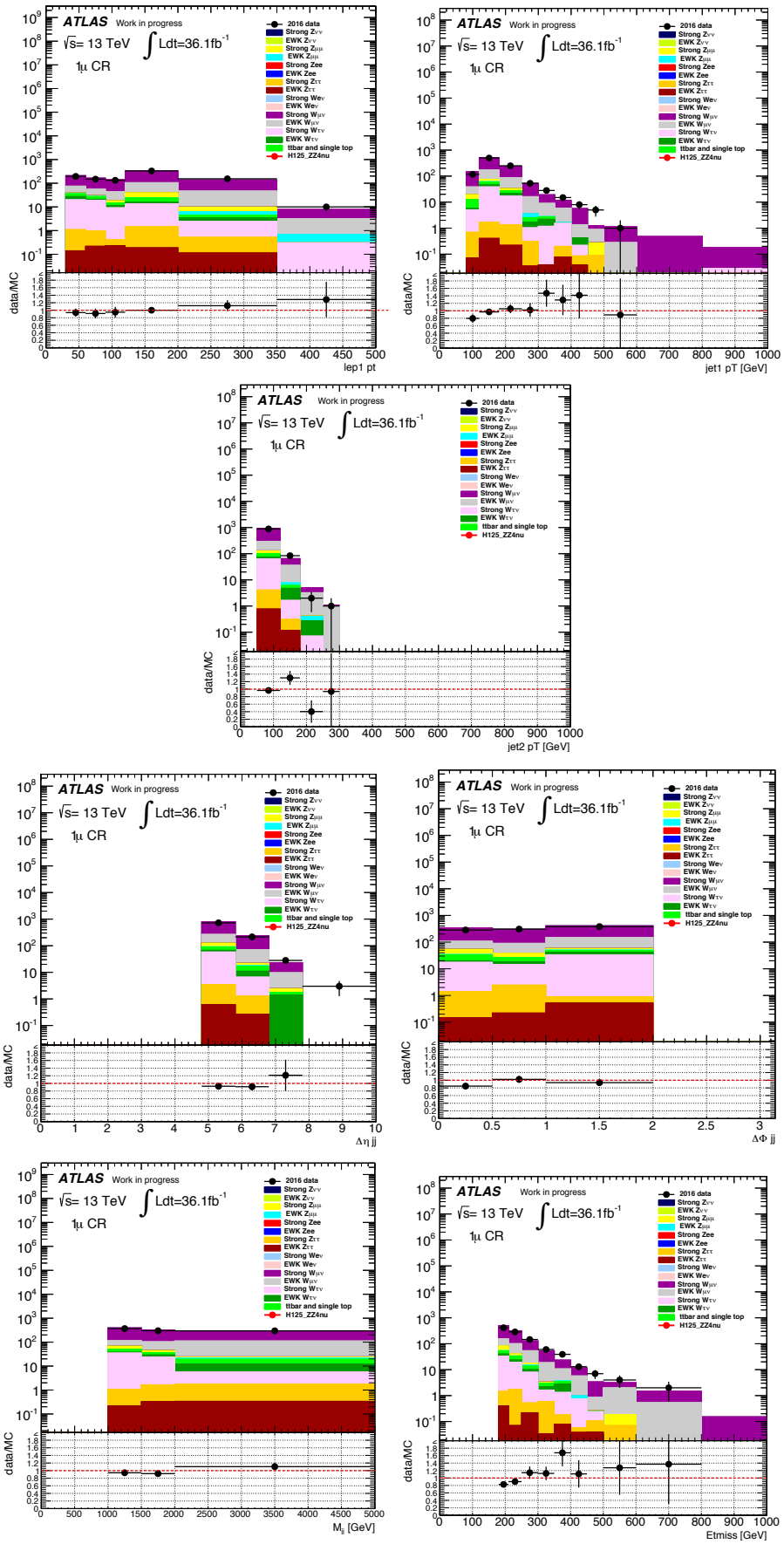

Figure 5.31: Several kinematic distributions for data and simulated events in the $W \to mu\nu$ CR, after all cuts.

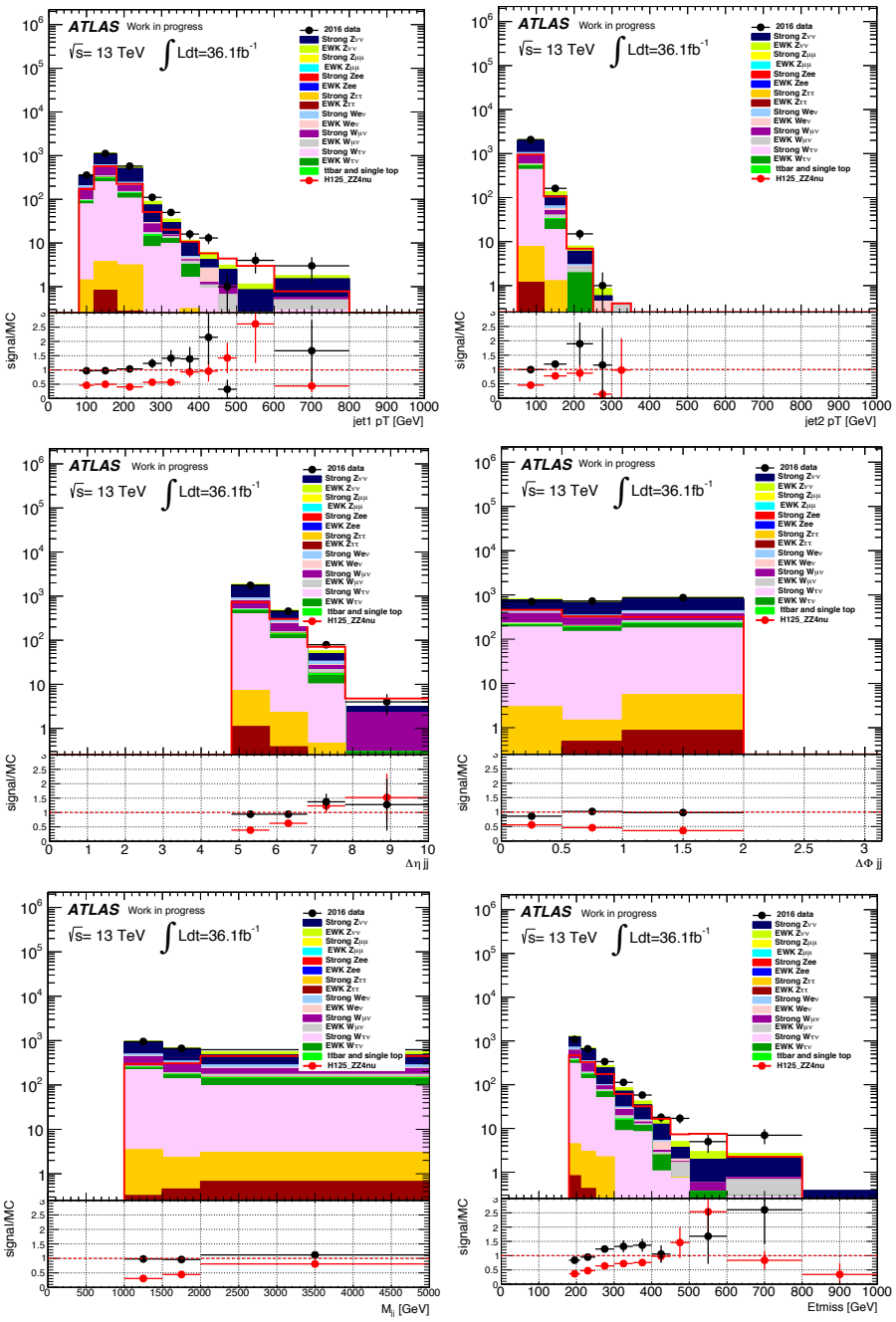

Figure 5.32: Several kinematic distributions for simulated events in the signal region, after all cuts. The bottom plots show the ratio of signal (VBF and ggF) over MC prediction.

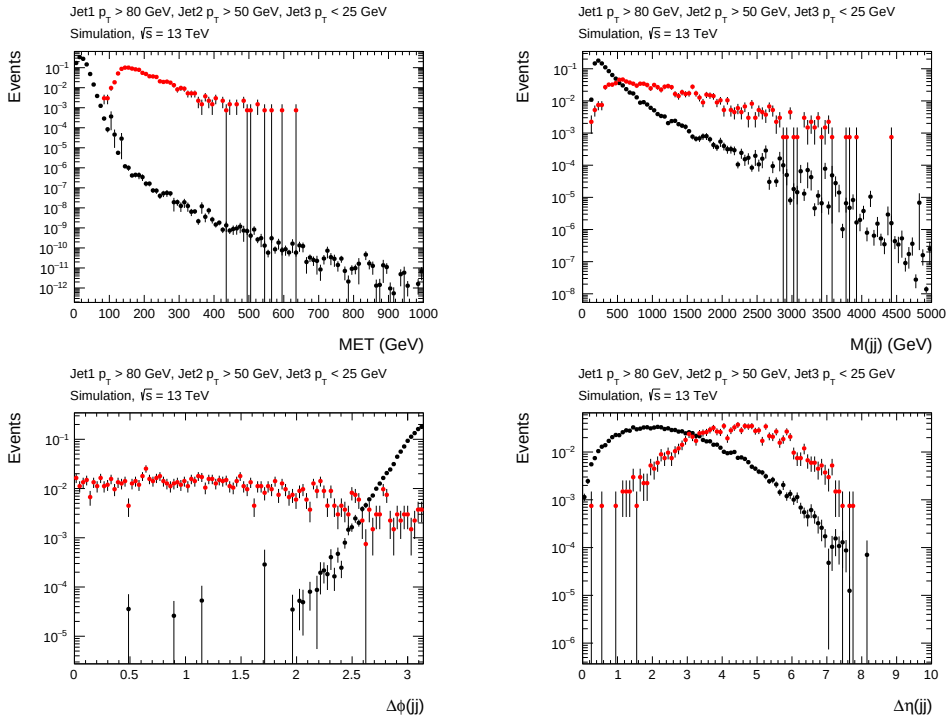

Figure 5.33: Several distributions of variables for simulated multijet events (black) in comparison to $H(125) \rightarrow$ inv signal events (red). The applied selection requires only two jets with $p_T > 25$ GeV, with the two leading jets passing p_T cuts of 80 GeV and 50 GeV respectively. [130]

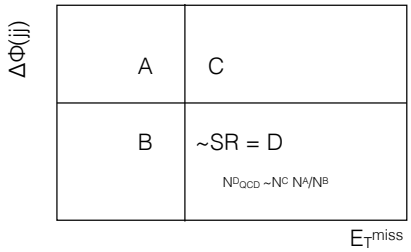

Figure 5.34: Illustration of ABCD like methods for multijet estimation.

structed $E_{\mathrm{T}}^{\mathrm{miss}}$. At this step all the jets are used including pile up jets, regardless the JVT requirements. To reject effectively non-QCD contributions of the seed sample with large real $E_{\mathrm{T}}^{\mathrm{miss}}$, a cut on the $E_{\mathrm{T}}^{\mathrm{miss}}$ significance is applied ($E_{\mathrm{T}}^{\mathrm{miss}}$ $sig.$ $<4\mathrm{GeV}^{\frac{1}{2}}$). This sample constitutes the seed sample. These events are smeared multiple times with jet energy response templates which model the response of the calorimeters and are obtained from simulations. The jet response function quantifies the probability of fluctuation of the measured pT of jets. The method is tested in QCD enriched control region which is defined by loosening the $\Delta\Phi(j_1, j_2)$, allowing a soft third jet, and further loosening the cuts on $\Delta\eta(j_1, j_2)$, $E_{\mathrm{T}}^{\mathrm{miss}}$, $M(j_1, j_2)$. A good consistency is observed as shown in Fig. 5.35.

The final estimate of multijet background in SR is given in Table 5.11.

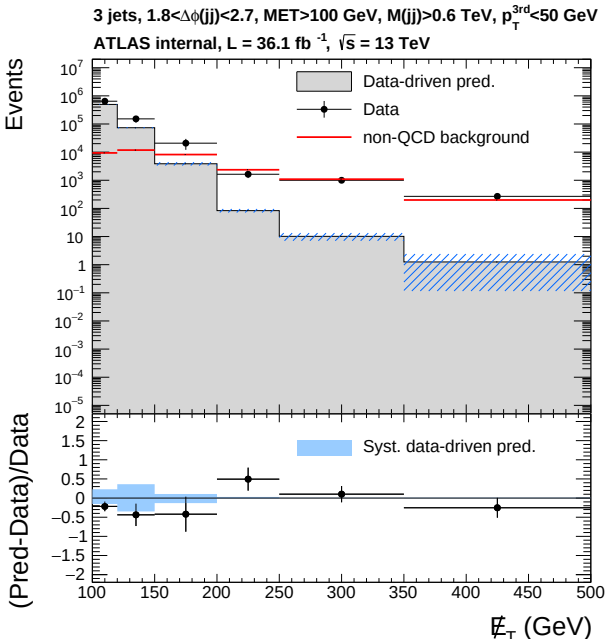

Figure 5.35: The $E_{\mathrm{T}}^{\mathrm{miss}}$ distribution including the background contributions other than QCD are shown. The selection includes a $\Delta\phi$ side band $1.8 < \Delta\phi < 2.7$, $\Delta\eta > 3.0$, $E_{\mathrm{T}}^{\mathrm{miss}} > 100$ GeV, and $M_{jj} > 600$ GeV, and further allows a third jet with $25 < p_T < 50$ GeV but no fourth jet with $p_T > 25$ GeV. The top plot shows the individual contributions (rather than a stacked plot), while the ratio includes the sum of the QCD and non-QCD components. The blue band in the lower panel reflects the systematic uncertainty of the R+S prediction on the overall ratio. At high MET this uncertainty is negligible because of the small size of the multijet background in this kinematic region. [130]

Table 5.11: The prediction for the multijet background in the signal region is shown inclusively and for each M_{jj} bin separately. [130]

Bin	Prediction
SR (inclusive)	12.5 ± 10.4
SR1	6.1 ± 5.3
SR2	4.7 ± 8.6
SR3	1.8 ± 2.5

5.16 Fake leptons estimation in $W \to e\nu$ CRs

As mentioned in Sec. 5.13.3, multijet events pass the $W \to e\nu$ CRs selection in case a jet is misidentified as a lepton (referred to as *misidentified* lepton or *fake* lepton background). This background is reduced with a $MET_{sig.}$ cut (Sec. 5.13.3) but its remaining contribution needs to be quantified carefully. The method explained below is used to obtain an explicit measurement and uncertainty for it. The idea of the method is to measure the fake lepton contamination in $W \to e\nu$ CRs directly in the fit by exploiting the W charge asymmetry [16] and using both *low* and *high* $MET_{sig.}$ $W \to e\nu$ regions.

The fraction of fake lepton events in *low-*$MET_{sig.}$ (fake enriched) and *high-*$MET_{sig.}$ is defined as:

$$R_{bin_i} = \frac{\text{N fake events with MET}_{\text{sig.}} < 4\sqrt{\text{GeV}}}{\text{N fake events with MET}_{\text{sig.}} > 4\sqrt{\text{GeV}}} \tag{5.7}$$

For each $M(j_1, j_2)$ bin, the ratio R_{bin_i} provides an estimate of how many times the *low-*$MET_{sig.}$ CR is more rich in fakes than the *high-*$MET_{sig.}$. These ratios are used as input to the fit as summarized in table 5.17: the fit uses them as a constraint. More details are given in Sec. 5.18.
R_{bin_i} is measured using the method outlined below.
In order to compute these ratios (eq. 5.7), for each $M(j_1, j_2)$ bin, control samples enriched in fake lepton events are constructed: a $W \to e\nu$ CR selection is used for electrons where the identification quality criteria is inverted, making this region completely dominated by fakes (∼90% rich in fakes). Real reconstructed electrons from simulations are subtracted to data in order to have a control sample pure in fakes. In these *fake-enriched* regions, templates of $MET_{sig.}$ distributions are built. These are the shape of met significance variable of fakes. Two bins are considered: $E_{\text{T}}^{\text{miss}}$ $sig. > (<)4$ GeV$^{\frac{1}{2}}$. From these two bins the ratios R_{bin_i} (for each $M(j_1, j_2)$ bin) are computed as shown in eq. 5.7 and used as inputs in the fit. For each bin the measured ratios are:

- R_{bin1} =9.0 ±0.4;
- R_{bin2} =9.7 ±0.6;
- R_{bin2} =5.0 ±0.4.

5.17 Systematic uncertainties

The systematic uncertainties can be grouped in:

- Experimental systematics;
- Theoretical systematics:
  - on backgrounds;
  - on signals.

In the following the main systematics affecting the analysis are introduced.

[16] $W \to l\nu$ events are asymmetric with respect to the W charge (more W^+ than W^-, due to the pp initial charge), multijets events (dominated by gluon-gluon and $q\bar{q}$ interactions from sea quarks and antiquarks) are expected to be symmetric.

5.17.1 Experimental systematics

Experimental systematics are related to the energy/momentum scale, reconstruction efficiency, identification for each reconstructed object, trigger efficiency, pile up modeling. Experimental systematics are generally provided by the ATLAS physics and Combined Performance (CP) groups. For each source of uncertainty, the expected yields are recomputed by varying each quantity by 1σ of its value and are introduced in the fit via nuisance parameters (Sec. 5.18.1).
The main experimental systematics are presented below. Each experimental uncertainty is treated as fully correlated between all the background [17] and signal samples, between all the $M(j_1, j_2)$ bins and regions.
A global 2.1% uncertainty on the luminosity has been used.

Jets systematics

The impact of the uncertainties related to jets is accounted for by varying each uncertainty according to the recommendations provided by the *Jet group*. Jet systematics may be grouped in Jet Energy Scale (JES) systematics and Jet Energy Resolution (JER) systematics. In addition to these two, a systematic associated to the Jet vertex tagger accounts for the uncertainty on the efficiency of the JVT.

Jet Energy Scale (JES) The full set of nuisance parameters (NP) (Sec. 5.18.1) contains 84 baseline nuisance parameters which come from in-situ analyses such as Z+jet balance, gamma+jet balance, and multi-jet balance (75 NP), 3 NP for eta intercalibration (modeling, statistics/method and calibration non-closure), 1 nuisance parameter from the behaviour of high-pT jets, 4 nuisance parameters from pile-up, 1 nuisance parameter for non-closure of fast simulation calibration. The *Jet group* also provides reduced sets of uncertainties. Here a category reduced set has been used, which includes 29 NP. In this configuration the 75 in situ parameters are combined together based on their source (statistical, modelling, detector, mixed) [127].

Jet Energy Resolution (JER) A single NP is used in the analysis to model the uncertainty related to the jet energy resolution.

Electron and muon systematics

Several different systematics account for:

- muon and electron trigger efficiency;
- electron and muon identification efficiency;
- uncertainty on the muon and electron/photon momentum scale;
- uncertainty on the electron/photon energy resolution;
- uncertainty on the electron reconstruction, identification and isolation efficiency scale factors;
- muon identification scale factors;

[17] Apart from multijets and fake leptons which have their uncertainties.

- various systematics modelling the uncertainties related to the muon track-to vertex association, variations in the scale of the muon momentum based on corrections using different methods etc...

$E_{\mathrm{T}}^{\mathrm{miss}}$ systematics

Since the $E_{\mathrm{T}}^{\mathrm{miss}}$ of an event is calculated as the sum of different terms (see chapter 4), the uncertainties for the various objects used in the analysis need to be propagated to the $E_{\mathrm{T}}^{\mathrm{miss}}$: the uncertainties provided for electrons, muons and jets are propagated into their respective $E_{\mathrm{T}}^{\mathrm{miss}}$ terms while the systematic uncertainties for the $E_{\mathrm{T}}^{\mathrm{miss}}$ track soft term[18] are derived separately.
The $E_{\mathrm{T}}^{\mathrm{miss}}$ track soft term uncertainties account for the response ($E_{\mathrm{T}}^{\mathrm{miss}}$ *scale*) and for the $E_{\mathrm{T}}^{\mathrm{miss}}$ resolution arising from the soft term. These uncertainties are evaluated from data-to-MC comparisons of distributions of observables which are sensitive to the balance between the soft term and the hard activity. These observables are the parallel and perpendicular projections of the soft term transverse momentum (p_T^{soft}) onto the transverse momentum of the hadronic recoil system (p_T^{hard}). See Sec. 4.7.2 for details about how the $E_{\mathrm{T}}^{\mathrm{miss}}$ systematics are estimated.
In total there are 3 nuisance parameters used in the fit which model the $E_{\mathrm{T}}^{\mathrm{miss}}$ uncertainties.

Pile up systematics

A nuisance parameter which accounts for the uncertainty on the ratio between the predicted and measured inelastic cross-section in the fiducial volume is introduced.

5.17.2 Theoretical uncertainties

In addition to detector systematics, there are uncertainties originating from the finite precision of the MC simulation. These affect the MC predictions of yields for both signal and background processes. These uncertainties arise from fixed scale choices in the event generation, as well as our description of the initial-state PDF and parton shower.

Theoretical uncertainties on W/Z backgrounds

For the W/Z background MC there are 4 mass or energy scales which are fixed during event generation: the renormalization, factorization, resummation and CKKW matching scales. To estimate the associated uncertainties, simulated events are generated with each of these scales varied up or down by a factor of 2[19]. While for the factorization and renormalization scale, on-the-fly varied event weights are available in the reconstructed Sherpa MC samples[20], for the resummation and CKKW matching scales separate varied MC samples need to be generated. Due to computing resource limitations, these varied samples cannot be reconstructed: the effect of the variation is computed at truth level and is then applied to the reconstructed samples. The results of the variations for the

[18] See Sec. 4.2 and 4.2.1 for the definition of the $E_{\mathrm{T}}^{\mathrm{miss}}$ soft term and for the $E_{\mathrm{T}}^{\mathrm{miss}}$ track soft term.
[19] The CKKW matching scale is an exception; its nominal value is 20 GeV and is varied to 15 and 30 GeV.
[20] The corresponding uncertainties (for factorization and renormalization scales) are calculated by taking an envelope of the 7-point factorization/renormalization scale variations (the central value, each scale independently varied up/down, and both scales coherently varied up/down).

factorization, renormalization, resummation, and CKKW scales are given in Table 5.12, Table 5.13, Table 5.14, and Table 5.15. These uncertainties are large (up to ∼20-30%) and are mostly limited by MC statistics. For the effect of PDF uncertainties on the W/Z background, we evaluate the background yield predictions with a full ensemble of 100 PDFs within the NNPDF set. The standard deviation of this set of yields is taken to be the corresponding PDF uncertainty. These uncertainties are evaluated separately in each signal and control region. Since the full ensemble of PDF weights is stored for each event in the main MC samples, this procedure can be carried out directly on fully reconstructed simulation. The results are shown in Table 5.16.
Each of the four mentioned theoretical systematics is treated as:

- not correlated among W and Z processes;
- not correlated between strong and electroweak processes;
- fully correlated among all the Z electroweak (strong) processes;
- fully correlated among all the W electroweak (strong) processes;
- not correlated among the three M_{jj} bins;
- fully correlated between all the regions for a fixed M_{jj} bin.

For instance, considering the pdf uncertainties, for each M_{jj} bin (bin_X) the following nuisance parameters are introduced in the fit: pdf_QCD-Z_binX, pdf_EWK-Z_binX, pdf_QCD-W_binX, pdf_EWK-W_binX for a total of 12 NP for each source of theoretical uncertainties.

Table 5.12: Relative changes of the event yields upon applying the "up" variation for the factorization/renormalization scale envelope. [130]

Selection	Process	1 TeV $< M_{jj} <$ 1.5 TeV	1.5 TeV $< M_{jj} <$ 2 TeV	$M_{jj} >$ 2 TeV
0-lepton (MET)	Strong Z	34.46%	32.72%	36.67%
	Strong W	25.06%	34.40%	39.85%
	EWK Z	16.36%	15.45%	20.64%
	EWK W	7.86%	13.12%	15.73%
1-lepton ($W\to\ell\nu$)	Strong W	25.51%	15.24%	53.89%
	EWK W	14.69%	8.93%	13.98%
2-lepton ($Z\to\ell\ell$)	Strong Z	51.31%	26.78%	13.17%
	EWK Z	17.23%	15.53%	18.10%

Table 5.13: Relative changes of the event yields upon applying the "down" variation for the factorization/renormalization scale envelope. [130]

Selection	Process	1 TeV $< M_{jj} <$ 1.5 TeV	1.5 TeV $< M_{jj} <$ 2 TeV	$M_{jj} >$ 2 TeV
0-lepton (MET)	Strong Z	-13.53%	-18.26%	-16.00%
	Strong W	-16.81%	-11.24%	-13.79%
	EWK Z	- 7.04%	-11.17%	-12.73%
	EWK W	-25.81%	- 9.76%	-16.13%
1-lepton ($W\to\ell\nu$)	Strong W	-15.02%	- 9.59%	-15.06%
	EWK W	- 8.41%	-15.73%	-25.11%
2-lepton ($Z\to\ell\ell$)	Strong Z	-15.38%	-17.92%	-26.19%
	EWK Z	- 6.52%	-10.56%	-15.34%

Table 5.14: Relative changes of the event yields upon varying the resummation scale by a factor of 2. These are symmetrized; only the "down" variation is shown. [130]

Selection	Process	1 TeV $< M_{jj} <$ 1.5 TeV	1.5 TeV $< M_{jj} <$ 2 TeV	$M_{jj} >$ 2 TeV
0-lepton (MET)	Strong Z	-10.15 ± 5.43 %	- 1.15 ± 6.08 %	- 3.93 ± 6.77 %
	Strong W	0.19 ± 9.14 %	9.03 ± 12.98 %	2.32 ± 11.08 %
	EWK Z	9.80 ± 3.04 %	7.67 ± 3.01 %	8.74 ± 2.69 %
	EWK W	14.77 ± 3.08 %	12.81 ± 2.99 %	12.27 ± 2.55 %
1-lepton ($W\to\ell\nu$)	Strong W	9.54 ± 3.99 %	- 3.52 ± 4.33 %	- 5.67 ± 5.47 %
	EWK W	17.75 ± 3.45 %	14.56 ± 3.34 %	10.27 ± 2.81 %
2-lepton ($Z\to\ell\ell$)	Strong Z	- 3.76 ± 7.63 %	21.85 ± 11.03 %	- 0.55 ± 16.02 %
	EWK Z	4.1 ± 8.3 %	20.1 ± 9.9 %	1.8 ± 7.0 %

Table 5.15: Relative changes of the event yields upon varying the CKKW merging scale between 15 GeV and 30 GeV. These are symmetrized; only the "up" variation is shown. [130]

Selection	Process	1 TeV $< M_{jj} <$ 1.5 TeV	1.5 TeV $< M_{jj} <$ 2 TeV	$M_{jj} >$ 2 TeV
0-lepton (MET)	Strong Z	- 6.01 ± 5.20 %	19.90 ± 14.89 %	- 0.24 ± 6.78 %
	Strong W	11.71 ± 7.11 %	- 7.34 ± 9.88 %	21.40 ± 10.44 %
	EWK Z	5.65 ± 3.18 %	1.21 ± 3.11 %	3.01 ± 2.70 %
	EWK W	8.54 ± 3.11 %	- 0.36 ± 3.19 %	- 0.34 ± 2.66 %
1-lepton ($W\to\ell\nu$)	Strong W	3.22 ± 3.47 %	5.27 ± 3.90 %	6.12 ± 5.35 %
	EWK W	11.43 ± 3.48 %	- 1.62 ± 3.58 %	- 1.13 ± 2.95 %
2-lepton ($Z\to\ell\ell$)	Strong Z	- 7.11 ± 10.54 %	11.82 ± 11.13 %	23.87 ± 11.06 %
	EWK Z	11.9 ± 9.1 %	- 8.5 ± 8.5 %	6.1 ± 7.9 %

Theoretical systematics on signals

For the $H \to inv$ signals, the following uncertainties have been considered:

- $VBF\ H \to inv$:
  - PDF Uncertainties (0.64%, 1.02%, 1.53% for each M_{jj} bin respectively);
  - QCD Scale Uncertainty (6%): VBF Higgs events are generated in MCFM [131], the factorization and renormalization scales are varied independently for seven scale settings and the SR selection is applied to the simulated events. The acceptance is studied as a function of the scale variation and the uncertainty is obtained as the maximum deviation from the central scale;
  - Electroweak radiative corrections to the VBF signal yield are estimated using HAWK [128]: negligible;
  - parton shower uncertainties (7.7%).
- $ggF\ H \to inv$:
  - jet bin migration Uncertainty (67.8%): this uncertainty on the ggF yield due to the jet selection is evaluated using the Stewart-Tackmann method [132].
  - parton shower uncertainties.

5.18 Fit Model

The analysis uses the same fit model for limit setting and for estimating the W/Z backgrounds in SR and the residual *fake lepton* background in $W \to e\nu$ CRs. The methods are presented in this section.

Table 5.16: Relative changes of the event yields upon applying the PDF variations described in the text. [130]

Selection	Process	1 TeV $< M_{jj} <$ 1.5 TeV	1.5 TeV $< M_{jj} <$ 2 TeV	$M_{jj} >$ 2 TeV
0-lepton (MET)	Strong Z	1.44%	2.51%	2.95%
	Strong W	2.27%	1.50%	3.12%
	EWK Z	1.73%	1.91%	3.76%
	EWK W	2.46%	2.00%	2.40%
1-lepton ($W\to\ell\nu$)	Strong W	1.02%	2.13%	2.13%
	EWK W	1.65%	1.51%	4.60%
2-lepton ($Z\to\ell\ell$)	Strong Z	1.99%	1.81%	1.65%
	EWK Z	2.88%	2.21%	3.79%

The main W/Z backgrounds in SR ($Z \to \nu\nu$ and $W \to \ell\nu$) cannot be modeled with MC simulations alone because it would give a too large theoretical uncertainty as well as a significant detector modeling uncertainty. A control region driven normalization scheme is therefore introduced. As explained in section 5.13, data CRs enriched in Z and W events are defined. Using a simultaneous fit technique the $Z \to \nu\nu$ and W backgrounds in SR are normalized by $Z \to ll$ and $W \to l\nu$ CRs respectively. In order to use the control regions rather than the pure MC predictions, the MC predictions in each of the three signal region bins and the corresponding $Z \to ee/Z \to \mu\mu$ and $W \to e\nu/W \to \mu\nu$ regions are rescaled by free parameters k_V^i, where V is either Z or W, and i runs over the $M(j_1, j_2)$ bin number, (a different k_V^i is used for each $M(j_1, j_2)$ bin). For example, in bin i, the estimated number of events for $Z \to \nu\nu + jets$ (omitting factors that model systematic uncertainties) is given by $Z_{SRi}^{\text{estimated}} = k_Z^i \; Z_{SRi}^{\text{predicted MC}}$, for $W \to l\nu + jets$ background in SR is $W_{SRi}^{\text{estimated}} = k_W^i \; W_{SRi}^{\text{predicted MC}}$. The scale factors k_Z^i (k_W^i) are common to all the $Z + jets$ ($W + jets$) processes and are constrained from the maximum Likelihood fit described later. The underlying key point of this method is the extrapolation from CRs to SRs. In the fit, ratios of expected event counts (called transfer factors) for each simulated background process between each SR and CR, are implicitly used. As mentioned above, the normalized background predictions for a certain process used in the fit are given by the following general relations:

$$N_{CR}^{\text{estimated}} = k \times N_{CR}^{\text{predicted MC}}; N_{SR}^{\text{estimated}} = k \times N_{SR}^{\text{predicted MC}}. \tag{5.8}$$

These relations can be equivalently written as :

$$N_{SR}^{\text{estimated}} \equiv N_{CR}^{\text{estimated}} \times \left[\frac{N_{SR}^{\text{predicted MC}}}{N_{CR}^{\text{predicted MC}}} \right] \tag{5.9}$$

where the ratio appearing in the square brackets is defined as the transfer factor TF between CR and SR. The fit internally uses equation 5.8 but according to eq. 5.9 it can be interpreted as the TF multiplied by the fitted number of background events in the CR.
An important feature of the transfer factor method is that systematic uncertainties on the predicted background processes can (partially) cancel out (due to the ratio of SR and CR events). The final uncertainty on the number of fitted background events in the SR is thus a combination of the statistical uncertainties in the CRs and the residual systematic uncertainties of the extrapolation.

The transfer factor method used for this Run2 analysis introduces a substantial novelty related to W/Z estimate with respect to the corresponding Run1 analysis [100]. In Run2

analysis, two separate scale factors k_Z and k_W are used to normalize respectively the Z and W processes. As the branching ratio of $Z \to ll$ is smaller than the one of $Z \to \nu\nu$ by a factor 3, the result depends on the statistical uncertainty on the available number of events in the control regions and can be limited if the CR statistics is poor. The corresponding strategy is not limited for the estimate of the $W \to l_{lost}\nu$ background in SR, which depends on the statistics in W CR which are more populated. To overcome this limitation, it is possible to normalize the $Z \to \nu\nu$ background by a combination of $Z \to ll$ and $W \to l\nu$ CRs, using a common scale factor (k_V) for W and Z processes. This second strategy relies on the assumption that Z processes can be modeled from W processes. This comes with the need to introduce an additional systematic to account for the modeling error in the extrapolation from W to Z processes. Therefore, while the precision of the *Z-to-Z* extrapolation is limited by the statistics in the $Z \to \ell\ell$ CRs, the *W-to-Z* extrapolation is limited by the theoretical uncertainties on the transfer factor. The latter strategy (i.e common scale factor (k_V) for W and Z processes) has been adopted in Run 1 analysis, since the statistics in Z CR did not allow the use of the former one. In Run 2, given our limited theoretical knowledge[21], the uncertainties on the *W-to-Z* extrapolation are roughly as large as the (mostly statistical) uncertainties on the *Z-to-Z* extrapolation. This indicates that we expect the two fit models to give roughly similar sensitivity. Comparisons of the results obtained with two different fit models demonstrated that the available statistics in Z CRs is such that makes the first strategy (separate k_Z and k_W) competitive, avoiding the complexity of modeling Z events from W process.

Background from misidentified leptons in W CRs is estimated introducing in the fit, for each bin, a freely floating parameter common to each $W \to e\nu$ CR. This parameter can be constrained in the fit by exploiting different information:

- W charge asymmetry: each W CR is split according to the charge of the lepton. While W is asymmetric in charge, the fake lepton background is expected to be symmetric, thus it should be the same in positively and negatively charged lepton regions;
- $W \to e\nu$ CRs are divided into low and high $E_{\mathrm{T}}^{\mathrm{miss}}$ significance values: low $E_{\mathrm{T}}^{\mathrm{miss}}$ significance regions are expected to be more rich in fakes of a fraction R_i (estimated via the method described in Sec. 5.16). The contribution of fakes in each $W \to e\nu$ CR must respect those ratios.

Multijet background in SR is estimated via the R+S method (Sec. 5.15) while $t\bar{t}$ and single top events are estimated with simulated samples. These backgrounds are given as an input to the fit and are not rescaled by any additional parameters.

5.18.1 Likelihood

All CRs, SRs and the background components described above are combined in the final fit model which is implemented as a maximum profiled likelihood fit. The likelihood

[21] In [133], the theoretical correlation factor between W and Z is calculated in an inclusive phase space as: $\delta^{(3)}K^{(W)}_{NLO}(x) = \Delta K^{(W)}_{NLO}(x) - \Delta K^{(Z)}_{NLO}(x)$, where ΔK_{NLO} is the difference in K factor between NNLO and NLO. Due to the lack of NNLO samples, we calculated the LO versus NLO. The existing LO samples we used are MadGraph generator. The NLO samples are Sherpa. The correlation factor can thus be calculated as: $N^W_{LO}/N^W_{NLO} - N^Z_{LO}/N^Z_{NLO} = 0.703 \pm 0.043 - 0.598 \pm 0.161 = 0.105 \pm 0.167$. The uncertainties are completely due to limited statistics on MC samples.

function is constructed from the observed events in data, the yields of signal and backgrounds taken from MC predictions and from R+S method in case of multijets in SRs, scaled by nuisance parameters representing statistical and systematic uncertainties. The fit uses the entire collection of signal regions bins and the corresponding W and Z CRs, for a total number of 27 regions given as input to the fit.
The likelihood function can be written as:

$$\mathcal{L}(\mu, k_Z, k_W, \theta) = \prod_{reg} \prod_{i} \text{Poiss}(N^{obs}_{reg_i} | \mu N^{exp,sig.}_{reg_i}(\theta) + N^{bkg}_{reg_i}(\theta, k^i_Z, k^i_W)) \cdot \mathcal{L}_{\text{constraint}}(\theta) \cdot \mathcal{L}_{\text{stat}}$$

where the $N^{bkg}_{reg_i}(\theta, k^i_Z, k^i_W))$ term can be explicitly written as:

$$\begin{aligned} N^{bkg}_{reg_i}(\theta, k^i_Z, k^i_W) = & \\ & k^i_Z(N^{Z\to\nu\nu}_{reg_i} + N^{Z\to\mu\mu}_{reg_i} + N^{Z\to ee}_{reg_i} + N^{Z\to\tau\tau}_{reg_i}) \\ & + k^i_W(N^{W\to\mu\nu}_{reg_i} + N^{W\to e\nu}_{reg_i} + N^{W\to\tau\nu}_{reg_i}) \\ & + N^{top}_{reg_i} \\ & + N^{multijets,R+S}_{SR_i} \\ & + \beta^{ele\ fakes}_{WCR_i}\ (only\ for\ high - E^{miss}_T sig.regions) \\ & + R_i \times \beta^{ele\ fakes}_{WCR_i}\ (only\ for\ low - E^{miss}_T sig.regions) \end{aligned}$$

In the previous expressions the different terms and parameters have the following meaning:

- reg: runs over the SR and CRs;
- i: runs over the invariant mass bin numbers ($1 \leq i \leq 3$);
- $N^{obs}_{reg_i}$: are the observed data events in the i-th bin of region reg;
- $N^{exp,sig.}_{reg_i}$: is the nominal expected number of events for signal, it includes both the VBF and ggF signal contributions, normalized by the same μ parameter;
- μ is the signal strength: the scale factor associated to the normalization of the signal expected from MC assuming BR($H \to inv$ =100%);
- $N^{bkg_X}_{reg_i}$: is the nominal expected number of events for each background;
- k^i_Z and k^i_W: are the scale factors associated to the normalization of W and Z processes (discussed in Sec. 5.18);
- $\beta^{ele\ \text{fakes}}_{WCR_i}$: is a free floating parameter to fit the remaining contribution of electron fakes in $W \to e\nu$ CRs. Since the fakes are symmetric with respect to the W charge, $\beta^{ele\ \text{fakes}}_{W^+\to e^+\nu CR_i} = \beta^{ele\ fakes}_{W^-\to e^-\nu CR_i} = \beta^{ele\ fakes}_{WCR_i}$.

The fit model and its parameters is summarized in table 5.17 (omitting the nuisance parameter dependence, for simplicity of notation). Each $N^{exp,sig.}_{reg_i}$ and $N^{bkg_X}_{reg_i}$ terms depends also on the nuisance parameters θ, to account the effect of systematic uncertainties.
$\mathcal{L}_{constraint}(\theta) \cdot \mathcal{L}_{\text{stat}}$ are the gaussian terms constraining MC stat errors and systematics uncertainties. The systematic uncertainties are introduced in the model via nuisance

parameters θ multiplied by the actual value of the uncertainty at one sigma variation. θ is supposed to follow a gaussian distribution centered on zero and with width equal to 1. Therefore $\mathcal{L}_{constraint}(\theta)$ can be written as:

$$\mathcal{L}_{constraint} = \prod_{n} \text{gauss}(0|\theta^{syst_n}, 1) \tag{5.10}$$

This likelihood allows to fit simultaneously all the regions and all the floating parameters.

Table 5.17: Summary table describing the transfer factor method and its parameters. B represents the number of background events from MC simulation (the indices corresponds to the region and bin are not shown), S is the number of signal events from MC simulation assuming BR(H$to\ inv$ =100%), R is the ratio of events with $\frac{MET_{sig}<4\sqrt{GeV}}{MET_{sig}>4\sqrt{GeV}}$, μ is the signal strenght. The free parameters in the fit are μ (1 single μ), k (6 different k), β (3 different β).

Transfer	Region	SR	$Z \to ee$	$Z \to \mu\mu$	$W \to e\nu$	$W \to e\nu$	$W \to \mu\nu$	$W \to \mu\nu$	$W \to e\nu$	$W \to e\nu$
Factor	N leptons	0	2	2	1	1	1	1	1	1
	lepton charge				+	−	+	−	+	−
	E_T^{miss} sig.				$> 4\sqrt{GeV}$	$> 4\sqrt{GeV}$			$< 4\sqrt{GeV}$	$< 4\sqrt{GeV}$
bin 1 :	Signal	$\mu \times S_1$	-	-	-	-	-	-		
i.e.	Z + jets	$k_Z^1 \times B_Z$	$k_Z^1 \times B_Z$	$k_Z^1 \times B_Z$	$k_Z^1 \times B_Z$	$k_Z^1 \times B_Z$	$k_Z^1 \times B_Z$	$k_Z^1 \times B_Z$	$k_Z^1 \times B_Z$	$k_Z^1 \times B_Z$
$M_{jj} \in$	W + jets	$k_W^1 \times B_W$	$k_W^1 \times B_W$	$k_W^1 \times B_W$	$k_W^1 \times B_W$	$k_W^1 \times B_W$	$k_W^1 \times B_W$	$k_W^1 \times B_W$	$k_W^1 \times B_W$	$k_W^1 \times B_W$
[1,1.5) TeV	ttbar	from MC	from MC	from MC	from MC	from MC	from MC	from MC	from MC	from MC
	multijet/fakes	R+S	-	-	$\beta_1^{ele,fake}$	$\beta_1^{ele,fake}$			$R_1 \times \beta_1^{ele,fake}$	$R_1 \times \beta_1^{ele,fake}$
bin 2 :	Signal	$\mu \times S_2$	-	-	-	-	-	-		
i.e.	Z + jets	$k_Z^2 \times B_Z$	$k_Z^2 \times B_Z$	$k_Z^2 \times B_Z$	$k_Z^2 \times B_Z$	$k_Z^2 \times B_Z$	$k_Z^2 \times B_Z$	$k_Z^2 \times B_Z$	$k_Z^2 \times B_Z$	$k_Z^2 \times B_Z$
$M_{jj} \in$	W + jets	$k_W^2 \times B_W$	$k_W^2 \times B_W$	$k_W^2 \times B_W$	$k_W^2 \times B_W$	$k_W^2 \times B_W$	$k_W^2 \times B_W$	$k_W^2 \times B_W$	$k_W^2 \times B_W$	$k_W^2 \times B_W$
[1.5,2) TeV	ttbar	from MC	from MC	from MC	from MC	from MC	from MC	from MC	from MC	from MC
	multijet/fakes	R+S	-	-	$\beta_2^{ele,fake}$	$\beta_2^{ele,fake}$			$R_2 \times \beta_2^{ele,fake}$	$R_2 \times \beta_2^{ele,fake}$
bin 3 :	Signal	$\mu \times S_3$	-	-	-	-	-	-		
i.e.	Z + jets	$k_Z^3 \times B_Z$	$k_Z^3 \times B_Z$	$k_Z^3 \times B_Z$	$k_Z^3 \times B_Z$	$k_Z^3 \times B_Z$	$k_Z^3 \times B_Z$	$k_Z^3 \times B_Z$	$k_Z^3 \times B_Z$	$k_Z^3 \times B_Z$
$M_{jj} \geq$2 TeV	W + jets	$k_W^3 \times B_W$	$k_W^3 \times B_W$	$k_W^3 \times B_W$	$k_W^3 \times B_W$	$k_W^3 \times B_W$	$k_W^3 \times B_W$	$k_W^3 \times B_W$	$k_W^3 \times B_W$	$k_W^3 \times B_W$
	ttbar	from MC	from MC	from MC	from MC	from MC	from MC	from MC	from MC	from MC
	multijet/fakes	R+S	-	-	$\beta_3^{ele,fake}$	$\beta_3^{ele,fake}$			$R_3 \times \beta_3^{ele,fake}$	$R_3 \times \beta_3^{ele,fake}$

5.18.2 Histfitter

The software framework used for the fit and limit setting is called Histfitter. HistFitter is a high-level user-interface to perform likelihood fits and follow-up with their statistical interpretation. The user interface and its underlying configuration manager are written in python, and are executing external computational software compiled in C++ such as HistFactory [134], RooStats [135] and RooFit [136].
HistFitter is a python run script that takes a python configuration file as input. The configuration file sets up the pdf of the control, validation, and signal regions of physics analysis and takes as inputs the data and MC in form of ROOT files [137].
For details the reader is referred to [138].

5.18.3 Optimizations

Higher $E_{\mathrm{T}}^{\mathrm{miss}}$ thresholds

In order to optimize the $E_{\mathrm{T}}^{\mathrm{miss}}$ cut, the impact on the BR($H \to inv$) has been studied by varying the $E_{\mathrm{T}}^{\mathrm{miss}}$ threshold to cut on. The fit model used is the one detailed in Sec. 5.18, using two different scale factors (k_Z and k_W) for W and Z processes.
This study has been performed using Asimov data [139] instead of the observed actual data both in SR and CRs. An Asimov dataset is an artificial dataset which is used instead of the actual data. It is an estimate of a dataset where all the statistical fluctuations are suppressed and all the observed quantities are set equal to their expected values (fixing μ =0).
A few assumptions have been adopted to perform this study:

- the theoretical systematics both on signal and on W/Z background are the ones computed for a SR with a $E_{\mathrm{T}}^{\mathrm{miss}} > 150$ GeV cut;
- the multijet contribution in SR is the one estimated for $E_{\mathrm{T}}^{\mathrm{miss}} > 150$ GeV cut;
- the ratios R used as input in the fit for the fakes lepton estimation, are the ones given in Sec. 5.16.

The results show the expected behavior: raising the $E_{\mathrm{T}}^{\mathrm{miss}}$ threshold leads to a degradation of the limit. In particular, increasing the $E_{\mathrm{T}}^{\mathrm{miss}}$ threshold up to 200 GeV leads to a results that is ∼4% (absolute) worse than keeping the threshold at 150 GeV. The optimal $E_{\mathrm{T}}^{\mathrm{miss}}$ cut in terms of the results is therefore $E_{\mathrm{T}}^{\mathrm{miss}}$ >150 GeV however, as presented in Sec. 5.8.4, a higher $E_{\mathrm{T}}^{\mathrm{miss}}$ threshold is needed to reduce the contamination of multijets in SR.

5.19 Results

Once the analysis is finalized and the methods and strategy are fixed and validated, the SR data are included in the analysis.
The observed data in SR correspond to 952, 667, 633 events for the three M_{jj} bins respectively. The prefit background estimate is shown in tables 5.9, 5.10 and in Fig. 5.27. The prefit disagreement between the observed data and the total background is of the level of 12% in the third bin, while it is of few % in the first two bins.
Various pre-fit kinematical distributions are shown in Fig. 5.32.

5.19.1 Background only fit with CR data

A background only fit is performed in the CRs for estimating the background in SR. A summary plot comparing post fit predictions from MC simulation with the number of observed events in each of the control regions is shown in Fig. 5.36. The dijet invariant mass ($M(j_1, j_2)$) and $E_{\mathrm{T}}^{\mathrm{miss}}$ (corrected by adding vectorially the lepton p_T) post fit distributions in each control region are shown in Figure 5.37-5.42. The fake lepton estimates in $W \to e\nu$ CRs cannot be shown there since only the yield is fitted and no information about the shape is provided. The data and the MC pre-fit and post-fit yields in all the CRs are shown in Tables 5.19- 5.21. The postfit distribution in SRs are shown in Fig. 5.43.
Table 5.18 shows the normalization factors for the W/Z background and fake electron contributions (in each of the electron charge-high $E_{\mathrm{T}}^{\mathrm{miss}}$ sig. W control region) obtained from a fit to the data in all the control regions. The scale factors are compatible with 1 and, as expected, the number of fakes in the $W \to e\nu$ CRs is small.
Summarizing the results, the predicted (post-fit) background in the SR bins corresponds to 854±113, 659±90, 584±76 events, to be compared to the observed data corresponding to 952, 667, 633 events.

M_{jj}	k_W	k_Z	β
1.0 – 1.5 TeV	0.97 ± 0.28	1.06 ± 0.34	4.02 ± 1.88
1.5 – 2.0 TeV	0.98 ± 0.25	0.95 ± 0.35	4.21 ± 1.53
$>$ 2.0 TeV	1.19 ± 0.49	1.29 ± 0.38	6.15 ± 2.48

Table 5.18: The best fit values for kW (kZ)-normalization factors for W (Z), $\beta^{\mathrm{ele,fake}}$ as the normalization factors for fake electrons in high $E_{\mathrm{T}}^{\mathrm{miss}}$ sig.-$W(\to e^{\pm}\nu)$+jets control regions of 3 binning in m_{jj}. This is done with the 36.1 fb^{-1} integrated luminosity using only the data in the control regions.

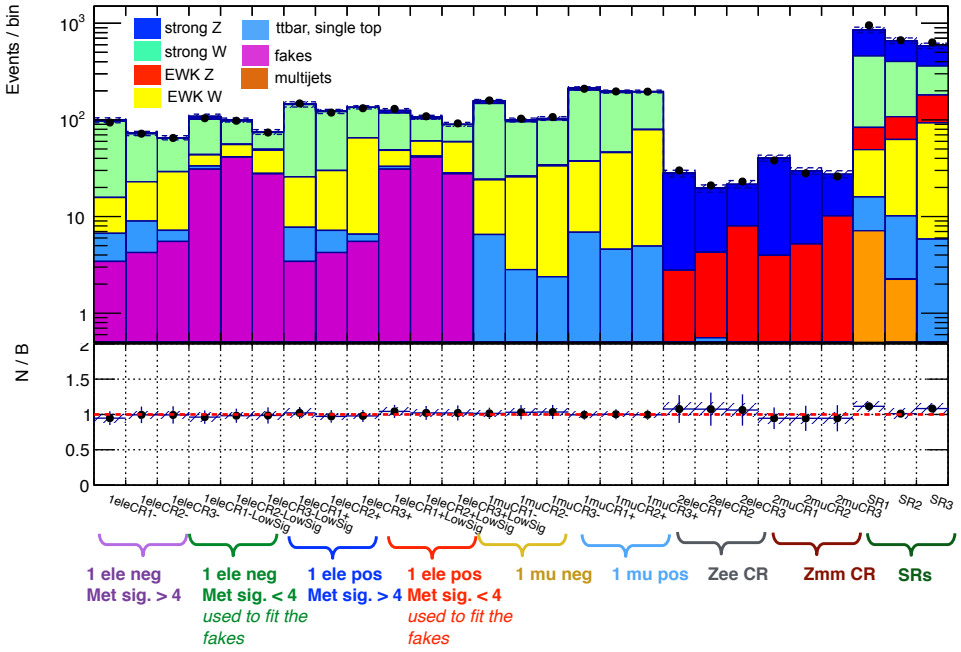

Figure 5.36: Plot showing data/MC comparison for each bin in the control regions and SR for 36.1 fb^{-1}. The MC predictions are the post fit results of a background only fit (see sec. 5.19.1). The error bars in the ratio plot are the statistical uncertainty (both on the MC statistics and the poisson uncertainty from the number of observed events in data). The systematic uncertainties are represented as a shaded band (both the theoretical systematics on W/Z and the main experimental uncertainties). As a result of the fit also the electron fakes in the $W \to e\nu$ CRs are shown.

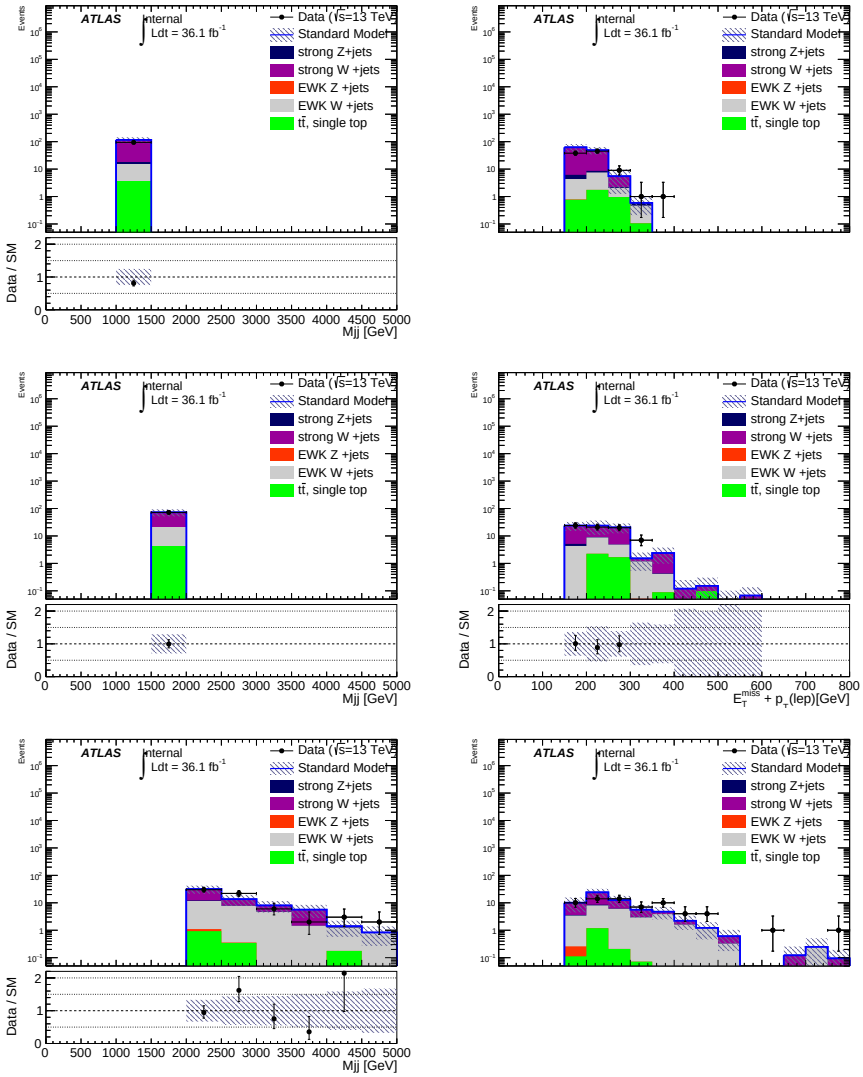

Figure 5.37: Dijet invariant mass ($M(j_1, j_2)$) and $E_{\mathrm{T}}^{\mathrm{miss}}$ (corrected by adding vectorially the lepton p_T) post fit distributions for data and simulated events in the $W^- \to e^-\nu$ CRs. From the top to the bottom: the distributions from the first $M(j_1, j_2)$ bin to the highest $M(j_1, j_2)$ bin are shown.

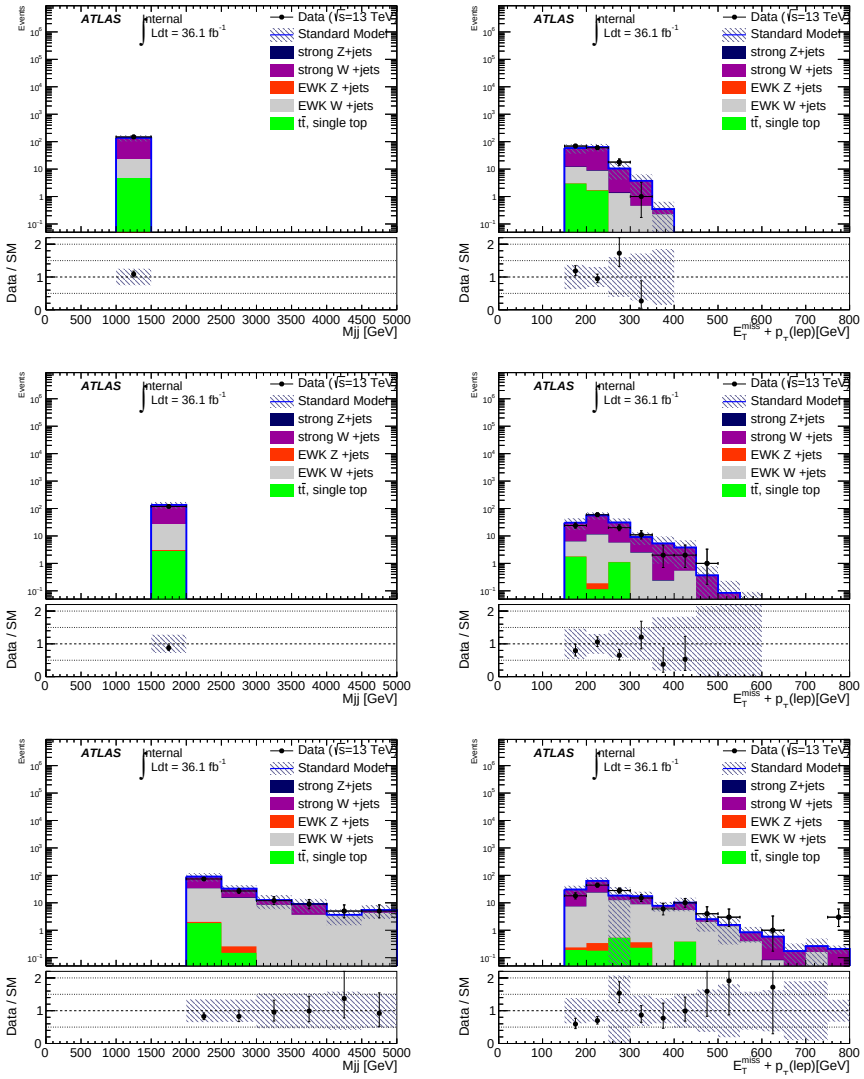

Figure 5.38: Dijet invariant mass ($M(j_1, j_2)$) and $E_{\mathrm{T}}^{\mathrm{miss}}$ (corrected by adding vectorially the lepton p_T) post fit distributions for data and simulated events in the $W^+ \to e^+\nu$ CRs. From the top to the bottom: the distributions from the first $M(j_1, j_2)$ bin to the highest $M(j_1, j_2)$ bin are shown.

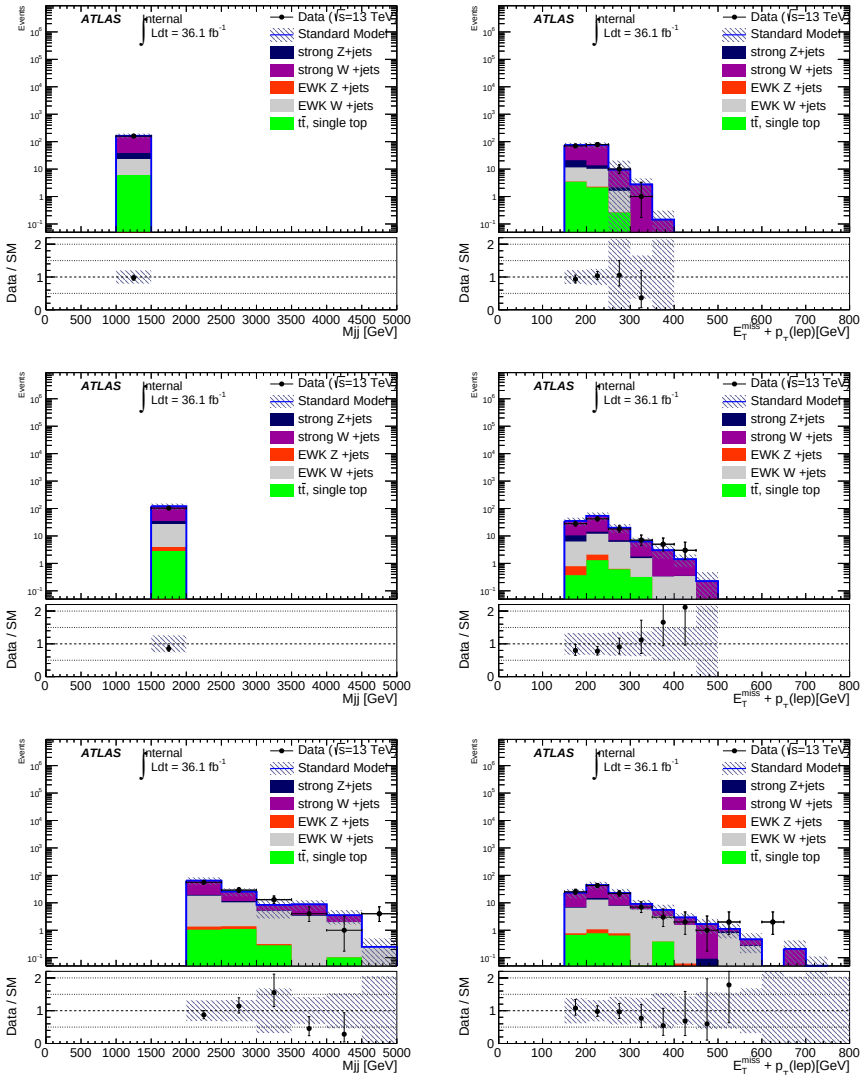

Figure 5.39: Dijet invariant mass ($M(j_1, j_2)$) and $E_{\mathrm{T}}^{\mathrm{miss}}$ (corrected by adding vectorially the lepton p_T) post fit distributions for data and simulated events in the $W^- \to \mu^- \nu$ CRs. From the top to the bottom: the distributions from the first $M(j_1, j_2)$ bin to the highest $M(j_1, j_2)$ bin are shown.

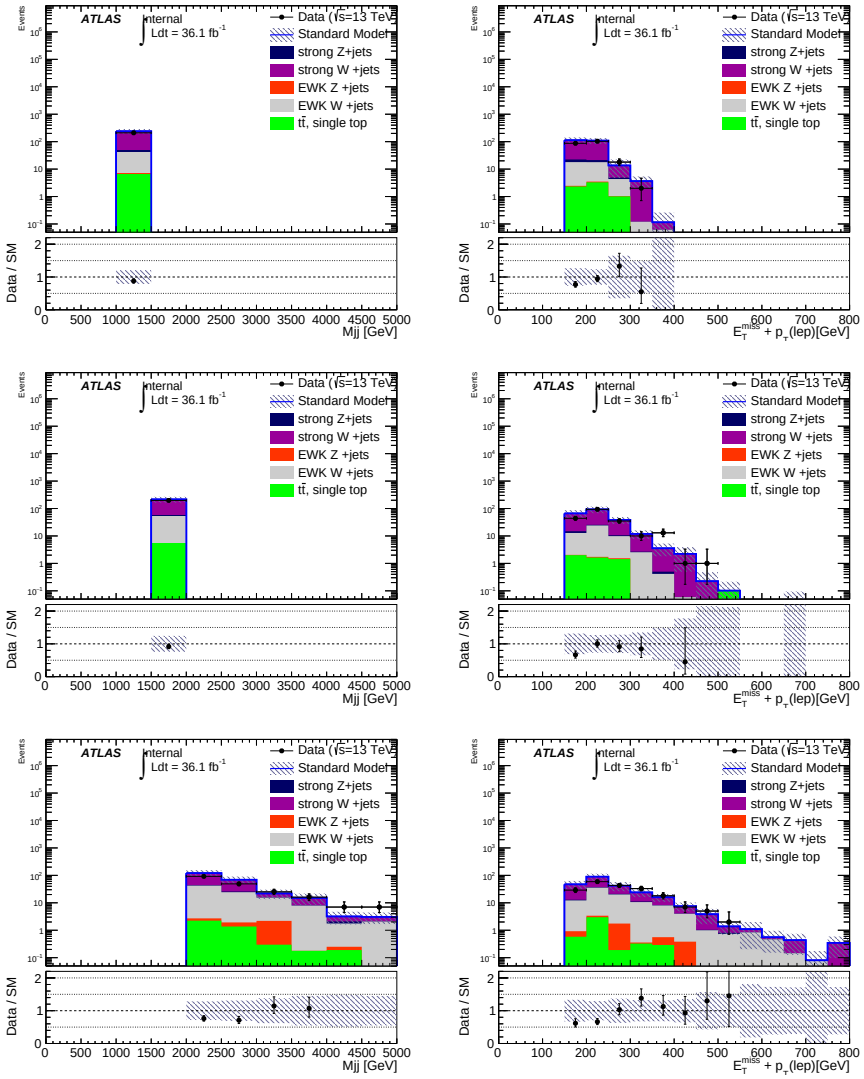

Figure 5.40: Dijet invariant mass ($M(j_1, j_2)$) and $E_{\mathrm{T}}^{\mathrm{miss}}$ (corrected by adding vectorially the lepton p_T) post fit distributions for data and simulated events in the $W^+ \to \mu^+\nu$ CRs. From the top to the bottom: the distributions from the first $M(j_1, j_2)$ bin to the highest $M(j_1, j_2)$ bin are shown.

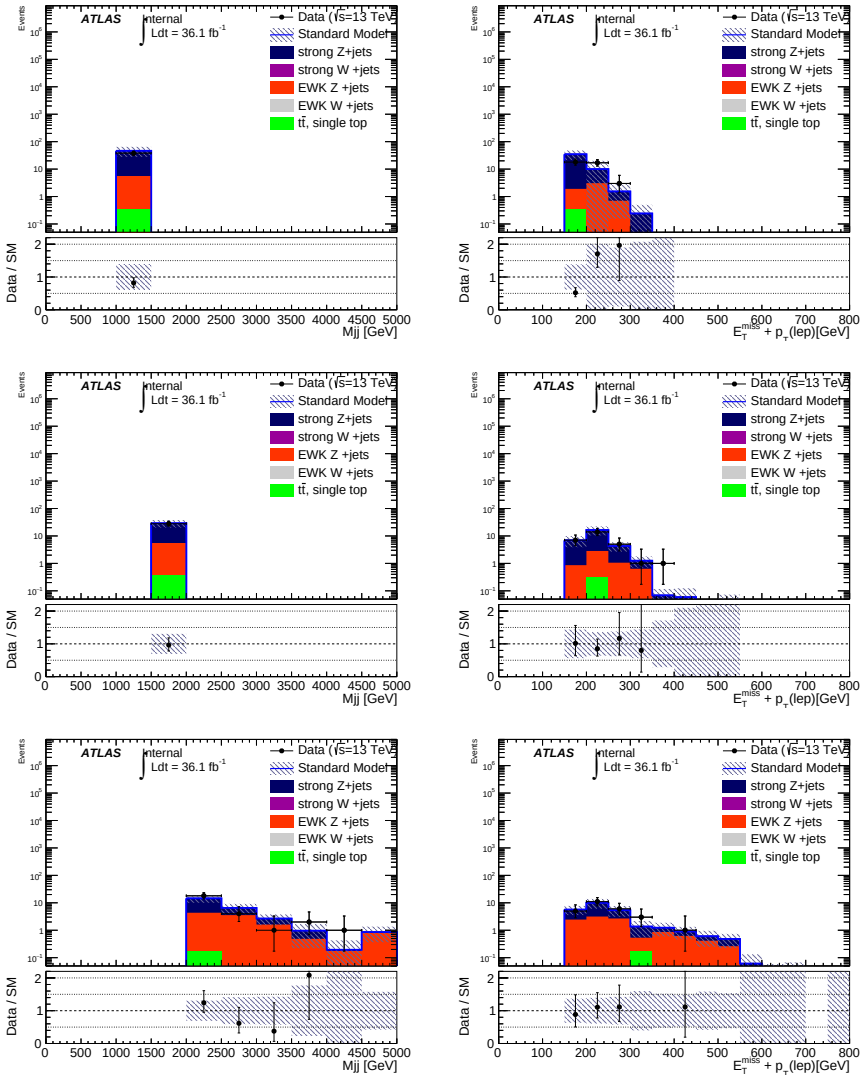

Figure 5.41: Dijet invariant mass ($M(j_1, j_2)$) and $E_{\mathrm{T}}^{\mathrm{miss}}$ (corrected by adding vectorially the lepton p_T) post fit distributions for data and simulated events in the $Z \to \mu^+\mu^-$ CRs. From the top to the bottom: the distributions from the first $M(j_1, j_2)$ bin to the highest $M(j_1, j_2)$ bin are shown.

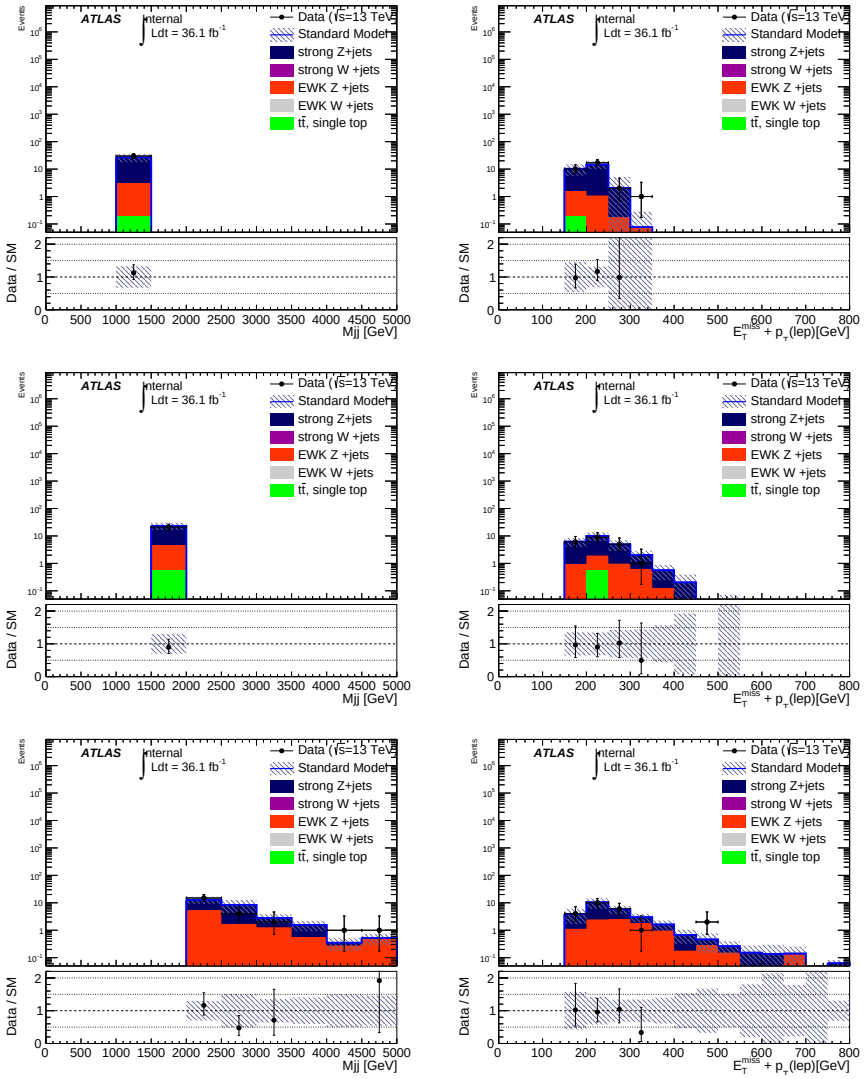

Figure 5.42: Dijet invariant mass ($M(j_1, j_2)$) and $E_{\mathrm{T}}^{\mathrm{miss}}$ (corrected by adding vectorially the lepton p_T) post fit distributions for data and simulated events in the $Z \to e^+e^-$ CRs. From the top to the bottom: the distributions from the first $M(j_1, j_2)$ bin to the highest $M(j_1, j_2)$ bin are shown.

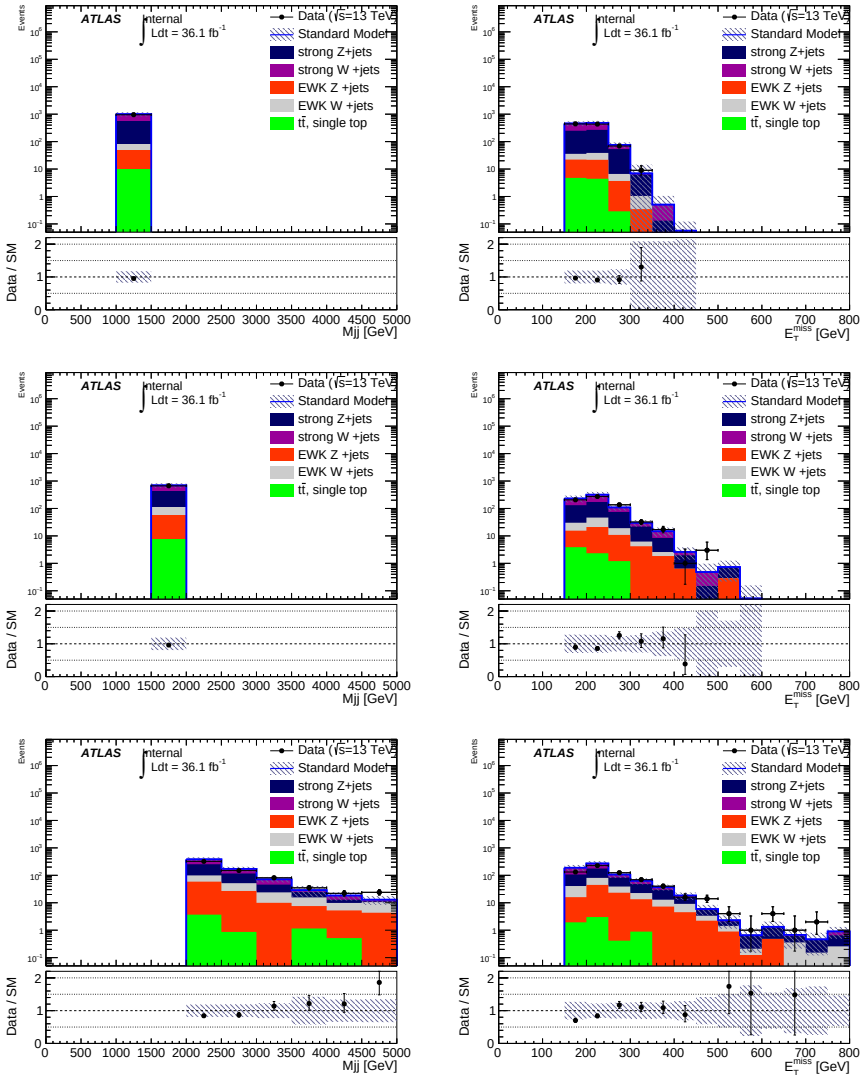

Figure 5.43: Dijet invariant mass (M_{jj}) and $E_{\mathrm{T}}^{\mathrm{miss}}$ post fit distributions for data and simulated events in the signal region. From the top to the bottom: the distributions from the first M_{jj} bin to the highest M_{jj} bin are shown.

Table 5.19: Pre-fit and post-fit summary of yields for M_{jj} 1–1.5 TeV.

	SR1	2μCR bin1	$2e$CR bin1	$1\mu^-$CR bin1	$1\mu^+$CR bin1	$1e^-$CR bin1	$1e^+$CR bin1	$1e^-$CR bin1 LowMETSig	$1e^+$CR bin1 LowMETSig
Observed events	952	38	30	159	210	94	148	104	130
Fitted bkg	853.74 ± 113.27	40.17 ± 6.01	27.85 ± 4.53	156.62 ± 11.96	211.07 ± 17.43	99.20 ± 11.72	144.87 ± 17.98	108.07 ± 13.28	124.64 ± 12.51
Fitted Z_strong	395.62 ± 73.48	36.20 ± 5.83	25.07 ± 4.26	8.88 ± 2.91	8.01 ± 2.43	2.44 ± 0.76	$0.91^{+1.05}_{-0.91}$	6.53 ± 2.11	7.00 ± 4.04
Fitted Z_EWK	34.37 ± 10.43	3.97 ± 1.19	2.57 ± 0.81	0.37 ± 0.18	0.54 ± 0.21	0.02 ± 0.01	0.08 ± 0.03	0.49 ± 0.16	0.58 ± 0.19
Fitted W_strong	374.56 ± 76.58	0.00 ± 0.00	0.00 ± 0.00	123.43 ± 12.11	165.20 ± 19.40	81.02 ± 12.55	118.20 ± 19.78	57.68 ± 13.93	68.69 ± 16.45
Fitted W_EWK	33.26 ± 11.01	0.00 ± 0.00	0.00 ± 0.00	17.43 ± 5.25	30.44 ± 10.65	9.02 ± 3.52	17.94 ± 6.21	10.07 ± 4.18	15.37 ± 5.21
Fitted ttbar	8.80 ± 1.67	0.00 ± 0.30	0.21 ± 0.04	6.52 ± 1.04	6.87 ± 1.39	3.27 ± 0.88	4.30 ± 1.45	2.41 ± 0.42	2.12 ± 1.04
Fitted eleFakes_1	0.00 ± 0.00	0.00 ± 0.00	0.00 ± 0.00	0.00 ± 0.00	0.00 ± 0.00	3.43 ± 1.91	3.43 ± 1.91	30.89 ± 17.22	30.89 ± 17.22
Fitted multijet_1	7.13 ± 5.10	0.00 ± 0.00	0.00 ± 0.00	0.00 ± 0.00	0.00 ± 0.00	0.00 ± 0.00	0.00 ± 0.00	0.00 ± 0.00	0.00 ± 0.00
MC exp. SM	988.37	51.09	23.31	158.82	235.62	126.71	150.35	167.78	172.38
MC exp. Z_strong	455.38	46.34	20.48	9.97	9.97	3.10	0.56	8.26	3.81
MC exp. Z_EWK	36.96	4.21	2.64	0.50	0.58	0.03	0.07	0.52	0.55
MC exp. W_strong	442.64	0.00	0.00	125.53	183.70	99.45	117.01	54.97	62.96
MC exp. W_EWK	36.81	0.00	0.00	16.50	34.55	11.02	19.09	11.43	12.42
MC exp. ttbar	9.45	0.54	0.19	6.32	6.82	3.11	3.62	2.60	2.63
MC exp. eleFakes_1	0.00	0.00	0.00	0.00	0.00	10.00	10.00	90.00	90.00
MC exp. multijet_1	7.13	0.00	0.00	0.00	0.00	0.00	0.00	0.00	0.00

Table 5.20: Pre-fit and post-fit summary of yields for M_{jj} 1.5–2.0 TeV.

	SR1	2μCR bin1	$2e$CR bin1	$1\mu^-$CR bin1	$1\mu^+$CR bin1	$1e^-$CR bin1	$1e^+$CR bin1	$1e^-$CR bin1 LowMETSig	$1e^+$CR bin1 LowMETSig
Observed	667	28	21	103	197	72	119	98	109
Fitted bkg	659.41 ± 90.32	29.62 ± 4.67	19.53 ± 3.41	99.90 ± 9.02	196.50 ± 13.98	72.39 ± 7.36	122.39 ± 12.08	99.76 ± 9.43	106.67 ± 9.83
Fitted Z_strong	257.54 ± 53.46	24.42 ± 4.14	15.27 ± 3.09	4.27 ± 1.42	4.95 ± 1.58	0.70 ± 0.43	0.63 ± 0.29	$2.69^{+4.11}_{-2.69}$	4.04 ± 1.34
Fitted Z_EWK	45.20 ± 14.34	4.75 ± 1.66	3.71 ± 1.33	0.61 ± 0.20	0.54 ± 0.21	0.04 ± 0.02	$0.05^{+0.05}_{-0.05}$	0.61 ± 0.22	0.37 ± 0.16
Fitted W_strong	293.97 ± 63.15	0.00 ± 0.00	0.00 ± 0.00	69.37 ± 10.03	145.18 ± 16.25	48.78 ± 7.52	91.82 ± 14.41	40.97 ± 10.98	41.97 ± 10.63
Fitted W_EWK	52.56 ± 15.53	0.00 ± 0.00	0.00 ± 0.00	22.83 ± 7.20	41.25 ± 12.01	13.89 ± 4.75	22.70 ± 7.40	13.95 ± 5.26	18.09 ± 5.89
Fitted ttbar	7.90 ± 1.01	0.44 ± 0.28	0.56 ± 0.12	2.82 ± 1.02	4.58 ± 1.07	4.73 ± 1.10	2.94 ± 0.83	0.41 ± 0.29	1.07 ± 0.62
Fitted eleFakes_2	0.00 ± 0.00	0.00 ± 0.00	0.00 ± 0.00	0.00 ± 0.00	0.00 ± 0.00	4.24 ± 1.45	4.24 ± 1.45	41.13 ± 14.04	41.13 ± 14.04
Fitted multijet_2	2.24 ± 1.60	0.00 ± 0.00	0.00 ± 0.00	0.00 ± 0.00	0.00 ± 0.00	0.00 ± 0.00	0.00 ± 0.00	0.00 ± 0.00	0.00 ± 0.00
MC exp. SM	710.21	35.82	25.13	111.36	213.22	85.40	137.15	169.87	154.71
MC exp. Z_strong	308.33	29.47	20.43	5.15	6.13	0.99	0.73	10.50	3.95
MC exp. Z_EWK	53.45	5.82	4.17	0.74	0.52	0.05	0.14	0.68	0.40
MC exp. W_strong	287.51	0.00	0.00	81.09	158.74	53.74	99.26	48.01	35.96
MC exp. W_EWK	51.84	0.00	0.00	22.53	43.15	16.05	24.71	13.38	16.58
MC exp. ttbar	6.83	0.53	0.53	1.85	4.68	4.57	2.32	0.30	0.83
MC exp. eleFakes_2	0.00	0.00	0.00	0.00	0.00	10.00	10.00	97.00	97.00
MC exp. multijet_2	2.24	0.00	0.00	0.00	0.00	0.00	0.00	0.00	0.00

Table 5.21: Pre-fit and post-fit summary of yields for $M_{jj} > 2.0$ TeV.

	SR1	2μCR bin1	$2e$CR bin1	$1\mu^-$CR bin1	$1\mu^+$CR bin1	$1e^-$CR bin1	$1e^+$CR bin1	$1e^-$CR bin1 LowMETSig	$1e^+$CR bin1 LowMETSig
Observed	633	26	23	107	196	65	132	74	92
Fitted bkg	584.24 ± 75.50	27.49 ± 4.57	21.64 ± 3.83	103.43 ± 9.22	196.81 ± 12.93	65.43 ± 6.52	134.84 ± 10.12	75.07 ± 8.54	90.13 ± 8.21
Fitted Z_strong	224.02 ± 52.66	17.35 ± 3.96	13.66 ± 3.29	3.52 ± 1.20	3.18 ± 1.19	0.85 ± 0.40	0.00 ± 0.26	$1.06^{+1.12}_{-1.06}$	$0.63^{+0.69}_{-0.63}$
Fitted Z_EWK	87.78 ± 26.93	9.96 ± 3.01	7.98 ± 2.36	0.98 ± 0.30	0.78 ± 0.25	0.14 ± 0.10	0.27 ± 0.12	1.19 ± 0.37	0.57 ± 0.19
Fitted W_strong	179.51 ± 50.76	0.00 ± 0.00	0.00 ± 0.00	65.58 ± 10.75	113.89 ± 19.51	35.38 ± 7.35	69.58 ± 13.86	24.33 ± 5.48	29.82 ± 6.61
Fitted W_EWK	87.08 ± 20.17	0.00 ± 0.00	0.00 ± 0.00	30.98 ± 7.64	74.01 ± 18.03	21.87 ± 6.77	58.43 ± 14.01	20.54 ± 6.33	30.75 ± 8.12
Fitted ttbar	5.39 ± 1.76	0.18 ± 0.11	0.00 ± 0.00	2.38 ± 0.47	4.94 ± 1.10	1.67 ± 0.67	1.04 ± 0.77	0.36 ± 0.14	0.76 ± 0.69
Fitted eleFakes_3	0.00 ± 0.00	0.00 ± 0.00	0.00 ± 0.00	0.00 ± 0.00	0.00 ± 0.00	5.52 ± 2.01	5.52 ± 2.01	27.60 ± 10.06	27.60 ± 10.06
Fitted multijet_3	$0.45^{+1.06}_{-0.45}$	0.00 ± 0.00	0.00 ± 0.00	0.00 ± 0.00	0.00 ± 0.00	0.00 ± 0.00	0.00 ± 0.00	0.00 ± 0.00	0.00 ± 0.00
MC exp. SM	547.40	26.27	22.14	83.99	185.51	68.30	129.84	91.97	100.32
MC exp. Z_strong	201.25	15.93	14.53	2.77	3.47	0.74	0.28	0.09	0.53
MC exp. Z_EWK	80.23	10.07	7.60	0.91	0.78	0.07	0.26	1.06	0.54
MC exp. W_strong	176.70	0.00	0.00	50.68	109.01	34.59	63.75	21.07	21.14
MC exp. W_EWK	82.09	0.00	0.00	27.05	67.85	21.54	55.00	19.46	27.26
MC exp. ttbar	6.67	0.26	0.00	2.59	4.41	1.37	0.55	0.29	0.86
MC exp. eleFakes_3	0.00	0.00	0.00	0.00	0.00	10.00	10.00	50.00	50.00
MC exp. multijet_3	0.45	0.00	0.00	0.00	0.00	0.00	0.00	0.00	0.00

5.19.2 Upper limit on $H \to inv$ BR

The fit is repeated by including the signal. The corresponding best fitted values for μ, k_Z, k_W scale factors and β parameters for fitting the electron fakes are shown in table 5.18. The signal strength μ is compatible with zero.
As no excess in SR data is found, an upper limit on the BR($H \to inv$) is set following the method presented in Appendix F.
The observed (expected) upper limit on BR($H \to inv$) at 95% CL, assuming the SM production cross section, acceptance and efficiency of the 125 GeV SM Higgs boson, is 29% (31%)[22] as shown in table 5.23.

M_{jj}	k_W	k_Z	β
1.0 – 1.5 TeV	0.94 ± 0.23	0.94 ± 0.25	4.5 ± 1.6
1.5 – 2.0 TeV	0.95 ± 0.25	0.80 ± 0.22	4.8 ± 1.3
> 2.0 TeV	1.11 ± 0.26	1.04 ± 0.28	6.2 ± 2.0
μ			
-3.66 x 10^{-2} ± 0.17			

Table 5.22: The best fit values for kW (kZ)-normalization factors for W (Z), $\beta^{\text{ele,fake}}$ as the normalization factors for fake electrons in high $E_{\text{T}}^{\text{miss}}$ sig.-$W(\to e^{\pm}\nu)$+jets control regions of 3 binning in m_{jj}. This is done with the 36.1 fb^{-1} integrated luminosity using a simultaneous fit of the signal region and control region data. The best fit value of the signal strength, μ and the associated uncertainty is also shown. [130]

Table 5.23: Expected and observed limits, calculated at the 95% C.L. [130]

Expected	Observed	+1 σ	-1 σ	+2 σ	-2 σ
0.28	0.37	0.39	0.20	0.58	0.15

5.19.3 Impact of systematic uncertainties and MC statistics

In order to estimate the total impact of the systematics and of MC statistics, the limit can be computed by removing from the calculation all the systematics (both experimental and theoretical) and the statistical errors associated to MC statistics. This study shows that the results on the BR($H \to inv$) upper limit could be improved of some % in case of infinite MC statistics and are improved substantially of ∼9% (in absolute value) in case of no systematics. This check can only give the idea of the impact of systematics and MC statistics, it does not correspond exactly to the ideal case of zero systematics and infinite MC statistics (in that case the nominal values would be different from the actual nominal value which is subject to fluctuations and systematic effects).
As an improvement on the result could be achieved by improving the MC statistics in the VBF phase space, different solutions have been investigated to generate MC samples with higher statistics. They are summarized in Appendix G. In particular, extended W/Z MC samples have been generated in order to improve the result. However, since they were not ready at the time this document has been written, the results with improved MC statistics are not shown here.

[22] This result is preliminary and may change slightly.

Table 5.24: Variations in the expected limit, listed in %, with respect to the default value of 28%, as various groups of systematic uncertainties are turned off in the limit calculation. Note that experimental uncertainties and the uncertainty related to the size of the MC sample (MC stat.) are considered separate categories. [130]

Group	Expected relative variation on limit
Jet energy scale	10%
Jet energy resolution	2%
MET soft term	1%
Lepton ID veto	2%
Pileup	1%
Resummation scale	1%
Renormalization / factorization scale	2%
CKKW matching	4%
Third jet veto (signal)	2%
All experimental	17%
All theory	10 %
Theory and exp.	28 %
Theory, exp and MC stats	42%

Similarly, to evaluate the impact of each category of systematic uncertainty, we remove groups of systematics from the limit calculation. Results are shown in Table 5.24. This gives a sense of where improvements can be made that will benefit the analysis, and which groups of uncertainties make a significant impact.

Impact of NP on the signal strength

In order to study the impact of the different nuisance parameters, for each nuisance parameter, the following procedure is adopted:

1. a fit is run and the best fit values for the signal strength μ and for the other nuisance parameters are found;
2. the considered nuisance parameter is fixed to his best fit value found in the previous step $\pm$ prefit 1σ. The likelihood is minimized again and a new best fit value is found for μ. This value is compared to the one from step 1. and the difference is counted as the impact on μ;
3. a similar procedure to step 2. is repeated using the $\pm$ postfit 1σ.

This allows to rank the NP according to their impact on the signal strength μ. By comparing the pre fit values of each NP to the best fit value (*pulls*), it is also possible to check how well the fit constrains each NP. The results are summarized in Fig. 5.44, which is usually called *ranking plot* or *pull plot* and it has two scales: one for the impact on μ the other for the pulls. The plot shows that the NP with higher impact on μ are:

- theoretical systematics on W/Z backgrounds;
- MC statistical uncertainties;
- Jet energy resolution;

- $E_{\mathrm{T}}^{\mathrm{miss}}$ systematics;
- Jet energy scale systematics;
- pile up reweighting uncertainty.

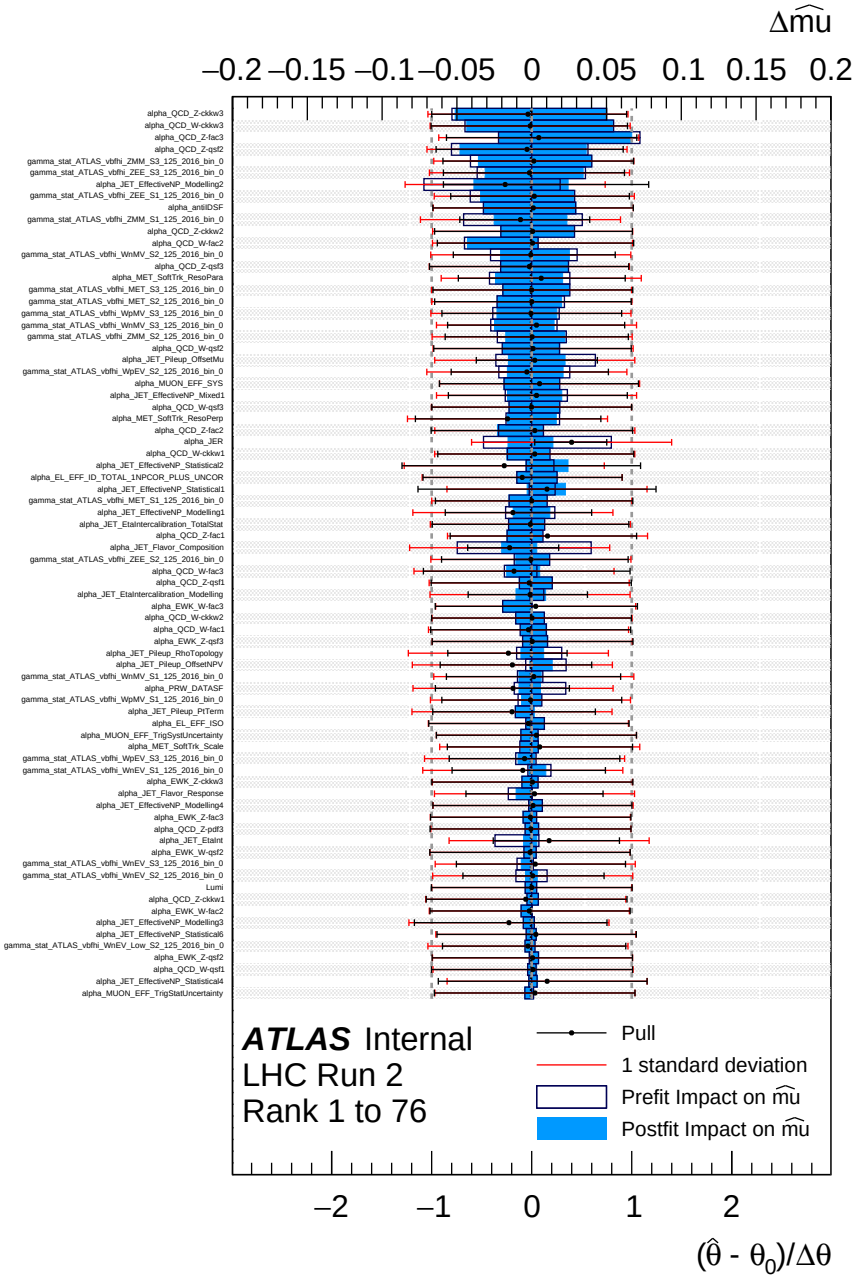

Figure 5.44: Pulls and ranking for impact of different nuisance parameters associated to the systematic uncertainties as well as the MC statistical uncertainties on the signal strength. Fit to all signal and control regions data of 36.1 fb^{-1}. This figure represent more than half of the nuisance parameters which have visible impact on the singal strengh. [130]

Figure 5.45 shows the correlation matrix of different parameters in the fit, while 5.46 shows the same but only for the JES NPs.

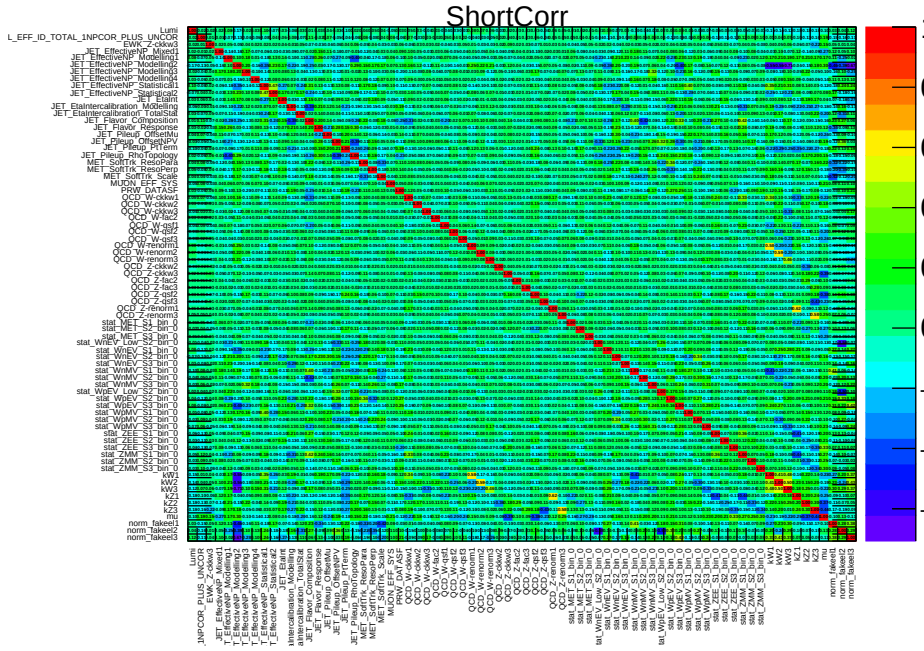

Figure 5.45: Correlation matrix among different nuisance parameter associated to the systematic uncertainties and the signal strength. The list was truncated to fit on a plot. [130]

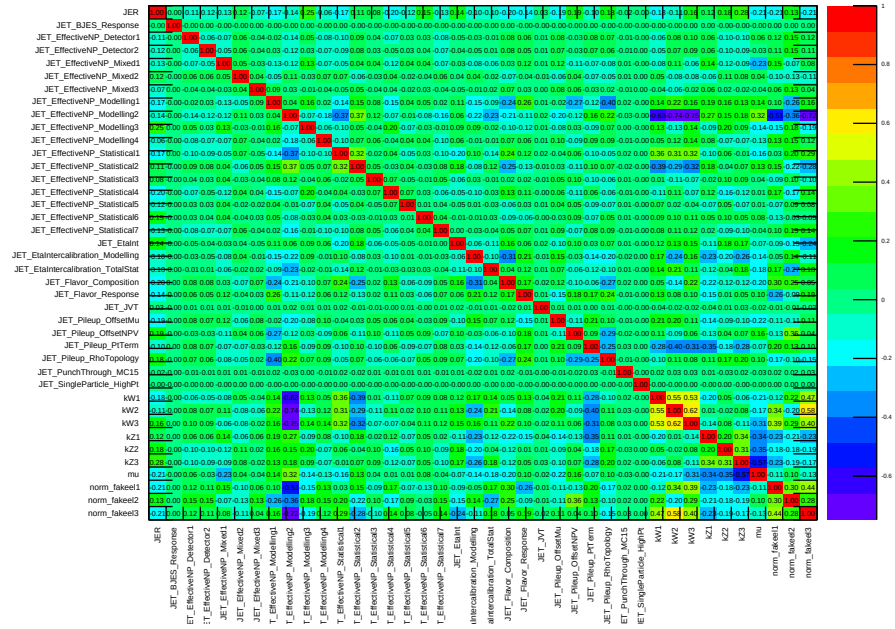

Figure 5.46: Correlation matrix among different nuisance parameter associated with the JES and normalization uncertainties only. [130]

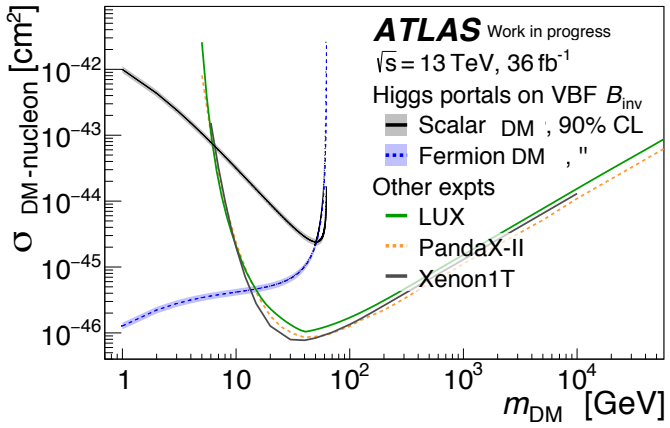

Figure 5.47: The DM-nucleon cross section is shown as a function of the DM mass. The exclusion limits of the direct detection experiments are compared to the ATLAS results from the BR($H \to inv$) limit in the Higgs-portal scenario, translated into the DM-nucleon cross section using the formulas presented in Sec. 1.5.2. The exclusion limits are shown at 90% CL. Updated uncertainty coming from the different estimations of the Higgs-nucleon coupling form factor have been used [43]. [130]

5.20 Interpretation

5.20.1 Higgs Portal Model

In the Higgs-portal dark matter scenario, a dark sector is coupled to the SM via the Higgs boson by introducing a dark matter singlet that only couples to the SM Higgs doublet (see Sec. 1.5.2). Results from direct detection searches can be compared to results from LHC $H \to$ invisible searches. In this context, the 90% CL branching fraction limit for VBF $H \to inv$ can be translated into an upper bound on the scattering cross section between nucleons and DM in the Higgs portal model as a function of the DM mass. This is done for DM masses less than $m_H/2$, under the assumption that the resulting Higgs boson decays to DM pairs account entirely for the BR($H \to inv$). The preliminary results are shown in Fig. 5.47 and are compared to the results from direct detection experiments. For DM masses less than 10 GeV, the ATLAS limits are stronger than the exclusion limits by the direct detection experiments. This is expected as there is no limitations for the production of low-mass particles at the LHC, while in direct detection experiments, the recoil energies produced in the interactions of sub-relativistic DM particles with nuclei are often below the sensitivity threshold for small DM masses. Additional data and the reduction of systematics will provide a much more stringent test of the potential link between the Higgs boson and dark matter.

5.20.2 Varied Higgs mass samples

In addition to the upper limit on BR($H \to inv$), for the 125 GeV Higgs boson, we also considered additional interpretations with hypothetical scalar bosons. As already presented (see Sec. 5.3.2), we generated different VBF $H \to inv$ points with masses between 75 GeV - 3 TeV in the narrow width approximation. Only the VBF contribution is considered, the ggF one is neglected. The efficiency for each of the sample is shown

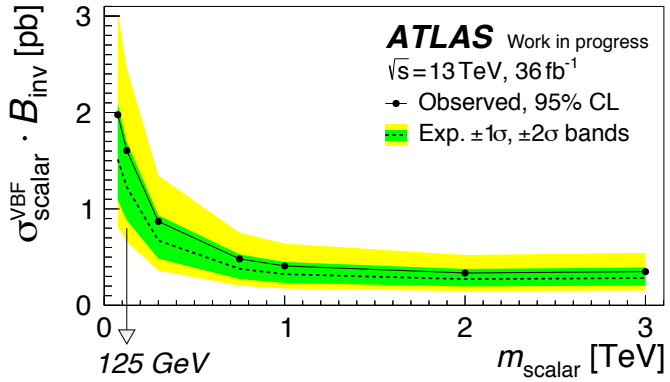

Figure 5.48: Results for upper limits on $\sigma \times \mathrm{BR}(H \to inv)$ as a function of mass (in the range 75 GeV - 3 TeV). [130]

in table 5.5. Upper limits on their cross section times invisible branching fraction ($\sigma \times \mathrm{BR}(H \to inv)$) can be studied as a function of mass. The results are shown in Fig. 5.48.

5.21 Conclusions and prospects

A search for the invisible decay of the Higgs boson produced via VBF using 36.1 fb^{-1} data at $\sqrt{s}$ =13 TeV has been presented. The final state is defined by large $E_{\mathrm{T}}^{\mathrm{miss}}$, given by the invisible particles from the Higgs decay, and two jets with typical VBF characteristics (well separated in η and with large invariant mass). The backgrounds of this analysis come from $Z \to \nu\nu$ and $W \to \ell\nu$ processes where the lepton is lost; multijets events, which represent a tiny fraction of the total background if dedicated cuts are applied but their estimation constitutes a challenge; $t\bar{t}$ and single top processes.
The analysis is performed as cut and count experiments in three different M_{jj} bins. Different control regions, enriched in W and Z events, are used to constrain the SR W/Z background with a transfer factor technique.
After the SR selection the total number of observed data in the three SR bins is 952, 667, 633 events to be compared to the predicted (post-fit) background 936±167, 672±92, 659±86 respectively.
As no excess is observed, an upper limit on the $\mathrm{BR}(H \to inv)$ is set. The observed (expected) result at 95% CL is 0.37 (0.28).

The Run1 result for the corresponding analysis was 0.30 (0.35) [100], therefore an improvement has been achieved in the expected result. One can wonder what could improve the result further. There are different windows of improvement which are under investigation for an updated version of this analysis using the full Run2 statistics (∼120 fb^{-1}), they include:

- optimized lepton veto: as described in this chapter the lepton veto is particularly important in order to suppress the W and Z background. The lepton veto could be optimized in order to reduce more $W \to \ell\nu$ events if the η range of the muon is extended up to η =2.7 and if the quality criteria of the vetoed electrons and muons are relaxed;

- MC statistics: an improved MC statistics could improve the result by few %;

- transfer factor method: as explained, in the transfer factor method two different scale factors are used to normalize the W and Z backgrounds separately. This has the advantage to avoid the assumption that the W and Z backgrounds are correlated. If the uncertainty about the level of correlation between W and Z processes would be estimated carefully, if small enough, it would be possible to take advantage from the statistics in the W regions to also constrain the Z background in SR;

- vertex: the vertex in the SR may be not well identified as a high fraction of events have both jets outside the tracker. This is not happening in the CRs, where in addition to the jets there are also leptons. In order to emulate the SR conditions for the vertex reconstruction, in CRs, the lepton(s) should be removed to reconstruct the hard scatter vertex;

- $E_{\mathrm{T}}^{\mathrm{miss}}$ definition: the optimal $E_{\mathrm{T}}^{\mathrm{miss}}$ cut for a better result would be $E_{\mathrm{T}}^{\mathrm{miss}}$ >150 GeV, however a higher $E_{\mathrm{T}}^{\mathrm{miss}}$ threshold together with a cut on $MHT(noJVT)$ is needed in order to suppress the background from multijet events which can enter the SR because of fake $E_{\mathrm{T}}^{\mathrm{miss}}$ created by the JVT removal of a hard scatter jet. An optimization of the $E_{\mathrm{T}}^{\mathrm{miss}}$ definition for this class of events could help to reduce this background without (potentially) raising the $E_{\mathrm{T}}^{\mathrm{miss}}$ threshold;

- reduced systematics: as discussed, the results could be improved if systematics could be reduced. In particular, the theoretical systematics on the W/Z backgrounds are affected by MC statistics. If they would be reduced a more stringent result on the BR($H \rightarrow inv$) could be set. Among the experimental systematics, jets-related uncertainties play an important role. Similarly, the result would benefit from a reduction of these uncertainties;

- cut based versus boosted decision tree: very preliminary studies to perform the analysis with a multivariate approach seem to be promising and worth to be investigated. In particular a boosted decision tree could be used to discriminate the signal events from the background events.

Chapter 6

Pure WIMP triplet DM in VBF+$E_{\mathrm{T}}^{\mathrm{miss}}$ final state

As described in the first chapter, astrophysical and cosmological observations support the existence of dark matter, made of new BSM particles, but its nature still remains a mistery.
Many theories predict dark matter candidates, but there have not yet been any direct measurements.
In this chapter we focus on models with pure WIMPs, inspired by Minimal Dark Matter models, which can be tested at the LHC in final states with VBF jets and large $E_{\mathrm{T}}^{\mathrm{miss}}$, such as the ones described in chapter 5.
In this chapter, firstly a brief introduction to the idea of the Minimal Dark Matter model is presented, then the case of a pure WIMP triplet is discussed. Details of MC generation for this model within the ATLAS software are described. The VBF+$E_{\mathrm{T}}^{\mathrm{miss}}$ search described in chapter 5 is reinterpreted in this context. Projections with higher luminosity are also discussed.

6.1 Introduction and motivations

The idea behind Minimal Dark Matter (MDM) models is to focus on the dark matter problem and add the minimal amount of new BSM physics which can provide a good DM candidate. Their candidates also provide a benchmark in the spirit of simplified models.

6.1.1 The Minimal Dark Matter model

As presented in Chapter 1, one of the most popular theory proposed as extension of the SM is Supersymmetry. It solves the Higgs mass hierarchy problem and it predicts a viable DM candidate. SUSY theories are characterized by many parameters and a complex phenomenology. Although they provide elegant solutions to the hierarchy problem, until now no experimental proof of these theories has been observed.
The Minimal Dark Matter model [141], [142], [143], as a contrast to these theories, follows a minimalistic approach. It focuses on the Dark Matter problem only, without the pretence of solving other problems. The minimal amount of new physics is added to the SM and the quantum numbers which give a good DM candidate are assigned to it.

An unique extra multiplet χ, with n components, is added on top of the SM:

$$\chi = \begin{pmatrix} \chi_1 \\ \chi_2 \\ \vdots \\ \chi_n \end{pmatrix} \tag{6.1}$$

The SM is extended by adding a new lagrangian term:

$$\mathcal{L} = \mathcal{L}_{SM} + \mathcal{L}_{MDM} \tag{6.2}$$

If χ is a fermion:

$$\mathcal{L}_{MDM} = \bar{\chi}(i\not{D} - M)\chi \tag{6.3}$$

while if χ is a scalar:

$$\mathcal{L}_{MDM} = |D_\mu \chi|^2 - M^2\chi^2 \tag{6.4}$$

where M is the tree-level mass of the particle.
The properties that a good DM candidate should respect are: stability on cosmological time scales, the candidate must be neutral and still allowed by DM searches. The only free parameter is the DM mass, which can be fixed by imposing the thermal relic density. Therefore χ has no strong interactions and it is a multiplet of the $SU(2)_L$ group (*pure WIMP*). Its hypercharge Y is determined by requiring that one of the multiplet components is neutral ($Q = T_3 + Y \equiv 0$), therefore for each n there are few possible values of Y. However multiplets with non null Y are already excluded by direct detection DM searches[1].
Table 6.1 summarizes the main properties of the possible DM candidates for each choice of quantum numbers. The multiplets with low n can decay into SM particles in different ways, in these cases a stable DM candidate can be obtained after suppressing these decays, for instance by requiring additional symmetries. The cases where χ presents a DM candidate automatically stable are for $n \geq 5$ for fermions and $n \geq 7$ for scalars. In these cases, χ is stable for an *accidental symmetry*, as it happens to the proton in the SM. An upper bound to the size n of the representation is imposed by the need of of avoiding Landau poles in α_2. The initial computation at 1 loop in [141] found $n \leq 5$ for fermions and $n \leq 7$ for scalars. A more refined computation at 2 loops in [144] showed that the case $n = 7$ for scalars is excluded. Combined with the stability-induced lower limit mentioned above, this leaves the $n = 5$ fermions as the only and fully minimal case.
At tree level all the χ components have the same mass M, but a mass splitting is induced by the electroweak corrections given by loops of SM gauge bosons between the charged and neutral components of χ. These corrections make the charged components heavier than the neutral one. The neutral component is therefore the lightest one and its mass differs by hundreds of MeV from the one of the charged components.
Assuming that DM is a thermal relic of the early universe, the abundance can be computed as a function of M. Under the hypothesis that all the DM is made of χ^0 particles, the χ^0 mass can be univocally computed. Typically the χ mass is in the multi-TeV range.

Summarizing, if a minimalistic approach is followed, a fermionic $SU(2)_L$ quintuplet with hypercharge $Y = 0$ provides a good dark matter candidate. It has mass $M = 11.5$

[1] They could be recovered using non-minimal mechanisms which preclude Z-mediated DM/nuclei couplings

Quantum numbers $SU(2)_L$	$U(1)_Y$	Spin	DM can decay into	DM mass in TeV without corrections	$m_{DM^\pm} - m_{DM}$ in MeV	DM mass in TeV with corrections	$\sigma_{\rm SI}$ in 10^{-45} cm^2
2	1/2	0	EL	0.54 ± 0.01	350		0.2
2	1/2	1/2	EH	1.1 ± 0.03	341		0.2
3	0	0	HH^*	2.0 ± 0.05	166		1.3
3	0	1/2	LH	2.4 ± 0.06	166	$3.0 \div 3.2$	1.3
3	1	0	HH, LL	1.6 ± 0.04	540		1.7
3	1	1/2	LH	1.8 ± 0.05	525		1.7
4	1/2	0	HHH^*	2.4 ± 0.06	353		1.6
4	1/2	1/2	(LHH^*)	2.4 ± 0.06	347		1.6
4	3/2	0	HHH	2.9 ± 0.07	729		7.5
4	3/2	1/2	(LHH)	2.6 ± 0.07	712		7.5
5	0	0	(HHH^*H^*)	5.0 ± 0.1	166		12
5	0	1/2	–	4.4 ± 0.1	166	11.5	12
7	0	0	–	8.5 ± 0.2	166		46

Table 6.1: The table lists the quantum numbers and the properties of the multiplet χ: possible decays into SM particles (L stands for lepton doublet, E lepton singlet, H Higgs doublet); DM mass (obtained by matching the thermal relic) without accounting for corrections; mass splitting between the states; updated values of the DM mass for the triplet and the quintuplet by considering the Sommerfeld effect (as computed in [142]) and the effect of bound states [145]; and spin-independent cross sections. Multiplets with non null Y are excluded by Direct Detection experiments. [141]

TeV [145] (if the thermal relic abundance is assumed) and the lightest component is neutral and automatically stable (full minimality). The charged partners are 166 MeV heavier than χ^0. The existence of such a particle is still allowed by DM searches.
Minimal Dark Matter can be probed via direct detection, indirect detection and in principle at colliders, however a particle of 11.5 TeV is out of reach at the LHC.

By relaxing the request of full minimality, other DM candidates can be recovered within the multiplets listed in Table 6.1 which decay into SM particles.
Particularly interesting is the case of the fermionic triplet, with $Y = 0$, which could be produced at the LHC. It is described in the next section.

6.1.2 Wino-like Minimal Dark Matter

Following the same strategy as before, an electroweak fermionic triplet added on top of the SM, can constitute a DM candidate if the request of fully minimality is relaxed: the stability of the lightest neutral component is not automatic. In particular, the lightest component of the triplet is stable if the lepton number or the B-L number is preserved.

Such a triplet:

$$\chi = \begin{pmatrix} \chi^+ \\ \chi^0 \\ \chi^- \end{pmatrix} \tag{6.5}$$

is added to the SM with a Lagrangian:

$$\begin{aligned}\mathcal{L}_{MDM} &= \frac{1}{2}\bar{\chi}(i\not{D} + M)\chi \\ &= \frac{1}{2}\bar{\chi^0}(i\not{\partial} - M_{\chi^0})\chi^0 + \bar{\chi^+}(i\not{\partial} - M_{\chi^+})\chi^+ \\ &+ g(\bar{\chi^+}\gamma_\mu\chi^+(\sin\theta_W A_\mu + \cos\theta_W Z_\mu)) + \bar{\chi^+}\gamma_\mu\chi^0 W_\mu^- + \bar{\chi^0}\gamma_\mu\chi^+ W_\mu^+\end{aligned}$$

where g is the $SU(2)$ gauge coupling.
The only free parameter is the mass of χ and, as before, it can be obtained by requiring to match the thermal relic abundance. In this case $M_\chi = 3.0 \div 3.2$ TeV. However, if χ is not the only particle making the whole dark matter or if it is not thermally produced, its mass can be M_χ <3.2 TeV.
This model provides a benchmark of a typical WIMP DM candidate and its phenomenology recreates the phenomenology of cases of supersymmetric models where the Wino is the lightest supersymmetric particle (LSP). For this reason this triplet is referred to as *Wino-like*.
Together with providing a good DM candidate, this Wino-like triplet has other interesting features, for instance it modifies the running of the Higgs quartic coupling stabilizing the EW vacuum, it also changes the running of the gauge couplings helping with their unification.

As studied in [146], leaving M a free parameter, the MDM triplet can be probed at colliders in different ways. In particular it can be produced at proton-proton colliders such as LHC. Once produced the charged components of the triplet decay into the lightest neutral component χ_0 plus very soft charged pions. χ^0 is reconstructed as $E_{\mathrm{T}}^{\mathrm{miss}}$ in the detector while the pions, because of the small mass splitting between the neutral and charged components, are so soft that they are lost and are not reconstructed. Therefore, the production of χ can be searched for by:

- mono-X searches, such as mono-jet and mono-photon (illustration diagrams are shown in Fig. 6.1);
- VBF+$E_{\mathrm{T}}^{\mathrm{miss}}$ searches: χ can also be produced via VBF, leading to a final state with VBF jets and large $E_{\mathrm{T}}^{\mathrm{miss}}$;
- disappearing tracks searches: the lifetime of $\chi^\pm$ is about $\tau \simeq 0.2$ ns and it corresponds to a decay length at rest $d = c\tau \simeq 6$ cm, this means that almost all the $\chi^\pm$ particles decay before reaching the detector. However, a small fraction of them can travel enough to leave a track in the detector. In this case, the signature of these events is characterized by high p_T tracks (caused by $\chi^\pm$) which end inside the detector once they are decayed into χ_0 and soft pions. This signature is usually referred to as *disappearing tracks* [146]. Searches targeting disappearing tracks signatures performed by ATLAS during Run1 [148] and Run2 [149] set constraints on $M_{\chi^\pm}$. Masses up to 270 GeV were excluded by Run 1 analysis while masses up to 460 GeV are excluded by the recent Run2 analysis.

In this thesis we focus on the VBF production mode which is described in the next section.

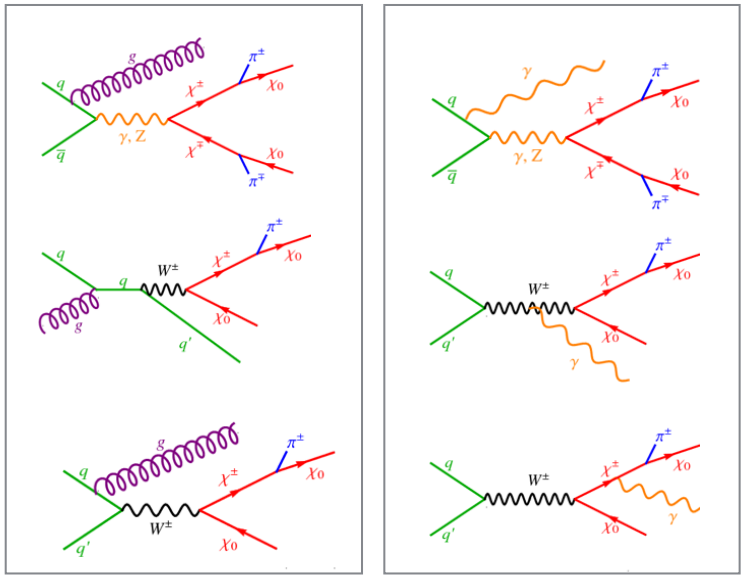

Figure 6.1: Some representative Feynman diagrams for Wino-like MDM triplet for monojet (left) and monophoton (right) processes. [146]

6.1.3 Triplet in VBF production mode

As previously mentioned, Wino-like triplets can be produced at the LHC also via VBF. Some illustration diagrams for this process are shown in Fig. 6.2.
As the mass splitting ΔM between $\chi^{\pm}$ and χ^0 is small ($\Delta M \sim 165$ MeV), the $\chi^{\pm}$ particles decay into χ^0 and very soft pions, which are not reconstructed and lost in the detector. Therefore the signature of a triplet produced via VBF is defined by the presence of two energetic jets with VBF topology and large $E_{\mathrm{T}}^{\mathrm{miss}}$, that is the same final state than the one of the VBF $H \rightarrow inv$ analysis discussed in Chapter 5. This allows to reinterpret that analysis in the context of this model: exactly the same analysis strategy and cuts are used to test the MDM triplet.
Following the idea of what has been done in [146], here a full analysis has been performed within ATLAS using $36 fb^{-1}$ data collected along 2015 and 2016.
The one described in this chapter is the first attempt in ATLAS to test this particular model.

6.2 Signal generation

In order to test the MDM triplet in VBF production mode, the signal events had to be generated within the ATLAS framework.
As presented in Section 2.3, there are different steps to simulate events. Events are generated using Madgraph+Pythia generators, as described below.

6.2.1 Model Implementation

The same model implementation which has been used by M. Cirelli, F. Sala and M. Taoso for the studies in [146] has been re-used here. The model has been implemented in FeynRules 2.3.24 and considers the electroweak triplet $\chi = (\chi^+, \chi^0, \chi^-)$ described in

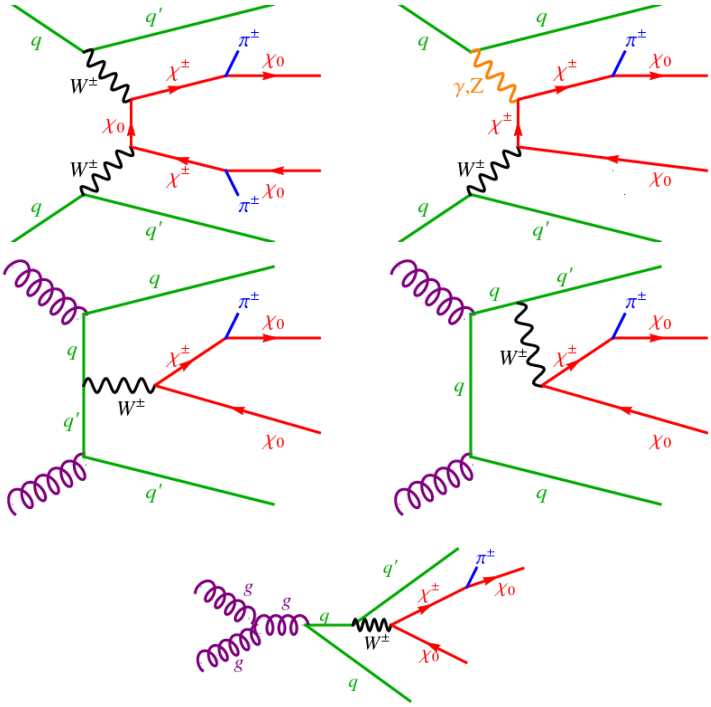

Figure 6.2: Some representative diagrams for the MDM triplet produced via VBF. The $\chi^{\pm}$ particles decay into the stable χ^0 DM candidate and soft pions which are not reconstructed [146].

6.1.2.
Some modifications are needed with respect to the original version of the implementation in order to perform the ATLAS analysis. In fact, the phenomenological studies in reference [146] are performed at parton level, using Delphes 3 as a detector simulator [147]. More in detail, in reference [146] the final state for a VBF produced triplet is defined by the presence of quarks (and gluons) and the $E_{\mathrm{T}}^{\mathrm{miss}}$ is reconstructed by the transverse momenta of the charged $\chi^{\pm}$ particles, which are not forced to decay into χ^0 and $\pi^{\pm}$.
In order to perform such an analysis in ATLAS, the objects need to be reconstructed as they are detected in the detector, therefore the simulation cannot be limited to the simulation of partons but jets have to be reconstructed from the energy deposits in calorimeters (see Sec. 3.4). As described in 2.3.2, the `GEANT4` program is used to simulate the interactions of the particles with the detector material. As the model involves new particles, dedicated `GEANT4` extensions would be needed to describe their interactions with the detector material. In particular, `GEANT4` should be properly instructed about the interactions and decays of $\chi^{\pm}$. This strategy would imply to treat these particles as stable at the generator level and let `GEANT4` trace them until they decay or interact. In order to overcome this step, and since the $\chi^{\pm}$ interactions within the detector are not considered, here a different strategy is adopted:

- the particle identification number[2] of χ^0 is replaced with the one of the SUSY neutralino as, from the point of view of interactions with the detector, they behave in the same way. The advantage of this replacement is that the SUSY neutralino is

[2]It is a number which uniquely identifies a particle in the MC simulations.

χ Mass	Madgraph Cross-section [pb]
90 GeV	0.1958 ± 0.0006109 pb
100 GeV	0.1409 ± 0.0004169 pb
110 GeV	0.1056 ± 0.0004023 pb
120 GeV	0.08073 ± 0.0002508 pb
200 GeV	0.01649 ± 4.451e-05 pb
500 GeV	0.000612 ± 1.887e-06 pb
1 TeV	2.132e-05 ± 8.527e-08 pb

Table 6.2: Summary of cross sections for triplet χ generated with Madgraph. Note that the cross section depends on the cuts at generation level: for tighter cuts the cross section is reduced.

already known by GEANT4, therefore there is no need to add additional description of the χ^0 particle;

- $\chi^\pm$ are forced to decay into χ^0 and $\pi^\pm$ before reaching the detector, so that only known particles are used as inputs of the detector simulation

For this second step there are different possibilities which have been investigated. The adopted strategy is to force $\chi^\pm$ to decay during the simulation of the matrix elements (in Madgraph), before hadronization. Since χ^0 gives $E_{\mathrm{T}}^{\mathrm{miss}}$ and the pions are so soft that are not reconstructed, there is no need to let them decay after Pythia. To do this an effective coupling to pions is added in the model description[3].
It should be noted that this strategy would not work for an analysis searching for disappearing tracks. In that case $\chi^\pm$ should be properly described in GEANT4.

Another important modification, which has been applied to the model, has been considering a mass splitting $\Delta M_{\chi^0-\chi^\pm} = 1$ GeV instead of $\Delta M_{\chi^0-\chi^\pm} \simeq$165 MeV. The reason is to avoid phase-space integration problems in Madgraph. The mapping of the phase-space is known to struggle in presence of VBF topology and we observed that such a small mass splitting can give problems. The value $\Delta M =$ 1 GeV has been chosen as a balance between two effects: large enough to avoid problems in Madgraph and small enough to have very soft pions from the $\chi^\pm$ decay.
The mass of χ is a parameter and can be changed in the model.

6.2.2 Matrix Element generation

MadGraph [150], [151], [152] at Leading Order (LO) has been used to generate the hard scatter process. The model is passed via a so called *UFO*[4] *file* to the Madgraph framework. Events of the following type have been generated:

$$pp > \chi\chi\ j\ j \tag{6.6}$$

where p are the proton's partons of the incoming beams, j are quarks and gluons, and $\chi\chi$ includes all the combinations of χ^+, χ^-, χ^0. Only events with two hard scatter jets have been generated, this is because a tight third jet veto is applied in the analysis (see sec. 5.8). In particular the following processes have been considered. In the Madgraph

[3]The coupling is chosen so that for ΔM =1 GeV, the BR($\chi^\pm \to jj\chi^0$) and BR($\chi^\pm \to \ell\nu\chi^0$) are at the level of per mille of the total. In this way one can simply generate events of the type $\chi^\pm \to \pi^\pm\chi^0$.
[4]Universal FeynRules Output

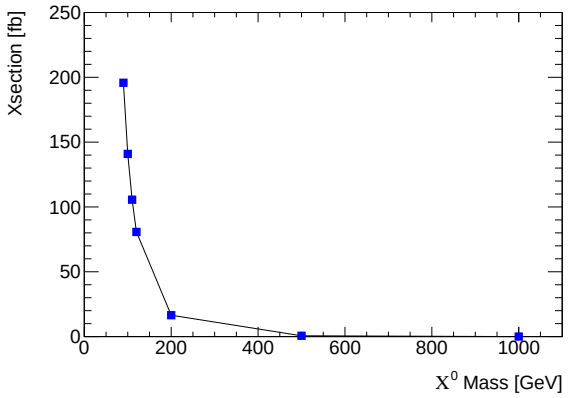

Figure 6.3: Different mass points have been generated with Madgraph. Their cross section is shown as a function of χ^0 mass. Results are obtained generating 10k events for each mass points. The corresponding values are also given in table 6.2.

language they can be written as:

```
generate pp > chi+ chi- jj QED=10 QCD=10, chi+>pi+ chi0, chi- >pi- chi0
add process pp > chi+ chi0 jj QED=10 QCD=10, chi+>pi+ chi0
add process pp > chi- chi0 jj QED=10 QCD=10, chi- >pi- chi0
add process pp > chi0 chi0 jj QED=10 QCD=10
```

As already mentioned we only generate events with two final state partons. The reason is that the pure VBF processes have two partons in the final state and in the SR requirement we apply a tight cut on the third jet. Then, as we are generating events at LO, we do not generate the matrix element with 3 jets. Therefore, since we only generate events with a single two jet multiplicity, there is no need to apply matching between the matrix elements and parton shower.
Cuts on kinematic variables are used at this level to populate the region of phase space of interest. In particular cuts are set on the minimum separation in rapidity between the two jets ($\Delta\eta$ >3); on the minimum invariant mass of the jet pair (M_{jj} >500 GeV); on the minimum p_T for the jets (p_T > 40 GeV).

Madgraph is then interfaced to Pythia8 for parton shower, hadronization and underlying event simulation.

Different mass points have been generated for validation purposes. As LEP limits on charginos, valid for any value of the chargino-neutralino mass splittings, correspond to chargino masses of m ∼90 GeV ([153], [154], [155]), we focus on m_χ ≥90 GeV. Fig. 6.3 and Table 6.2 summarize the cross sections for masses in the range ∼100 GeV up to 1 TeV. Cross sections corresponding to ∼500 GeV/1 TeV masses are very small and cannot be probed with Run2 data. For this reason we focus instead on low masses (∼100 GeV).

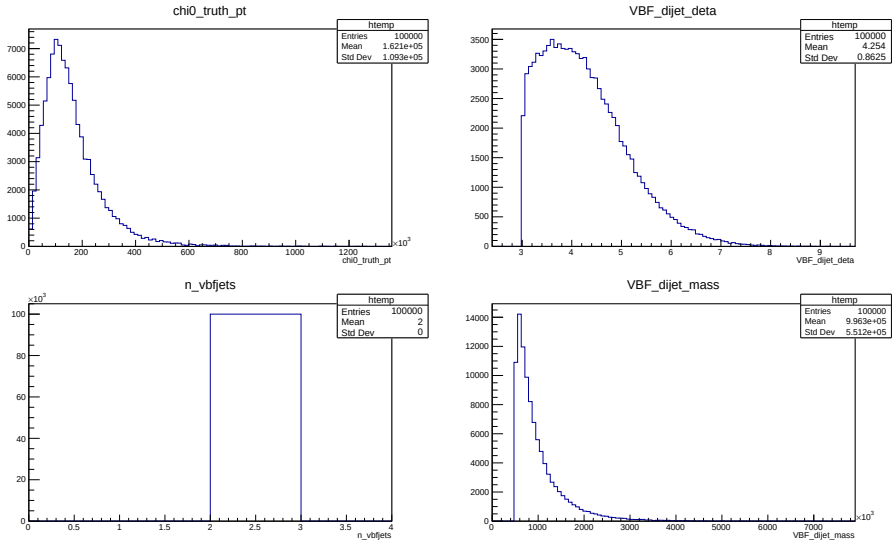

Figure 6.4: Parton level plots for truth sample of 100k events generated with M_χ =110 GeV. From the upper left: χ^0 p_T [GeV], $\Delta\eta(jj)$, parton multiplicity, invariant mass of the dijet M_{jj}.

Table 6.3: Summary of the samples which have been generated with the offical ATLAS fast simulation.

χ Mass	N generated events	Generator Cross-section [pb]
90 GeV	300 k	0.1958
110 GeV	300 k	0.1056
200 GeV	200 k	0.01649

6.2.3 Truth Level studies

Several samples have been generated at truth level[5] to validate the model implementation and to check the kinematics of the generated events.
Sanity plots at parton level are shown in Fig 6.4 for one mass point before any cuts: quarks from the hard process are selected within the truth particles container. This preliminary step is to check that there is no fundamental issue and that the parton level distributions reflect what has been generated. The plots clearly show the expected behavior and reflect the cuts set at generation level.
As a further step, validation distributions for jets (AntiKt4TruthJets with pT $>$ 25 GeV) and $E_{\mathrm{T}}^{\mathrm{miss}}$ (Truth $E_{\mathrm{T}}^{\mathrm{miss}}$ corresponding to the momentum of χ^0) have been checked for different simulated mass points. The shape comparisons (Fig. 6.5) show that there is no big differences in kinematics between the ∼100 GeV mass points, the difference arises at higher masses. As expected, in these distributions, the cuts at generation level are not as sharp as for the parton level plots. This is due to additional contribution of jets coming from parton shower radiation.

Three different mass points, with mass in the range 90-200 GeV, have been generated with the official ATLAS fast simulation of the detector. Table 6.3 summarizes the samples which have been reconstructed.

[5] I.e. no detector reconstruction is performed.

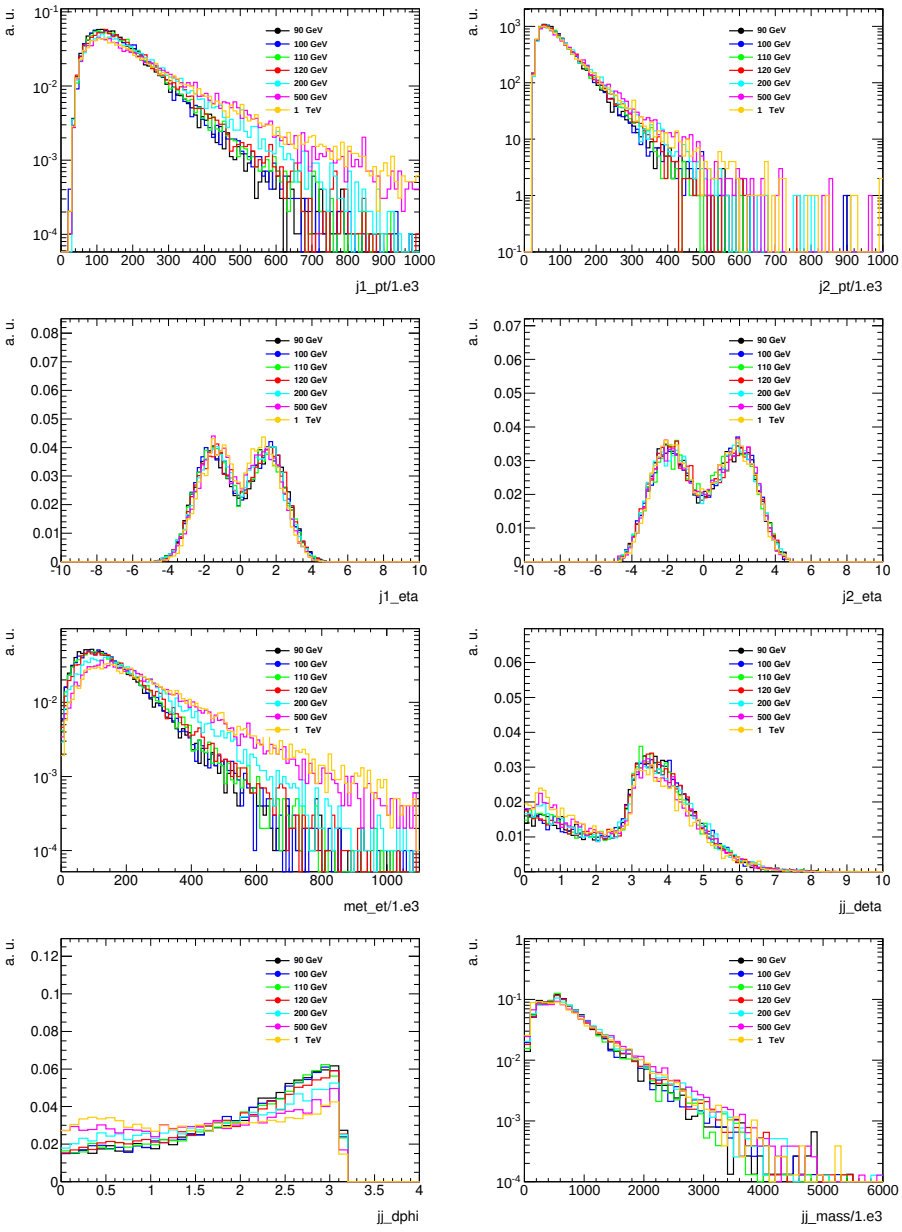

Figure 6.5: Truth plots for different kinematic variables for different mass points (10000 events each): 90 GeV (black), 100 GeV (blue), 110 GeV (green), 120 GeV (red), 200 GeV (cyan), 500 GeV (magenta), 1 TeV (orange). From the upper left: leading and subleading jet p_T [GeV] and η, $E_{\mathrm{T}}^{\mathrm{miss}}$ [GeV], $\Delta\eta(jj)$, $\Delta\Phi(jj)$, $M(jj)$ [GeV].

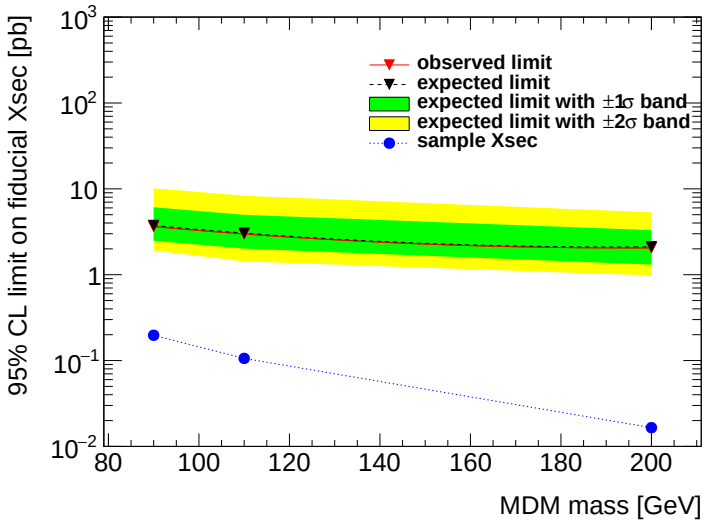

Figure 6.6: Expected and observed upper limit on fiducial cross section, using 36.1 fb^{-1} data. All the theoretical systematics on background and all experimental systematics described in 5.17 have been taken into account.

6.3 Analysis

The same analysis strategy and analysis cuts described in chapter 5 have been considered to perform this analysis. The analysis is performed using the three signal samples listed in table 6.3.
The number of signal events, passing the SR requirements (Sec. 5.8) and reweighted by the generator cross section, are shown in table 6.4. The table shows that for $36fb^{-1}$ the expected sensitivity of this analysis for this model is very small.
An exclusion fit, using the method described in Sec. 5.18, is performed to set an upper limit on the fiducial cross section of the model: the signal cross section is treated as free parameter in the fit and it corresponds to the signal strength μ.

To perform the fit, all the theoretical systematics on the backgrounds and all the experimental systematics, presented in 5.17, have been taken into account. For the signal, an inclusive systematics of 30% has been considered[6]. The results are shown in Fig. 6.6 and table 6.5. The estimated upper limits are much higher than the generator cross section, meaning that with the current dataset there is no sensitivity to the model in this analysis.

6.3.1 Impact of systematics

In order to study the impact of the systematics and of the limited MC statistics on the potential reach of such analysis, the upper limit is recomputed neglecting all the systematics and the MC statistical error. As shown in Fig. 6.7 and as summarized in table 6.6, the results are improved by more than a factor of two. However the model is still far from being tested.
As the selection criteria used here were optimized for the Higgs decaying to invisible,

[6] Additional systematics on the signal may have been neglected but they do not impact on the result.

Table 6.4: Number of events passing the SR selection (see Sec. 5.8) for the signals (table 6.3) and the total estimated background (Sec. 5.19) for 36.1 fb^{-1}. Projections for higher luminosities are also shown. As described in 6.4, these are simple extrapolations to higher luminosities, keeping the same detector simulation and background MC as it has been used for 36 fb^{-1}.

	Number of events passing the SRs selection				$\frac{Sig}{\sqrt{bkg}}$
	90 GeV	110 GeV	200 GeV	TOT background	for 90 GeV
Luminosity: 36.1 fb^{-1}					
bin 1 1.0 TeV< M_{jj} <1.5 TeV	7.4	4.0	0.6	936	0.24
bin 2 1.5 TeV< M_{jj} <2.0 TeV	10.6	5.7	0.9	672	0.41
bin 3 M_{jj} > 2 TeV	14.8	8.0	1.2	659	0.57
Luminosity: 300 fb^{-1} (Run2+Run3 statistics)					
bin 1 1.0 TeV< M_{jj} <1.5 TeV	61.0	32.8	5.1	7778	0.69
bin 2 1.5 TeV< M_{jj} <2.0 TeV	88.5	47.6	7.4	5584	1.18
bin 3 M_{jj} > 2 TeV	123.0	66.1	10.3	5476	1.66
Luminosity: 4000 fb^{-1} (High Lumi statistics)					
bin 1 1.0 TeV< M_{jj} <1.5 TeV	813.8	437.9	68.2	103711	2.52
bin 2 1.5 TeV< M_{jj} <2.0 TeV	1179.6	634.7	98.8	74459	4.32
bin 3 M_{jj} > 2 TeV	1639.2	882.0	137.3	73019	6.06

MDM mass =	90 GeV	110 GeV	200 GeV
expected limit (median)	3.744	3.052	2.116
expected limit (-1σ)	2.483	2.012	1.310
expected limit ($+1\sigma$)	6.104	4.980	3.303
expected limit (-2σ)	1.912	1.428	0.979
expected limit ($+2\sigma$)	10.172	8.313	5.327
sample cross section [pb]	0.197	0.106	0.01653

Table 6.5: Summary of observed and expected upper limits for 36.1 fb^{-1} data. All the systematics have been considered here, the error associated to the MC statistics is also included.

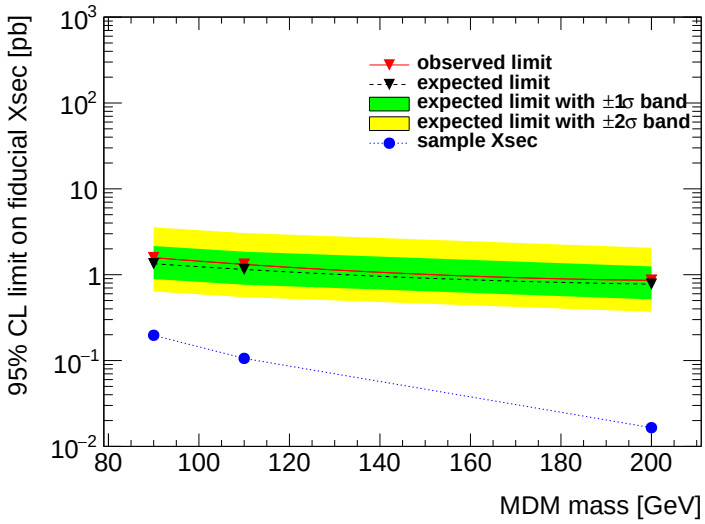

Figure 6.7: Expected and observed upper limit on fiducial cross section, using 36.1 fb^{-1} data. Both the MC statistical error and all the systematics have been neglected.

for a better reach, the analysis cuts should be re-optimized for this model in particular. Truth level studies indicates that a relaxed $\Delta\eta(j,j)$ requirement would be helpful. This of course requires dedicated studies on the multijet background which need to be kept at a negligible level.
However, even with optimized selection, more statistics is needed. In the following section an extrapolation to higher luminosities is presented.

.

MDM mass =	90 GeV	110 GeV	200 GeV
observed limit	1.579	1.318	0.859
expected limit (median)	1.341	1.151	0.776
expected limit (-1σ)	0.890	0.764	0.516
expected limit ($+1\sigma$)	2.158	1.852	1.248
expected limit (-2σ)	0.637	0.547	0.369
expected limit ($+2\sigma$)	3.563	3.056	2.058
sample cross section [pb]	0.197	0.106	0.01653

Table 6.6: Summary of observed and expected upper limits for 36.1 fb^{-1} data. In this case none of the systematics have been considered, also the error associated to the MC statistics is not considered (approximation of infinite MC statistics).

6.4 Prospect studies with higher luminosity

As with 36.1 fb^{-1} data there is no sensitivity to the model, studies with higher luminosities have been performed using a simplified approach.

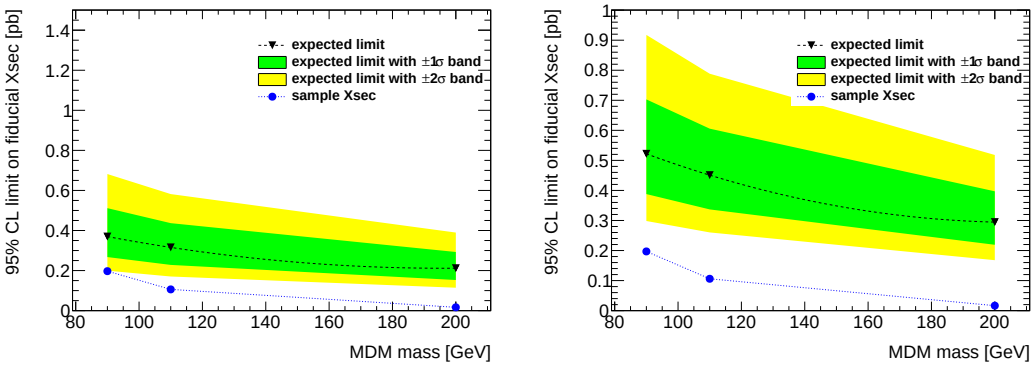

Figure 6.8: Expected upper limit on fiducial cross section, extrapolating to 300 fb^{-1}. Left: both the MC statistical error and all the systematics have been neglected. Right: some of the highest systematics are considered, the MC statistical error is neglected.

6.4.1 Run2+Run3 statistics

The expected luminosity that will be collected at the end of Run2 is estimated to be at least ∼120 fb^{-1} (end of 2018) with an instantaneous luminosity of ∼1.5×10^{34} cm^{-2}s^{-1} and an average number of collisions per bunch crossing $< \mu >$∼30. The Run2 phase will be followed by a long shutdown (2019-2020). Collisions will restart in early 2021, in the so called Run3 phase. During this phase, the instantaneous luminosity will increase up to ∼2×10^{34} cm^{-2}s^{-1} and the average number of proton-proton collisions per bunch crossing is expected to be $< \mu >$∼60. The amount of data which is expected at the end of Run3 is ∼300-400 fb^{-1}. An increase of the centre-of-mass-energy to $\sqrt{s}$ =14 TeV is possible but it has been neglected in this study (it is expected to play a small effect).
An extrapolation of the results to an integrated luminosity equal to the Run2+Run3 statistics, has been performed using Asimov data (Sec. 5.18.3).The backgrounds and the signals have been rescaled to ∼300fb^{-1}. The effect of the increased pile up has not been taken into account, assuming that ways to mitigate it will be developed.
The same experimental and theoretical systematics which has been evaluated for 36.1 fb^{-1} have been used also in this case. The MC statistical error has been neglected, in order to evaluate the sensitivity of this search, without taking into account the finite MC statistics[7].
The results are shown in Fig. 6.8 and Table 6.7, both neglecting the systematics uncertainties and considering the main ones. They show that, if the systematics uncertainties will be reduced to negligible levels, the model will start to be close to the -2σ band.

6.4.2 High Luminosity

A phase called High-Luminosity Large Hadron Collider (HL-LHC) will start after the Run3 phase (after 2025). The objective is to increase luminosity by a factor of 10 beyond the LHC design value. The HL-LHC will provide an instantaneous luminosity of 5-7×10^{34} cm^{-2}s^{-1} with the aim to achieve ∼3000-4000 fb^{-1} of total integrated luminosity delivered to ATLAS in ten years of running time. The large data sample will allow significant improvements in the precision of the measurements of Higgs couplings and

[7]This is an approximation as with infinite MC statistics both the nominal values and the systematics would be different.

Table 6.7: Expected upper limit on fiducial cross section [pb], with a simple extrapolation to Run2+Run3 Luminosity (∼300 fb^{-1} data). Results obtained both without considering systematics and with some of the main systematics. The MC statistics is treated as infinite. The fit as been performed using Asimov data. The effect of systematics may be underestimated as only a subset of the main systematics has been considered.

MDM mass =	90 GeV		110 GeV		200 GeV	
	no Syst.	with Syst.	no Syst.	with Syst.	no Syst.	with Syst.
expected limit (median)	0.369	0.522	0.315	0.450	0.212	0.294
expected limit (-1σ)	0.267	0.388	0.228	0.337	0.152	0.219
expected limit (+1σ)	0.511	0.703	0.437	0.605	0.293	0.397
expected limit (-2σ)	0.199	0.298	0.170	0.260	0.114	0.168
expected limit (+2σ)	0.682	0.917	0.582	0.788	0.389	0.518
sample cross section [pb]	0.197		0.106		0.01653	

will allow to extend the reach of searches for new physics.
The pile-up will increase substantially, in fact the higher instantaneous luminosity results in the expected mean number of interactions per bunch crossing ($<\mu>$) growing up to $<\mu>$∼140-200. This implies the necessity of developing techniques able to mitigate it in order to perform physics analysis.
The ATLAS detector and the trigger system will undergo several upgrades to collect data during the HL-LHC phase. Some of the upgrades that are planned are listed below:

- to deal with the higher trigger rate, improved triggers will be needed. A two-level trigger system will be used to select events, reducing the event rate to below 10kHz, while keeping the trigger thresholds at roughly the same values as the ones for Run2 and Run3;
- in order to achieve good performance in vertex and track reconstruction, lepton identification and heavy flavour tagging in the HL-LHC conditions, the entire tracking system will be replaced. The ID acceptance will be extended to pseudorapidities $|\eta|$ =4.0. This is particularly important because it will allow better background rejection and better reconstruction of the vertex, even for events with forward jets;
- installation of a High Granularity Timing Detector (HGTD) in front of the LAr calorimeter ($2.4<\eta<4.2$) which will allow a rejection of the pile-up forward jets (build from accidental contribution of hadrons coming from different vertices) and of jet not associated with the hard scatter vertex. This will be a helpful in case of VBF analysis;
- the muon spectrometer will be upgraded with the addition of a very forward muon tagger.

A simple extrapolation of the results to the HL scenario has been obtained by rescaling the signals and backgrounds (produced at $\sqrt{s}$ =13 TeV) to an integrated luminosity of 4000 fb^{-1}. This study is not taking into account the upgrades in the detector (which will lead to a better background rejection) and of the higher pile up (which constitute a challenge for physics analysis). Here the assumption is that the detector improvements will compensate the higher pile-up. This study is aimed at providing a first idea of the potential reach of such an analysis with an increased luminosity.
Results are shown in Fig. 6.9 and Table 6.8. The results indicate that with such a luminosity, if the systematics are kept to a negligible effect, there is exclusion potential for the lowest masses considered (M_χ ∼100 GeV).

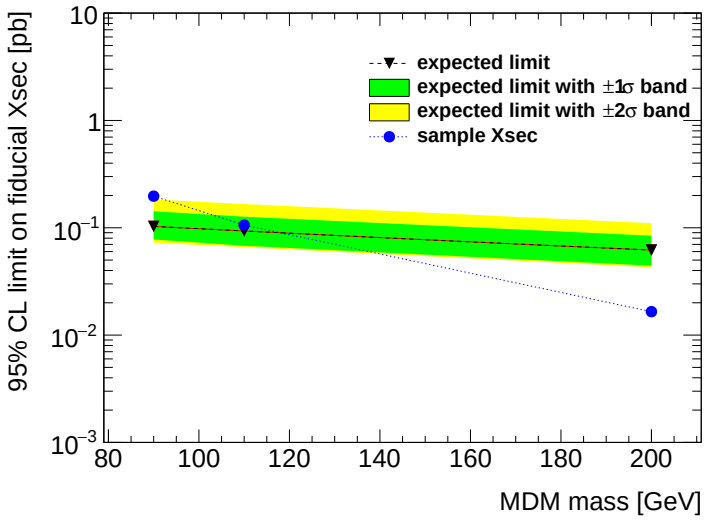

Figure 6.9: Expected upper limit on fiducial cross section, with a simple extrapolation to High Luminosity (∼4000 fb^{-1} data). Here no systematics have been considered. The MC statistics is treated as infinite. The fit as been performed using Asimov data.

A more refined analysis taking into account the expected pile up conditions and the improved detector should be performed to strengthen the result. Also, as already mentioned, cuts optimized on this model could help to achieve a better reach.

MDM mass =	90 GeV	110 GeV	200 GeV
expected limit (median)	0.103	0.093	0.062
expected limit (-1σ)	0.078	0.068	0.044
expected limit ($+1\sigma$)	0.142	0.127	0.084
expected limit (-2σ)	0.072	0.066	0.042
expected limit ($+2\sigma$)	0.183	0.166	0.110
sample cross section [pb]	0.197	0.106	0.01653

Table 6.8: Summary of expected upper limits for an extrapolation to 4000 fb^{-1} (High Lumi scenario). No systematics have been considered here, the MC statistics is treated as infinite.

6.5 Conclusions and prospects

A new $SU(2)$ fermionic triplet, added on top of the SM with an approach inspired by Minimal Dark Matter model, provides a good dark matter candidate if the B-L symmetry of the SM is respected. This triplet has mass ∼3÷3.2 TeV if the relic abundance is matched, however smaller masses are also allowed in case of non-thermal production mechanisms or if it constitute only a fraction of the DM abundance. Such a triplet can be produced at the LHC and it can be probed in different ways. It can be produced via VBF giving rise to a final states with VBF jets and $E_{\mathrm{T}}^{\mathrm{miss}}$. This final state is the same final state that has been defined to look for the invisible decay of the Higgs boson produced via VBF, described in chapter 5. The same analysis is therefore performed to test the triplet using 36.1 fb^{-1} data. To perform this analysis it has been necessary to

first produce the signal samples within the ATLAS framework. The results show that with such an integrated luminosity there is no sensitivity to the model.
The results are also extrapolated to higher luminosities, using a simplified approach. These studies indicate that with the dataset available after the HL-LHC phase it will be possible to test the lower masses of this model, assuming that the upgraded detector will lead to a better background rejection and that new techniques to deal with the pile up will be developed. Some improvements in the result can also be achieved with a proper optimization of the analysis cuts on this model, which has not been studied here.

At the LHC, the most promising ways to look for the production of these particles are the monojet searches and the disappearing track searches. The latter especially seems to be the best strategy [146].
In order to increase the sensitivity to this model when produced via VBF, we also investigated a new possibility, inspired by the approach suggested in [156]. The idea is that, before decaying into the neutral component of the triplet, the charged component can radiate a photon. This photon has peculiar characteristics: it is preferentially soft and preferentially aligned to χ^0. By exploiting these features with an appropriate selection, a final state defined by VBF jets, $E_{\mathrm{T}}^{\mathrm{miss}}$ and an additional soft photon, could in principle increase the sensitivity[8]. However, the generation of signal events for a triplet with an additional photon shows that the cross section of this process is too small to perform such an analysis in case of VBF production mode. This strategy is probably helpful in case of a mono-jet final state, where the request of an additional photon reduces the electroweak backgrounds. However, detailed studies are needed in order to evaluate carefully the contribution of soft photons from pile up and background from fake photons.

[8] The W/Z backgrounds should be heavily reduced by the request of an additional photon.

Chapter 7

Conclusions

A search for an invisibly decaying Higgs boson produced via VBF has been presented. The search uses data events from LHC proton-proton collisions at $\sqrt{s}$ =13 TeV collected with the ATLAS detector, with large missing transverse momentum and with two jets with the typical VBF characteristics. The analysis is performed as *cut and count* experiments in bins of the dijet invariant mass and no excess is observed in data with respect to the predicted backgrounds. Assuming the SM production cross section, acceptance and efficiency of the 125 GeV SM Higgs boson, a 95%CL observed (expected) upper limit is set on the BR($H \rightarrow$invisible) at 0.37% (0.28%). This result improves the ATLAS Run1 expected result for the corresponding analysis where an observed (expected) upper limit on BR($H \rightarrow$invisible) was set at 0.30% (0.35%).
More data, reduced systematics, improved MC statistics, an optimized definition for $E_{\mathrm{T}}^{\mathrm{miss}}$ and ways to deal with multijet background entering the SR because of JVT removal of hard scatter jets could bring to further improvements in the result in the future.
The results are reinterpreted in the context of the Higgs portal model where the 90%CL limit on BR($H \rightarrow$invisible) is converted into upper bounds on the dark matter nucleon scattering cross section as a function of the dark matter mass. ATLAS results are compared to direct detection searches, and they provide more stringent constraints in the low DM mass range.
Additional interpretations with hypothetical scalar bosons with mass from 75 GeV to 3 TeV in the narrow width approximation have been considered. In this case, upper limits are set on the cross section times invisible branching fraction.
This analysis has been reinterpreted in the context of models inspired by the Minimal Dark Matter model. The case of a pure WIMP triplet produced via VBF has been considered. The results show that with 36.1 fb^{-1} of integrated luminosity there is no sensitivity to the model. Higher luminosities, reduced systematics and an optimized SR selection are needed to test this model in the VBF channel.

Appendices

Appendix A

Dijet invariant mass Sherpa mismodeling

As explained in Sec. 5.4, a characteristic feature of VBF topologies is the presence of two final state jets with high invariant mass ($M(j_1, j_2)$).
The invariant mass of the dijet system is then an important variable to discriminate signal like events from the background.
High $M(j_1, j_2)$ events are selected in the analysis both for SR (see Sec. 5.8) and CRs (Sec. 5.13).
Sherpa samples have been used to simulate $W/Z+jets$ events. Data/MC comparisons in W- and Z-enriched control regions show a good data MC agreement. However comparisons at earlier levels of the selection reveal an $M(j_1, j_2)$ mismodeling. The mismodeling seems to be reduced after the third jet veto requirement, however the large statistical uncertainties do not allow to rule out the hypothesis that the mismodeling is still there. In order to not be biased by any remaining mismodeling, the analysis is designed as a cut and count experiment in three different $M(j_1, j_2)$ bins. The shape information of $M(j_1, j_2)$ is not used in the fit, this fit correspond to a data based reweighting.
The studies shown in this appendix have been done with MC Sherpa 2.2 samples, using a reduced set of 2016 data ($\sim 10 fb^{-1}$), when the selection still included a cut on $p_T(j_1, j_2)$ instead of a cut on $E_{\mathrm{T}}^{\mathrm{miss}}$. Figure A.1, A.2 and A.3 show some example distributions for $Z \to ee$, $Z \to \mu\mu$ and $W \to \mu\nu$ enriched CRs[1].

[1] Corresponding plots for $W \to e\nu$ CR are not shown here because with loose jet requirements the data can be rich of fake leptons.

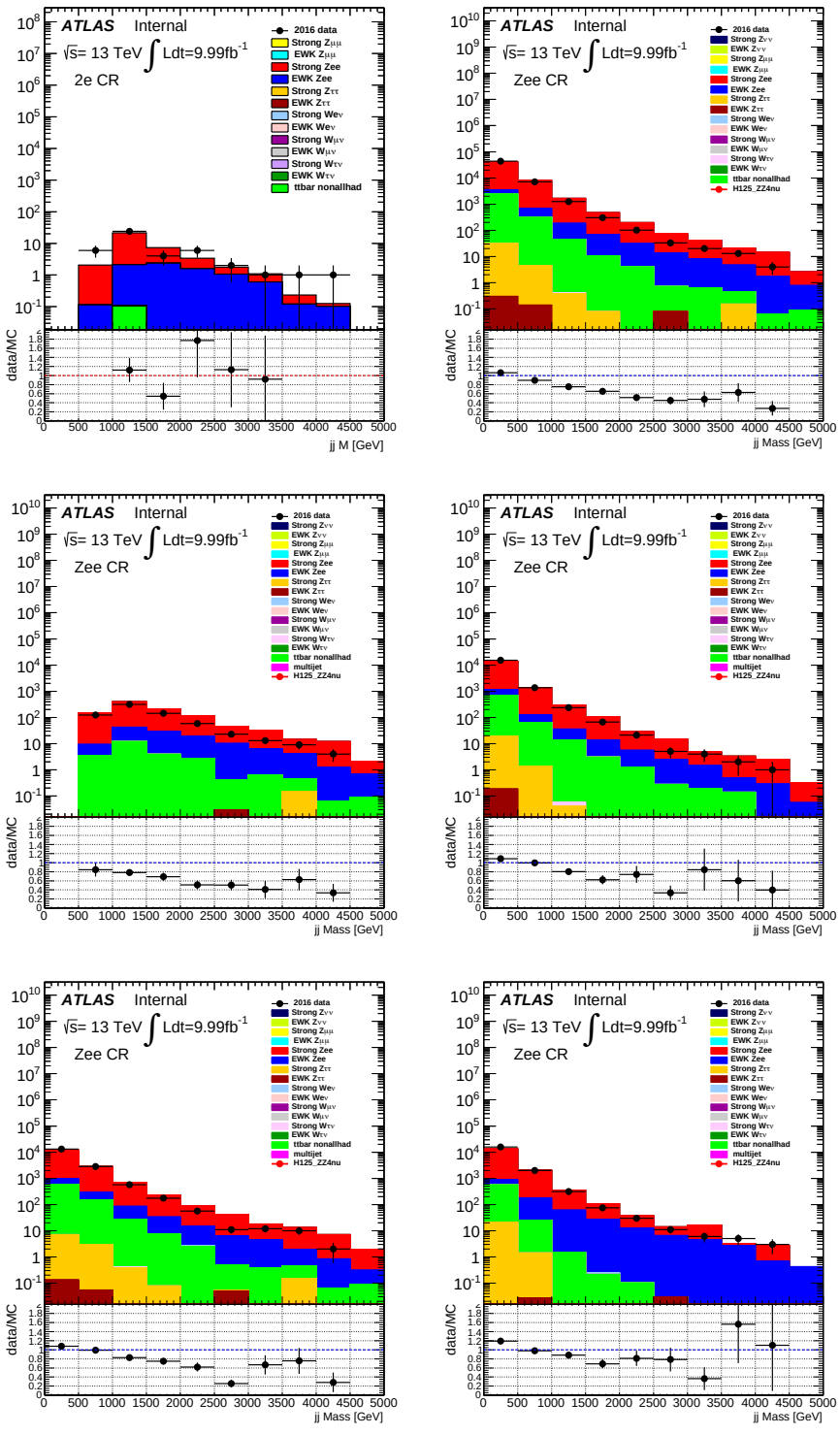

Figure A.1: $M(j_1, j_2)$ distribution for $10 fb^{-1}$ 2016 data and MC in a Zee enriched CR. From the upper left: after all the Zee CR cuts; after relaxed cuts on jets (at least 2 jets with $p_T(j1)(p_T(j1)) > 80(50)$ GeV). In the following plots to each plot is added separately a cut on a jet variable, following the order: $\Delta\eta(jj)$ >4.8; $\Delta\phi(jj)$ <1.8; $p_T(jj)$ >150 GeV; third jet veto.

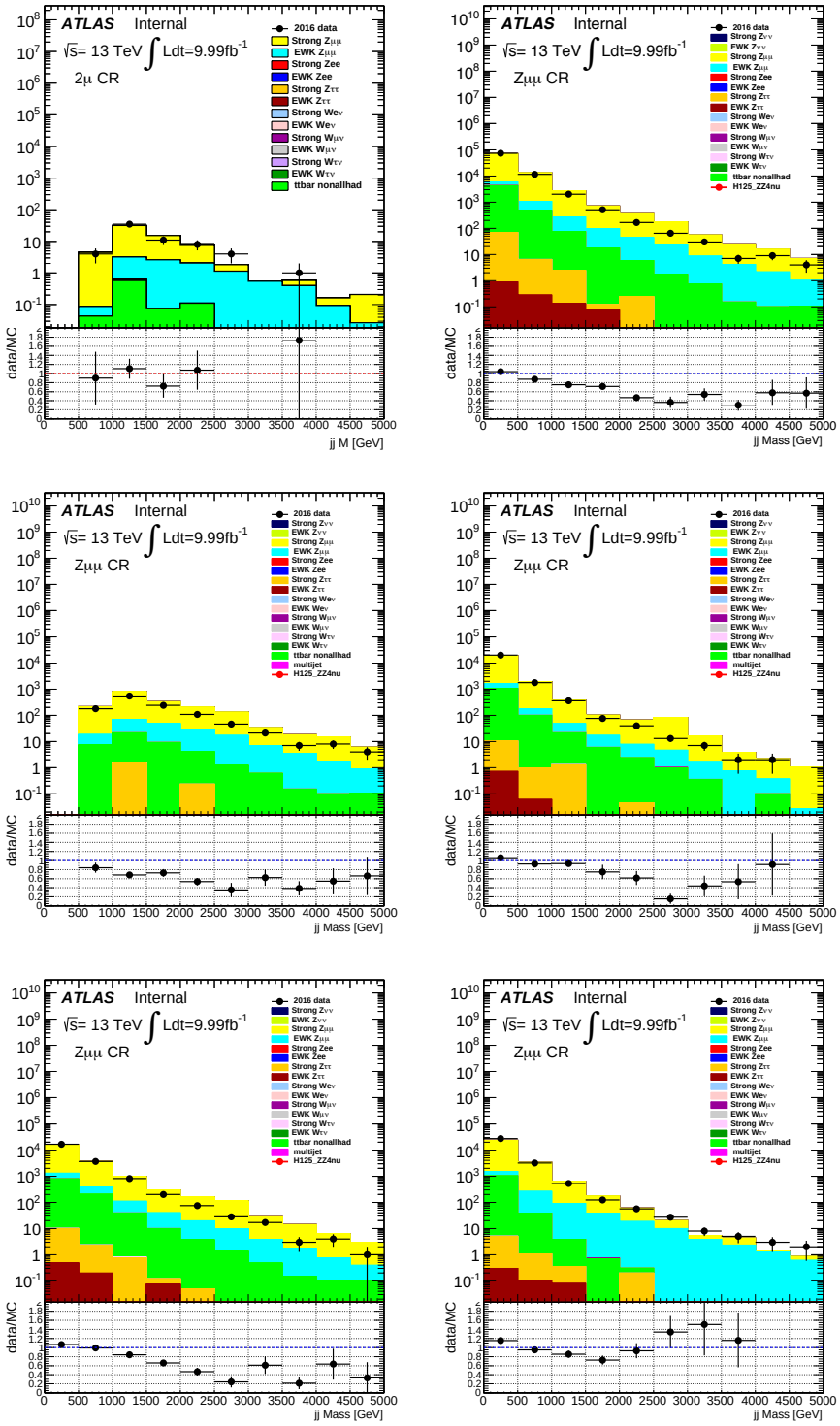

Figure A.2: $M(j_1, j_2)$ distribution for $10 fb^{-1}$ 2016 data and MC in a $Z \to \mu\mu + jets$ enriched CR. From the upper left: after all the Zee CR cuts; after relaxed cuts on jets (at least 2 jets with $p_T(j1)(p_T(j1)) > 80(50)$ GeV). In the following plots to each plot is added separately a cut on a jet variable, following the order: $\Delta\eta(jj)$ >4.8; $\Delta\phi(jj)$ <1.8; $p_T(jj)$ >150 GeV; third jet veto.

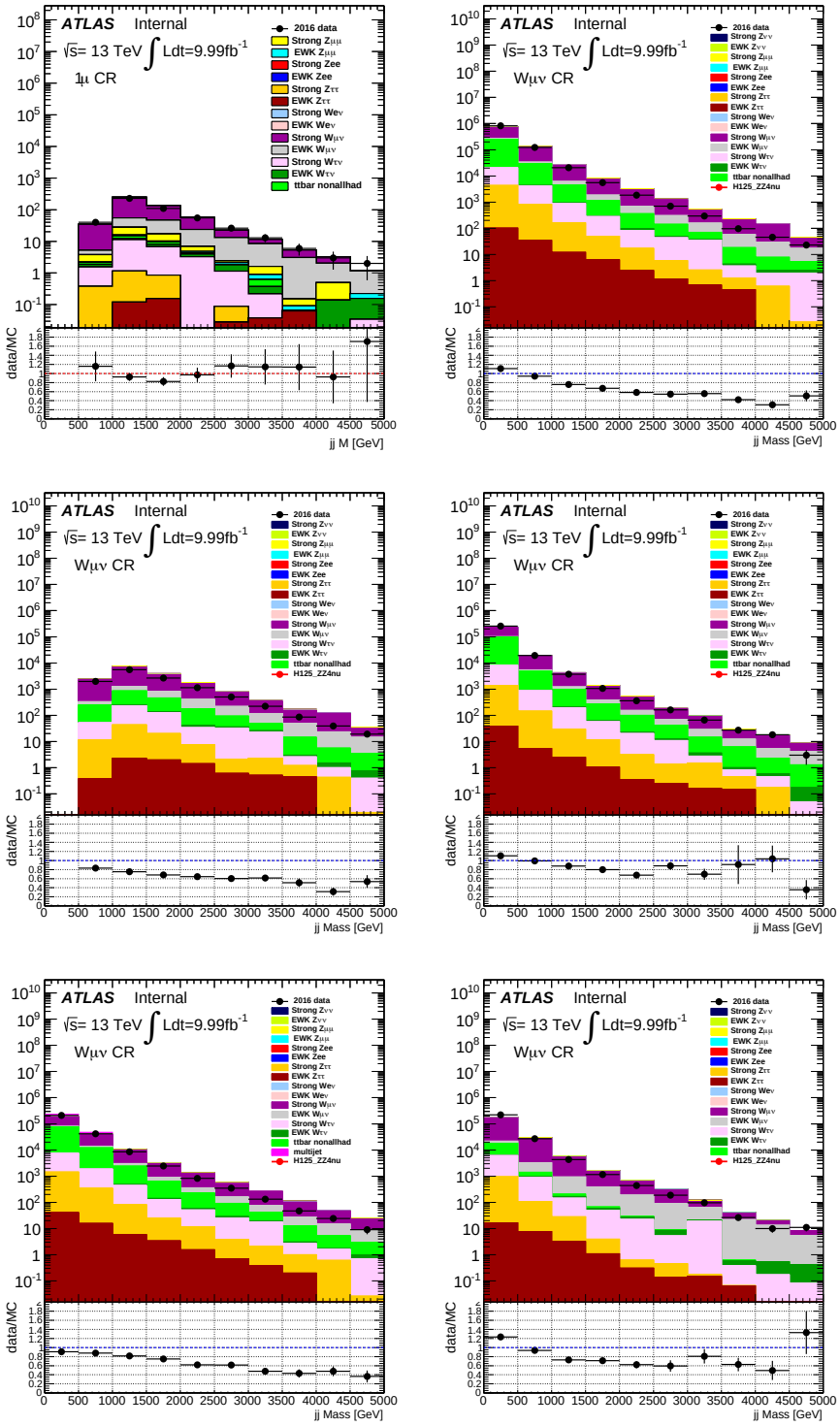

Figure A.3: $M(j_1, j_2)$ distribution for $10 fb^{-1}$ 2016 data and MC in a $W \rightarrow \mu\nu + jets$ enriched CR. From the upper left: after all the Zee CR cuts; after relaxed cuts on jets (at least 2 jets with $p_T(j1)(p_T(j1)) > 80(50)$ GeV). In the following plots to each plot is added separately a cut on a jet variable, following the order: $\Delta\eta(jj)$ >4.8; $\Delta\phi(jj)$ <1.8; $p_T(jj)$ >150 GeV; third jet veto.

Appendix B

$E_{\mathrm{T}}^{\mathrm{miss}}$ in the analysis: TST vs CST

A characteristic feature of VBF topologies is the presence of two jets highly separated in pseudorapidity (large $\Delta\eta(j_1, j_2)$). Therefore to enrich the SR of signal-like events, the SR selections requires two jets that have a wide $\Delta\eta$ separation resulting in one or both jets to be outside tracker coverage for a large fraction of events. For *VBF* $H \to inv$ signal samples 66% of the events have 1 jet falling outside the tracker acceptance, while 33% of the times both jets are outside the tracker. Given the scenario that the signal jets do not have tracking information for a significant fraction of selected events, the primary vertex may be not well defined and it is likely that a pile-up vertex is chosen as the hard-scatter one. To address possible issues that may arise when using $E_{\mathrm{T}}^{\mathrm{miss}}$ with *track based* (TST) soft term, detailed comparison of reconstructed $E_{\mathrm{T}}^{\mathrm{miss}}$ calculated using both *calorimeter based* soft term (CST) and TST prescriptions have been performed. $E_{\mathrm{T}}^{\mathrm{miss}}$ distributions are compared on a cumulative as well as on an event-by-event basis. These comparisons are done for several event categorizations of interest, namely

- reconstructed hard-scatter vertex is near or farther to the true hard-scatter vertex;
- events with zero/one/two signal jets within the tracker acceptance.

The $E_{\mathrm{T}}^{\mathrm{miss}}$ studies done for this analysis are organized in the following way. Detailed comparisons of reconstructed $E_{\mathrm{T}}^{\mathrm{miss}}$ computed using both CST and TST prescriptions are shown for signal and background MC.

B.0.1 TST/CST $E_{\mathrm{T}}^{\mathrm{miss}}$ studies for background MC

Comparisons between CST and TST $E_{\mathrm{T}}^{\mathrm{miss}}$ have been performed for some of the main background samples in the Signal Region. The backgrounds considered are:

- $Z \to \nu\nu +$ jets background;
- $W \to e\nu +$ jets background.

$Z \to \nu\nu +$ jets events pass the SR selection as their final state is very similar to the signal one. The $E_{\mathrm{T}}^{\mathrm{miss}}$ in these events is *genuine* $E_{\mathrm{T}}^{\mathrm{miss}}$, given by the two neutrinos. $W \to e\nu +$ jets events enter the SR as the electron is *lost*, that is it is not reconstructed or it falls out of the acceptance. In this case the electron contributes to the $E_{\mathrm{T}}^{\mathrm{miss}}$ reconstruction.
For *multijets* samples contaminating the SR the genuine $E_{\mathrm{T}}^{\mathrm{miss}}$ is small and most of the $E_{\mathrm{T}}^{\mathrm{miss}}$ is *fake* $E_{\mathrm{T}}^{\mathrm{miss}}$, due to (mainly) jet mis-measurements. Some studies on *multijets*

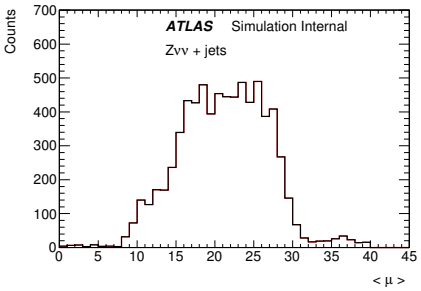

Figure B.1: Average μ distribution for $Z \to \nu\nu +$ jets MC sample.

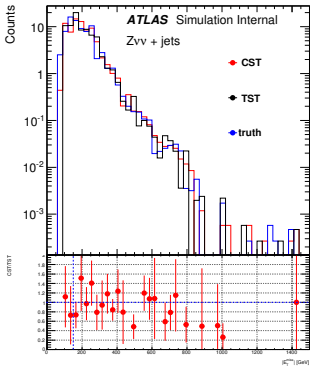

Figure B.2: CST, TST and true $E_{\mathrm{T}}^{\mathrm{miss}}$ distributions for the $Z \to \nu\nu +$ jetssample after all the analysis cuts (apart from $E_{\mathrm{T}}^{\mathrm{miss}} > 150$ GeV cut)

samples have been done but they are limited by the MC statistics: the MC statistics of dijet samples after requiring forward jets is very limited and it makes difficult the use of the *multijets* sample to investigate differences between CST and TST $E_{\mathrm{T}}^{\mathrm{miss}}$ in this analysis. For this reason the studies performed on the *multijets* samples will not be shown here.

$Z \to \nu\nu +$ jets events

The MC samples used for these studies are the strong-produced $Z \to \nu\nu +$ jets samples discussed in 5.3.2. The luminosity considered here as a reference is 11.571 fb^{-1}. The $< \mu >$ distributions of these samples is shown in Fig B.1.

Figure B.2 shows the CST, TST and true $E_{\mathrm{T}}^{\mathrm{miss}}$ distributions for the $Z \to \nu\nu +$ jets sample in the Signal Region after all the analysis cuts, excluding the one involving directly the $E_{\mathrm{T}}^{\mathrm{miss}}$ (no $E_{\mathrm{T}}^{\mathrm{miss}} > 150$ GeV cut is applied). Since the statistics after all the cuts is too limited to draw any conclusions, TST and CST comparisons are done at different levels of the cutflow (Fig. B.3).

The $E_{\mathrm{T}}^{\mathrm{miss}}$ distributions have been studied also in categories of events, in order to better check the effects on the missing transverse momentum caused by events where the reconstructed primary vertex is not the real hard scatter one or where the jets are outside the tracker acceptance. In particular two categorizations have been considered:

- events with good/bad reconstructed vertex: to select events with a good or bad reconstructed primary vertex, the Z distance between the truth primary vertex and the reconstructed primary vertex (Δz) has been computed. If Δz >0.3 mm, the

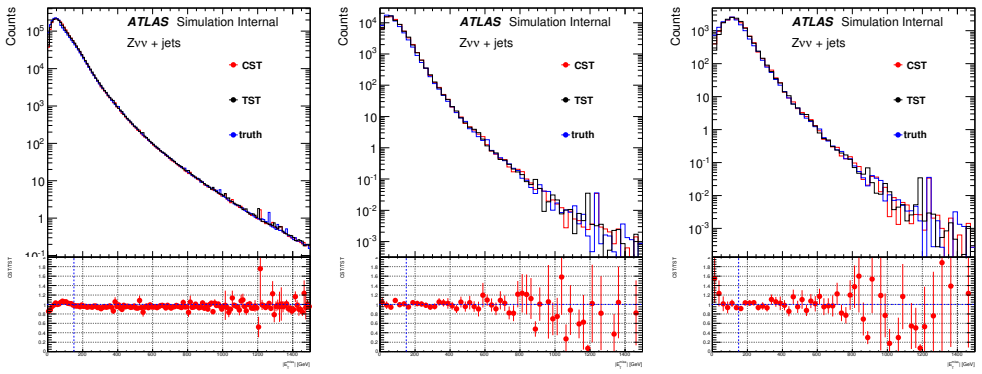

(a) (b) (c)

Figure B.3: CST, TST and true $E_{\mathrm{T}}^{\mathrm{miss}}$ distributions for the $Z \to \nu\nu$ + jetssample at different levels of the cutflow. No trigger is applied. In Figure B.3a the distributions are plotted after requiring at least two jets with $p_{\mathrm{T}} > 80$ GeV and $p_{\mathrm{T}} > 50$ GeV. In Figure B.3b also the $\Delta\eta$jj > 4.6 cut is applied and in Figure B.3c, in addition to the mentioned cuts, also the $\Delta\Phi$jj < 1.8 cut is added.

primary vertex is considered to be badly reconstructed, otherwise it is considered to be well reconstructed.

- number of jets within the tracker acceptance: the events are selected according to the number of jets which are within the tracker acceptance. If $|\eta(jet)| < 2.5$ the jet is considered to be within the tracker acceptance.

In Figure B.4 the $E_{\mathrm{T}}^{\mathrm{miss}}$ distributions are shown in bins of the number of jets within the tracker acceptance. By looking at the CST/TST ratio plots, there is no evidence for a different trend in the three bins considered and the differences between the two versions of $E_{\mathrm{T}}^{\mathrm{miss}}$ are small also when only 1 jet is reconstructed within the tracker acceptance.

Figure B.5 shows the distribution of the z distance between the truth primary vertex and the reconstructed primary vertex (Δz) for the $Z \to \nu\nu$ + jetssample after all the analysis cuts. The fraction of events with a recontructed primary vertex close to the truth primary vertex (Δz <0.3 mm) is $\sim$ 80%. In Figure B.6a, the $E_{\mathrm{T}}^{\mathrm{miss}}$ distributions are shown for events where the reconstructed primary vertex is close to the truth primary vertex (Δz < 0.3 mm), meaning that the reconstructed primary vertex is the hard scatter one, while Figure B.6b shows the case where the primary vertex has been badly reconstructed.

B.0.2 $W \to e\nu$ + jets

Some checks to compare the TST and CST $E_{\mathrm{T}}^{\mathrm{miss}}$ have been done also for the $W \to e\nu$ + jets sample. Figure B.8 shows the TST, CST and true $E_{\mathrm{T}}^{\mathrm{miss}}$ distributions for the $W \to e\nu$ + jets sample after different cuts. As shown by the plots, also for this sample the differences between the two versions of the reconstructed $E_{\mathrm{T}}^{\mathrm{miss}}$ are compatible with 1 within the statistical error bars for $E_{\mathrm{T}}^{\mathrm{miss}}$ >150 GeV.

B.0.3 $E_{\mathrm{T}}^{\mathrm{miss}}$ studies for signal MC

Similarly to what has been done for W/Z backgrounds, comparisons between TST and CST $E_{\mathrm{T}}^{\mathrm{miss}}$ have been performed also for the VBF $H \to$ invisible signal in SR. Further

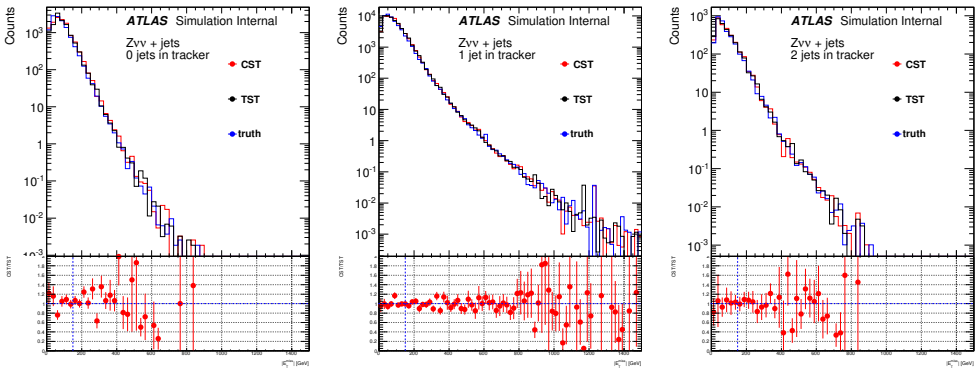

(a) (b) (c)

Figure B.4: CST, TST and true $E_{\mathrm{T}}^{\mathrm{miss}}$ distributions for the $Z \to \nu\nu$ + jetssample after after requiring at least two jets with $p_{\mathrm{T}} > 80$ GeV and $p_{\mathrm{T}} > 50$ GeV, $\Delta\eta$jj > 4.6 , $\Delta\Phi$jj < 1.8. No trigger is applied. In Figure B.4a only the events with 0 jets within the tracker acceptance are plotted, in Figure B.4b and B.4c the ones with 1 and 2 jets within the tracker acceptance respectively.

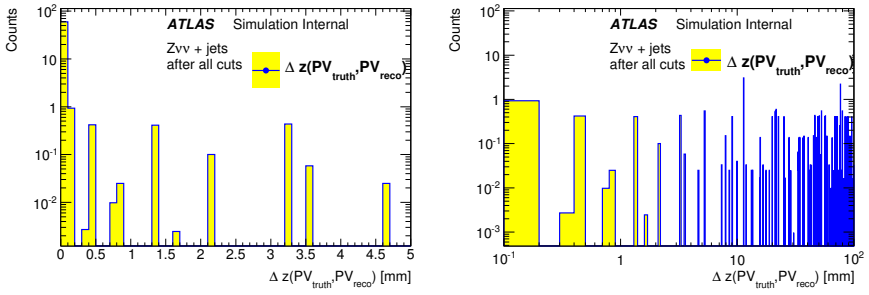

(a) (b)

Figure B.5: The plots shows the distribution of the z distance between the truth primary vertex and the reconstructed primary vertex (Δz) for the $Z \to \nu\nu$ + jetssample after all the analysis cuts (linear and log X scale).

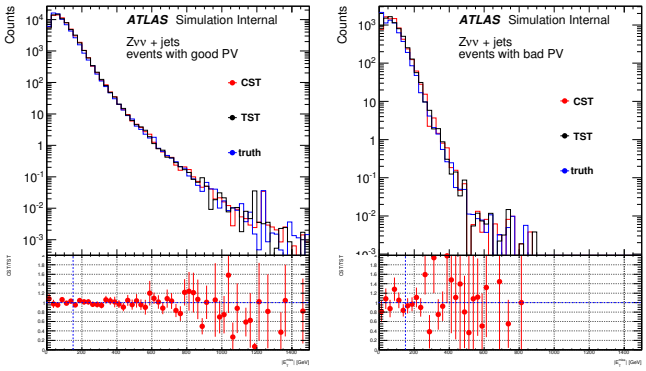

(a) (b)

Figure B.6: CST, TST and true $E_{\mathrm{T}}^{\mathrm{miss}}$ distributions for the $Z \to \nu\nu$ + jetssample after after requiring at least two jets with $p_{\mathrm{T}} > 80$ GeV and $p_{\mathrm{T}} > 50$ GeV, $\Delta\eta$jj > 4.6 , $\Delta\Phi$jj < 1.8. No trigger is applied. Figure B.6a shows the events where the reconstructed primary vertex correspond to the hard scatter one ($\Delta z(PV_{truth}, PV_{reco})$ <0.3 mm), Figure B.6b shows the events where the reconstructed primary vertex has been badly reconstructed.

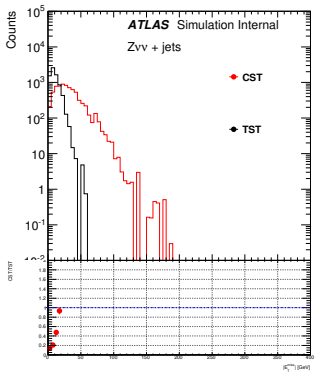

Figure B.7: CST, TST soft term distributions for the $Z \to \nu\nu$ + jetssample after the following cuts: trigger, at least two jets with $p_{\mathrm{T}} > 80$ GeV and $p_{\mathrm{T}} > 50$ GeV, $\Delta\eta$jj > 4.6 and $\Delta\Phi$jj < 1.8.

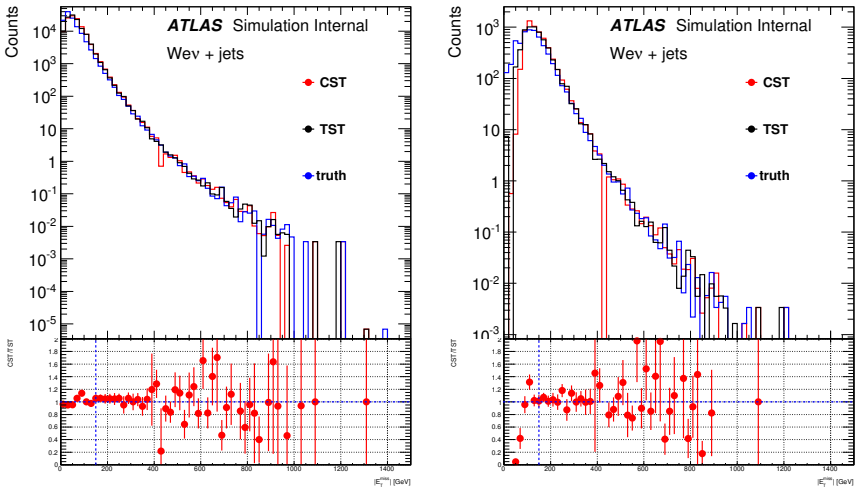

(a) (b)

Figure B.8: $E_{\mathrm{T}}^{\mathrm{miss}}$ distributions for the $W \to e\nu$ + jets sample.

comparisons of the two versions of reconstructed $E_{\mathrm{T}}^{\mathrm{miss}}$ is done in classifications of the quality of reconstructed vertex and numbers of signal jets/event that are within tracker acceptance.
For the studied classifications, we note that the decent agreement between the two prescriptions of reconstructed $E_{\mathrm{T}}^{\mathrm{miss}}$ is still valid.
Further studies of $E_{\mathrm{T}}^{\mathrm{miss}}$ were done by comparing individual reconstructed $E_{\mathrm{T}}^{\mathrm{miss}}$ terms of interest for this final state with total reconstructed $E_{\mathrm{T}}^{\mathrm{miss}}$. We note that the total term is dominated and thereby approximated by the jet term while the soft $E_{\mathrm{T}}^{\mathrm{miss}}$ is of much smaller scale than the total $E_{\mathrm{T}}^{\mathrm{miss}}$. The fact that the soft term is of much smaller scale than the total term means that the detail of CST-based or TST-based $E_{\mathrm{T}}^{\mathrm{miss}}$ does not affect the total reconstructed $E_{\mathrm{T}}^{\mathrm{miss}}$ for signal.

B.0.4 Signal Significance for TST/CST

A further check has been to compute the signal significance defined as:

$$Z = \frac{N_{signal}}{\sqrt{N_{bkg,MC}}} \tag{B.1}$$

(where N_{signal} is the number of signal events and $N_{bkg,MC}$ is the number of simulated background events), after all analysis cuts, both in case the CST $E_{\mathrm{T}}^{\mathrm{miss}}$ is used and in case the TST $E_{\mathrm{T}}^{\mathrm{miss}}$ is used. The backgrounds considered for this study are the main backgrounds contributing to the Signal Region:

- strong-produced $Z \to \nu\nu +$ jets;
- electroweak-produced $Z \to \nu\nu +$ jets;
- strong-produced $W \to \mu\nu +$ jet and $W \to e\nu +$ jets;
- electroweak-produced $W \to \mu\nu +$ jet and $W \to e\nu +$ jets;

For the signal, only the $VBFH125$ sample has been used.

Figure B.9 shows the $E_{\mathrm{T}}^{\mathrm{miss}}$ distributions for the signal and backgrounds considered, after the analysis cuts. The significance has been computed also for the different categories of events mentioned above. The luminosity, used as a reference here, is 11.571 fb^{-1}. The results are shown in Table B.1. The differences between the signal significance for TST and CST $E_{\mathrm{T}}^{\mathrm{miss}}$ are very small.

Category of events	$Z = \frac{N_S}{\sqrt{N_{bkg}}}$ for CST $E_{\mathrm{T}}^{\mathrm{miss}}$	$Z = \frac{N_S}{\sqrt{N_{bkg}}}$ for TST $E_{\mathrm{T}}^{\mathrm{miss}}$
Inclusive Events	$\frac{137.424}{\sqrt{120.703}} = 12.5085$	$\frac{138.902}{\sqrt{125.988}} = 12.375$
Good Vtx	$\frac{64.0328}{\sqrt{88.9554}} = 6.78917$	$\frac{66.9882}{\sqrt{92.0294}} = 6.98288$
Bad Vtx	$\frac{73.3915}{\sqrt{31.7477}} = 13.0254$	$\frac{71.9138}{\sqrt{33.9584}} = 12.3407$
0 jets in Trk	$\frac{90.6311}{\sqrt{62.421}} = 11.4713$	$\frac{88.6608}{\sqrt{68.15}} = 10.7399$
1 jet in Trk	$\frac{46.7932}{\sqrt{58.0236}} = 6.143$	$\frac{50.2411}{\sqrt{57.5793}} = 6.62104$
2 jets in Trk	0	0

Table B.1: The table shows the signal significance, defined as $Z = \frac{N_S}{\sqrt{N_{bkg}}}$, both for TST and CST MET, in different categories of events.

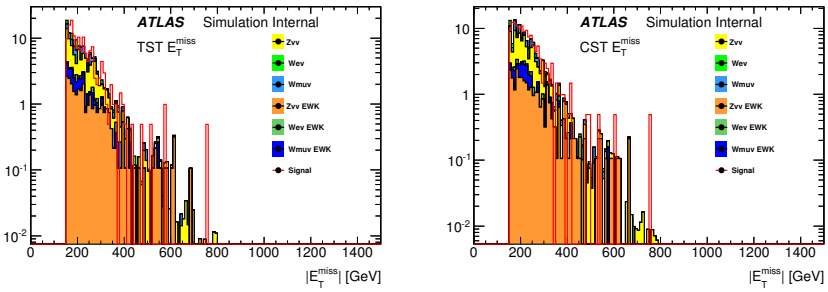

(a) (b)

Figure B.9: TST (Figure B.9a) and CST (Figure B.9b) $E_{\mathrm{T}}^{\mathrm{miss}}$ distributions for the signal and background MC sample used to compute the signal significance defined in Eq. B.0.4. The distributions are shown after all the analysis cuts.

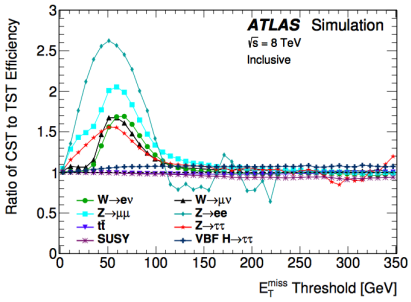

Figure B.10: Topology dependence of the CST vs TST difference: the ratio of CST to TST efficiency versus $E_{\mathrm{T}}^{\mathrm{miss}}$ threshold is shown for different processes. [157]

B.0.5 Conclusion of $E_{\mathrm{T}}^{\mathrm{miss}}$ studies

For both signal and W/Z background MC samples, it has been shown that there is no discernible difference in using TST or CST $E_{\mathrm{T}}^{\mathrm{miss}}$ for this analysis. The reason is that both the signal and background samples have relatively large genuine missing transverse momentum and the soft term scale is very small compared to the total $E_{\mathrm{T}}^{\mathrm{miss}}$ scale, so differences between CST and TST soft term are not affecting the total $E_{\mathrm{T}}^{\mathrm{miss}}$ distribution for $E_{\mathrm{T}}^{\mathrm{miss}} > 150$ GeV. This results is in agreement with previous studies carried out in ATLAS [157], Fig B.10 shows that processes with large genuine $E_{\mathrm{T}}^{\mathrm{miss}}$ (such as SUSY and ttbar) have small differences between TST and CST $E_{\mathrm{T}}^{\mathrm{miss}}$ while processes with little genuine $E_{\mathrm{T}}^{\mathrm{miss}}$ have large differences (such as $Z \to ee$ and $Z \to \mu\mu$).

Based on these studies it has been decided to use the TST $E_{\mathrm{T}}^{\mathrm{miss}}$ for this analysis. However, as discussed in Sec. 5.8.4, multijet events where fake $E_{\mathrm{T}}^{\mathrm{miss}}$ is caused by the JVT removal of hard scatter jets can contaminate the SR. A cut on CST $E_{\mathrm{T}}^{\mathrm{miss}}$ would help to reduce this contamination as all the jets, including the ones not passing JVT are used to build the CST jet term. In order to reduce this background, the threshold of TST $E_{\mathrm{T}}^{\mathrm{miss}}$ has been raised to 180 GeV (TST $E_{\mathrm{T}}^{\mathrm{miss}}$ >180 GeV) and in addition a cut on $MHT(noJVT)$ (see Sec. 5.6) has been used. This variable, correspond to the jet term of CST $E_{\mathrm{T}}^{\mathrm{miss}}$.

Appendix C

MC samples tables

In this appendix all the tables with the MC samples described in chapter 5, in section 5.3, and used through the full analysis are listed. The sample cross section (including the branching ratio), the filter efficiency, k-factor and generator are shown.

Table C.1: Sherpa Strong Produced $Z\nu\nu$ samples

Process	Generator	Xsec [pb]	k factor	filter efficiency	mc ID
$Z(\rightarrow \nu\nu) + jets$					
MAXHTPTV 0-70 CVetoBVeto	Sherpa 2.2.1	10700	0.9728	0.8216	364142
MAXHTPTV0_70 CFilterBVeto	Sherpa 2.2.1	10702	0.9728	0.11123	364143
MAXHTPTV0_70 BFilter	Sherpa 2.2.1	10709	0.9728	0.066175	364144
MAXHTPTV70_140 CVetoBVeto	Sherpa 2.2.1	603.23	0.9728	0.68924	364145
MAXHTPTV70_140 CFilterBVeto	Sherpa 2.2.1	608.15	0.9728	0.18243	364146
MAXHTPTV70_140 BFilter	Sherpa 2.2.1	603.32	0.9728	0.11955	364147
MAXHTPTV140_280 CVetoBVeto	Sherpa 2.2.1	222.28	0.9728	0.60735	364148
MAXHTPTV140_280 CFilterBVeto	Sherpa 2.2.1	221.88	0.9728	0.22527	364149
MAXHTPTV140_280 BFilter	Sherpa 2.2.1	222.4	0.9728	0.15103	364150
MAXHTPTV280_500 CVetoBVeto	Sherpa 2.2.1	47.375	0.9728	0.55887	364151
MAXHTPTV280_500 CFilterBVeto	Sherpa 2.2.1	47.397	0.9728	0.26201	364152
MAXHTPTV280_500 BFilter	Sherpa 2.2.1	47.476	0.9728	0.17514	364153
MAXHTPTV500_1000	Sherpa 2.2.1	9.9099	0.9728	1	364154
MAXHTPTV1000_E_CMS	Sherpa 2.2.1	0.81809	0.9728	1	364155

Table C.2: Sherpa Strong Produced $Z\mu\mu$ samples

Process	Generator	Xsec [pb]	k factor	filter efficiency	mc ID
$Z(\rightarrow \mu\mu) + jets$					
MAXHTPTV 0-70 CVetoBVeto	Sherpa 2.2.1	1983	0.9751	0.8221	364100
MAXHTPTV0_70 CFilterBVeto	Sherpa 2.2.1	1978.4	0.9751	0.11308	364101
MAXHTPTV0_70 BFilter	Sherpa 2.2.1	1982.2	0.9751	0.064161	364102
MAXHTPTV70_140 CVetoBVeto	Sherpa 2.2.1	108.92	0.9751	0.68873	364103
MAXHTPTV70_140 CFilterBVeto	Sherpa 2.2.1	109.42	0.9751	0.18596	364104
MAXHTPTV70_140 BFilter	Sherpa 2.2.1	108.91	0.9751	0.11375	364105
MAXHTPTV140_280 CVetoBVeto	Sherpa 2.2.1	39.878	0.9751	0.60899	364106
MAXHTPTV140_280 CFilterBVeto	Sherpa 2.2.1	39.795	0.9751	0.23308	364107
MAXHTPTV140_280 BFilter	Sherpa 2.2.1	39.908	0.9751	0.23308	364108
MAXHTPTV280_500 CVetoBVeto	Sherpa 2.2.1	8.5375	0.9751	0.55906	364109
MAXHTPTV280_500 CFilterBVeto	Sherpa 2.2.1	8.5403	0.9751	0.26528	364110
MAXHTPTV280_500 BFilter	Sherpa 2.2.1	8.4932	0.9751	0.17559	364111
MAXHTPTV500_1000	Sherpa 2.2.1	1.7881	0.9751	1	364112
MAXHTPTV1000_E_CMS	Sherpa 2.2.1	0.14769	0.9751	1	364113

Table C.3: Sherpa Strong Produced Zee samples

Process	Generator	Xsec [pb]	k factor	filter efficiency	mc ID
$Z(\rightarrow ee) + jets$					
MAXHTPTV 0-70 CVetoBVeto	Sherpa 2.2.1	1981.8	0.9751	0.82106	364114
MAXHTPTV0_70 CFilterBVeto	Sherpa 2.2.1	1980.8	0.9751	0.11295	364115
MAXHTPTV0_70 BFilter	Sherpa 2.2.1	1981.7	0.9751	0.063809	364116
MAXHTPTV70_140 CVetoBVeto	Sherpa 2.2.1	110.5	0.9751	0.69043	364117
MAXHTPTV70_140 CFilterBVeto	Sherpa 2.2.1	110.63	0.9751	0.18382	364118
MAXHTPTV70_140 BFilter	Sherpa 2.2.1	110.31	0.9751	0.11443	364119
MAXHTPTV140_280 CVetoBVeto	Sherpa 2.2.1	40.731	0.9751	0.61452	364120
MAXHTPTV140_280 CFilterBVeto	Sherpa 2.2.1	40.67	0.9751	0.23044	364121
MAXHTPTV140_280 BFilter	Sherpa 2.2.1	40.694	0.9751	0.14927	364122
MAXHTPTV280_500 CVetoBVeto	Sherpa 2.2.1	8.6743	0.9751	0.56134	364123
MAXHTPTV280_500 CFilterBVeto	Sherpa 2.2.1	8.6711	0.9751	0.26294	364124
MAXHTPTV280_500 BFilter	Sherpa 2.2.1	8.6766	0.9751	0.17223	364125
MAXHTPTV500_1000	Sherpa 2.2.1	1.8081	0.9751	1	364126
MAXHTPTV1000_E_CMS	Sherpa 2.2.1	0.14857	0.9751	1	364127

Table C.4: Sherpa Strong Produced $Z\tau\tau$ samples

Process	Generator	Xsec [pb]	k factor	filter efficiency	mc ID
$Z(\rightarrow \tau\tau) + jets$					
MAXHTPTV 0-70 CVetoBVeto	Sherpa 2.2.1	1981.6	0.9751	0.82142	364128
MAXHTPTV0_70 CFilterBVeto	Sherpa 2.2.1	1978.8	0.9751	0.11314	364129
MAXHTPTV0_70 BFilter	Sherpa 2.2.1	1981.8	0.9751	0.064453	364130
MAXHTPTV70_140 CVetoBVeto	Sherpa 2.2.1	110.37	0.9751	0.68883	364131
MAXHTPTV70_140 CFilterBVeto	Sherpa 2.2.1	110.51	0.9751	0.1829	364132
MAXHTPTV70_140 BFilter	Sherpa 2.2.1	110.87	0.9751	0.110886	364133
MAXHTPTV140_280 CVetoBVeto	Sherpa 2.2.1	40.781	0.9751	0.60821	364134
MAXHTPTV140_280 CFilterBVeto	Sherpa 2.2.1	40.74	0.9751	0.22897	364135
MAXHTPTV140_280 BFilter	Sherpa 2.2.1	40.761	0.9751	0.13442	364136
MAXHTPTV280_500 CVetoBVeto	Sherpa 2.2.1	8.5502	0.9751	0.56036	364137
MAXHTPTV280_500 CFilterBVeto	Sherpa 2.2.1	8.6707	0.9751	0.26245	364138
MAXHTPTV280_500 BFilter	Sherpa 2.2.1	8.6804	0.9751	0.17313	364139
MAXHTPTV500_1000	Sherpa 2.2.1	1.8096	0.9751	1	364140
MAXHTPTV1000_E_CMS	Sherpa 2.2.1	0.14834	0.9751	1	364141

Table C.5: Sherpa Strong Produced $We\nu$ samples

Process	Generator	Xsec [pb]	k factor	filter efficiency	mc ID
$W(\rightarrow e\nu) + jets$					
MAXHTPTV 0-70 CVetoBVeto	Sherpa 2.2.1	19127	0.9702	0.82447	364170
MAXHTPTV0_70 CFilterBVeto	Sherpa 2.2.1	19130	0.9702	0.1303	364171
MAXHTPTV0_70 BFilter	Sherpa 2.2.1	19135	0.9702	0.044141	364171
MAXHTPTV70_140 CVetoBVeto	Sherpa 2.2.1	942.58	0.9702	0.66872	364173
MAXHTPTV70_140 CFilterBVeto	Sherpa 2.2.1	945.67	0.9702	0.22787	364174
MAXHTPTV70_140 BFilter	Sherpa 2.2.1	945.15	0.9702	0.10341	364175
MAXHTPTV140_280 CVetoBVeto	Sherpa 2.2.1	339.81	0.9702	0.59691	364176
MAXHTPTV140_280 CFilterBVeto	Sherpa 2.2.1	339.87	0.9702	0.28965	364177
MAXHTPTV140_280 BFilter	Sherpa 2.2.1	339.79	0.9702	0.10898	364178
MAXHTPTV280_500 CVetoBVeto	Sherpa 2.2.1	72.084	0.9702	0.54441	364179
MAXHTPTV280_500 CFilterBVeto	Sherpa 2.2.1	72.128	0.9702	0.31675	364180
MAXHTPTV280_500 BFilter	Sherpa 2.2.1	72.113	0.9702	0.13391	364181
MAXHTPTV500_1000	Sherpa 2.2.1	15.224	0.9702	1	364182
MAXHTPTV1000_E_CMS	Sherpa 2.2.1	1.2334	0.9702	1	364183

Table C.6: Sherpa Strong Produced $W\mu\nu$ samples

Process	Generator	Xsec [pb]	k factor	filter efficiency	mc ID
$W(\rightarrow \mu\nu) + jets$					
MAXHTPTV 0-70 CVetoBVeto	Sherpa 2.2.1	19143	0.9702	0.82380	364156
MAXHTPTV0_70 CFilterBVeto	Sherpa 2.2.1	19121	0.9702	0.1303	364157
MAXHTPTV0_70 BFilter	Sherpa 2.2.1	19135	0.9702	0.044141	364158
MAXHTPTV70_140 CVetoBVeto	Sherpa 2.2.1	944.85	0.9702	0.67463	364159
MAXHTPTV70_140 CFilterBVeto	Sherpa 2.2.1	937.78	0.9702	0.23456	364160
MAXHTPTV70_140 BFilter	Sherpa 2.2.1	944.63	0.9702	0.075648	364161
MAXHTPTV140_280 CVetoBVeto	Sherpa 2.2.1	339.54	0.9702	0.9702	364162
MAXHTPTV140_280 CFilterBVeto	Sherpa 2.2.1	340.06	0.9702	0.28947	364163
MAXHTPTV140_280 BFilter	Sherpa 2.2.1	339.54	0.9702	0.10872	364164
MAXHTPTV280_500 CVetoBVeto	Sherpa 2.2.1	72.067	0.9702	0.54647	364165
MAXHTPTV280_500 CFilterBVeto	Sherpa 2.2.1	72.198	0.9702	0.31743	364166
MAXHTPTV280_500 BFilter	Sherpa 2.2.1	72.045	0.9702	0.13337	364167
MAXHTPTV500_1000	Sherpa 2.2.1	15.01	0.9702	1	364168
MAXHTPTV1000_E_CMS	Sherpa 2.2.1	1.2344	0.9702	1	364169

Table C.7: Sherpa Strong Produced $W\tau\nu$ samples

Process	Generator	Xsec [pb]	k factor	filter efficiency	mc ID
$W(\rightarrow \tau\nu) + jets$					
MAXHTPTV 0-70 CVetoBVeto	Sherpa 2.2.1	19152	0.9702	0.82495	364184
MAXHTPTV0_70 CFilterBVeto	Sherpa 2.2.1	19153	0.9702	0.12934	364185
MAXHTPTV0_70 BFilter	Sherpa 2.2.1	19163	0.9702	0.044594	364186
MAXHTPTV70_140 CVetoBVeto	Sherpa 2.2.1	947.65	0.9702	0.67382	364187
MAXHTPTV70_140 CFilterBVeto	Sherpa 2.2.1	946.73	0.9702	0.22222	364188
MAXHTPTV70_140 BFilter	Sherpa 2.2.1	943.3	0.9702	0.10391	364189
MAXHTPTV140_280 CVetoBVeto	Sherpa 2.2.1	339.36	0.9702	0.59622	364190
MAXHTPTV140_280 CFilterBVeto	Sherpa 2.2.1	339.63	0.9702	0.29025	364191
MAXHTPTV140_280 BFilter	Sherpa 2.2.1	339.55	0.9702	0.11229	364192
MAXHTPTV280_500 CVetoBVeto	Sherpa 2.2.1	72.065	0.9702	0.54569	364193
MAXHTPTV280_500 CFilterBVeto	Sherpa 2.2.1	71.976	0.9702	0.31648	364194
MAXHTPTV280_500 BFilter	Sherpa 2.2.1	72.026	0.9702	0.13426	364111
MAXHTPTV500_1000	Sherpa 2.2.1	15.046	0.9702	1	364112
MAXHTPTV1000_E_CMS	Sherpa 2.2.1	1.2339	0.9702	1	364113

Table C.8: Powheg $t\bar{t}$, single top samples

Process	Generator	Xsec [pb]	k factor	filter efficiency	mc ID
$t\bar{t}$, single top,					
ttbar hdamp172p5_nonallhad	Powheg	451.59151575	1	1	410000
singletop tchan_lept_top	Powheg	43.739	1.0094	0.1303	410011
singletop tchan_lept_antitop	Powheg	25.778	1.0093	0.044141	410012
Wt inclusive_top	Powheg	34.009	1.0193	0.66872	410013
Wt inclusive_antitop	Powheg	33.989	1.054	0.22787	410014

Table C.9: Diboson samples ($VV + jets$)

Process	Generator	Xsec [pb]	k factor	filter efficiency	mc ID
$W(\rightarrow e\nu) + jets$					
ZqqZvv	Sherpa 2.2.1	15.564	1	0.27976	363355
ZqqZll	Sherpa 2.2.1	15.563	1	0.13961	363356
WqqZvv	Sherpa 2.2.1	6.7973	1	1	363357
WqqZll	Sherpa 2.2.1	3.437	1	1	363358
WpqqWmlv	Sherpa 2.2.1	24.717	1	1	363359
WplvWmqq	Sherpa 2.2.1	112.74	1	1	363360
WlvZqq	Sherpa 2.2.1	11.413	1	1	363489

Table C.10: ewk produced $V + jets$ samples

Process	Generator	Xsec [pb]	k factor	filter efficiency	mc ID
ewk produced $V + jets$					
Zee2jets Min_N_TChannel	Sherpa 2.2.1	0.63051	1	1	308092
Zmm2jets Min_N_TChannel	Sherpa 2.2.1	0.63591	1	1	308093
Ztautau2jets Min_N_TChannel	Sherpa 2.2.1	0.63287	1	1	308094
Znunu2jets Min_N_TChannel	Sherpa 2.2.1	2.9327	1	1	308095
Wenu2jets Min_N_TChannel	Sherpa 2.2.1	6.8072	1	1	308096
Wmunu2jets Min_N_TChannel	Sherpa 2.2.1	6.81	1	1	308097
Wtaunu2jets Min_N_TChannel	Sherpa 2.2.1	6.791	1	1	308098

Appendix D

Lepton veto optimization in SR

In the scope of trying to reduce the SR background coming from events containing leptons, a lepton veto optimization study has been performed.
These studies have been performed at an early stage of the analysis when there were some differences in SR selection with respect to the one presented in Sec. 5.8. In particular:

- the SR $E_{\mathrm{T}}^{\mathrm{miss}}$ cut was replaced by a cut on the transverse momentum of the dijet system ($p_T(j_1, j_2)$);
- the $p_T(j_1, j_2)$ was required to be $p_T(j_1, j_2)$ >150 GeV (instead of 180 GeV);
- the lepton veto p_T threshold was set to 10 GeV instead of 7 GeV (due to limitations of the samples available at that time);
- no requirement on $MHT(noJVT)$ was applied;
- a partial dataset of $10fb_{-1}$ has been used.

D.1 Lepton veto: nominal working point

Leptons satisfying the following criteria are currently vetoed when selecting SR events:

- isolated muons selected with medium track quality criteria, as outlined in section 5.6;
- isolated tight electrons which are not in the so called crack region of the calorimeter ($1.37<|\eta|<1.52$), as outlined in section 5.6;

This means that all the events which contain either non isolated leptons, leptons having looser quality criteria or electrons falling into the crack region, are selected as signal events. The contribution of Monte Carlo backgrounds events entering the SR using this definition for the lepton veto is shown in table D.1.

D.2 Lepton veto: looser working point

The backgrounds with final state leptons could be reduced more efficiently using a looser working point. In particular the following veto has been tested:

- veto non isolated muons with loose track selection criteria. These muons include also the standalone muons, which can be reconstructed up to $\eta = 2.7$;

- veto non isolated electrons with loose likelihood criteria, including electrons in the crack region of the calorimeter.

This new lepton veto helps reducing by 5.4 % the total background in SR, as shown in table D.2. In particular $We\nu$ background is reduced by 3.4 % , $W\mu\nu$ background is reduced by 17 % and $W\tau\nu$ background is reduced by 4 % . The signal yield is not affected by changes in the lepton veto definition.

SR	Nevents
Zvv :	558.8 ± 26.6
Zvv EWK :	91.2 ± 3.1
Zmumu :	12.2 ± 3.1
Zmumu EWK :	0.9 ± 0.2
Zee :	0.0 ± 0.0
Zee EWK :	0.0 ± 0.0
Ztautau :	7.6 ± 2.2
Ztautau EWK :	0.4 ± 0.1
Wenu :	79.0 ± 15.8
Wenu WEK :	12.7 ± 1.4
Wmunu :	260.7 ± 17.6
Wmunu EWK :	29.3 ± 2.1
Wtaunu :	248.0 ± 16.8
Wtaunu EWK:	55.9 ± 3.0
ttbar :	3.9 ± 0.6
multijet :	0.0 ± 0.0
sum all bkg :	1360.8 ± 39.9
signal :	464.3 ± 15.0
S/sqrt(bkg) :	12.6

Table D.1: tab: MC background events in SR region (inclusive Mjj bin). Yields are normalized to 10 fb^{-1}. The MC used have p tag p2669 (cache 20.7.6.4, Sherpa 2.2). Veto tight isolated leptons as described in D.1.

SR	Nevents
Zvv :	558.3 ± 26.6
Zvv EWK :	90.9 ± 3.1
Zmumu :	5.8 ± 2.4
Zmumu EWK :	0.5 ± 0.2
Zee :	0.0 ± 0.0
Zee EWK :	0.0 ± 0.0
Ztautau :	6.9 ± 2.1
Ztautau EWK :	0.3 ± 0.1
Wenu :	75.8 ± 15.7
Wenu WEK :	12.2 ± 1.4
Wmunu :	218.3 ± 15.9
Wmunu EWK :	21.6 ± 1.8
Wtaunu :	238.2 ± 16.5
Wtaunu EWK:	54.3 ± 3.0
ttbar :	3.4 ± 0.6
multijet :	0.0 ± 0.0
sum all bkg :	1286.7 ± 38.9
signal :	463.5 ± 15.0
S/sqrt(bkg) :	12.9

Table D.2: tab: MC background events in SR region (inclusive Mjj bin). Yields are normalized to 10 fb^{-1}. The MC used have p tag p2669 (cache 20.7.6.4, Sherpa 2.2). Veto non isolated leptons with looser quality criteria as described in D.2.

The SR background could be reduced more efficiently with a tighter lepton veto, however the final analysis did not use the lepton veto criteria shown here. It has been preferred to increase the signal significance by changing other selections in order to add complexity to the analysis due to different collections of leptons.

Appendix E

Systematics tables

The following sections show the pre and post-fit systematic uncertainty tables. Note that individual systematic uncertainties with less than a 1% impact on the total yield have been truncated from the list, though they are of course included in the fit.

E.1 Signal region

Table E.1: Pre-fit signal region. Breakdown of the dominant systematic uncertainties on background estimates in the various signal regions. Note that the individual uncertainties can be correlated, and do not necessarily add up quadratically to the total background uncertainty. The percentages show the size of the uncertainty relative to the total expected background.

Uncertainty of channel	SR1	SR2	SR3
Total background expectation	980.66	697.00	560.27
Total statistical ($\sqrt{N_{\text{exp}}}$)	±31.32	±26.40	±23.67
Total background systematic	±187.28 [19.10%]	±134.10 [19.24%]	±100.94 [18.02%]
alpha_REN_QCD_W_bin1	±74.57 [7.6%]	±0.00 [0.00%]	±0.00 [0.00%]
alpha_REN_QCD_Z_bin1	±74.28 [7.6%]	±0.00 [0.00%]	±0.00 [0.00%]
alpha_JET_Flavor_Composition	±69.62 [7.1%]	±15.76 [2.3%]	±13.73 [2.5%]
alpha_JET_Pileup_PtTerm	±66.85 [6.8%]	±26.64 [3.8%]	±30.76 [5.5%]
alpha_JET_EffectiveNP_Modelling2	±49.37 [5.0%]	±49.51 [7.1%]	±28.86 [5.2%]
alpha_JET_EtaIntercalibration_Modelling	±44.96 [4.6%]	±38.31 [5.5%]	±31.77 [5.7%]
alpha_RESUM_QCD_W_bin1	±44.58 [4.5%]	±0.00 [0.00%]	±0.00 [0.00%]
alpha_CKKW_QCD_W_bin1	±39.81 [4.1%]	±0.00 [0.00%]	±0.00 [0.00%]
alpha_RESUM_QCD_Z_bin1	±39.37 [4.0%]	±0.00 [0.00%]	±0.00 [0.00%]
gamma_stat_SR1_cuts_bin_0	±32.70 [3.3%]	±0.00 [0.00%]	±0.00 [0.00%]
alpha_PRW_DATASF	±26.13 [2.7%]	±17.35 [2.5%]	±10.57 [1.9%]
Lumi	±21.42 [2.2%]	±15.28 [2.2%]	±12.32 [2.2%]
alpha_JER	±20.82 [2.1%]	±35.61 [5.1%]	±26.19 [4.7%]
alpha_FACT_QCD_W_bin1	±19.36 [2.0%]	±0.00 [0.00%]	±0.00 [0.00%]
alpha_FACT_QCD_Z_bin1	±17.57 [1.8%]	±0.00 [0.00%]	±0.00 [0.00%]
alpha_MET_SoftTrk_ResoPara	±15.56 [1.6%]	±1.83 [0.26%]	±12.94 [2.3%]
alpha_MET_SoftTrk_Scale	±15.43 [1.6%]	±5.24 [0.75%]	±3.87 [0.69%]
alpha_JET_EffectiveNP_Modelling1	±15.20 [1.5%]	±23.15 [3.3%]	±15.20 [2.7%]
alpha_JET_Flavor_Response	±13.12 [1.3%]	±0.37 [0.05%]	±6.90 [1.2%]
alpha_CKKW_QCD_Z_bin1	±12.24 [1.2%]	±0.00 [0.00%]	±0.00 [0.00%]
alpha_JET_EtaIntercalibration_TotalStat	±10.58 [1.1%]	±0.03 [0.00%]	±0.80 [0.14%]
alpha_JET_EtaInt	±10.02 [1.0%]	±19.60 [2.8%]	±15.10 [2.7%]
alpha_MET_SoftTrk_ResoPerp	±8.90 [0.91%]	±7.16 [1.0%]	±4.54 [0.81%]
alpha_JET_Pileup_RhoTopology	±8.07 [0.82%]	±28.53 [4.1%]	±17.61 [3.1%]
alpha_JET_EffectiveNP_Mixed1	±5.89 [0.60%]	±11.89 [1.7%]	±11.64 [2.1%]
alpha_JET_Pileup_OffsetNPV	±5.61 [0.57%]	±0.30 [0.04%]	±8.69 [1.6%]
alpha_JET_EffectiveNP_Modelling3	±4.82 [0.49%]	±9.99 [1.4%]	±3.35 [0.60%]
alpha_JET_Pileup_OffsetMu	±4.32 [0.44%]	±8.01 [1.1%]	±4.40 [0.79%]
alpha_JET_EffectiveNP_Statistical6	±0.98 [0.10%]	±7.75 [1.1%]	±1.59 [0.28%]
alpha_RESUM_QCD_W_bin3	±0.00 [0.00%]	±0.00 [0.00%]	±19.97 [3.6%]
alpha_CKKW_QCD_Z_bin2	±0.00 [0.00%]	±13.57 [1.9%]	±0.00 [0.00%]
alpha_CKKW_QCD_W_bin3	±0.00 [0.00%]	±0.00 [0.00%]	±19.54 [3.5%]
alpha_CKKW_QCD_W_bin2	±0.00 [0.00%]	±22.23 [3.2%]	±0.00 [0.00%]
alpha_RESUM_EWK_W_bin3	±0.00 [0.00%]	±0.00 [0.00%]	±10.07 [1.8%]
alpha_CKKW_QCD_Z_bin3	±0.00 [0.00%]	±0.00 [0.00%]	±5.67 [1.0%]
alpha_FACT_QCD_W_bin3	±0.00 [0.00%]	±0.00 [0.00%]	±9.43 [1.7%]
alpha_FACT_QCD_W_bin2	±0.00 [0.00%]	±16.36 [2.3%]	±0.00 [0.00%]
alpha_RESUM_EWK_Z_bin3	±0.00 [0.00%]	±0.00 [0.00%]	±7.34 [1.3%]
alpha_REN_QCD_Z_bin2	±0.00 [0.00%]	±55.61 [8.0%]	±0.00 [0.00%]
alpha_REN_QCD_Z_bin3	±0.00 [0.00%]	±0.00 [0.00%]	±40.69 [7.3%]
alpha_RESUM_QCD_Z_bin3	±0.00 [0.00%]	±0.00 [0.00%]	±27.78 [5.0%]
alpha_PDF_QCD_Z_bin3	±0.00 [0.00%]	±0.00 [0.00%]	±6.15 [1.1%]
alpha_RESUM_QCD_W_bin2	±0.00 [0.00%]	±27.95 [4.0%]	±0.00 [0.00%]
alpha_REN_QCD_W_bin3	±0.00 [0.00%]	±0.00 [0.00%]	±28.18 [5.0%]
alpha_REN_QCD_W_bin2	±0.00 [0.00%]	±45.23 [6.5%]	±0.00 [0.00%]
alpha_PDF_QCD_W_bin2	±0.00 [0.00%]	±8.74 [1.3%]	±0.00 [0.00%]
alpha_FACT_QCD_Z_bin2	±0.00 [0.00%]	±17.15 [2.5%]	±0.00 [0.00%]
alpha_FACT_QCD_Z_bin3	±0.00 [0.00%]	±0.00 [0.00%]	±11.52 [2.1%]
gamma_stat_SR2_cuts_bin_0	±0.00 [0.00%]	±27.97 [4.0%]	±0.00 [0.00%]
alpha_FACT_EWK_W_bin3	±0.00 [0.00%]	±0.00 [0.00%]	±10.11 [1.8%]
alpha_RESUM_QCD_Z_bin2	±0.00 [0.00%]	±28.31 [4.1%]	±0.00 [0.00%]
alpha_FACT_EWK_Z_bin3	±0.00 [0.00%]	±0.00 [0.00%]	±10.20 [1.8%]
gamma_stat_SR3_cuts_bin_0	±0.00 [0.00%]	±0.00 [0.00%]	±15.70 [2.8%]

Table E.2: Post-fit signal region. Breakdown of the dominant systematic uncertainties on background estimates in the various signal regions. Note that the individual uncertainties can be correlated, and do not necessarily add up quadratically to the total background uncertainty. The percentages show the size of the uncertainty relative to the total expected background.

Uncertainty of channel	SR1	SR2	SR3
Total background expectation	980.66	697.00	560.27
Total statistical ($\sqrt{N_{\text{exp}}}$)	±31.32	±26.40	±23.67
Total background systematic	±30.57 [3.12%]	±25.64 [3.68%]	±23.31 [4.16%]
k_Zbin1	±121.51 [12.4%]	±0.00 [0.00%]	±0.00 [0.00%]
k_Wbin1	±99.12 [10.1%]	±0.00 [0.00%]	±0.00 [0.00%]
alpha_REN_QCD_W_bin1	±73.89 [7.5%]	±0.00 [0.00%]	±0.00 [0.00%]
alpha_REN_QCD_Z_bin1	±73.71 [7.5%]	±0.00 [0.00%]	±0.00 [0.00%]
alpha_JET_Pileup_PtTerm	±62.32 [6.4%]	±24.83 [3.6%]	±28.68 [5.1%]
alpha_JET_Flavor_Composition	±47.02 [4.8%]	±10.65 [1.5%]	±9.27 [1.7%]
alpha_RESUM_QCD_W_bin1	±42.96 [4.4%]	±0.00 [0.00%]	±0.00 [0.00%]
alpha_JET_EffectiveNP_Modelling2	±42.22 [4.3%]	±42.34 [6.1%]	±24.68 [4.4%]
mu_SIG	±40.99 [4.2%]	±42.58 [6.1%]	±63.23 [11.3%]
alpha_CKKW_QCD_W_bin1	±39.44 [4.0%]	±0.00 [0.00%]	±0.00 [0.00%]
alpha_RESUM_QCD_Z_bin1	±39.07 [4.0%]	±0.00 [0.00%]	±0.00 [0.00%]
alpha_JET_EtaIntercalibration_Modelling	±38.84 [4.0%]	±33.09 [4.7%]	±27.45 [4.9%]
gamma_stat_SR1_cuts_bin_0	±31.79 [3.2%]	±0.00 [0.00%]	±0.00 [0.00%]
Lumi	±21.32 [2.2%]	±15.21 [2.2%]	±12.26 [2.2%]
alpha_FACT_QCD_W_bin1	±19.21 [2.0%]	±0.00 [0.00%]	±0.00 [0.00%]
alpha_PRW_DATASF	±18.01 [1.8%]	±11.95 [1.7%]	±7.28 [1.3%]
alpha_FACT_QCD_Z_bin1	±17.45 [1.8%]	±0.00 [0.00%]	±0.00 [0.00%]
alpha_MET_SoftTrk_Scale	±14.84 [1.5%]	±5.04 [0.72%]	±3.72 [0.66%]
alpha_JET_EffectiveNP_Modelling1	±13.40 [1.4%]	±20.41 [2.9%]	±13.40 [2.4%]
alpha_MET_SoftTrk_ResoPara	±12.74 [1.3%]	±1.50 [0.22%]	±10.60 [1.9%]
alpha_JET_Flavor_Response	±11.94 [1.2%]	±0.34 [0.05%]	±6.28 [1.1%]
alpha_CKKW_QCD_Z_bin1	±11.90 [1.2%]	±0.00 [0.00%]	±0.00 [0.00%]
alpha_JET_EtaIntercalibration_TotalStat	±10.31 [1.1%]	±0.03 [0.00%]	±0.78 [0.14%]
alpha_JET_EtaInt	±8.41 [0.86%]	±16.46 [2.4%]	±12.68 [2.3%]
alpha_JER	±8.36 [0.85%]	±14.30 [2.1%]	±10.52 [1.9%]
alpha_JET_Pileup_RhoTopology	±6.82 [0.70%]	±24.10 [3.5%]	±14.88 [2.7%]
alpha_JET_EffectiveNP_Mixed1	±5.76 [0.59%]	±11.62 [1.7%]	±11.37 [2.0%]
alpha_JET_Pileup_OffsetNPV	±5.19 [0.53%]	±0.28 [0.04%]	±8.04 [1.4%]
alpha_JET_EffectiveNP_Modelling3	±4.62 [0.47%]	±9.58 [1.4%]	±3.21 [0.57%]
alpha_JET_Pileup_OffsetMu	±3.76 [0.38%]	±6.97 [1.0%]	±3.83 [0.68%]
alpha_JET_EffectiveNP_Statistical6	±0.97 [0.10%]	±7.67 [1.1%]	±1.58 [0.28%]
alpha_RESUM_QCD_W_bin3	±0.00 [0.00%]	±0.00 [0.00%]	±19.74 [3.5%]
alpha_CKKW_QCD_Z_bin2	±0.00 [0.00%]	±13.07 [1.9%]	±0.00 [0.00%]
alpha_CKKW_QCD_W_bin3	±0.00 [0.00%]	±0.00 [0.00%]	±19.39 [3.5%]
alpha_CKKW_QCD_W_bin2	±0.00 [0.00%]	±21.68 [3.1%]	±0.00 [0.00%]
alpha_RESUM_EWK_W_bin3	±0.00 [0.00%]	±0.00 [0.00%]	±10.00 [1.8%]
k_Wbin3	±0.00 [0.00%]	±0.00 [0.00%]	±62.96 [11.2%]
k_Wbin2	±0.00 [0.00%]	±73.06 [10.5%]	±0.00 [0.00%]
k_Zbin2	±0.00 [0.00%]	±82.10 [11.8%]	±0.00 [0.00%]
k_Zbin3	±0.00 [0.00%]	±0.00 [0.00%]	±69.71 [12.4%]
alpha_CKKW_QCD_Z_bin3	±0.00 [0.00%]	±0.00 [0.00%]	±5.63 [1.0%]
alpha_FACT_QCD_W_bin3	±0.00 [0.00%]	±0.00 [0.00%]	±9.36 [1.7%]
alpha_FACT_QCD_W_bin2	±0.00 [0.00%]	±16.22 [2.3%]	±0.00 [0.00%]
alpha_RESUM_EWK_Z_bin3	±0.00 [0.00%]	±0.00 [0.00%]	±7.29 [1.3%]
alpha_REN_QCD_Z_bin2	±0.00 [0.00%]	±55.19 [7.9%]	±0.00 [0.00%]
alpha_REN_QCD_Z_bin3	±0.00 [0.00%]	±0.00 [0.00%]	±40.28 [7.2%]
alpha_RESUM_QCD_Z_bin3	±0.00 [0.00%]	±0.00 [0.00%]	±27.52 [4.9%]
alpha_PDF_QCD_Z_bin3	±0.00 [0.00%]	±0.00 [0.00%]	±6.11 [1.1%]
alpha_RESUM_QCD_W_bin2	±0.00 [0.00%]	±27.46 [3.9%]	±0.00 [0.00%]
alpha_REN_QCD_W_bin3	±0.00 [0.00%]	±0.00 [0.00%]	±27.93 [5.0%]
alpha_REN_QCD_W_bin2	±0.00 [0.00%]	±44.91 [6.4%]	±0.00 [0.00%]
alpha_PDF_QCD_W_bin2	±0.00 [0.00%]	±8.68 [1.2%]	±0.00 [0.00%]
alpha_FACT_QCD_Z_bin2	±0.00 [0.00%]	±17.02 [2.4%]	±0.00 [0.00%]
alpha_FACT_QCD_Z_bin3	±0.00 [0.00%]	±0.00 [0.00%]	±11.45 [2.0%]
gamma_stat_SR2_cuts_bin_0	±0.00 [0.00%]	±26.99 [3.9%]	±0.00 [0.00%]
alpha_FACT_EWK_W_bin3	±0.00 [0.00%]	±0.00 [0.00%]	±10.03 [1.8%]
alpha_RESUM_QCD_Z_bin2	±0.00 [0.00%]	±26.73 [3.8%]	±0.00 [0.00%]
alpha_FACT_EWK_Z_bin3	±0.00 [0.00%]	±0.00 [0.00%]	±10.12 [1.8%]
gamma_stat_SR3_cuts_bin_0	±0.00 [0.00%]	±0.00 [0.00%]	±15.52 [2.8%]

E.2 Control region Wenu

Table E.3: Pre-fit Wenu CR pos. Breakdown of the dominant systematic uncertainties on background estimates in the various signal regions. Note that the individual uncertainties can be correlated, and do not necessarily add up quadratically to the total background uncertainty. The percentages show the size of the uncertainty relative to the total expected background.

Uncertainty of channel	ONEeleCR1pos	ONEeleCR2pos	ONEeleCR3pos
Total background expectation	153.52	139.94	132.02
Total statistical ($\sqrt{N_{\text{exp}}}$)	±12.39	±11.83	±11.49
Total background systematic	±47.00 [30.62%]	±47.79 [34.15%]	±40.93 [31.01%]
alpha_JET_EffectiveNP_Modelling2	±24.71 [16.1%]	±18.59 [13.3%]	±27.78 [21.0%]
gamma_stat_ONEeleCR1pos_cuts_bin_0	±21.28 [13.9%]	±0.00 [0.00%]	±0.00 [0.00%]
alpha_REN_QCD_W_bin1	±18.90 [12.3%]	±0.00 [0.00%]	±0.00 [0.00%]
alpha_JET_Pileup_RhoTopology	±11.47 [7.5%]	±2.03 [1.4%]	±9.15 [6.9%]
alpha_MET_SoftTrk_ResoPara	±10.27 [6.7%]	±7.64 [5.5%]	±0.31 [0.24%]
alpha_JER	±9.27 [6.0%]	±19.77 [14.1%]	±2.30 [1.7%]
alpha_JET_EtaInt	±8.77 [5.7%]	±12.17 [8.7%]	±6.22 [4.7%]
alpha_CKKW_QCD_W_bin1	±8.53 [5.6%]	±0.00 [0.00%]	±0.00 [0.00%]
alpha_JET_Pileup_OffsetNPV	±6.17 [4.0%]	±2.06 [1.5%]	±0.07 [0.06%]
alpha_MET_SoftTrk_ResoPerp	±4.65 [3.0%]	±3.31 [2.4%]	±0.36 [0.27%]
alpha_PDF_QCD_W_bin1	±4.24 [2.8%]	±0.00 [0.00%]	±0.00 [0.00%]
alpha_FACT_QCD_W_bin1	±4.05 [2.6%]	±0.00 [0.00%]	±0.00 [0.00%]
alpha_MET_SoftTrk_Scale	±4.00 [2.6%]	±4.01 [2.9%]	±0.38 [0.29%]
alpha_JET_EffectiveNP_Mixed1	±3.97 [2.6%]	±1.28 [0.91%]	±1.60 [1.2%]
alpha_JET_EffectiveNP_Modelling4	±3.90 [2.5%]	±0.59 [0.42%]	±0.32 [0.24%]
alpha_JET_EffectiveNP_Statistical7	±3.84 [2.5%]	±0.69 [0.50%]	±0.78 [0.59%]
alpha_JET_EffectiveNP_Modelling1	±3.79 [2.5%]	±2.74 [2.0%]	±7.94 [6.0%]
alpha_JET_EffectiveNP_Detector1	±3.77 [2.5%]	±0.69 [0.50%]	±0.32 [0.24%]
alpha_JET_EffectiveNP_Statistical4	±3.70 [2.4%]	±0.52 [0.38%]	±1.13 [0.86%]
alpha_JET_EffectiveNP_Modelling3	±3.66 [2.4%]	±2.52 [1.8%]	±1.45 [1.1%]
alpha_JET_Flavor_Composition	±3.50 [2.3%]	±9.67 [6.9%]	±5.02 [3.8%]
alpha_RESUM_EWK_W_bin1	±3.39 [2.2%]	±0.00 [0.00%]	±0.00 [0.00%]
Lumi	±3.16 [2.1%]	±2.86 [2.0%]	±2.68 [2.0%]
alpha_EG_RESO	±3.10 [2.0%]	±0.02 [0.01%]	±0.16 [0.12%]
alpha_JET_EffectiveNP_Statistical1	±3.02 [2.0%]	±0.11 [0.08%]	±0.45 [0.34%]
alpha_JET_EffectiveNP_Statistical2	±2.70 [1.8%]	±0.19 [0.13%]	±0.15 [0.12%]
alpha_JET_EtaIntercalibration_TotalStat	±2.33 [1.5%]	±0.75 [0.54%]	±2.31 [1.8%]
alpha_JET_EffectiveNP_Detector2	±2.25 [1.5%]	±0.69 [0.50%]	±0.35 [0.26%]
alpha_CKKW_EWK_W_bin1	±2.18 [1.4%]	±0.00 [0.00%]	±0.00 [0.00%]
alpha_RESUM_QCD_W_bin1	±2.04 [1.3%]	±0.00 [0.00%]	±0.00 [0.00%]
alpha_JET_Flavor_Response	±1.91 [1.2%]	±0.89 [0.63%]	±1.43 [1.1%]
alpha_JET_EffectiveNP_Mixed2	±1.80 [1.2%]	±0.21 [0.15%]	±0.32 [0.24%]
alpha_JET_EffectiveNP_Statistical5	±1.77 [1.2%]	±0.10 [0.07%]	±0.16 [0.12%]
alpha_JET_EffectiveNP_Statistical3	±1.77 [1.2%]	±0.11 [0.08%]	±0.51 [0.38%]
alpha_JET_Pileup_PtTerm	±1.70 [1.1%]	±10.49 [7.5%]	±5.93 [4.5%]
alpha_JET_Pileup_OffsetMu	±1.59 [1.0%]	±0.51 [0.36%]	±4.13 [3.1%]
alpha_PRW_DATASF	±1.28 [0.84%]	±16.69 [11.9%]	±9.27 [7.0%]
alpha_JET_EtaIntercalibration_Modelling	±0.18 [0.12%]	±11.63 [8.3%]	±0.48 [0.37%]
alpha_RESUM_QCD_W_bin3	±0.00 [0.00%]	±0.00 [0.00%]	±2.31 [1.8%]
alpha_CKKW_QCD_W_bin3	±0.00 [0.00%]	±0.00 [0.00%]	±5.95 [4.5%]
alpha_RESUM_EWK_W_bin3	±0.00 [0.00%]	±0.00 [0.00%]	±5.65 [4.3%]
alpha_RESUM_EWK_W_bin2	±0.00 [0.00%]	±3.60 [2.6%]	±0.00 [0.00%]
alpha_PDF_EWK_W_bin3	±0.00 [0.00%]	±0.00 [0.00%]	±1.44 [1.1%]
alpha_FACT_QCD_W_bin3	±0.00 [0.00%]	±0.00 [0.00%]	±2.76 [2.1%]
alpha_FACT_QCD_W_bin2	±0.00 [0.00%]	±3.53 [2.5%]	±0.00 [0.00%]
gamma_stat_ONEeleCR2pos_cuts_bin_0	±0.00 [0.00%]	±17.13 [12.2%]	±0.00 [0.00%]
alpha_RESUM_QCD_W_bin2	±0.00 [0.00%]	±4.23 [3.0%]	±0.00 [0.00%]
alpha_REN_QCD_W_bin3	±0.00 [0.00%]	±0.00 [0.00%]	±11.48 [8.7%]
alpha_REN_QCD_W_bin2	±0.00 [0.00%]	±17.62 [12.6%]	±0.00 [0.00%]
alpha_PDF_QCD_W_bin2	±0.00 [0.00%]	±1.92 [1.4%]	±0.00 [0.00%]
alpha_PDF_QCD_W_bin3	±0.00 [0.00%]	±0.00 [0.00%]	±1.33 [1.0%]
alpha_REN_EWK_W_bin3	±0.00 [0.00%]	±0.00 [0.00%]	±2.33 [1.8%]
alpha_FACT_EWK_W_bin2	±0.00 [0.00%]	±2.05 [1.5%]	±0.00 [0.00%]
alpha_FACT_EWK_W_bin3	±0.00 [0.00%]	±0.00 [0.00%]	±6.64 [5.0%]
gamma_stat_ONEeleCR3pos_cuts_bin_0	±0.00 [0.00%]	±0.00 [0.00%]	±16.09 [12.2%]

Table E.4: Post-fit Wenu CR pos. Breakdown of the dominant systematic uncertainties on background estimates in the various signal regions. Note that the individual uncertainties can be correlated, and do not necessarily add up quadratically to the total background uncertainty. The percentages show the size of the uncertainty relative to the total expected background.

Uncertainty of channel	ONEeleCR1pos	ONEeleCR2pos	ONEeleCR3pos
Total background expectation	153.52	139.94	132.02
Total statistical ($\sqrt{N_{\text{exp}}}$)	±12.39	±11.83	±11.49
Total background systematic	±11.60 [7.56%]	±10.86 [7.76%]	±10.23 [7.75%]
k_Wbin1	±29.08 [18.9%]	±0.00 [0.00%]	±0.00 [0.00%]
alpha_JET_EffectiveNP_Modelling2	±21.13 [13.8%]	±15.89 [11.4%]	±23.75 [18.0%]
alpha_REN_QCD_W_bin1	±18.73 [12.2%]	±0.00 [0.00%]	±0.00 [0.00%]
gamma_stat_ONEeleCR1pos_cuts_bin_0	±17.22 [11.2%]	±0.00 [0.00%]	±0.00 [0.00%]
alpha_JET_Pileup_RhoTopology	±9.69 [6.3%]	±1.71 [1.2%]	±7.73 [5.9%]
alpha_CKKW_QCD_W_bin1	±8.45 [5.5%]	±0.00 [0.00%]	±0.00 [0.00%]
alpha_MET_SoftTrk_ResoPara	±8.41 [5.5%]	±6.26 [4.5%]	±0.26 [0.19%]
alpha_JET_EtaInt	±7.36 [4.8%]	±10.22 [7.3%]	±5.22 [4.0%]
alpha_JET_Pileup_OffsetNPV	±5.71 [3.7%]	±1.91 [1.4%]	±0.07 [0.05%]
alpha_MET_SoftTrk_ResoPerp	±4.29 [2.8%]	±3.05 [2.2%]	±0.33 [0.25%]
alpha_PDF_QCD_W_bin1	±4.21 [2.7%]	±0.00 [0.00%]	±0.00 [0.00%]
alpha_FACT_QCD_W_bin1	±4.02 [2.6%]	±0.00 [0.00%]	±0.00 [0.00%]
alpha_JET_EffectiveNP_Mixed1	±3.88 [2.5%]	±1.25 [0.89%]	±1.56 [1.2%]
alpha_MET_SoftTrk_Scale	±3.84 [2.5%]	±3.86 [2.8%]	±0.36 [0.28%]
alpha_JET_EffectiveNP_Modelling4	±3.82 [2.5%]	±0.58 [0.41%]	±0.32 [0.24%]
alpha_JET_EffectiveNP_Statistical7	±3.77 [2.5%]	±0.68 [0.49%]	±0.77 [0.58%]
alpha_JET_EffectiveNP_Detector1	±3.72 [2.4%]	±0.68 [0.49%]	±0.32 [0.24%]
alpha_JER	±3.72 [2.4%]	±7.94 [5.7%]	±0.92 [0.70%]
alpha_JET_EffectiveNP_Statistical4	±3.61 [2.4%]	±0.51 [0.37%]	±1.10 [0.84%]
alpha_JET_EffectiveNP_Modelling3	±3.51 [2.3%]	±2.41 [1.7%]	±1.39 [1.1%]
alpha_RESUM_EWK_W_bin1	±3.36 [2.2%]	±0.00 [0.00%]	±0.00 [0.00%]
alpha_JET_EffectiveNP_Modelling1	±3.34 [2.2%]	±2.41 [1.7%]	±7.00 [5.3%]
Lumi	±3.14 [2.0%]	±2.85 [2.0%]	±2.67 [2.0%]
alpha_EG_RESO	±3.06 [2.0%]	±0.01 [0.01%]	±0.16 [0.12%]
alpha_JET_EffectiveNP_Statistical1	±2.93 [1.9%]	±0.11 [0.08%]	±0.43 [0.33%]
alpha_JET_EffectiveNP_Statistical2	±2.62 [1.7%]	±0.18 [0.13%]	±0.15 [0.11%]
alpha_JET_Flavor_Composition	±2.37 [1.5%]	±6.53 [4.7%]	±3.39 [2.6%]
alpha_JET_EtaIntercalibration_TotalStat	±2.27 [1.5%]	±0.73 [0.52%]	±2.25 [1.7%]
alpha_JET_EffectiveNP_Detector2	±2.23 [1.5%]	±0.69 [0.49%]	±0.35 [0.26%]
alpha_CKKW_EWK_W_bin1	±2.17 [1.4%]	±0.00 [0.00%]	±0.00 [0.00%]
alpha_RESUM_QCD_W_bin1	±1.97 [1.3%]	±0.00 [0.00%]	±0.00 [0.00%]
norm_fakeEl_1	±1.82 [1.2%]	±0.00 [0.00%]	±0.00 [0.00%]
alpha_JET_EffectiveNP_Mixed2	±1.78 [1.2%]	±0.21 [0.15%]	±0.32 [0.24%]
alpha_JET_EffectiveNP_Statistical5	±1.75 [1.1%]	±0.10 [0.07%]	±0.16 [0.12%]
alpha_JET_EffectiveNP_Statistical3	±1.74 [1.1%]	±0.11 [0.08%]	±0.50 [0.38%]
alpha_JET_Flavor_Response	±1.74 [1.1%]	±0.81 [0.58%]	±1.30 [0.98%]
alpha_JET_Pileup_PtTerm	±1.59 [1.0%]	±9.78 [7.0%]	±5.53 [4.2%]
alpha_JET_Pileup_OffsetMu	±1.39 [0.90%]	±0.44 [0.31%]	±3.60 [2.7%]
alpha_PRW_DATASF	±0.89 [0.58%]	±11.50 [8.2%]	±6.39 [4.8%]
alpha_JET_EtaIntercalibration_Modelling	±0.15 [0.10%]	±10.05 [7.2%]	±0.42 [0.32%]
alpha_RESUM_QCD_W_bin3	±0.00 [0.00%]	±0.00 [0.00%]	±2.29 [1.7%]
alpha_CKKW_QCD_W_bin3	±0.00 [0.00%]	±0.00 [0.00%]	±5.90 [4.5%]
alpha_RESUM_EWK_W_bin3	±0.00 [0.00%]	±0.00 [0.00%]	±5.61 [4.2%]
alpha_RESUM_EWK_W_bin2	±0.00 [0.00%]	±3.57 [2.6%]	±0.00 [0.00%]
k_Wbin3	±0.00 [0.00%]	±0.00 [0.00%]	±28.33 [21.5%]
k_Wbin2	±0.00 [0.00%]	±27.97 [20.0%]	±0.00 [0.00%]
alpha_PDF_EWK_W_bin3	±0.00 [0.00%]	±0.00 [0.00%]	±1.43 [1.1%]
alpha_FACT_QCD_W_bin3	±0.00 [0.00%]	±0.00 [0.00%]	±2.74 [2.1%]
alpha_FACT_QCD_W_bin2	±0.00 [0.00%]	±3.50 [2.5%]	±0.00 [0.00%]
norm_fakeEl_3	±0.00 [0.00%]	±0.00 [0.00%]	±2.21 [1.7%]
norm_fakeEl_2	±0.00 [0.00%]	±1.67 [1.2%]	±0.00 [0.00%]
gamma_stat_ONEeleCR2pos_cuts_bin_0	±0.00 [0.00%]	±14.13 [10.1%]	±0.00 [0.00%]
alpha_RESUM_QCD_W_bin2	±0.00 [0.00%]	±4.16 [3.0%]	±0.00 [0.00%]
alpha_REN_QCD_W_bin3	±0.00 [0.00%]	±0.00 [0.00%]	±11.37 [8.6%]
alpha_REN_QCD_W_bin2	±0.00 [0.00%]	±17.49 [12.5%]	±0.00 [0.00%]
alpha_PDF_QCD_W_bin2	±0.00 [0.00%]	±1.90 [1.4%]	±0.00 [0.00%]
alpha_PDF_QCD_W_bin3	±0.00 [0.00%]	±0.00 [0.00%]	±1.32 [1.0%]
alpha_REN_EWK_W_bin3	±0.00 [0.00%]	±0.00 [0.00%]	±2.32 [1.8%]
alpha_FACT_EWK_W_bin2	±0.00 [0.00%]	±2.04 [1.5%]	±0.00 [0.00%]
alpha_FACT_EWK_W_bin3	±0.00 [0.00%]	±0.00 [0.00%]	±6.59 [5.0%]
gamma_stat_ONEeleCR3pos_cuts_bin_0	±0.00 [0.00%]	±0.00 [0.00%]	±12.49 [9.5%]

Table E.5: Pre-fit WenuCRneg. Breakdown of the dominant systematic uncertainties on background estimates in the various signal regions. Note that the individual uncertainties can be correlated, and do not necessarily add up quadratically to the total background uncertainty. The percentages show the size of the uncertainty relative to the total expected background.

Uncertainty of channel	ONEeleCR1neg	ONEeleCR2neg	ONEeleCR3neg
Total background expectation	119.17	83.06	60.91
Total statistical ($\sqrt{N_{\text{exp}}}$)	±10.92	±9.11	±7.80
Total background systematic	±38.50 [32.31%]	±21.53 [25.92%]	±15.52 [25.48%]
alpha_JER	±22.93 [19.2%]	±1.17 [1.4%]	±0.60 [0.99%]
alpha_JET_EffectiveNP_Modelling2	±16.23 [13.6%]	±7.55 [9.1%]	±9.92 [16.3%]
gamma_stat_ONEeleCR1neg_cuts_bin_0	±15.14 [12.7%]	±0.00 [0.00%]	±0.00 [0.00%]
alpha_REN_QCD_W_bin1	±14.47 [12.1%]	±0.00 [0.00%]	±0.00 [0.00%]
alpha_JET_Flavor_Composition	±9.15 [7.7%]	±3.74 [4.5%]	±3.02 [5.0%]
alpha_CKKW_QCD_W_bin1	±6.53 [5.5%]	±0.00 [0.00%]	±0.00 [0.00%]
alpha_JET_Pileup_PtTerm	±5.09 [4.3%]	±5.41 [6.5%]	±1.19 [1.9%]
alpha_MET_SoftTrk_ResoPerp	±3.37 [2.8%]	±2.69 [3.2%]	±0.27 [0.45%]
alpha_PDF_QCD_W_bin1	±3.25 [2.7%]	±0.00 [0.00%]	±0.00 [0.00%]
alpha_JET_EtaIntercalibration_Modelling	±3.23 [2.7%]	±4.78 [5.8%]	±5.41 [8.9%]
alpha_FACT_QCD_W_bin1	±3.10 [2.6%]	±0.00 [0.00%]	±0.00 [0.00%]
alpha_MET_SoftTrk_ResoPara	±3.02 [2.5%]	±2.02 [2.4%]	±0.69 [1.1%]
Lumi	±2.40 [2.0%]	±1.61 [1.9%]	±1.12 [1.8%]
alpha_MET_SoftTrk_Scale	±2.40 [2.0%]	±0.04 [0.04%]	±0.18 [0.29%]
alpha_JET_Pileup_RhoTopology	±2.33 [2.0%]	±1.26 [1.5%]	±1.59 [2.6%]
alpha_RESUM_EWK_W_bin1	±1.96 [1.6%]	±0.00 [0.00%]	±0.00 [0.00%]
alpha_JET_EffectiveNP_Mixed1	±1.87 [1.6%]	±0.61 [0.74%]	±0.62 [1.0%]
alpha_JET_Pileup_OffsetMu	±1.84 [1.5%]	±4.80 [5.8%]	±0.69 [1.1%]
alpha_JET_Flavor_Response	±1.78 [1.5%]	±2.83 [3.4%]	±0.46 [0.75%]
alpha_JET_EtaIntercalibration_TotalStat	±1.59 [1.3%]	±0.51 [0.62%]	±0.24 [0.40%]
alpha_RESUM_QCD_W_bin1	±1.56 [1.3%]	±0.00 [0.00%]	±0.00 [0.00%]
alpha_JET_EffectiveNP_Modelling1	±1.46 [1.2%]	±0.54 [0.65%]	±1.51 [2.5%]
alpha_EL_EFF_ID	±1.28 [1.1%]	±0.78 [0.94%]	±0.48 [0.79%]
alpha_CKKW_EWK_W_bin1	±1.26 [1.1%]	±0.00 [0.00%]	±0.00 [0.00%]
alpha_JET_Pileup_OffsetNPV	±1.12 [0.94%]	±1.29 [1.5%]	±0.34 [0.55%]
alpha_JET_EffectiveNP_Modelling3	±0.90 [0.76%]	±0.89 [1.1%]	±0.45 [0.74%]
alpha_JET_EffectiveNP_Statistical4	±0.84 [0.71%]	±0.91 [1.1%]	±0.45 [0.75%]
alpha_JET_EffectiveNP_Statistical3	±0.82 [0.69%]	±1.22 [1.5%]	±0.42 [0.69%]
alpha_JET_EtaInt	±0.62 [0.52%]	±1.56 [1.9%]	±1.17 [1.9%]
alpha_JET_EffectiveNP_Mixed3	±0.00 [0.00%]	±0.94 [1.1%]	±0.14 [0.23%]
alpha_RESUM_QCD_W_bin3	±0.00 [0.00%]	±0.00 [0.00%]	±0.96 [1.6%]
alpha_CKKW_QCD_W_bin3	±0.00 [0.00%]	±0.00 [0.00%]	±2.45 [4.0%]
alpha_RESUM_EWK_W_bin3	±0.00 [0.00%]	±0.00 [0.00%]	±2.21 [3.6%]
alpha_RESUM_EWK_W_bin2	±0.00 [0.00%]	±2.34 [2.8%]	±0.00 [0.00%]
gamma_stat_ONEeleCR2neg_cuts_bin_0	±0.00 [0.00%]	±13.57 [16.3%]	±0.00 [0.00%]
alpha_FACT_QCD_W_bin3	±0.00 [0.00%]	±0.00 [0.00%]	±1.14 [1.9%]
alpha_FACT_QCD_W_bin2	±0.00 [0.00%]	±1.78 [2.1%]	±0.00 [0.00%]
gamma_stat_ONEeleCR3neg_cuts_bin_0	±0.00 [0.00%]	±0.00 [0.00%]	±6.85 [11.2%]
alpha_RESUM_QCD_W_bin2	±0.00 [0.00%]	±2.13 [2.6%]	±0.00 [0.00%]
alpha_REN_QCD_W_bin3	±0.00 [0.00%]	±0.00 [0.00%]	±4.74 [7.8%]
alpha_REN_QCD_W_bin2	±0.00 [0.00%]	±8.88 [10.7%]	±0.00 [0.00%]
alpha_PDF_QCD_W_bin2	±0.00 [0.00%]	±0.97 [1.2%]	±0.00 [0.00%]
alpha_REN_EWK_W_bin3	±0.00 [0.00%]	±0.00 [0.00%]	±0.91 [1.5%]
alpha_FACT_EWK_W_bin2	±0.00 [0.00%]	±1.33 [1.6%]	±0.00 [0.00%]
alpha_FACT_EWK_W_bin3	±0.00 [0.00%]	±0.00 [0.00%]	±2.60 [4.3%]

Table E.6: Post-fit WenuCR neg. Breakdown of the dominant systematic uncertainties on background estimates in the various signal regions. Note that the individual uncertainties can be correlated, and do not necessarily add up quadratically to the total background uncertainty. The percentages show the size of the uncertainty relative to the total expected background.

Uncertainty of channel	ONEeleCR1neg	ONEeleCR2neg	ONEeleCR3neg
Total background expectation	119.17	83.06	60.91
Total statistical ($\sqrt{N_{\text{exp}}}$)	±10.92	±9.11	±7.80
Total background systematic	±9.71 [8.15%]	±7.94 [9.56%]	±5.81 [9.54%]
k_Wbin1	±21.50 [18.0%]	±0.00 [0.00%]	±0.00 [0.00%]
alpha_REN_QCD_W_bin1	±14.33 [12.0%]	±0.00 [0.00%]	±0.00 [0.00%]
alpha_JET_EffectiveNP_Modelling2	±13.88 [11.6%]	±6.46 [7.8%]	±8.48 [13.9%]
gamma_stat_ONEeleCR1neg_cuts_bin_0	±11.76 [9.9%]	±0.00 [0.00%]	±0.00 [0.00%]
alpha_JER	±9.21 [7.7%]	±0.47 [0.57%]	±0.24 [0.40%]
alpha_CKKW_QCD_W_bin1	±6.47 [5.4%]	±0.00 [0.00%]	±0.00 [0.00%]
alpha_JET_Flavor_Composition	±6.18 [5.2%]	±2.53 [3.0%]	±2.04 [3.4%]
alpha_JET_Pileup_PtTerm	±4.75 [4.0%]	±5.05 [6.1%]	±1.11 [1.8%]
alpha_PDF_QCD_W_bin1	±3.22 [2.7%]	±0.00 [0.00%]	±0.00 [0.00%]
alpha_MET_SoftTrk_ResoPerp	±3.11 [2.6%]	±2.48 [3.0%]	±0.25 [0.41%]
alpha_FACT_QCD_W_bin1	±3.08 [2.6%]	±0.00 [0.00%]	±0.00 [0.00%]
alpha_JET_EtaIntercalibration_Modelling	±2.79 [2.3%]	±4.13 [5.0%]	±4.68 [7.7%]
alpha_MET_SoftTrk_ResoPara	±2.47 [2.1%]	±1.65 [2.0%]	±0.56 [0.93%]
Lumi	±2.39 [2.0%]	±1.60 [1.9%]	±1.11 [1.8%]
alpha_MET_SoftTrk_Scale	±2.31 [1.9%]	±0.04 [0.04%]	±0.17 [0.28%]
alpha_JET_Pileup_RhoTopology	±1.97 [1.7%]	±1.07 [1.3%]	±1.34 [2.2%]
alpha_RESUM_EWK_W_bin1	±1.94 [1.6%]	±0.00 [0.00%]	±0.00 [0.00%]
alpha_JET_EffectiveNP_Mixed1	±1.83 [1.5%]	±0.60 [0.72%]	±0.61 [1.00%]
norm_fakeEl_1	±1.82 [1.5%]	±0.00 [0.00%]	±0.00 [0.00%]
alpha_JET_Flavor_Response	±1.62 [1.4%]	±2.57 [3.1%]	±0.41 [0.68%]
alpha_JET_Pileup_OffsetMu	±1.60 [1.3%]	±4.18 [5.0%]	±0.60 [0.98%]
alpha_JET_EtaIntercalibration_TotalStat	±1.55 [1.3%]	±0.50 [0.60%]	±0.24 [0.39%]
alpha_RESUM_QCD_W_bin1	±1.51 [1.3%]	±0.00 [0.00%]	±0.00 [0.00%]
alpha_JET_EffectiveNP_Modelling1	±1.29 [1.1%]	±0.48 [0.57%]	±1.33 [2.2%]
alpha_EL_EFF_ID	±1.26 [1.1%]	±0.77 [0.92%]	±0.48 [0.78%]
alpha_CKKW_EWK_W_bin1	±1.25 [1.0%]	±0.00 [0.00%]	±0.00 [0.00%]
alpha_JET_Pileup_OffsetNPV	±1.04 [0.87%]	±1.19 [1.4%]	±0.31 [0.51%]
alpha_JET_EffectiveNP_Modelling3	±0.87 [0.73%]	±0.85 [1.0%]	±0.43 [0.71%]
alpha_JET_EffectiveNP_Statistical4	±0.82 [0.69%]	±0.89 [1.1%]	±0.44 [0.73%]
alpha_JET_EffectiveNP_Statistical3	±0.81 [0.68%]	±1.20 [1.4%]	±0.41 [0.68%]
alpha_JET_EtaInt	±0.52 [0.44%]	±1.31 [1.6%]	±0.98 [1.6%]
alpha_JET_EffectiveNP_Mixed3	±0.00 [0.00%]	±0.93 [1.1%]	±0.14 [0.23%]
alpha_RESUM_QCD_W_bin3	±0.00 [0.00%]	±0.00 [0.00%]	±0.94 [1.5%]
alpha_CKKW_QCD_W_bin3	±0.00 [0.00%]	±0.00 [0.00%]	±2.44 [4.0%]
alpha_RESUM_EWK_W_bin3	±0.00 [0.00%]	±0.00 [0.00%]	±2.20 [3.6%]
alpha_RESUM_EWK_W_bin2	±0.00 [0.00%]	±2.32 [2.8%]	±0.00 [0.00%]
k_Wbin3	±0.00 [0.00%]	±0.00 [0.00%]	±11.42 [18.8%]
k_Wbin2	±0.00 [0.00%]	±14.89 [17.9%]	±0.00 [0.00%]
gamma_stat_ONEeleCR2neg_cuts_bin_0	±0.00 [0.00%]	±9.33 [11.2%]	±0.00 [0.00%]
alpha_FACT_QCD_W_bin3	±0.00 [0.00%]	±0.00 [0.00%]	±1.13 [1.9%]
alpha_FACT_QCD_W_bin2	±0.00 [0.00%]	±1.76 [2.1%]	±0.00 [0.00%]
norm_fakeEl_3	±0.00 [0.00%]	±0.00 [0.00%]	±2.21 [3.6%]
norm_fakeEl_2	±0.00 [0.00%]	±1.67 [2.0%]	±0.00 [0.00%]
gamma_stat_ONEeleCR3neg_cuts_bin_0	±0.00 [0.00%]	±0.00 [0.00%]	±5.54 [9.1%]
alpha_RESUM_QCD_W_bin2	±0.00 [0.00%]	±2.10 [2.5%]	±0.00 [0.00%]
alpha_REN_QCD_W_bin3	±0.00 [0.00%]	±0.00 [0.00%]	±4.70 [7.7%]
alpha_REN_QCD_W_bin2	±0.00 [0.00%]	±8.82 [10.6%]	±0.00 [0.00%]
alpha_PDF_QCD_W_bin2	±0.00 [0.00%]	±0.96 [1.2%]	±0.00 [0.00%]
alpha_REN_EWK_W_bin3	±0.00 [0.00%]	±0.00 [0.00%]	±0.91 [1.5%]
alpha_FACT_EWK_W_bin2	±0.00 [0.00%]	±1.32 [1.6%]	±0.00 [0.00%]
alpha_FACT_EWK_W_bin3	±0.00 [0.00%]	±0.00 [0.00%]	±2.58 [4.2%]

E.3 Control region Wmunu

Table E.7: Pre-fit Wmunu post. Breakdown of the dominant systematic uncertainties on background estimates in the various signal regions. Note that the individual uncertainties can be correlated, and do not necessarily add up quadratically to the total background uncertainty. The percentages show the size of the uncertainty relative to the total expected background.

Uncertainty of channel	ONEmuCR1pos	ONEmuCR2pos	ONEmuCR3pos
Total background expectation	231.91	213.27	186.91
Total statistical ($\sqrt{N_{\text{exp}}}$)	±15.23	±14.60	±13.67
Total background systematic	±52.84 [22.78%]	±50.65 [23.75%]	±44.40 [23.75%]
alpha_REN_QCD_W_bin1	±28.64 [12.3%]	±0.00 [0.00%]	±0.00 [0.00%]
gamma_stat_ONEmuCR1pos_cuts_bin_0	±22.43 [9.7%]	±0.00 [0.00%]	±0.00 [0.00%]
alpha_JET_Flavor_Composition	±14.39 [6.2%]	±0.76 [0.36%]	±9.78 [5.2%]
alpha_JET_EffectiveNP_Modelling2	±13.51 [5.8%]	±23.86 [11.2%]	±25.02 [13.4%]
alpha_CKKW_QCD_W_bin1	±12.93 [5.6%]	±0.00 [0.00%]	±0.00 [0.00%]
alpha_JET_Pileup_OffsetMu	±11.84 [5.1%]	±4.91 [2.3%]	±3.84 [2.1%]
alpha_JET_Pileup_PtTerm	±10.78 [4.7%]	±10.18 [4.8%]	±8.23 [4.4%]
alpha_MET_SoftTrk_Scale	±9.45 [4.1%]	±2.30 [1.1%]	±0.68 [0.36%]
alpha_JET_EtaInt	±8.32 [3.6%]	±4.22 [2.0%]	±6.63 [3.5%]
alpha_JET_EffectiveNP_Statistical2	±7.59 [3.3%]	±0.78 [0.37%]	±3.32 [1.8%]
alpha_JET_EffectiveNP_Statistical1	±7.48 [3.2%]	±0.85 [0.40%]	±3.12 [1.7%]
alpha_JET_Pileup_OffsetNPV	±7.48 [3.2%]	±4.30 [2.0%]	±2.80 [1.5%]
alpha_PDF_QCD_W_bin1	±6.43 [2.8%]	±0.00 [0.00%]	±0.00 [0.00%]
alpha_FACT_QCD_W_bin1	±6.14 [2.6%]	±0.00 [0.00%]	±0.00 [0.00%]
alpha_RESUM_EWK_W_bin1	±6.13 [2.6%]	±0.00 [0.00%]	±0.00 [0.00%]
alpha_JER	±5.64 [2.4%]	±12.46 [5.8%]	±8.88 [4.8%]
alpha_JET_EffectiveNP_Modelling3	±5.10 [2.2%]	±0.04 [0.02%]	±2.78 [1.5%]
Lumi	±5.10 [2.2%]	±4.69 [2.2%]	±4.11 [2.2%]
alpha_MET_SoftTrk_ResoPara	±4.03 [1.7%]	±0.82 [0.39%]	±0.41 [0.22%]
alpha_CKKW_EWK_W_bin1	±3.95 [1.7%]	±0.00 [0.00%]	±0.00 [0.00%]
alpha_JET_EffectiveNP_Statistical4	±3.53 [1.5%]	±0.42 [0.20%]	±0.32 [0.17%]
alpha_JET_EffectiveNP_Modelling1	±3.50 [1.5%]	±7.13 [3.3%]	±0.81 [0.43%]
alpha_JET_EffectiveNP_Mixed1	±3.24 [1.4%]	±0.94 [0.44%]	±2.16 [1.2%]
alpha_JET_EtaIntercalibration_TotalStat	±3.17 [1.4%]	±0.54 [0.25%]	±0.31 [0.16%]
alpha_RESUM_QCD_W_bin1	±3.10 [1.3%]	±0.00 [0.00%]	±0.00 [0.00%]
alpha_MU_EFF_SYST	±2.44 [1.1%]	±2.32 [1.1%]	±2.15 [1.2%]
alpha_JET_EtaIntercalibration_Modelling	±2.19 [0.94%]	±14.19 [6.7%]	±7.88 [4.2%]
alpha_JET_Pileup_RhoTopology	±2.14 [0.92%]	±9.77 [4.6%]	±3.11 [1.7%]
alpha_PRW_DATASF	±1.88 [0.81%]	±1.13 [0.53%]	±7.26 [3.9%]
alpha_MET_SoftTrk_ResoPerp	±1.15 [0.50%]	±8.18 [3.8%]	±0.40 [0.21%]
alpha_JET_Flavor_Response	±0.89 [0.39%]	±1.10 [0.52%]	±3.04 [1.6%]
alpha_RESUM_QCD_W_bin3	±0.00 [0.00%]	±0.00 [0.00%]	±3.87 [2.1%]
alpha_CKKW_QCD_W_bin3	±0.00 [0.00%]	±0.00 [0.00%]	±9.94 [5.3%]
alpha_RESUM_EWK_W_bin3	±0.00 [0.00%]	±0.00 [0.00%]	±6.97 [3.7%]
alpha_RESUM_EWK_W_bin2	±0.00 [0.00%]	±6.28 [2.9%]	±0.00 [0.00%]
gamma_stat_ONEmuCR2pos_cuts_bin_0	±0.00 [0.00%]	±17.43 [8.2%]	±0.00 [0.00%]
alpha_FACT_QCD_W_bin3	±0.00 [0.00%]	±0.00 [0.00%]	±4.60 [2.5%]
alpha_FACT_QCD_W_bin2	±0.00 [0.00%]	±5.56 [2.6%]	±0.00 [0.00%]
alpha_RESUM_QCD_W_bin2	±0.00 [0.00%]	±6.67 [3.1%]	±0.00 [0.00%]
alpha_REN_QCD_W_bin3	±0.00 [0.00%]	±0.00 [0.00%]	±19.18 [10.3%]
alpha_REN_QCD_W_bin2	±0.00 [0.00%]	±27.77 [13.0%]	±0.00 [0.00%]
alpha_PDF_QCD_W_bin2	±0.00 [0.00%]	±3.02 [1.4%]	±0.00 [0.00%]
alpha_PDF_QCD_W_bin3	±0.00 [0.00%]	±0.00 [0.00%]	±2.22 [1.2%]
alpha_REN_EWK_W_bin3	±0.00 [0.00%]	±0.00 [0.00%]	±2.88 [1.5%]
alpha_FACT_EWK_W_bin2	±0.00 [0.00%]	±3.59 [1.7%]	±0.00 [0.00%]
alpha_FACT_EWK_W_bin3	±0.00 [0.00%]	±0.00 [0.00%]	±8.19 [4.4%]
gamma_stat_ONEmuCR3pos_cuts_bin_0	±0.00 [0.00%]	±0.00 [0.00%]	±14.32 [7.7%]

Table E.8: Post-fit Wmunu CR pos. Breakdown of the dominant systematic uncertainties on background estimates in the various signal regions. Note that the individual uncertainties can be correlated, and do not necessarily add up quadratically to the total background uncertainty. The percentages show the size of the uncertainty relative to the total expected background.

Uncertainty of channel	ONEmuCR1pos	ONEmuCR2pos	ONEmuCR3pos
Total background expectation	231.91	213.27	186.91
Total statistical ($\sqrt{N_{\text{exp}}}$)	±15.23	±14.60	±13.67
Total background systematic	±14.14 [6.10%]	±13.43 [6.30%]	±12.37 [6.62%]
k_Wbin1	±45.23 [19.5%]	±0.00 [0.00%]	±0.00 [0.00%]
alpha_REN_QCD_W_bin1	±28.37 [12.2%]	±0.00 [0.00%]	±0.00 [0.00%]
gamma_stat_ONEmuCR1pos_cuts_bin_0	±18.88 [8.1%]	±0.00 [0.00%]	±0.00 [0.00%]
alpha_CKKW_QCD_W_bin1	±12.81 [5.5%]	±0.00 [0.00%]	±0.00 [0.00%]
alpha_JET_EffectiveNP_Modelling2	±11.55 [5.0%]	±20.40 [9.6%]	±21.40 [11.4%]
alpha_JET_Pileup_OffsetMu	±10.31 [4.4%]	±4.27 [2.0%]	±3.34 [1.8%]
alpha_JET_Pileup_PtTerm	±10.05 [4.3%]	±9.49 [4.4%]	±7.68 [4.1%]
alpha_JET_Flavor_Composition	±9.72 [4.2%]	±0.52 [0.24%]	±6.60 [3.5%]
alpha_MET_SoftTrk_Scale	±9.09 [3.9%]	±2.22 [1.0%]	±0.65 [0.35%]
alpha_JET_EffectiveNP_Statistical2	±7.37 [3.2%]	±0.76 [0.35%]	±3.23 [1.7%]
alpha_JET_EffectiveNP_Statistical1	±7.25 [3.1%]	±0.82 [0.38%]	±3.02 [1.6%]
alpha_JET_EtaInt	±6.98 [3.0%]	±3.54 [1.7%]	±5.56 [3.0%]
alpha_JET_Pileup_OffsetNPV	±6.92 [3.0%]	±3.98 [1.9%]	±2.59 [1.4%]
alpha_PDF_QCD_W_bin1	±6.38 [2.7%]	±0.00 [0.00%]	±0.00 [0.00%]
alpha_FACT_QCD_W_bin1	±6.09 [2.6%]	±0.00 [0.00%]	±0.00 [0.00%]
alpha_RESUM_EWK_W_bin1	±6.08 [2.6%]	±0.00 [0.00%]	±0.00 [0.00%]
Lumi	±5.08 [2.2%]	±4.67 [2.2%]	±4.09 [2.2%]
alpha_JET_EffectiveNP_Modelling3	±4.89 [2.1%]	±0.04 [0.02%]	±2.66 [1.4%]
alpha_CKKW_EWK_W_bin1	±3.92 [1.7%]	±0.00 [0.00%]	±0.00 [0.00%]
alpha_JET_EffectiveNP_Statistical4	±3.44 [1.5%]	±0.41 [0.19%]	±0.31 [0.17%]
alpha_MET_SoftTrk_ResoPara	±3.30 [1.4%]	±0.67 [0.32%]	±0.34 [0.18%]
alpha_JET_EffectiveNP_Mixed1	±3.17 [1.4%]	±0.92 [0.43%]	±2.11 [1.1%]
alpha_JET_EtaIntercalibration_TotalStat	±3.09 [1.3%]	±0.53 [0.25%]	±0.30 [0.16%]
alpha_JET_EffectiveNP_Modelling1	±3.08 [1.3%]	±6.29 [2.9%]	±0.71 [0.38%]
alpha_RESUM_QCD_W_bin1	±2.98 [1.3%]	±0.00 [0.00%]	±0.00 [0.00%]
alpha_MU_EFF_SYST	±2.40 [1.0%]	±2.28 [1.1%]	±2.12 [1.1%]
alpha_JER	±2.26 [0.98%]	±5.00 [2.3%]	±3.57 [1.9%]
alpha_JET_EtaIntercalibration_Modelling	±1.89 [0.81%]	±12.26 [5.7%]	±6.80 [3.6%]
alpha_JET_Pileup_RhoTopology	±1.81 [0.78%]	±8.25 [3.9%]	±2.63 [1.4%]
alpha_PRW_DATASF	±1.29 [0.56%]	±0.78 [0.36%]	±5.00 [2.7%]
alpha_MET_SoftTrk_ResoPerp	±1.06 [0.46%]	±7.55 [3.5%]	±0.36 [0.20%]
alpha_JET_Flavor_Response	±0.81 [0.35%]	±1.00 [0.47%]	±2.77 [1.5%]
alpha_RESUM_QCD_W_bin3	±0.00 [0.00%]	±0.00 [0.00%]	±3.82 [2.0%]
alpha_CKKW_QCD_W_bin3	±0.00 [0.00%]	±0.00 [0.00%]	±9.86 [5.3%]
alpha_RESUM_EWK_W_bin3	±0.00 [0.00%]	±0.00 [0.00%]	±6.92 [3.7%]
alpha_RESUM_EWK_W_bin2	±0.00 [0.00%]	±6.24 [2.9%]	±0.00 [0.00%]
k_Wbin3	±0.00 [0.00%]	±0.00 [0.00%]	±41.70 [22.3%]
k_Wbin2	±0.00 [0.00%]	±45.00 [21.1%]	±0.00 [0.00%]
gamma_stat_ONEmuCR2pos_cuts_bin_0	±0.00 [0.00%]	±15.40 [7.2%]	±0.00 [0.00%]
alpha_FACT_QCD_W_bin3	±0.00 [0.00%]	±0.00 [0.00%]	±4.57 [2.4%]
alpha_FACT_QCD_W_bin2	±0.00 [0.00%]	±5.51 [2.6%]	±0.00 [0.00%]
alpha_RESUM_QCD_W_bin2	±0.00 [0.00%]	±6.55 [3.1%]	±0.00 [0.00%]
alpha_REN_QCD_W_bin3	±0.00 [0.00%]	±0.00 [0.00%]	±19.00 [10.2%]
alpha_REN_QCD_W_bin2	±0.00 [0.00%]	±27.57 [12.9%]	±0.00 [0.00%]
alpha_PDF_QCD_W_bin2	±0.00 [0.00%]	±3.00 [1.4%]	±0.00 [0.00%]
alpha_PDF_QCD_W_bin3	±0.00 [0.00%]	±0.00 [0.00%]	±2.21 [1.2%]
alpha_REN_EWK_W_bin3	±0.00 [0.00%]	±0.00 [0.00%]	±2.86 [1.5%]
alpha_FACT_EWK_W_bin2	±0.00 [0.00%]	±3.56 [1.7%]	±0.00 [0.00%]
alpha_FACT_EWK_W_bin3	±0.00 [0.00%]	±0.00 [0.00%]	±8.12 [4.3%]
gamma_stat_ONEmuCR3pos_cuts_bin_0	±0.00 [0.00%]	±0.00 [0.00%]	±12.79 [6.8%]

Table E.9: Pre-fit Wmunu CR neg. Breakdown of the dominant systematic uncertainties on background estimates in the various signal regions. Note that the individual uncertainties can be correlated, and do not necessarily add up quadratically to the total background uncertainty. The percentages show the size of the uncertainty relative to the total expected background.

Uncertainty of channel	ONEmuCR1neg	ONEmuCR2neg	ONEmuCR3neg
Total background expectation	160.23	113.40	82.94
Total statistical ($\sqrt{N_{\text{exp}}}$)	±12.66	±10.65	±9.11
Total background systematic	±38.68 [24.14%]	±31.85 [28.08%]	±25.42 [30.65%]
alpha_REN_QCD_W_bin1	±20.11 [12.6%]	±0.00 [0.00%]	±0.00 [0.00%]
gamma_stat_ONEmuCR1neg_cuts_bin_0	±16.55 [10.3%]	±0.00 [0.00%]	±0.00 [0.00%]
alpha_JET_Flavor_Composition	±15.51 [9.7%]	±12.13 [10.7%]	±2.20 [2.7%]
alpha_JET_EffectiveNP_Modelling2	±10.83 [6.8%]	±12.39 [10.9%]	±13.84 [16.7%]
alpha_JER	±9.48 [5.9%]	±11.71 [10.3%]	±5.71 [6.9%]
alpha_CKKW_QCD_W_bin1	±9.08 [5.7%]	±0.00 [0.00%]	±0.00 [0.00%]
alpha_JET_Pileup_RhoTopology	±7.31 [4.6%]	±2.87 [2.5%]	±3.35 [4.0%]
alpha_JET_EffectiveNP_Modelling1	±7.00 [4.4%]	±1.06 [0.93%]	±2.50 [3.0%]
alpha_PRW_DATASF	±5.82 [3.6%]	±2.56 [2.3%]	±8.85 [10.7%]
alpha_PDF_QCD_W_bin1	±4.51 [2.8%]	±0.00 [0.00%]	±0.00 [0.00%]
alpha_JET_Pileup_PtTerm	±4.47 [2.8%]	±3.79 [3.3%]	±4.63 [5.6%]
alpha_FACT_QCD_W_bin1	±4.31 [2.7%]	±0.00 [0.00%]	±0.00 [0.00%]
alpha_MET_SoftTrk_ResoPerp	±3.95 [2.5%]	±1.69 [1.5%]	±2.86 [3.4%]
Lumi	±3.53 [2.2%]	±2.49 [2.2%]	±1.82 [2.2%]
alpha_JET_EtaIntercalibration_Modelling	±3.35 [2.1%]	±9.58 [8.4%]	±5.04 [6.1%]
alpha_JET_Pileup_OffsetNPV	±3.17 [2.0%]	±0.76 [0.67%]	±3.11 [3.8%]
alpha_RESUM_EWK_W_bin1	±2.93 [1.8%]	±0.00 [0.00%]	±0.00 [0.00%]
alpha_JET_Pileup_OffsetMu	±2.18 [1.4%]	±1.62 [1.4%]	±1.06 [1.3%]
alpha_RESUM_QCD_W_bin1	±2.17 [1.4%]	±0.00 [0.00%]	±0.00 [0.00%]
alpha_MET_SoftTrk_ResoPara	±2.10 [1.3%]	±3.50 [3.1%]	±1.31 [1.6%]
alpha_CKKW_EWK_W_bin1	±1.89 [1.2%]	±0.00 [0.00%]	±0.00 [0.00%]
alpha_MU_EFF_SYST	±1.83 [1.1%]	±1.42 [1.3%]	±1.07 [1.3%]
alpha_JET_EffectiveNP_Statistical1	±1.32 [0.82%]	±0.64 [0.57%]	±1.19 [1.4%]
alpha_MET_SoftTrk_Scale	±1.25 [0.78%]	±0.14 [0.12%]	±2.13 [2.6%]
alpha_JET_Flavor_Response	±0.93 [0.58%]	±0.23 [0.20%]	±0.92 [1.1%]
alpha_JET_EffectiveNP_Statistical2	±0.93 [0.58%]	±0.57 [0.50%]	±1.21 [1.5%]
alpha_JET_EffectiveNP_Statistical4	±0.91 [0.57%]	±0.18 [0.16%]	±1.93 [2.3%]
alpha_JET_EffectiveNP_Modelling4	±0.91 [0.57%]	±0.12 [0.10%]	±1.52 [1.8%]
alpha_JET_EffectiveNP_Mixed1	±0.75 [0.47%]	±0.22 [0.19%]	±1.15 [1.4%]
alpha_JET_EtaInt	±0.51 [0.32%]	±1.64 [1.4%]	±2.16 [2.6%]
alpha_JET_EffectiveNP_Modelling3	±0.27 [0.17%]	±0.05 [0.05%]	±3.60 [4.3%]
alpha_JET_EtaIntercalibration_TotalStat	±0.03 [0.02%]	±0.01 [0.01%]	±0.92 [1.1%]
alpha_RESUM_QCD_W_bin3	±0.00 [0.00%]	±0.00 [0.00%]	±1.79 [2.2%]
alpha_CKKW_QCD_W_bin3	±0.00 [0.00%]	±0.00 [0.00%]	±4.60 [5.5%]
alpha_RESUM_EWK_W_bin3	±0.00 [0.00%]	±0.00 [0.00%]	±2.78 [3.3%]
alpha_RESUM_EWK_W_bin2	±0.00 [0.00%]	±3.28 [2.9%]	±0.00 [0.00%]
gamma_stat_ONEmuCR2neg_cuts_bin_0	±0.00 [0.00%]	±13.28 [11.7%]	±0.00 [0.00%]
alpha_FACT_QCD_W_bin3	±0.00 [0.00%]	±0.00 [0.00%]	±2.13 [2.6%]
alpha_FACT_QCD_W_bin2	±0.00 [0.00%]	±2.88 [2.5%]	±0.00 [0.00%]
gamma_stat_ONEmuCR3neg_cuts_bin_0	±0.00 [0.00%]	±0.00 [0.00%]	±9.23 [11.1%]
alpha_RESUM_QCD_W_bin2	±0.00 [0.00%]	±3.46 [3.0%]	±0.00 [0.00%]
alpha_REN_QCD_W_bin3	±0.00 [0.00%]	±0.00 [0.00%]	±8.88 [10.7%]
alpha_REN_QCD_W_bin2	±0.00 [0.00%]	±14.38 [12.7%]	±0.00 [0.00%]
alpha_PDF_QCD_W_bin2	±0.00 [0.00%]	±1.57 [1.4%]	±0.00 [0.00%]
alpha_PDF_QCD_W_bin3	±0.00 [0.00%]	±0.00 [0.00%]	±1.03 [1.2%]
alpha_REN_EWK_W_bin3	±0.00 [0.00%]	±0.00 [0.00%]	±1.15 [1.4%]
alpha_FACT_EWK_W_bin2	±0.00 [0.00%]	±1.87 [1.7%]	±0.00 [0.00%]
alpha_FACT_EWK_W_bin3	±0.00 [0.00%]	±0.00 [0.00%]	±3.26 [3.9%]

Table E.10: Post-fit Wmunu CR neg. Breakdown of the dominant systematic uncertainties on background estimates in the various signal regions. Note that the individual uncertainties can be correlated, and do not necessarily add up quadratically to the total background uncertainty. The percentages show the size of the uncertainty relative to the total expected background.

Uncertainty of channel	ONEmuCR1neg	ONEmuCR2neg	ONEmuCR3neg
Total background expectation	160.23	113.40	82.94
Total statistical ($\sqrt{N_{\text{exp}}}$)	±12.66	±10.65	±9.11
Total background systematic	±11.67 [7.28%]	±9.27 [8.18%]	±7.78 [9.38%]
k_Wbin1	±30.14 [18.8%]	±0.00 [0.00%]	±0.00 [0.00%]
alpha_REN_QCD_W_bin1	±19.92 [12.4%]	±0.00 [0.00%]	±0.00 [0.00%]
gamma_stat_ONEmuCR1neg_cuts_bin_0	±14.28 [8.9%]	±0.00 [0.00%]	±0.00 [0.00%]
alpha_JET_Flavor_Composition	±10.47 [6.5%]	±8.19 [7.2%]	±1.48 [1.8%]
alpha_JET_EffectiveNP_Modelling2	±9.26 [5.8%]	±10.59 [9.3%]	±11.84 [14.3%]
alpha_CKKW_QCD_W_bin1	±8.99 [5.6%]	±0.00 [0.00%]	±0.00 [0.00%]
alpha_JET_Pileup_RhoTopology	±6.17 [3.9%]	±2.43 [2.1%]	±2.83 [3.4%]
alpha_JET_EffectiveNP_Modelling1	±6.17 [3.9%]	±0.93 [0.82%]	±2.21 [2.7%]
alpha_PDF_QCD_W_bin1	±4.48 [2.8%]	±0.00 [0.00%]	±0.00 [0.00%]
alpha_FACT_QCD_W_bin1	±4.28 [2.7%]	±0.00 [0.00%]	±0.00 [0.00%]
alpha_JET_Pileup_PtTerm	±4.16 [2.6%]	±3.53 [3.1%]	±4.31 [5.2%]
alpha_PRW_DATASF	±4.01 [2.5%]	±1.77 [1.6%]	±6.10 [7.4%]
alpha_JER	±3.81 [2.4%]	±4.70 [4.1%]	±2.29 [2.8%]
alpha_MET_SoftTrk_ResoPerp	±3.64 [2.3%]	±1.56 [1.4%]	±2.64 [3.2%]
Lumi	±3.51 [2.2%]	±2.48 [2.2%]	±1.82 [2.2%]
alpha_JET_Pileup_OffsetNPV	±2.94 [1.8%]	±0.70 [0.62%]	±2.88 [3.5%]
alpha_RESUM_EWK_W_bin1	±2.90 [1.8%]	±0.00 [0.00%]	±0.00 [0.00%]
alpha_JET_EtaIntercalibration_Modelling	±2.90 [1.8%]	±8.28 [7.3%]	±4.35 [5.3%]
k_Zbin1	±2.38 [1.5%]	±0.00 [0.00%]	±0.00 [0.00%]
alpha_RESUM_QCD_W_bin1	±2.09 [1.3%]	±0.00 [0.00%]	±0.00 [0.00%]
alpha_JET_Pileup_OffsetMu	±1.90 [1.2%]	±1.41 [1.2%]	±0.92 [1.1%]
alpha_CKKW_EWK_W_bin1	±1.87 [1.2%]	±0.00 [0.00%]	±0.00 [0.00%]
alpha_MU_EFF_SYST	±1.80 [1.1%]	±1.40 [1.2%]	±1.06 [1.3%]
alpha_MET_SoftTrk_ResoPara	±1.72 [1.1%]	±2.86 [2.5%]	±1.07 [1.3%]
alpha_JET_EffectiveNP_Statistical1	±1.28 [0.80%]	±0.62 [0.55%]	±1.15 [1.4%]
alpha_MET_SoftTrk_Scale	±1.20 [0.75%]	±0.13 [0.12%]	±2.05 [2.5%]
alpha_JET_EffectiveNP_Statistical2	±0.90 [0.56%]	±0.55 [0.49%]	±1.17 [1.4%]
alpha_JET_EffectiveNP_Modelling4	±0.89 [0.55%]	±0.11 [0.10%]	±1.49 [1.8%]
alpha_JET_EffectiveNP_Statistical4	±0.88 [0.55%]	±0.18 [0.15%]	±1.88 [2.3%]
alpha_JET_Flavor_Response	±0.85 [0.53%]	±0.21 [0.19%]	±0.84 [1.0%]
alpha_JET_EffectiveNP_Mixed1	±0.73 [0.46%]	±0.21 [0.19%]	±1.12 [1.4%]
alpha_JET_EtaInt	±0.43 [0.27%]	±1.38 [1.2%]	±1.81 [2.2%]
alpha_JET_EffectiveNP_Modelling3	±0.26 [0.16%]	±0.05 [0.05%]	±3.45 [4.2%]
alpha_JET_EtaIntercalibration_TotalStat	±0.03 [0.02%]	±0.01 [0.01%]	±0.90 [1.1%]
alpha_RESUM_QCD_W_bin3	±0.00 [0.00%]	±0.00 [0.00%]	±1.77 [2.1%]
alpha_CKKW_QCD_W_bin3	±0.00 [0.00%]	±0.00 [0.00%]	±4.57 [5.5%]
alpha_RESUM_EWK_W_bin3	±0.00 [0.00%]	±0.00 [0.00%]	±2.76 [3.3%]
alpha_RESUM_EWK_W_bin2	±0.00 [0.00%]	±3.26 [2.9%]	±0.00 [0.00%]
k_Wbin3	±0.00 [0.00%]	±0.00 [0.00%]	±18.29 [22.0%]
k_Wbin2	±0.00 [0.00%]	±23.35 [20.6%]	±0.00 [0.00%]
gamma_stat_ONEmuCR2neg_cuts_bin_0	±0.00 [0.00%]	±10.51 [9.3%]	±0.00 [0.00%]
k_Zbin2	±0.00 [0.00%]	±1.32 [1.2%]	±0.00 [0.00%]
alpha_FACT_QCD_W_bin3	±0.00 [0.00%]	±0.00 [0.00%]	±2.12 [2.6%]
alpha_FACT_QCD_W_bin2	±0.00 [0.00%]	±2.86 [2.5%]	±0.00 [0.00%]
gamma_stat_ONEmuCR3neg_cuts_bin_0	±0.00 [0.00%]	±0.00 [0.00%]	±7.84 [9.5%]
alpha_RESUM_QCD_W_bin2	±0.00 [0.00%]	±3.39 [3.0%]	±0.00 [0.00%]
alpha_REN_QCD_W_bin3	±0.00 [0.00%]	±0.00 [0.00%]	±8.80 [10.6%]
alpha_REN_QCD_W_bin2	±0.00 [0.00%]	±14.28 [12.6%]	±0.00 [0.00%]
alpha_PDF_QCD_W_bin2	±0.00 [0.00%]	±1.55 [1.4%]	±0.00 [0.00%]
alpha_PDF_QCD_W_bin3	±0.00 [0.00%]	±0.00 [0.00%]	±1.02 [1.2%]
alpha_REN_EWK_W_bin3	±0.00 [0.00%]	±0.00 [0.00%]	±1.14 [1.4%]
alpha_FACT_EWK_W_bin2	±0.00 [0.00%]	±1.86 [1.6%]	±0.00 [0.00%]
alpha_FACT_EWK_W_bin3	±0.00 [0.00%]	±0.00 [0.00%]	±3.24 [3.9%]

Table E.11: Pre-fit Zmumu CR. Breakdown of the dominant systematic uncertainties on background estimates in the various signal regions. Note that the individual uncertainties can be correlated, and do not necessarily add up quadratically to the total background uncertainty. The percentages show the size of the uncertainty relative to the total expected background.

Uncertainty of channel	TWOmuCR1	TWOmuCR2	TWOmuCR3
Total background expectation	47.11	30.83	18.48
Total statistical ($\sqrt{N_{\text{exp}}}$)	±6.86	±5.55	±4.30
Total background systematic	±20.69 [43.92%]	±8.81 [28.56%]	±4.82 [26.07%]
gamma_stat_TWOmuCR1_cuts_bin_0	±13.46 [28.6%]	±0.00 [0.00%]	±0.00 [0.00%]
alpha_JER	±11.28 [23.9%]	±4.68 [15.2%]	±0.89 [4.8%]
alpha_REN_QCD_Z_bin1	±6.85 [14.5%]	±0.00 [0.00%]	±0.00 [0.00%]
alpha_RESUM_QCD_Z_bin1	±4.40 [9.3%]	±0.00 [0.00%]	±0.00 [0.00%]
alpha_JET_EtaIntercalibration_Modelling	±4.12 [8.7%]	±1.40 [4.5%]	±0.77 [4.2%]
alpha_JET_Pileup_PtTerm	±3.98 [8.5%]	±2.21 [7.2%]	±0.77 [4.2%]
alpha_CKKW_QCD_Z_bin1	±1.97 [4.2%]	±0.00 [0.00%]	±0.00 [0.00%]
alpha_FACT_QCD_Z_bin1	±1.81 [3.8%]	±0.00 [0.00%]	±0.00 [0.00%]
alpha_JET_Flavor_Response	±1.66 [3.5%]	±0.05 [0.17%]	±0.09 [0.47%]
alpha_JET_Pileup_OffsetMu	±1.64 [3.5%]	±0.40 [1.3%]	±0.44 [2.4%]
alpha_PRW_DATASF	±1.22 [2.6%]	±0.29 [0.94%]	±2.15 [11.6%]
Lumi	±1.04 [2.2%]	±0.68 [2.2%]	±0.41 [2.2%]
alpha_JET_EffectiveNP_Modelling1	±1.01 [2.1%]	±0.94 [3.1%]	±0.89 [4.8%]
alpha_MU_EFF_SYST	±0.87 [1.8%]	±0.66 [2.2%]	±0.44 [2.4%]
alpha_MET_SoftTrk_ResoPerp	±0.81 [1.7%]	±0.17 [0.55%]	±0.17 [0.94%]
alpha_JET_Pileup_RhoTopology	±0.77 [1.6%]	±0.68 [2.2%]	±0.84 [4.6%]
alpha_JET_EtaInt	±0.75 [1.6%]	±0.37 [1.2%]	±1.12 [6.1%]
alpha_CKKW_EWK_Z_bin1	±0.60 [1.3%]	±0.00 [0.00%]	±0.00 [0.00%]
alpha_PDF_QCD_Z_bin1	±0.48 [1.0%]	±0.00 [0.00%]	±0.00 [0.00%]
alpha_JET_EffectiveNP_Statistical1	±0.44 [0.93%]	±0.44 [1.4%]	±0.31 [1.7%]
alpha_JET_Flavor_Composition	±0.36 [0.77%]	±0.99 [3.2%]	±0.92 [5.0%]
alpha_JET_EffectiveNP_Statistical2	±0.33 [0.70%]	±0.40 [1.3%]	±0.32 [1.7%]
alpha_JET_EtaIntercalibration_TotalStat	±0.26 [0.55%]	±0.15 [0.49%]	±0.60 [3.3%]
alpha_JET_EffectiveNP_Modelling3	±0.25 [0.53%]	±0.40 [1.3%]	±0.13 [0.68%]
alpha_JET_EffectiveNP_Modelling2	±0.19 [0.40%]	±0.52 [1.7%]	±0.25 [1.3%]
alpha_JET_Pileup_OffsetNPV	±0.11 [0.23%]	±0.77 [2.5%]	±0.10 [0.55%]
alpha_CKKW_QCD_Z_bin2	±0.00 [0.00%]	±1.28 [4.2%]	±0.00 [0.00%]
alpha_CKKW_QCD_Z_bin3	±0.00 [0.00%]	±0.00 [0.00%]	±0.27 [1.5%]
alpha_PDF_EWK_Z_bin3	±0.00 [0.00%]	±0.00 [0.00%]	±0.23 [1.2%]
alpha_RESUM_EWK_Z_bin2	±0.00 [0.00%]	±1.01 [3.3%]	±0.00 [0.00%]
alpha_REN_EWK_Z_bin3	±0.00 [0.00%]	±0.00 [0.00%]	±0.34 [1.8%]
gamma_stat_TWOmuCR2_cuts_bin_0	±0.00 [0.00%]	±4.01 [13.0%]	±0.00 [0.00%]
alpha_REN_QCD_Z_bin2	±0.00 [0.00%]	±4.76 [15.4%]	±0.00 [0.00%]
alpha_REN_QCD_Z_bin3	±0.00 [0.00%]	±0.00 [0.00%]	±1.83 [9.9%]
alpha_CKKW_EWK_Z_bin3	±0.00 [0.00%]	±0.00 [0.00%]	±0.49 [2.7%]
alpha_CKKW_EWK_Z_bin2	±0.00 [0.00%]	±0.43 [1.4%]	±0.00 [0.00%]
alpha_RESUM_QCD_Z_bin3	±0.00 [0.00%]	±0.00 [0.00%]	±1.09 [5.9%]
alpha_PDF_QCD_Z_bin3	±0.00 [0.00%]	±0.00 [0.00%]	±0.27 [1.5%]
alpha_FACT_QCD_Z_bin2	±0.00 [0.00%]	±1.10 [3.6%]	±0.00 [0.00%]
alpha_FACT_QCD_Z_bin3	±0.00 [0.00%]	±0.00 [0.00%]	±0.62 [3.4%]
gamma_stat_TWOmuCR3_cuts_bin_0	±0.00 [0.00%]	±0.00 [0.00%]	±2.30 [12.4%]
alpha_RESUM_QCD_Z_bin2	±0.00 [0.00%]	±0.67 [2.2%]	±0.00 [0.00%]
alpha_FACT_EWK_Z_bin3	±0.00 [0.00%]	±0.00 [0.00%]	±0.90 [4.9%]
alpha_FACT_EWK_Z_bin2	±0.00 [0.00%]	±0.43 [1.4%]	±0.00 [0.00%]

E.4 Control region Zmumu

Table E.12: Post-fit Zmumu CR. Breakdown of the dominant systematic uncertainties on background estimates in the various signal regions. Note that the individual uncertainties can be correlated, and do not necessarily add up quadratically to the total background uncertainty. The percentages show the size of the uncertainty relative to the total expected background.

Uncertainty of channel	TWOmuCR1	TWOmuCR2	TWOmuCR3
Total background expectation	47.11	30.83	18.48
Total statistical ($\sqrt{N_{\text{exp}}}$)	±6.86	±5.55	±4.30
Total background systematic	±6.33 [13.44%]	±4.34 [14.08%]	±3.39 [18.33%]
k_Zbin1	±11.56 [24.5%]	±0.00 [0.00%]	±0.00 [0.00%]
gamma_stat_TWOmuCR1_cuts_bin_0	±9.02 [19.1%]	±0.00 [0.00%]	±0.00 [0.00%]
alpha_REN_QCD_Z_bin1	±6.79 [14.4%]	±0.00 [0.00%]	±0.00 [0.00%]
alpha_JER	±4.53 [9.6%]	±1.88 [6.1%]	±0.36 [1.9%]
alpha_RESUM_QCD_Z_bin1	±4.36 [9.3%]	±0.00 [0.00%]	±0.00 [0.00%]
alpha_JET_Pileup_PtTerm	±3.71 [7.9%]	±2.06 [6.7%]	±0.72 [3.9%]
alpha_JET_EtaIntercalibration_Modelling	±3.56 [7.5%]	±1.21 [3.9%]	±0.67 [3.6%]
alpha_CKKW_QCD_Z_bin1	±1.91 [4.1%]	±0.00 [0.00%]	±0.00 [0.00%]
alpha_FACT_QCD_Z_bin1	±1.80 [3.8%]	±0.00 [0.00%]	±0.00 [0.00%]
alpha_JET_Flavor_Response	±1.51 [3.2%]	±0.05 [0.15%]	±0.08 [0.43%]
alpha_JET_Pileup_OffsetMu	±1.43 [3.0%]	±0.35 [1.1%]	±0.38 [2.1%]
Lumi	±1.03 [2.2%]	±0.68 [2.2%]	±0.40 [2.2%]
alpha_JET_EffectiveNP_Modelling1	±0.89 [1.9%]	±0.83 [2.7%]	±0.79 [4.2%]
alpha_MU_EFF_SYST	±0.85 [1.8%]	±0.65 [2.1%]	±0.44 [2.4%]
alpha_PRW_DATASF	±0.84 [1.8%]	±0.20 [0.65%]	±1.48 [8.0%]
alpha_MET_SoftTrk_ResoPerp	±0.75 [1.6%]	±0.16 [0.51%]	±0.16 [0.87%]
alpha_JET_Pileup_RhoTopology	±0.65 [1.4%]	±0.58 [1.9%]	±0.71 [3.8%]
alpha_JET_EtaInt	±0.63 [1.3%]	±0.31 [1.00%]	±0.94 [5.1%]
alpha_CKKW_EWK_Z_bin1	±0.59 [1.3%]	±0.00 [0.00%]	±0.00 [0.00%]
alpha_PDF_QCD_Z_bin1	±0.47 [1.0%]	±0.00 [0.00%]	±0.00 [0.00%]
alpha_JET_EffectiveNP_Statistical1	±0.43 [0.91%]	±0.42 [1.4%]	±0.30 [1.6%]
alpha_JET_EffectiveNP_Statistical2	±0.32 [0.68%]	±0.38 [1.2%]	±0.31 [1.7%]
alpha_JET_EtaIntercalibration_TotalStat	±0.25 [0.54%]	±0.15 [0.48%]	±0.59 [3.2%]
alpha_JET_Flavor_Composition	±0.24 [0.52%]	±0.67 [2.2%]	±0.62 [3.4%]
alpha_JET_EffectiveNP_Modelling3	±0.24 [0.51%]	±0.39 [1.3%]	±0.12 [0.65%]
alpha_JET_EffectiveNP_Modelling2	±0.16 [0.34%]	±0.45 [1.5%]	±0.21 [1.1%]
alpha_JET_Pileup_OffsetNPV	±0.10 [0.21%]	±0.72 [2.3%]	±0.09 [0.51%]
alpha_CKKW_QCD_Z_bin2	±0.00 [0.00%]	±1.23 [4.0%]	±0.00 [0.00%]
k_Zbin2	±0.00 [0.00%]	±6.97 [22.6%]	±0.00 [0.00%]
k_Zbin3	±0.00 [0.00%]	±0.00 [0.00%]	±4.46 [24.2%]
alpha_CKKW_QCD_Z_bin3	±0.00 [0.00%]	±0.00 [0.00%]	±0.27 [1.4%]
alpha_PDF_EWK_Z_bin3	±0.00 [0.00%]	±0.00 [0.00%]	±0.23 [1.2%]
alpha_RESUM_EWK_Z_bin2	±0.00 [0.00%]	±1.00 [3.2%]	±0.00 [0.00%]
alpha_REN_EWK_Z_bin3	±0.00 [0.00%]	±0.00 [0.00%]	±0.34 [1.8%]
gamma_stat_TWOmuCR2_cuts_bin_0	±0.00 [0.00%]	±3.57 [11.6%]	±0.00 [0.00%]
alpha_REN_QCD_Z_bin2	±0.00 [0.00%]	±4.72 [15.3%]	±0.00 [0.00%]
alpha_REN_QCD_Z_bin3	±0.00 [0.00%]	±0.00 [0.00%]	±1.81 [9.8%]
alpha_CKKW_EWK_Z_bin3	±0.00 [0.00%]	±0.00 [0.00%]	±0.49 [2.6%]
alpha_CKKW_EWK_Z_bin2	±0.00 [0.00%]	±0.42 [1.4%]	±0.00 [0.00%]
alpha_RESUM_QCD_Z_bin3	±0.00 [0.00%]	±0.00 [0.00%]	±1.08 [5.9%]
alpha_PDF_QCD_Z_bin3	±0.00 [0.00%]	±0.00 [0.00%]	±0.27 [1.5%]
alpha_FACT_QCD_Z_bin2	±0.00 [0.00%]	±1.09 [3.5%]	±0.00 [0.00%]
alpha_FACT_QCD_Z_bin3	±0.00 [0.00%]	±0.00 [0.00%]	±0.62 [3.3%]
gamma_stat_TWOmuCR3_cuts_bin_0	±0.00 [0.00%]	±0.00 [0.00%]	±2.16 [11.7%]
alpha_RESUM_QCD_Z_bin2	±0.00 [0.00%]	±0.63 [2.1%]	±0.00 [0.00%]
alpha_FACT_EWK_Z_bin3	±0.00 [0.00%]	±0.00 [0.00%]	±0.90 [4.8%]
alpha_FACT_EWK_Z_bin2	±0.00 [0.00%]	±0.43 [1.4%]	±0.00 [0.00%]

Table E.13: Pre-fit Zee CR. Breakdown of the dominant systematic uncertainties on background estimates in the various signal regions. Note that the individual uncertainties can be correlated, and do not necessarily add up quadratically to the total background uncertainty. The percentages show the size of the uncertainty relative to the total expected background.

Uncertainty of channel	TWOeleCR1	TWOeleCR2	TWOeleCR3
Total background expectation	23.26	25.27	22.09
Total statistical ($\sqrt{N_{\text{exp}}}$)	±4.82	±5.03	±4.70
Total background systematic	±8.76 [37.65%]	±7.91 [31.31%]	±6.36 [28.78%]
alpha_JER	±5.02 [21.6%]	±3.53 [14.0%]	±3.41 [15.4%]
gamma_stat_TWOeleCR1_cuts_bin_0	±4.16 [17.9%]	±0.00 [0.00%]	±0.00 [0.00%]
alpha_REN_QCD_Z_bin1	±3.36 [14.5%]	±0.00 [0.00%]	±0.00 [0.00%]
alpha_RESUM_QCD_Z_bin1	±2.16 [9.3%]	±0.00 [0.00%]	±0.00 [0.00%]
alpha_JET_Pileup_RhoTopology	±1.89 [8.1%]	±0.80 [3.2%]	±0.00 [0.02%]
alpha_JET_Flavor_Response	±1.65 [7.1%]	±1.21 [4.8%]	±0.31 [1.4%]
alpha_JET_Flavor_Composition	±1.64 [7.0%]	±1.91 [7.5%]	±1.00 [4.5%]
alpha_JET_EffectiveNP_Modelling1	±1.26 [5.4%]	±0.10 [0.39%]	±0.04 [0.19%]
alpha_JET_Pileup_PtTerm	±1.15 [4.9%]	±1.62 [6.4%]	±0.63 [2.8%]
alpha_JET_EtaIntercalibration_Modelling	±1.08 [4.6%]	±1.94 [7.7%]	±1.37 [6.2%]
alpha_JET_EtaInt	±0.98 [4.2%]	±2.16 [8.5%]	±0.41 [1.9%]
alpha_CKKW_QCD_Z_bin1	±0.97 [4.2%]	±0.00 [0.00%]	±0.00 [0.00%]
alpha_FACT_QCD_Z_bin1	±0.89 [3.8%]	±0.00 [0.00%]	±0.00 [0.00%]
alpha_JET_Pileup_OffsetMu	±0.62 [2.7%]	±2.10 [8.3%]	±0.18 [0.82%]
alpha_EL_EFF_ID	±0.58 [2.5%]	±0.64 [2.5%]	±0.60 [2.7%]
alpha_JET_EffectiveNP_Modelling2	±0.56 [2.4%]	±0.22 [0.86%]	±0.12 [0.52%]
Lumi	±0.51 [2.2%]	±0.56 [2.2%]	±0.49 [2.2%]
alpha_PRW_DATASF	±0.45 [1.9%]	±0.17 [0.66%]	±1.62 [7.3%]
alpha_JET_Pileup_OffsetNPV	±0.35 [1.5%]	±0.44 [1.7%]	±0.12 [0.54%]
alpha_EL_EFF_ISO	±0.33 [1.4%]	±0.35 [1.4%]	±0.37 [1.7%]
alpha_CKKW_EWK_Z_bin1	±0.31 [1.3%]	±0.00 [0.00%]	±0.00 [0.00%]
alpha_JET_EffectiveNP_Modelling3	±0.31 [1.3%]	±0.22 [0.86%]	±0.10 [0.45%]
alpha_MET_SoftTrk_Scale	±0.25 [1.1%]	±0.09 [0.35%]	±0.02 [0.08%]
alpha_PDF_QCD_Z_bin1	±0.23 [1.0%]	±0.00 [0.00%]	±0.00 [0.00%]
alpha_JET_EffectiveNP_Mixed1	±0.18 [0.78%]	±0.47 [1.9%]	±0.01 [0.03%]
alpha_MET_SoftTrk_ResoPerp	±0.15 [0.64%]	±0.35 [1.4%]	±0.16 [0.71%]
alpha_JET_EtaIntercalibration_TotalStat	±0.13 [0.56%]	±0.35 [1.4%]	±0.18 [0.82%]
alpha_CKKW_QCD_Z_bin2	±0.00 [0.00%]	±1.04 [4.1%]	±0.00 [0.00%]
gamma_stat_TWOeleCR2_cuts_bin_0	±0.00 [0.00%]	±3.00 [11.9%]	±0.00 [0.00%]
alpha_CKKW_QCD_Z_bin3	±0.00 [0.00%]	±0.00 [0.00%]	±0.38 [1.7%]
alpha_RESUM_EWK_Z_bin2	±0.00 [0.00%]	±0.84 [3.3%]	±0.00 [0.00%]
alpha_REN_EWK_Z_bin3	±0.00 [0.00%]	±0.00 [0.00%]	±0.32 [1.4%]
alpha_REN_QCD_Z_bin2	±0.00 [0.00%]	±3.87 [15.3%]	±0.00 [0.00%]
alpha_REN_QCD_Z_bin3	±0.00 [0.00%]	±0.00 [0.00%]	±2.62 [11.8%]
alpha_CKKW_EWK_Z_bin3	±0.00 [0.00%]	±0.00 [0.00%]	±0.46 [2.1%]
alpha_CKKW_EWK_Z_bin2	±0.00 [0.00%]	±0.35 [1.4%]	±0.00 [0.00%]
alpha_RESUM_QCD_Z_bin3	±0.00 [0.00%]	±0.00 [0.00%]	±1.56 [7.1%]
alpha_PDF_QCD_Z_bin3	±0.00 [0.00%]	±0.00 [0.00%]	±0.39 [1.8%]
gamma_stat_TWOeleCR3_cuts_bin_0	±0.00 [0.00%]	±0.00 [0.00%]	±3.19 [14.5%]
alpha_FACT_QCD_Z_bin2	±0.00 [0.00%]	±0.89 [3.5%]	±0.00 [0.00%]
alpha_FACT_QCD_Z_bin3	±0.00 [0.00%]	±0.00 [0.00%]	±0.89 [4.0%]
alpha_RESUM_QCD_Z_bin2	±0.00 [0.00%]	±0.55 [2.2%]	±0.00 [0.00%]
alpha_FACT_EWK_Z_bin3	±0.00 [0.00%]	±0.00 [0.00%]	±0.85 [3.8%]
alpha_FACT_EWK_Z_bin2	±0.00 [0.00%]	±0.36 [1.4%]	±0.00 [0.00%]

E.5 Control region Zee

Table E.14: Post-fit Zee CR. Breakdown of the dominant systematic uncertainties on background estimates in the various signal regions. Note that the individual uncertainties can be correlated, and do not necessarily add up quadratically to the total background uncertainty. The percentages show the size of the uncertainty relative to the total expected background.

Uncertainty of channel	TWOeleCR1	TWOeleCR2	TWOeleCR3
Total background expectation	23.26	25.27	22.09
Total statistical ($\sqrt{N_{\text{exp}}}$)	±4.82	±5.03	±4.70
Total background systematic	±4.12 [17.71%]	±3.84 [15.20%]	±3.78 [17.12%]
k_Zbin1	±5.73 [24.6%]	±0.00 [0.00%]	±0.00 [0.00%]
gamma_stat_TWOeleCR1_cuts_bin_0	±3.71 [16.0%]	±0.00 [0.00%]	±0.00 [0.00%]
alpha_REN_QCD_Z_bin1	±3.34 [14.4%]	±0.00 [0.00%]	±0.00 [0.00%]
alpha_RESUM_QCD_Z_bin1	±2.15 [9.2%]	±0.00 [0.00%]	±0.00 [0.00%]
alpha_JER	±2.02 [8.7%]	±1.42 [5.6%]	±1.37 [6.2%]
alpha_JET_Pileup_RhoTopology	±1.60 [6.9%]	±0.68 [2.7%]	±0.00 [0.02%]
alpha_JET_Flavor_Response	±1.50 [6.5%]	±1.10 [4.4%]	±0.29 [1.3%]
alpha_JET_EffectiveNP_Modelling1	±1.11 [4.8%]	±0.09 [0.34%]	±0.04 [0.17%]
alpha_JET_Flavor_Composition	±1.11 [4.8%]	±1.29 [5.1%]	±0.67 [3.0%]
alpha_JET_Pileup_PtTerm	±1.07 [4.6%]	±1.51 [6.0%]	±0.58 [2.6%]
alpha_CKKW_QCD_Z_bin1	±0.94 [4.0%]	±0.00 [0.00%]	±0.00 [0.00%]
alpha_JET_EtaIntercalibration_Modelling	±0.93 [4.0%]	±1.67 [6.6%]	±1.18 [5.3%]
alpha_FACT_QCD_Z_bin1	±0.88 [3.8%]	±0.00 [0.00%]	±0.00 [0.00%]
alpha_JET_EtaInt	±0.82 [3.5%]	±1.81 [7.2%]	±0.34 [1.6%]
alpha_EL_EFF_ID	±0.57 [2.5%]	±0.63 [2.5%]	±0.59 [2.7%]
alpha_JET_Pileup_OffsetMu	±0.54 [2.3%]	±1.83 [7.2%]	±0.16 [0.72%]
Lumi	±0.51 [2.2%]	±0.55 [2.2%]	±0.48 [2.2%]
alpha_JET_EffectiveNP_Modelling2	±0.48 [2.1%]	±0.19 [0.73%]	±0.10 [0.45%]
alpha_EL_EFF_ISO	±0.32 [1.4%]	±0.35 [1.4%]	±0.37 [1.7%]
alpha_JET_Pileup_OffsetNPV	±0.32 [1.4%]	±0.41 [1.6%]	±0.11 [0.50%]
alpha_CKKW_EWK_Z_bin1	±0.31 [1.3%]	±0.00 [0.00%]	±0.00 [0.00%]
alpha_PRW_DATASF	±0.31 [1.3%]	±0.11 [0.45%]	±1.12 [5.1%]
alpha_JET_EffectiveNP_Modelling3	±0.29 [1.3%]	±0.21 [0.82%]	±0.10 [0.44%]
alpha_MET_SoftTrk_Scale	±0.24 [1.0%]	±0.09 [0.34%]	±0.02 [0.08%]
alpha_PDF_QCD_Z_bin1	±0.23 [1.0%]	±0.00 [0.00%]	±0.00 [0.00%]
alpha_JET_EffectiveNP_Mixed1	±0.18 [0.77%]	±0.46 [1.8%]	±0.01 [0.03%]
alpha_MET_SoftTrk_ResoPerp	±0.14 [0.59%]	±0.32 [1.3%]	±0.14 [0.65%]
alpha_JET_EtaIntercalibration_TotalStat	±0.13 [0.55%]	±0.35 [1.4%]	±0.18 [0.80%]
alpha_CKKW_QCD_Z_bin2	±0.00 [0.00%]	±1.00 [4.0%]	±0.00 [0.00%]
gamma_stat_TWOeleCR2_cuts_bin_0	±0.00 [0.00%]	±2.76 [10.9%]	±0.00 [0.00%]
k_Zbin2	±0.00 [0.00%]	±5.69 [22.5%]	±0.00 [0.00%]
k_Zbin3	±0.00 [0.00%]	±0.00 [0.00%]	±5.42 [24.5%]
alpha_CKKW_QCD_Z_bin3	±0.00 [0.00%]	±0.00 [0.00%]	±0.38 [1.7%]
alpha_RESUM_EWK_Z_bin2	±0.00 [0.00%]	±0.83 [3.3%]	±0.00 [0.00%]
alpha_REN_EWK_Z_bin3	±0.00 [0.00%]	±0.00 [0.00%]	±0.32 [1.4%]
alpha_REN_QCD_Z_bin2	±0.00 [0.00%]	±3.84 [15.2%]	±0.00 [0.00%]
alpha_REN_QCD_Z_bin3	±0.00 [0.00%]	±0.00 [0.00%]	±2.59 [11.7%]
alpha_CKKW_EWK_Z_bin3	±0.00 [0.00%]	±0.00 [0.00%]	±0.46 [2.1%]
alpha_CKKW_EWK_Z_bin2	±0.00 [0.00%]	±0.35 [1.4%]	±0.00 [0.00%]
alpha_RESUM_QCD_Z_bin3	±0.00 [0.00%]	±0.00 [0.00%]	±1.54 [7.0%]
alpha_PDF_QCD_Z_bin3	±0.00 [0.00%]	±0.00 [0.00%]	±0.38 [1.7%]
gamma_stat_TWOeleCR3_cuts_bin_0	±0.00 [0.00%]	±0.00 [0.00%]	±2.91 [13.2%]
alpha_FACT_QCD_Z_bin2	±0.00 [0.00%]	±0.88 [3.5%]	±0.00 [0.00%]
alpha_FACT_QCD_Z_bin3	±0.00 [0.00%]	±0.00 [0.00%]	±0.88 [4.0%]
alpha_RESUM_QCD_Z_bin2	±0.00 [0.00%]	±0.51 [2.0%]	±0.00 [0.00%]
alpha_FACT_EWK_Z_bin3	±0.00 [0.00%]	±0.00 [0.00%]	±0.84 [3.8%]
alpha_FACT_EWK_Z_bin2	±0.00 [0.00%]	±0.36 [1.4%]	±0.00 [0.00%]

Appendix F

Upper Limit on Higgs invisible branching ratio

In absence of an excess in SR data, an upper limit on the Higgs invisible branching ratio can be set.
Since the signal MC events $N_{regi}^{exp,sig.}$ used as inputs in the likelihood function are normalized to the cross section of the process, the signal strength μ represents the branching ratio of the signal process.
The underlying idea is to estimate an upper limit on μ by comparing the probability of the data events in SR to be compatible with the predicted background, and with the background plus a given signal. To compute the limits, a profiled likelihood ratio statistical test is used. To test a hypothesized value of μ a test statistic based on the profiled likelihood ratio is used.
The test statistic q_μ used [139] is defined as:

$$q_\mu = \begin{cases} -2\ln \frac{\mathcal{L}(\mu,\hat{\hat{\theta}}(\mu))}{\mathcal{L}(\mu=0,\hat{\hat{\theta}}(\mu=0))} & \text{if } \hat{\mu} < 0, \\ -2\ln \frac{\mathcal{L}(\mu,\hat{\hat{\theta}})}{\mathcal{L}(\hat{\mu},\hat{\theta})} & \text{if } 0 \leq \hat{\mu} < \mu, \\ 0 & \text{if } \hat{\mu} > \mu. \end{cases} \tag{F.1}$$

where $\hat{\hat{\theta}}(\mu)$ denotes the value of θ which maximizes $\mathcal{L}$ for a specific μ ($\hat{\hat{\theta}}$ is called *conditional* maximum likelihood estimator); $\hat{\mu}$, $\hat{\theta}$ are the values of μ and θ which maximize $\mathcal{L}(\mu,\theta)$ ($\hat{\mu}$ and $\hat{\theta}$ are called *unconditional* maximum likelihood estimators). The test is performed as follows:

- $\hat{\mu} < 0$: the numerator is computed for each tested value of the Parameter Of Interest (POI) μ, maximizing $\mathcal{L}$ with μ fixed. The denominator is maximized fixing μ =0, (hence $\theta(\hat{\mu} = 0)$ is the set of parameters which maximize $\mathcal{L}$ for μ =0);
- $0 \leq \hat{\mu} < \mu$: as before, the numerator is computed for each tested value of the POI μ: $\mathcal{L}$ is maximized with μ fixed. The denominator is maximized with all the parameters free.

To extract the upper limit on μ the modified frequentist CL_s approach is used [140]. For each tested value of μ the CL_s is computed as:

$$\mathrm{CL}_s = \frac{\mathrm{CL}_{s+b}}{\mathrm{CL}_b} = \frac{p_\mu}{1-p_b} = \frac{\int_{q_\mu{}^{\mathrm{obs}}}^{\infty} f(q_\mu|\mu,\hat{\theta}_\mu)dq_\mu}{\int_{-\infty}^{q_\mu{}^{\mathrm{obs}}} f(q_\mu|0,\hat{\theta}_0)dq_\mu}.$$

where:

- q_μ^{obs} is the observed value (after fit);
- $f(q_\mu|\mu,\hat{\theta}_\mu)$ is the probability density function (pdf) of q_μ when the value μ of the POI is tested;
- $f(q_\mu|0,\hat{\theta}_0)$ is the pdf of q_μ when the background only hypothesis is tested (i.e. μ is set to zero).

The 95% CL limit on μ is then given by the solution to the equation $\text{CL}_s = 0.05$. The procedure described above is used to compute "observed" limits. To compute "expected" limits (i.e. to set limits without using the number of observed events in data) an Asimov dataset [139] is used instead of data.
The first step to compute expected limits is to perform a simultaneous fit including in the fit both control regions and the signal region with μ set to 0. Scale factors (k_W, k_Z) and the nuisance parameters related to systematic uncertainties are extracted and then used to built an Asimov dataset in the SR. The resulting number of events in the SR are used in place of N_{SR}^{obs}.

Appendix G

Improved MC statistics for W/Z backgrounds

As discussed in 5.19.3, an improvement result could be achieved by reducing systematics and improving MC statistics in the VBF phase space. Different efforts have been made on this topic and different solutions have been investigated to generate MC samples with higher statistics:

- define parton level filters on M_{jj} to populate the phase space of interest: the low M_{jj} bins have large cross sections, so even if only few events fluctuate to high-M_{jj} they have large statistical uncertainties. This implies to simulate and reconstruct a high fraction of events also in the low M_{jj} bins;
- use a generator at LO and apply the parton level filters described above. An LO generator (for instance Sherpa LO or Madgraph LO) would allow a faster generation of events (also in the low M_{jj} bins). However this comes with the complications of finding ways to estimate the theoretical systematics (if the theoretical systematics also increase the gain on the limit could be null). The strategy used by CMS has been to compare LO samples to NLO samples. This lead to a 30% theoretical uncertainty. Studies on this have shown that generating events with Sherpa LO or Madgraph LO is not fast enough to make it worth;
- generate a massive amounts of event at EVTGEN level, running a truth jet filter and reconstructing a small number of events needed for the analysis.

The third strategy has been the one adopted. A total of 552 million events for W and Z processes have been generated and a filter on *truth* jets has been applied. However, since the extended MC samples were not ready at the time this document has been written, the results with improved MC statistics are not shown here.

Bibliography

[1] ATLAS Collaboration, *Search for invisible Higgs boson decays in vector boson fusion at $\sqrt{s}$ =13 TeV with the ATLAS detector*, submitted to Physics Letters B., arXiv:1809.06682

[2] P. Warren Anderson, *Plasmons, Gauge Invariance, and Mass*, Phys.Rev., vol. 130, pp. 439-442, 1963.

[3] P. Higgs, *Broken Symmetries and the Masses of Gauge Bosons*, Phys.Rev.Lett., vol. 13, pp. 508-509, 1964.

[4] F. Englert, R. Brout, *Broken Symmetry and the Mass of Gauge Vector Mesons*, Phys.Rev.Lett., vol. 13, pp. 321-323, 1964.

[5] G. Guralnik, C. Hagen, T. Kibble, *Global Conservation Laws and Massless Particles*, Phys.Rev.Lett., vol. 13, pp. 585-587, 1964.

[6] Atlas Collaboration,*Updated coupling measurements of the Higgs boson with the ATLAS detector using up to 25fb^{-1} of proton-proton collision data*, ATLAS-CONF-2014-009

[7] LHC Higgs Cross Section Working Group. CERN Yellow Report 4

[8] The ATLAS collaboration, *Evidence for the $H \to b\bar{b}$ decay with the ATLAS detector* J. High Energ. Phys. (2017) 2017: 24. https://doi.org/10.1007/JHEP12(2017)024

[9] LHC Higgs Cross section Working Group collaboration, S. Heinemeyer, C. Mariotti, G. Passarino and R. Tanaka eds., *Handbook of LHC Higgs Cross sections: 3. Higgs Properties*, arXiv:1307.1347

[10] Gianfranco Bertone, Dan Hooper, and Joseph Silk, *Particle Dark Matter: Evidence, Candidates and Constraints*, Phys.Rept.405:279-390,2005

[11] M. Taoso, G. Bertone, A. Masiero, *Dark Matter Candidates: A Ten-Point Test*, JCAP 0803:022,2008

[12] Annika H. G. Peter, *Dark Matter: A Brief Review*, arXiv:1201.3942v1

[13] Matts Roos, *Dark Matter: The evidence from astronomy, astrophysics and cosmology*, (2010), arXiv:1001.0316 [astro-ph.CO]

[14] K. G. Begeman, A. Broeils, and R. Sanders, Mon. Not. R. Astr. Soc. 249, 523 (1991)

[15] M. J. Jee at al.*Discovery of a Ringlike Dark Matter Structure in the Core of the Galaxy Cluster Cl 0024+17*, (2007), The Astrophysical Journal Volume 661 Number 2

[16] S. Dodelson and L. M. Widrow, *Sterile Neutrinos as Dark Matter*, Phys. Rev. Lett. 72 (1994) 17 [arXiv:hep-ph/9303287]

[17] C. Skordis, *The Tensor-Vector-Scalar theory and its cosmology*, arXiv:0903.3602 [astro-ph.CO]

[18] R. Sanders, S. McGaugh, *Modified Newtonian Dynamics as an Alternative to Dark Matter*, Ann.Rev.Astron.Astrophys. 40 (2002) 263-317, arXiv:astro-ph/0204521

[19] Angus at al., *On the Law of Gravity, the Mass of Neutrinos and the Proof of Dark Matter*, Astrophys.J. 654 (2007) L13-L16

[20] Clowe at al., *Weak-Lensing Mass Reconstruction of the Interacting Cluster 1E 0657-558: Direct Evidence for the Existence of Dark Matter*, (2007), The Astr. Journal, Vol. 604, Issue 2, 596-603.

[21] Angus et al., *On the Proof of Dark Matter, the Law of Gravity and the Mass of Neutrinos*, Astrophys.J.654:L13-L16,2007

[22] P. Tisserand et al., *Limits on the Macho Content of the Galactic Halo from the EROS-2 Survey of the Magellanic Clouds*, Astron.Astrophys.469:387-404,2007, arXiv:astro-ph/0607207

[23] L. J. Rosenberg and K. A. van Bibber, Phys. Rept. 325 (2000) 1.

[24] Peccei, R. D.; Quinn, H. R. (1977). *CP Conservation in the Presence of Pseudoparticles*. Physical Review Letters 38 (25): 1440-1443

[25] Plank Collaboration, *Planck 2015 results. XIII. Cosmological parameters*, Astron.Astrophys. 594, A13 (2016)

[26] E. Kolb, M. Turner (1990), *The Early Universe*,Front.Phys. 69 (1990) 1-547

[27] Edward W. Kolb, Daniel J. H. Chung, Antonio Riotto, *WIMPZILLAS!*, AIP Conf.Proc. 484 (1999) no.1, 91-105 hep-ph/9810361 FERMILAB-CONF-98-325-A, arXiv:hep-ph/9810361

[28] Alexander Kusenko, Mikhail Shaposhnikov, *Supersymmetric Q-balls as dark matter*, Phys.Lett.B418:46-54,1998, arXiv:hep-ph/9709492

[29] David N. Spergel, Paul J. Steinhardt, *Observational evidence for self-interacting cold dark matter*, Phys.Rev.Lett.84:3760-3763,2000, arXiv:astro-ph/9909386

[30] John Ellis, *Particle Candidates for Dark Matter*, Phys.Scripta T85:221-230,2000, arXiv:astro-ph/9812211

[31] G. Bertone et al., *Particle Dark Matter - Observations, Models and Searches*, Cambridge Univ. Press (2010) DOI: 10.1017/CBO9780511770739

[32] G. Busoni, A. De Simone, E. Morgante, A. Riotto, *On the validity of the effective field theory for dark matter searchs at the LHC*, Physics Letters B 728C (2014)

[33] Supernova Search Team Collaboration, A. G. Riess et al., *Observational Evidence from Supernovae for an Accelerating Universe and a Cosmological Constant*, Astron. J. 116 (1998) 1009-1038, arXiv:astro-ph/9805201.

[34] Supernova Cosmology Project Collaboration, S. Perlmutter et al., *Measurements of Omega and Lambda from 42 High-Redshift Supernovae*, Astrophys. J. 517 (1999) 565-586, arXiv:astro-ph/9812133.

[35] SDSS Collaboration, M. Tegmark et al., *Cosmological parameters from SDSS and WMAP*, Phys.Rev. D69 (2004) 103501, arXiv:astro-ph/0310723 [astro-ph].

[36] E. Hawkins, S. Maddox, S. Cole, D. Madgwick, P. Norberg, et al., *The 2dF Galaxy Redshift Survey: Correlation functions, peculiar velocities and the matter density of the universe*, Mon.Not.Roy.Astron.Soc. 346 (2003) 78, arXiv:astro-ph/0212375 [astro-ph].

[37] Nima Arkani-Hamed, Savas Dimopoulos, and G.R. Dvali. (1998) *The Hierarchy problem and new dimensions at a millimeter* Phys.Lett., B429:263-272

[38] R. J. Gaitskell, *Direct Detection of dark matter*, Ann. Rev. of Nuclear and Particle Science. 54 (2004) 315

[39] S. Profumo, *Astrophysical probes of dark matter*, arXiv:1301.0952v1 [hep-ph]

[40] F. Kahlhoefer, *Review of LHC Dark Matter Searches*, Int.J.Mod.Phys. A32 (2017) 1730006

[41] S. Kanemura, S. Matsumoto, T. Nabeshima and N. Okada, *Can WIMP dark matter overcome the nightmare scenario?*, Phys. Rev. D 82 (2010) 055026 [arXiv:1005.5651]

[42] A. Djouadi, O. Lebedev, Y. Mambrini and J. Quevillon, *Implications of LHC searches for Higgs-portal dark matter*, Phys. Lett. B 709 (2012) 65 [arXiv:1112.3299]

[43] M. Hoferichter et al., *Improved limits for Higgs-portal dark matter from LHC searches*, Phys. Rev. Lett. 119, 181803 (2017)

[44] Lyndon Evans and Philip Bryant, *LHC Machine*, JINST, 3:S08001, 2008

[45] The ATLAS Collaboration, Luminosity public results *https* : *//twiki.cern.ch/twiki/bin/view/AtlasPublic/LuminosityPublicResultsRun*2

[46] The ATLAS Collaboration, *The ATLAS Experiment at the CERN Large Hadron Collider*, JINST 3 (2008) S08003

[47] *ATLAS: letter of intent for a general-purpose pp experiment at the large hadron collider at CERN*, Letter of Intent, CERN, Geneva, 1992

[48] ATLAS Collaboration, *ATLAS: Technical proposal for a general-purpose pp experiment at the Large Hadron Collider at CERN*, CERN-LHCC-94-43

[49] S. Myers and E. Picasso, *The Design, construction and commissioning of the CERN Large Electron Positron collider*, Contemp. Phys., 31:387-403, 1990

[50] The CMS Collaboration, *The CMS experiment at the CERN LHC*, JINST 3 (2008) S08004

[51] The LHCb Collaboration, *The LHCb Detector at the LHC*, JINST 3 (2008) S08005

[52] The ALICE Collaboration, *The ALICE experiment at the CERN LHC*, JINST 3 (2008) S08002

[53] http://atlasexperiment.org/photos/how-atlas-works.html

[54] The TOTEM Collaboration, *The TOTEM experiment at the CERN Large Hadron Collider*, JINST 3 (2008) S08007

[55] The MoEDAL Collaboration, *Techinical Deisgn Report of the MoEDAL experiment*, Tech. rep. CERN-LHCC-2009-006. MoEDAL-TDR-001. Geneva: CERN,2009

[56] The LHCf Collaboration, *The LHCf detector at the CERN Large Hadron Collider*, JINST 3 (2008) S08006

[57] The ATLAS Collaboration, *The ATLAS Inner Detector commissioning and calibration*, Eur.Phys.J. C70 (2010) 787-821

[58] T. G. Corneissen et al., *Updates of the ATLAS Tracking Event Data Model*, ATL-SOFT-PUB-2007-003

[59] Norbert Wermes and G Hallewel, *ATLAS pixel detector: Technical Design Report*, Technical Design Report ATLAS. CERN, Geneva, 1998

[60] M. Capeans et al. *ATLAS Insertable B-Layer Technical Design Report*, Technical Report CERN-LHCC-2010-013. ATLAS-TDR- 19, Sep 2010

[61] A. Abdesselam et al. *The barrel modules of the ATLAS semiconductor tracker*, Nucl. Instrum. Meth., A568:642-671, 2006

[62] E. Abat et al. *The ATLAS TRT barrel detector* JINST, 3:P02014, 2008

[63] E. Abat et al. *The ATLAS TRT end-cap detectors* JINST, 3:P10003, 2008

[64] ATLAS Collaboration, G. Aad et al., *Expected Performance of the ATLAS Experiment, Detector, Trigger and Physics*, CERN-OPEN-2008-020 (2008) , arXiv:0901.0512 [hep-ex]

[65] ATLAS Collaboration, *Electron and photon energy calibration with the ATLAS detector using LHC Run 1 data*, CERN-PH-EP-2014-153, arXiv:1407.5063 [hep-ex]

[66] ATLAS Collaboration, *Measurement of the W-boson mass in pp collisions at* $\sqrt{s}$ *=7 TeV with the ATLAS detector*, arXiv:1701.07240

[67] ATLAS Collaboration, *ATLAS level-1 trigger: Technical Design Report*, CERN-LHCC-98-014.

[68] ATLAS Collaboration, *Performance of the ATLAS trigger system in 2015*, Eur. Phys. J. C (2017) 77: 317. https://doi.org/10.1140/epjc/s10052-017-4852-3

[69] S. Hoche, *Introduction to parton-shower event generators*, SLAC-PUB-16160, arXiv:1411.4085

[70] J D Chapman et al. , *The ATLAS detector digitization project for 2009 data taking*, Journal of Physics: Conference Series 219 (2010) no. 3, 032031.

[71] ATLAS Collaboration, *The ATLAS Simulation Infrastructure*, Eur. Phys. J. C 70 (2010) 823, arXiv: 1005.4568

[72] S. Agostinelli et al. *GEANT4: A simulation toolkit*, Nucl. Instrum. Meth. , A506:250-303,2003. doi: 10.1016/S0168-9002(03)01368-8.

[73] ATLAS Collaboration, *The simulation principle and performance of the ATLAS fast calorimeter simulation FastCaloSim*, ATLAS-PHYS-PUB-2010-013, (2010).

[74] T. Cornelissen et al., *Concepts, Design and Implementation of the ATLAS New Tracking (NEWT)*, ATL-SOFT-PUB-2007-007 (2007)

[75] ATLAS Collaboration, *Performance of the ATLAS Silicon Pattern Recognition Algorithm in Data and simulation at* $\sqrt{s}$ *=7 TeV*, ATLAS-CONF-2010-072 (2010)

[76] ATLAS Collaboration, *Electron efficiency measurements with the ATLAS detector using the 2015 LHC proton-proton collision data*, ATLAS-CONF-2016-024

[77] ATLAS Collaboration, *Electron and photon energy calibration with the ATLAS detector using data collected in 2015 at* $\sqrt{s}$ *=13 TeV*, ATL-PHYS-PUB-2016-015

[78] ATLAS Collaboration, *Muon reconstruction performance of the ATLAS detector in protonproton collision data at* $\sqrt{s}$ *=13 TeV*, Eur.Phys.J. C76 (2016) no.5, 292

[79] M. Cacciari, G. P. Salam, and G. Soyez, *The anti-kt jet clustering algorithm*, JHEP 04 (2008) 063, arXiv:0802.1189 [hep-ph]

[80] J. E. Huth, N. Wainer, K. Meier, N. Hadley, F. Aversa, et al., *Toward a standardization of jet definitions*, In Snowmass 1990, Proceedings, Research directions for the decade 134-136 and Fermilab Batavia - FERMILAB-Conf-90-249 (90/12,rec.Mar.91) 6 p. (105313) FERMILAB-CONF-90-249-E, FNAL-C-90-249-E

[81] ATLAS Collaboration, *Topological cell clustering in the ATLAS calorimeters and its performance in LHC Run 1*, Eur.Phys.J. C77 (2017) 490

[82] ATLAS Collaboration, *Jet Calibration and Systematic Uncertainties for jets reconstructed in the ATLAS Detector at* $\sqrt{s}$ *= 13 TeV*, ATL-PHYS-PUB-2015-015 (2015)

[83] ATLAS Collaboration, *Pile-up subtraction and suppression for jets in ATLAS*, ATLAS-CONF-2013-083, 2013

[84] ATLAS Collaboration, *Tagging and suppression of pileup jets with the ATLAS detector*, ATLAS-CONF-2014-018

[85] ATLAS Collaboration, *Expected performance of missing transverse momentum reconstruction for the ATLAS detector at* $\sqrt{(s)}$ *= 13 TeV*, ATL-PHYS-PUB-2015-023

[86] ATLAS Collaboration, *Performance of missing transverse momentum reconstruction for the ATLAS detector in the first proton-proton collisions at* $\sqrt{(s)}$ *= 13 TeV*, ATL-PHYS-PUB-2015-027

[87] ATLAS Collaboration *Data-driven determination of the energy scale and resolution of jets reconstructed in the ATLAS calorimeters using dijet and multijet events at* $\sqrt{s}$ *=8 TeV*, ATLAS-CONF-2015-017

[88] Gavin P. Salam, Towards Jetography, The European Physical Journal C, June 2010, Volume 67, Issue 3-4, pp 637-686. arXiv:0906.1833 [hep-ph].

[89] P. Nason, *A new method for combining NLO QCD with shower Monte Carlo algorithms*, JHEP 0411 (2004) 040, arXiv: hep-ph/0409146 [hep-ph]

[90] T. Sjostrand, S. Mrenna and P. Z. Skands, *A Brief Introduction to PYTHIA 8.1*, Comput.Phys.Commun. 178 (2008) 852-867, arXiv:0710.3820 [hep-ph].

[91] P. Z. Skands, *Tuning Monte Carlo generators: The Perugia tunes*, Phys. Rev. D 82 (7 2010) 074018

[92] G. Corcella et al., *HERWIG 6: An Event generator for hadron emission reactions with interfering gluons (including supersymmetric processes)*, JHEP 0101 (2001) 010.

[93] I. Antoniadis, M. Tuckmantel and F. Zwirner, *Phenomenology of a leptonic goldstino and invisible Higgs boson decays*, Nucl.Phys. B707 (2005) 215-232

[94] N. Arkani-Hamed et al., *Neutrino masses from large extra dimensions*, Phys.Rev. D65 (2002) 024032

[95] A. Datta et al., *Invisible Higgs in theories of large extra dimensions*, Phys.Rev. D70 (2004) 075003

[96] S. Kanemura et al., *Can WIMP Dark Matter overcome the Nightmare Scenario?*, Phys.Rev. D82 (2010) 055026

[97] A. Djouadi et al., *Implications of LHC searches for Higgs portal dark matter*, Phys.Lett. B709 (2012) 65-69

[98] R. E. Shrock and M. Suzuki, *Invisible decays of Higgs bosons*, Phy. Lett. B 110 (1982) 250

[99] ATLAS, CMS Collaborations, *Measurements of the Higgs boson production and decay rates and constraints on its couplings from a combined ATLAS and CMS analysis of the LHC pp collision data at* $\sqrt{s} = 7$ *and 8 TeV*, JHEP08(2016)045

[100] ATLAS Collaboration, *Search for invisible decays of a Higgs boson using vector-boson fusion in pp collisions at* $\sqrt{s}$ *=8 TeV with the ATLAS detector*, J. High Energ. Phys. (2016) 2016: 172. https://doi.org/10.1007/JHEP01(2016)172

[101] ATLAS Collaboration, *Search for Invisible Decays of a Higgs Boson Produced in Association with a Z Boson in ATLAS*, Phys. Rev. Lett. 112 (2014) 201802, arXiv: 1402.3244 [hep-ex].

[102] The ATLAS Collaboration, *Search for new phenomena in the* $Z(\rightarrow \ell\ell) + E_{\mathrm{T}}^{\mathrm{miss}}$ *final state at* $\sqrt{s} = 13$ *TeV with the ATLAS detector*, ATLAS-CONF-2016-056

[103] The ATLAS Collaboration, *Search for an invisibly decaying Higgs boson or dark matter candidates produced in association with a Z boson in pp collisions at* $\sqrt{s} =$ *13 TeV with the ATLAS detector*, Submitted to: Phys. Lett. B, arXiv:1708.09624

[104] The ATLAS Collaboration, *Search for invisible decays of the Higgs boson produced in association with a hadronically decaying vector boson in pp collisions at* $\sqrt{s}$ *=8 TeV with the ATLAS detector*, Eur. Phys. J. C (2015) 75: 337. https://doi.org/10.1140/epjc/s10052-015-3551-1

[105] The ATLAS collaboration, *Constraints on new phenomena via Higgs boson couplings and invisible decays with the ATLAS detector* J. High Energ. Phys. (2015) 2015: 206

[106] CMS collaboration, *Search for invisible decays of Higgs bosons in the vector boson fusion and associated ZH production modes*, EPJC 74 (2014) 2980

[107] CMS Collaboration, *A combination of searches for the invisible decays of the Higgs boson using the CMS detector*, CMS PAS HIG-15-012

[108] CMS Collaboration, *Search for invisible decays of a Higgs boson produced via vector boson fusion at* $\sqrt{s}$ *= 13 TeV*, CMS PAS HIG-16-009

[109] CMS Collaboration, *Search for invisible decays of the Higgs boson produced through vector boson fusion at* $\sqrt{s}$ *= 13 TeV*, CMS PAS HIG-17-023

[110] CMS collaboration, *Search for dark matter, invisible Higgs boson decays, and large extra dimensions in the* $\ell\ell + E_{\mathrm{T}}^{\mathrm{miss}}$ *final state using 2016 data*, CMS-PAS-EXO-16-052

[111] CMS collaboration, *Search for dark matter produced with an energetic jet or a hadronically decaying W or Z boson at* $\sqrt{(s)}$ *= 13 TeV*, JHEP 07 (2017) 014

[112] CMS collaboration, *Searches for invisible decays of the Higgs boson in pp collisions at* $\sqrt{s}$ *= 7, 8, and 13 TeV*, JHEP 02 (2017) 135

[113] M. Ciccolini et al, *Electroweak and QCD corrections to Higgs production via vector-boson fusion at the LHC*, Phys.Rev.D77:013002,2008

[114] M. Ciccolini et al., *Strong and electroweak corrections to the production of Higgs+2jets via weak interactions at the LHC*, Phys.Rev.Lett.99:161803,2007

[115] T. Han et al, *Structure Function Approach to Vector-Boson Scattering in pp Collisions*, Phys.Rev.Lett. 69 (1992) 3274-3277

[116] Matteo Cacciari et al, *Fully Differential Vector-Boson-Fusion Higgs Production at Next-to-Next-to-Leading Order*, Phys Rev Lett. 115(8):082002 (2015)

[117] T. Gleisberg et al., *Event generation with SHERPA 1.1*, JHEP 02 (2009) 007, arXiv:0811.4622

[118] T. Gleisberg and S. Hoche, *Comix, a new matrix element generator*, JHEP 12 (2008) 039, arXiv:0808.3674

[119] F. Cascioli at al, *Scattering Amplitudes with Open Loops*, Phys. Rev. Lett. 108 (2012) 111601, arXiv:1111.5206

[120] S. Schumann and F. Krauss, *A Parton shower algorithm based on Catani-Seymour dipole factorisation*, JHEP 03 (2008) 038, arXiv:0709.1027

[121] S. Hoche et al., *QCD matrix elements + parton showers: The NLO case*, JHEP 04 (2013) 027, arXiv:1207.5030

[122] R. D. Ball et al., *Parton distributions for the LHC Run II*, JHEP 04 (2015) 040, arXiv:1410.8849

[123] S. Frixione, P. Nason and G. Ridolfi, *A Positive-weight next-to-leading-order Monte Carlo for heavy flavour hadroproduction*, JHEP 09 (2007) 126

[124] H.-L. Lai et al., *New parton distributions for collider physics*, Phys. Rev. D 82 (2010) 074024

[125] T. Sjostrand, S. Mrenna and P. Z. Skands, *PYTHIA 6.4 physics and manual*, JHEP 05 (2006) 026

[126] ATLAS Collaboration, *Selection of jets produced in 13 TeV proton-proton collisions with the ATLAS detector*, ATLAS-CONF-2015-029

[127] ATLAS Collaboration, *Monte Carlo Calibration and Combination of In-situ Measurements of Jet Energy Scale, Jet Energy Resolution and Jet Mass in ATLAS*, Technical Report ATLAS-CONF-2015-037, CERN, Geneva (2015)

[128] A. Denner et al., *HAWK 2.0: A Monte Carlo program for Higgs production in vector-boson fusion and Higgs strahlung at hadron colliders*, Comput. Phys. Commun. 195 (2015) 161-171, arXiv:1412.5390 [hep-ph].

[129] ATLAS Collaboration, *Search for squarks and gluinos with the ATLAS detector in final states with jets and missing transverse momentum using 4.7 fb^{-1} of $\sqrt{s}$ = 7 TeV proton-proton collision data*, Phys. Rev. D87, 012008

[130] VBF Higgs invisible analysis team, *Search for an invisibly decaying Higgs boson produced via Vector Boson Fusion in pp collisions at $\sqrt{s}$ =13 TeV using data collected by the ATLAS Experiment*, ATLAS Internal Note, ATL-COM-PHYS-2016-1802, https://cds.cern.ch/record/2239661

[131] J. M. Campbell, R. K. Ellis, and C. Williams, *Vector boson pair production at the LHC*, JHEP 07 (2011) 018, arXiv:1105.0020 [hep-ph]

[132] I. W. Stewart and F. J. Tackmann, *Theory uncertainties for Higgs and other searches using jet bins*, Phys. Rev. D85 (2012) 034011, arXiv:1107.2117 [hep-ph]

[133] J. M. Lindert et al., *Precise predictions for V+jets dark matter backgrounds*, Eur.Phys.J. C77 (2017) no.12, 829, arXiv: 1705.04664 [hep-ph]

[134] K. Cranmer et al, *HistFactory: A tool for creating statistical models for use with RooFit and RooStats*, (2012), CERN-OPEN-2012-016

[135] *https://twiki.cern.ch/twiki/bin/view/RooStats/WebHome*

[136] *http://root.cern.ch/drupal/content/roofit*

[137] Ilka Antcheva et al., *ROOT - A C++ framework for petabyte data storage, statistical analysis and visualization*, Computer Physics Communications; Anniversary Issue; Volume 180, Issue 12, December 2009, Pages 2499-2512.

[138] Baak, M. et al., *HistFitter software framework for statistical data analysis*, Eur. Phys. J. C (2015)

[139] G. Cowan, K. Cranmer, E. Gross, and O. Vitells, *Asymptotic formulae for likelihood-based tests of new physics*, Eur. Phys. J. C71 (2011) 1554, arXiv:1007.1727

[140] L. Read, *Presentation of search results: The CL(s) technique*, J. Phys. G 28(2002) 2693-2704.

[141] M. Cirelli, N. Fornengo, A. Strumia, *Minimal Dark Matter*, Nucl.Phys.B753:178-194,2006, arXiv:hep-ph/0512090v4

[142] M. Cirelli, A. Strumia, M. Tamburini, *Cosmology and Astrophysics of Minimal Dark Matter*, Nucl.Phys.B787:152-175,2007, arXiv:0706.4071v2

[143] M. Cirelli, A. Strumia, *Minimal Dark Matter: model and results*, New J.Phys.11:105005,2009, arXiv:0903.3381v3

[144] L. Di Luzio, R. Grober, J. F. Kamenik, M. Nardecchia, *Accidental matter at the LHC*, High Energ. Phys. (2015) 2015: 74, arXiv:1504.00359

[145] Andrea Mitridate, Michele Redi, Juri Smirnov, Alessandro Strumia, *Cosmological Implications of Dark Matter Bound States*, Journal of Cosmology and Astroparticle Physics, JCAP05(2017)006

[146] M. Cirelli, F. Sala, M. Taoso, *Wino-like Minimal Dark Matter and future colliders*, JHEP 1410 (2014) 033, arXiv:1407.7058v2

[147] J. de Favereau et al., *DELPHES 3*, JHEP 1402 (2014) 057, arXiv:1307.6346 [hep-ex]

[148] ATLAS Collaboration, *Search for charginos nearly mass-degenerate with the lightest neutralino based on a disappearing-track signature in pp collisions at* $\sqrt{s} = 8$ *TeV with the ATLAS detector*, Phys. Rev. D 88 112006 (2013)

[149] ATLAS Collaboration, *Search for long-lived charginos based on a disappearing-track signature in pp collisions at* $\sqrt{s} = 13$ *TeV with the ATLAS detector*, arXiv:1712.02118v1

[150] J. Alwall et al., *The automated computation of tree-level and next-to-leading order differential cross sections, and their matching to parton shower simulations*, JHEP07(2014)079

[151] F. Maltoni, Stelzer, *MADEVENT: Automatic Event Generation with MADGRAPH*, J. High Energy Phys. 02, 027 (2003)

[152] J. Alwall, M. Herquet, F. Maltoni, O. Mattelaer, T. Stelzer, *MadGraph 5 : Going Beyond*, JHEP 06, 128 (2011)

[153] ALEPH Collaboration, *Search for charginos nearly mass degenerate with the lightest neutralino in* e^+e^- *collisions at centre-of-mass energies up to 209GeV*, Phys.Lett.B533:223-236,2002

[154] OPAL collaboration, *Search for Nearly Mass-Degenerate Charginos and Neutralinos at LEP*, Eur.Phys.J.C29:479-489,2003

[155] Jonathan L. Feng, Jean-Francois Grivaz, Jane Nachtman, *Searches for Supersymmetry at High-Energy Colliders*, Rev. Mod. Phys. 82:699-727,2010

[156] Ahmed Ismail, Eder Izaguirre, Brian Shuve, *Illuminating New Electroweak States at Hadron Colliders*, Phys. Rev. D 94, 015001 (2016)

[157] ATLAS Collaboration, *Performance of algorithms that reconstruct missing transverse momentum in $\sqrt{s} = 8$ TeV proton-proton collisions in the ATLAS detector*, Eur. Phys. J. C77 (2017) 241

université PARIS-SACLAY | ÉCOLE DOCTORALE PHENIICS

Titre : Recherche de nouvelle physique dans le mode de production VBF dans un état final avec une grande énergie transverse manquante avec le détecteur ATLAS

Mots clés : matière noire, boson de Higgs, Large Hadron Collider, physique au-delà du modèle standard, Physique au LHC, désintégration du boson de Higgs en particules invisibles, Minimal Dark Matter

Résumé : Cette thèse présente des recherches sur la nouvelle physique produite par le processus de Fusion de Bosons Vecteur (VBF) dans les états finaux avec une grand impulsion transverse manquante (Etmiss) en utilisant 36.1 fb^{-1} de données de collisions proton-proton avec une énergie dans le centre de masse de 13 TeV, recueillies par l'expérience ATLAS au Large Hadron Collider (LHC) au CERN en 2015 et 2016. En particulier, elle se concentre sur la recherche de la désintégration invisible du boson de Higgs produit via le mode VBF. Comme le modèle standard de la physique des particules (MS) prédit une désintégration invisible de Higgs uniquement à travers le mode H→ZZ*→ νννν avec un rapport d'embranchement BR~0.1%, si une désintégration en particules invisibles du boson de Higgs était observée avec un BR supérieur, ce serait un signe de nouvelle physique. Plusieurs modèles au-delà du modèle standard (BSM) prédisent des désintégrations du boson de Higgs en particules de matière noire (DM, non détectées) ou en particules massives neutres à vie longue. Parmi les recherches H → particules invisibles, la plus sensible est celle où le Higgs est produit via le mode VBF. Son état final est caractérisé par deux jets énergétiques, avec les caractéristiques typiques du mode VBF (c'est-à-dire une grande séparation angulaire et une grande masse invariante des deux jets) et une grande impulsion transverse manquante (Etmiss> 180 GeV). Pour sélectionner un échantillon d'événements candidats de signal, une région de signal (SR) est définie pour maximiser la fraction d'événements de signal attendus par rapport à la prédiction du MS (bruit de fond). Les processus MS qui peuvent peupler la SR proviennent principalement des processus Z → νν + jets et W → lν + jets, où le lepton est perdu ou non reconstruit. Leur contribution est estimée avec une approche semi-*data driven*: des régions dédiées enrichies en événements W→ lν / Z→ ll sont utilisées pour normaliser les données des estimations de Monte Carlo (MC) en utilisant une technique de fit simultané (méthode du facteur de transfert) et pour les extrapoler à la SR.
L'estimation de fond prédit est comparée aux données SR observées. Comme aucun excès n'est trouvé, une limite supérieure sur le BR (H→ invisible) est calculée.
L'analyse est ensuite réinterprétée dans le cadre de modèles inspirés du modèle Minimal Dark Matter. Le cas d'un nouveau triplet fermionique électrofaible, avec une hypercharge nulle et respectant le nombre B-L, ajouté au MS fournit un bon candidat Dark Matter (WIMP pur). Si on considère l'abondance thermique, la masse du composant neutre est d'environ 3 TeV. Cependant des masses plus faibles sont également envisageables dans le cas de mécanismes de production non thermiques ou lorsque le triplet ne constitue qu'une fraction de l'abondance de DM. Il peut être produit à des collisionneurs proton-proton tels que le LHC et il peut être sondé de différentes manières. Une fois produites, les composantes chargées du triplet se désintègrent dans le composant neutre le plus léger, $\chi 0$, avec en plus des pions très mous, en raison de la petite différence de masse entre les composants neutres et chargés. Ces pions de très faible impulsion ne peuvent pas être reconstruits et sont donc perdus. Le $\chi 0$ est reconstruit comme de l'Etmiss dans le détecteur. Par conséquent, lorsqu'il est produit via VBF, il donne lieu à une signature avec deux jets VBF et de l'Etmiss, le même état final que celui qui a été étudié pour l'analyse de VBF Higgs→invisible. Des points de masse différentes (de 90 GeV à 200 GeV) ont été engendrés avec les programmes Monte Carlo Madgraph + Pythia, dans le cadre du logiciel officiel ATLAS, et les limites supérieures sont définies sur la section efficace fiducielle de production. Des extrapolations à des luminosités plus élevées (Run3 et HL-LHC) en utilisant une approche simplifiée sont également présentées.

Université Paris-Saclay
Espace Technologique / Immeuble Discovery
Route de l'Orme aux Merisiers RD 128 / 91190 Saint-Aubin, France

université PARIS-SACLAY | ÉCOLE DOCTORALE PHENIICS

Title : Search for new physics produced via Vector Boson Fusion in final states with large missing transverse momentum with the ATLAS detector

Keywords : Dark Matter, Higgs boson, Large Hadron Collider, Physics beyond the Standard Model, Physics at the LHC, Higgs invisible decay, Minimal Dark Matter

Abstract : This thesis presents searches for new physics produced via Vector Boson Fusion (VBF) in final states with large Missing Transverse Momentum (Etmiss) using 36.1 fb^{-1} of data from proton-proton collisions at center-of-mass-energy of 13 TeV, collected by the ATLAS experiment at the Large Hadron Collider at CERN during 2015 and 2016. In particular, it focuses on the search for the invisible decay of the Higgs boson produced via the vector boson fusion (VBF) process. As the SM predicts an Higgs invisible decay only through $H \rightarrow ZZ^* \rightarrow \nu\nu\nu\nu$ with Branching Ratio BR~0.1%, if an invisibly decaying Higgs boson would be observed with a higher BR, this would be a sign of new physics. Several Beyond the Standard Model (BSM) models predict invisibly decaying Higgs boson where the Higgs can decay into dark matter particles or neutral long-lived massive particles. Among the $H \rightarrow$ invisible searches the most sensitive one is the one where the Higgs is produced via the VBF process. Its final state is characterized by two energetic jets, with the typical features of the VBF mode (i.e. large angular separation and large invariant mass) and large missing transverse momentum (Etmiss>180 GeV). To select a sample of signal candidate events, a Signal Region (SR) is designed to maximize the fraction of expected signal events with respect to the SM prediction (backgrounds). The SM processes, which can populate the SR, comes mainly from $Z \rightarrow \nu\nu$+jets and $W \rightarrow l\nu$+jets processes, where the lepton is lost or not reconstructed. Their contribution is estimated with a semi data driven approach: dedicated regions enriched in $W \rightarrow l\nu$/$Z \rightarrow ll$ events are used to normalize to data the Monte Carlo (MC) estimates using a simultaneous fitting technique (transfer factor) and to extrapolate them to the SR. The predicted background estimate is compared to the observed SR data. Since no excess is found, an upper limit on the BR($H \rightarrow$inv) is set.

The analysis is then reinterpreted in the context of models inspired by the Minimal Dark Matter model. The case of a new electroweak fermionic triplet, with null hypercharge and respecting the B-L number, added on top of the SM provides a good Dark Matter candidate (pure WIMP). If the thermal abundance is assumed, the mass of the neutral component is 3 TeV, however smaller masses are also allowed in case of non-thermal production mechanisms or if the triplet constitutes only a fraction of the DM abundance. It can be produced at proton-proton colliders such as the LHC and it can be probed in different ways. Once produced, the charged components of the triplet decays into the lightest neutral component χ^0 plus very soft charged pions. χ^0 is reconstructed as Etmiss in the detector while the pions, because of the small mass splitting between the neutral and charged components, are so soft that are lost and are not reconstructed. Therefore, when produced via VBF, it gives rise to a signature with two VBF jets and Etmiss, the same final state that has been investigated for the VBF Higgs invisible analysis. Different mass point (from 90 GeV to 200 GeV) have been generated with the Madgraph+Pythia, Monte Carlo programs within the official ATLAS software, and upper limits are set on the fiducial cross section. Extrapolations to higher luminosities using a simplified approach are also presented.

Université Paris-Saclay
Espace Technologique / Immeuble Discovery
Route de l'Orme aux Merisiers RD 128 / 91190 Saint-Aubin, France